Aus dem Institut für Physik der Universität Potsdam


# CIRCUMPLANETARY DUST DYNAMICS:

# APPLICATION TO MARTIAN DUST TORI AND ENCELADUS DUST PLUMES

**Dissertation**

zur Erlangung des akademischen Grades
"doctor rerum naturalium"
(Dr. rer. nat.)
in der Wissenschaftsdisziplin Theoretische Physik

eingereicht an der
Mathematisch–Naturwissenschaftlichen Fakultät
der Universität Potsdam

von
Martin Makuch

Potsdam, den 15. November 2006

**Abstract**

Our Solar system contains a large amount of dust, containing valuable information about our close cosmic environment. If created in a planet's system, the particles stay predominantly in its vicinity and can form extended dust envelopes, tori or rings around them. A fascinating example of these complexes are Saturnian rings containing a wide range of particles sizes from house-size objects in the main rings up to micron-sized grains constituting the E ring. Other example are ring systems in general, containing a large fraction of dust or also the putative dust-tori surrounding the planet Mars. The dynamical " life" of such circumplanetary dust populations is the main subject of our study.

In this thesis a general model of creation, dynamics and "death" of circumplanetary dust is developed. Endogenic and exogenic processes creating dust at atmosphereless bodies are presented. Then, we describe the main forces influencing the particle dynamics and study dynamical responses induced by stochastic fluctuations. In order to estimate the properties of steady-state population of considered dust complex, the grain mean lifetime as a result of a balance of dust creation, "life" and loss mechanisms is determined. The latter strongly depends on the surrounding environment, the particle properties and its dynamical history. The presented model can be readily applied to study any circumplanetary dust complex.

As an example we study dynamics of two dust populations in the Solar system. First we explore the dynamics of particles, ejected from Martian moon Deimos by impacts of micrometeoroids, which should form a putative tori along the orbit of the moon. The long-term influence of indirect component of radiation pressure, the Poynting-Robertson drag gives rise in significant change of torus geometry. Furthermore, the action of radiation pressure on rotating non-spherical dust particles results in stochastic dispersion of initially confined ensemble of particles, which causes decrease of particle number densities and corresponding optical depth of the torus.

Second, we investigate the dust dynamics in the vicinity of Saturnian moon Enceladus. During three flybys of the Cassini spacecraft with Enceladus, the on-board dust detector registered a micron-sized dust population around the moon. Surprisingly, the peak of the measured impact rate occurred 1 minute before the closest approach of the spacecraft to the moon. This asymmetry of the measured rate can be associated with locally enhanced dust production near Enceladus south pole. Other Cassini instruments also detected evidence of geophysical activity in the south polar region of the moon: high surface temperature and extended plumes of gas and dust leaving the surface. Comparison of our results with this in situ measurements reveals that the south polar ejecta may provide the dominant source of particles sustaining the Saturn's E ring.

# Contents

# Chapter 1

# Introduction

Our Solar system is not composed by the Sun and the eight planets only. Additionally besides asteroidal and cometary objects it contains a significant amount of dust. In the past, the cosmic dust was being overlooked or even considered as nonexistent. Some well known phenomena as meteors, zodiacal light or cometary tails, which were for long time being considered to be of atmospheric origin, have been related to cosmic dust for the first time in the 17th century. The observation of a spectacular Leonid meteor shower (left panel of Fig. 1.1) and the fact that the meteors appeared to emerge from a stationary point in the constellation Leo led many scientists to the conclusion that these meteors were of extraterrestrial origin. The idea that the observed meteors or so-called "shooting stars" are caused by dust particles entering the Earth's atmosphere was put forward for the first time by Ernst Chladni, the father of acoustics. Similarly, Giovanni Cassini proposed that the phenomena as zodiacal light (right panel of Fig. 1.1) or gegenschein are results of light being scattered at dust complexes in the ecliptic. Slowly, with the overall headway in astronomy, "empty" space between planets and stars "got filled" by gas clouds and dust particles. Even in the beginning of the 20th century astronomers considered dust in space merely as an annoying obstacle, that blocks the light coming from astronomical objects.

Figure 1.1: left: An all-sky image taken during the maximum of the 1998 Leonid meteor shower, when the peak rate of meteors reached about 400 per hour. There are 156 shooting stars brighter than $-2$ magnitudes recorded in this image (Juraj Toth, Modra Observatory, Slovakia). right: A photograph of the *zodiacal light* near the Eastern horizon before sunrise in Namibia. Sunlight is scattered at interplanetary dust particles lying predominantly along the plane of ecliptic (Stefan Seip, APOD, ap040825). A similar band of light located at 180° from the Sun is called *gegenschein*.

However, this view changed with the technological progress at the beginning of the era of space research and dust became increasingly interesting and important in astronomy. Techniques as *Remote sensing* (infrared astronomy) and *in situ* measurements (dust detectors mounted on space probes, particles gathered with aircrafts in the upper atmosphere) uncovered secrets encrypted in the grains. In many respects *dust astronomy* (Grün, 2002) is similar to classical optical astronomy: Photons as well as dust grains are created at an observed cosmic object a star, planet, satellite, asteroid, comet, etc. and then they travel through space until they reach our (optical or infrared) telescopes or dust detectors. Thus the dust population carries information about place (cosmic object) and physical process of its creation. But, unlike photons, which point directly to the source of their creation by travelling along geodetic paths, a dust particle is subject to a set of perturbing forces. Beyond gravity there are e.g. radiation forces, electro-magnetic forces, and drag forces causing rather complicated trajectory obscuring their origin. Thus, in situ or remote detection is not sufficient but has to be completed by the investigation of trajectories in order to identify their sources. In situ measurements actually allow for direct study of dust grains either directly in space (e.g. cosmic-dust analyser (CDA) on-board the Cassini-spacecraft) or on the Earth (e.g. Apollo Moon's samples, dust brought by Stardust spacecraft). In fact, it is not only sufficient to know the sources and the subsequent dynamics of dust, but also the places where dust grains "die" have to be known. Only the trio of "birth", dynamical "life" and "death" of dust grains gives a complete picture about the dust population. Representative examples of these are e.g. dust-disks around stars, dust constituting cometary tails and the diffuse, faint rings around all the giant planets in our Solar system, dust tori expected to surround the orbits of the Martian satellites Phobos and Deimos or dust-clouds enveloping atmosphereless satellites. But what is dust made of, where does it come from and how do we observe it?

In general, dust refers to particles in space ranging in the size from a compound of several molecules ($\sim$ a few nanometres) up to ten-millimeter grains. They show individual shapes, material composition and structure. Although this division is vague, the lower limit distinguishes a dust grain from plasma particles. Grains larger than the upper limit are conventionally defined as meteoroids (i.e. micrometeoroids). In contrast to meteoroids, which are mainly influenced by gravity, dust grains are subject to many non-gravitational forces. As already mentioned the latter is needed to identify the dust sources as well as to determine the mean lifetimes, and simultaneously the number densities of the members of a dust population.

What are the major processes and places in the universe where dust is generated? Based on their creation, we may divide the dust particles into primordial and secondary dust. The first scenario (i) is a progressive production of dust grains in the cool envelopes of red giants or in supernova explosions named here *primordial dust*. Such particles are manufactured in a stellar core and subsequently dragged in the outer envelope of the star and finally blown in the interstellar space by strong stellar winds and radiation pressure. Supernovae explosions release a huge amount of energy, which allows for creation of heavy atoms and are a potent source of dust particles. "Born" in this way, primordial dust is a major constituent in the formation of planets or stars of a next generation. Nurseries of young stars are very likely a related place of planet formation as e.g. the Orion nebula. If ejected from the parent system, primordial dust particles contribute to the interstellar dust background. The second mechanism (ii) is the production of *secondary dust* by a cosmic erosion of already evolved atmosphereless parent bodies, as for instance planets, satellites, asteroids, comets etc. This secondary degeneration can either be caused by mutual collisions between the parent bodies or by a perpetual bombardment of their surfaces by micrometeoroids or even by dust particles themselves. Additionally, if sustained by an efficient source of energy as e.g. tidal heating, secondary dust may be produced by geophysical processes as volcanism, cryovolcanism or geyser eruptions. Dust populations formed of secondary dust generally remain near the orbits of their parent bodies, i.e. they move in the equatorial plane of the central star (in our Solar system - the ecliptic) or the equatorial planes of the planets. These particles form so-called *interplanetary dust* complex or *zodiacal cloud*.

Primordial dust particles (nowadays present in the comets) provide information about the primitive material which made up our Solar system. It is the only material which has not been processed by heat or pressure as has happened in bigger bodies in the Solar system. Secondary dust, created by cosmic erosion, is important for older stars with an already evolved planetary system where the primordial dust has been already blown away by stellar winds during the evolution through the T-Tauri phase or is ceased by other processes like sputtering. Study of the secondary dust around planets (predominantly created in their vicinity) gives a unique chance for an indirect investigation of the parent bodies and their properties. Before we turn to the outline of this work we want to mention methods of dust observation which are of relevance for our studies.

In the past, before the cosmic flights era, the main source of information about cosmic dust were indirect observations of distant dust complexes or dust entering the Earth atmosphere and producing short-lived "streak" of light - the meteors. Now we know, that this phenomena is caused by dust particle (or meteoroid), predominantly of cometary origin crossing the Earth orbit and colliding with the planet. The dust particle travelling through the Earth's atmosphere produces a shock wave generated by the extremely rapid compression of air in front of it. It is primarily this ram pressure (rather than friction) which heats the air causing that air atoms are excited and emit light. Consequently the air heats the meteoroid as it flows around and cause that it usually vaporises in the upper atmosphere. However, particles smaller than approximately 1 mm are too small to produce the light signals characteristic for meteors. Instead, they produce ionised gas which reflects radar signals. This method of observation is widely used for particles passing into our atmosphere (e.g. Baggaley, 2000). Small particles travelling with a sufficiently low speed can survive the entry into the Earth atmosphere and can be collected in the upper atmosphere by aircrafts. This allows for a direct analysis of the morphology and composition of dust (see example of a grain collected in the stratosphere in Fig. 1.2). Similarly, the progress in space missions research allowed for direct analysis of the microcraters on samples of lunar material or parts of spacecrafts brought back to Earth, which were exposed to flux of interplanetary dust. The properties of microcraters contain information about mass, velocity, and density of impactors. Recently, the spacecraft Stardust, even collected cometary and interplanetary dust particles in ultra low density aerogel and brought it back to the Earth.

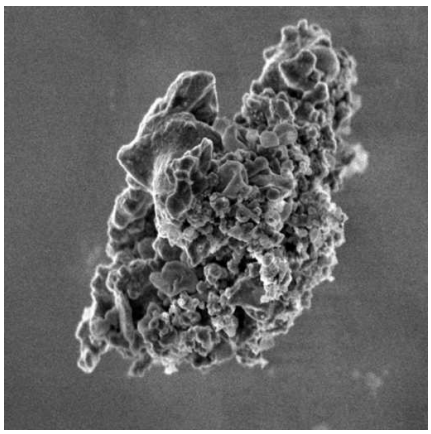

Figure 1.2: Electron microscope image of a sample of classic anhydrous porous "fluffy" interplanetary dust particle collected by NASA'S high altitude ER-2 aircraft in the stratosphere. This grain is about 10 $\mu$m across. When being in a comet, the voids probably would have been filled with ices, which sublimate, if heated by Sun. (NASA)

Composition and structure of dust particles depend on the process and location of their creation. For example, impact fragments from the surface of a rocky asteroid or satellite will be solid "chunks" of material of the parent body, i.e. rock (silicate). However, cometary dust has a more complicated morphology. It is usually an agglomerate of tiny silicate grains immersed in ice pointing to an accretional creation probably in the early Solar system. Additionally, exceptional particles consisting just of water ice without any silicate inclusions were detected. Such grains, for instance, maintain Saturn's E ring and primarily originate from the icy satellite Enceladus. Their origin and further dynamical evolution is one of the topics addressed in this thesis.

Another, Earth-based, method of dust detection is the infrared and optical observation by telescopes against star background. Since the size of individual particles is very small, using remote observation methods one usually observes an ensemble of grains rather than single objects. Based on star observations we know that about 30% of nearby stars are surrounded by dust disks or envelopes (Murdin, 2001). This gives evidence to the possible existence of asteroidal and cometary bodies which would be too small to be detected directly. Among many others ($\varepsilon$ Eridani, Vega, Fomalhaut) a typical example of dust disk surrounding a star is the $\beta$ Pictoris complex (Fig. 1.3). Some of the dust surrounding other stars is often ejected from parent system and contributes to the interstellar dust background.

The motion of the Sun through the interstellar medium causes a constant inflow of interstellar gas and dust. Using a Earth-based observations by AMOR radar in New Zealand (Taylor et al., 1996; Baggaley, 2000) it was possible to identify interstellar dust entering our Solar system. These measurements indicate existence of several

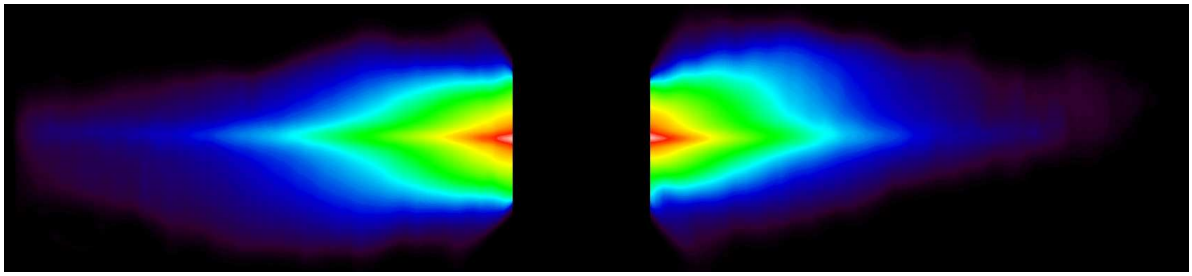

Figure 1.3: HST image showing the edge-on debris disk of dust around β Pictoris from June 1995. A more detailed view may support an idea of existence of one or more planets orbiting the star (Kalas et al., 2000).

very faint discrete sources, the dominant one being in direction of the debris-disk β Pictoris. Krivov et al. (2004) suggested two possible mechanisms of dust stream creation. They proposed scattering of dust particles by massive planet lying in the β Pictoris dust disk or ejection of dust from comets in eccentric orbits by radiation pressure. These observations indicate that the interstellar dust comprises an important contribution to the population of dust in the Solar system.

The flux of interstellar dust has also been successfully registered in the vicinity of Jupiter and in a heliocentric distance of at least 2.2 AU at high ecliptic latitudes by detectors on-board the spacecraft Ulysses (Grün et al., 1993, 1994), Galileo (Baguhl et al., 1995; Landgraf et al., 2000), and Cassini (Altobelli et al., 2003). Such in situ experiments on-board spacecrafts analyse the dust flux even in distant parts of the Solar system. Dust detectors use various techniques as e.g. penetration of thin foils, destruction of pressured cells (Pioneer 10,11 - Humes et al., 1974; Dikarev and Grün, 2002), depolarisation of electrically polarised material (Vega 1, Cassini's CDA subsystem (HRD) - Srama et al., 2004) or impact ionisation measurements (Heos2, Ulysses, Gallileo, Cassini's CDA subsystem (DA) - Grün et al., 1992b,a; Srama and Grün, 1997). Among the above mentioned, impact ionisation is the most sensitive detection method (Grün et al., 2001). A high speed dust particle striking a solid target produces a craters and ejecta of both particle and target material surrounded by a cloud of ions and electrons that expand in vacuum - called impact ionisation. The ions and electrons can be separated by electro-magnetic fields and measured with high sensitivity. Different species can be registered separately which even allows for the spectroscopy of impacting material. In addition, the particle's mass, its velocity and density can be determined. Moreover, using e.g. the Cassini dust detector the particle charge can be measured as well (Srama et al., 2004).

In the present work we focus on the populations of secondary dust surrounding planets, i.e. the *circumplanetary dust particles*. The majority of them are created by hypervelocity impacts of micrometeoroids on planetary satellites (impact ejecta process), or alternatively, by geophysical activities on the surfaces of parent bodies, e.g. outgasing of cometary material as well as geysers or volcanoes of satellites (Io - Graps et al., 2000; Triton - Soderblom et al., 1990; Enceladus - Porco et al., 2006; Spahn et al., 2006b). The particles predominantly remain within the planet's system and may form rings, tori or dust envelopes. All giant planets are encircled by rings, usually composed of bigger particles, but each system also contains a dusty ring component.

Listing all possible dust complexes of the Solar system and their characteristics would exceed the scope of this work. Here, we outline a general model of circumplanetary dynamics, which can be readily applied to any circumplanetary dust complex. Among many possible applications we choose two examples - the putative dust tori of Mars (Section 3.2) and the most extended dust ring of Saturn - E ring (Section 3.3). Both are made of secondary dust particles created directly in the planetary systems. However, the mechanisms of dust production significantly differ in both cases.

The faint and broad E ring was discovered in 1966 (Feibelman, 1967) and during the last decades intensively studied by many author (e.g. Horányi et al., 1992; Dikarev, 1999; Hamilton and Burns, 1994; Spahn et al., 2003). As a result, it was found to consist predominantly of micron-sized particles with short lifetimes originating at the moon Enceladus. Several models of particle ejection from the surface were proposed. Namely, the production by volcanic/cryovolcanic eruptions and the impact ejecta mechanism. Additionally to the theoretical study, the ring was extensively observed from Earth, over the years (Showalter et al., 1991; Pang et al., 1984). However, the Earth-based observations are possible just during the Earth passage through the ring plane and therefore provide

information just about the edge on structure. An excellent opportunity to observe the Saturns ring system occurred during the recent stay of Cassini in the Saturn's shadow, shown in Fig. 1.4. This is probably the best picture of Saturn's ring system ever made. Besides the main rings, due to the high phase angle of the observation (Sun is directly behind the Saturn) also the rings composed of tiny dust particles are clearly visible.

Figure 1.4: A unique panoramatic view of Saturn's rings complex observed by Cassini spacecraft from inside the shadow of the planet. The specific configuration of the observation brightens substantially the tiny dust particles. The outermost, diffuse ring is the E ring consisting of micron sized dust particles originating at moon Enceladus. (Planetary Photojournal, JPL, PIA08329)

A similar picture of faint rings could be probably be obtained also at other giant planets, which carry a significant amount of dust in their systems. However, the existence of putative dust tori was proposed also for rather small Mars already in 1971 by Steven Soter (Soter, 1971). He suggested that the orbits of Martian moons Phobos and Deimos are surrounded by dust tori or rings created by impact ejecta process. As shown by many studies (see Krivov et al., 2006, for a detailed overview) it is reasonable to consider that this dust production mechanism, which was successfully applied at several other dust systems as e.g. Galilean satellites (Krivov et al., 2003; Sremčević et al., 2003; Krüger et al., 2003; Sremčević et al., 2005), should bring comparable results also in the case of Mars. Krivov and Hamilton (1997) showed that the dust produced at Phobos and Deimos forms and extended, asymmetric dust tori with complex dynamics, which strongly depends on the size of ejecta. In order to confirm the results of theoretical studies, there were severall attempts of observational of in situ detection. However, all of these were unsuccessful up till now. Recently the Japanese spacecraft Planet-B (Nozomi) carrying an ionisation dust detector failed on its journey to Mars. These negative results motivate our study presented in this thesis (Section 3.1). We concentrate on the long-living Deimos ejecta, which is expected to dominate the dust population at Mars. The long lifetimes of these grains (up to $10^5$ years) implies that even a weak perturbations as indirect component of the radiation pressure force (Poynting-Robertson drag) or its steady fluctuations may have a significant contribution. We analyse the influence of these perturbations on the overall behaviour of the particles, their spatial distribution, and lifetimes.

In case of our second application, the Saturnian E ring, we use the opportunity to study the novel results from spacecraft Cassini, which has brought a lot of surprising information about Saturn's dust environment. In Section 3.3 we investigate data from dust detector on-board Cassini obtained during the close flyby of Enceladus on 14 July 2005. Several instruments on-board Cassini observed an unusual activity on the south polar region of the moon - high surface temperature and extended dust plumes. Comparing the observed data with the model of dust environment in the vicinity of this moon, allows to estimate the dust production rate from Enceladus. Additionally it allows to judge the importance of different dust production mechanisms maintaining the E-ring. We compare the contribution of two different dust mechanisms, the impact ejecta process and the the geyser eruptions in the south

polar region. Since the origin of the E ring and its dominant source are uncertain, our study could help to answer one of the open questions in the Saturnian system.

This thesis is organised as follows: Chapter 2 introduces the general aspects of a circumplanetary dust complex. We start with description of two main particle production mechanisms - the exogenic impact ejecta process and endogenic processes, here briefly characterised by Enceladus south polar geysers. We present the deterministic description of perturbations acting on dust grains and study the stochastic influence of fluctuating forces. Finally, different particle loss mechanisms are studied and corresponding lifetimes are derived. Chapter 3 is dedicated to the applications of the presented model. At first it presents deterministic and stochastic aspects of dynamics of particles forming the putative Martian tori. Second, a model of the Saturnian E ring with an emphasis on the close Enceladus environment is presented. In particular, two alternative dust production mechanisms are considered. The results of numerical studies are compared with data obtained by the Cassini Dust Detector during Enceladus flyby. Summary and conclusions are listed in Chapter 4.

At the end of the thesis, the following original papers are attached: Appendix A (Makuch et al., 2005, hereinafter referred to as Paper A) and the numerical part of Appendix B (Makuch et al., 2006, Paper B) form a base of Section 3.2 presenting the model of Martian tori. The theoretical part of Appendix B is presented in Section 2.2.2, which explores the stochastic influence of rotation of non-spherical particles on circumplanetary dust dynamics. Appendix C (Spahn et al., 2006a, Paper C) is a base for Section 2.1.1 which reviews the impact ejecta process on planetary satellites . Finally, Chapter 3.3, describing the contribution of different dust production mechanisms in the vicinity of Enceladus is based on Appendix D and E (Spahn et al., 2006b, Paper D and its supporting online material, Paper E).

# Chapter 2

# Dynamical "Life" of a Dust Grain

Dust found throughout our Solar system on bound orbits around the Sun forms the zodiacal cloud population of interplanetary dust particles (IDPs[1]). Outgassing comets, collisions among asteroids or Kuiper-disk objects, and dust grains ejected from satellites, rings, and other atmosphereless bodies constantly replenish these populations. The scenario of dust grains impacting and thereby eroding the surface of a body while releasing a bunch of particles that are ejected from the surface is called impact ejecta process. It is discussed in detail in Section 2.1.1. If particles are ejected from a body orbiting a planet, they predominantly stay in orbit around the planet thereby creating tori and other ring ensembles. Such *circumplanetary dust* denotes a dust family that is created by either exogenic (impact ejecta) or endogenic processes (geysers or volcanoes) at the planet's satellites or rings and remains in bound orbits. Any dust particle, if created in an impact ejecta scenario, belongs to the ejecta family by definition, but may in turn become an impactor since it "shares" its orbit with the satellite or ring of origin.

Each circumplanetary dust grain is subject to multiple forces, such as gravity, radiation pressure, Lorentz force, plasma drag, and other perturbing effects. Since each planetary environment is unique, the strength of these forces is different for each planet. The planets magnetic field crucially determines the Lorentz interaction while the distance from the Sun the radiation pressure. The dynamical "life" of a dust grain and eventually its "death" are directly given by the environment it is found in. In turn, physical properties of a dust family such as e.g. number density or equilibrium charge indirectly map the planets environment. Thus, dust grains, if measured in situ or remotely, are a handy tool to learn more about the source bodies or the planet itself. It is therefore essential to understand dust dynamics from dust grain creation, ensemble dynamics, to the extinction of a single grain.

In this chapter we describe circumplanetary dust ensembles and their evolution in time. Starting with the creation of grains, Section 2.1 provides an overview over exogenic and endogenic dust production at the surface of an atmosphereless body. Forces that influence dust dynamics, distinguished in deterministic and stochastic ones, are listed and their influence on a single grain's trajectory is explained separately in Section 2.2.1 and 2.2.2, respectively. All deterministic forces are considered for well defined properties of grains and fields. All deviations from such well defined states like fluctuation of parameters, fields or also the individuality of each grain are modeled as a stochasticity.

The description of a circumplanetary ensemble is completed if a balance between particle creation and extinction can be quantified. Knowing the amount of fresh ejected particle and particle lifetimes (Section 2.3) allows for determination of a steady distribution of particle number densities of the grains. At the end we summarise the theory and modelling of the "life'" of a dust grain.

[1]For simplicity, here we do not distinguish different particle populations present in the Solar system as e.g cometary dust, asteroidal dust or the one originating from Kuiper belt.

## 2.1 Dust Creation

Two fundamental creation processes play a role for the interplanetary dust population, namely the creation of particles at the surface (exogenic) by an impact ejecta mechanism and processes occurring beneath the surface of a satellite (endogenic) as volcanism, cryovolcanism or geyser eruptions.

### 2.1.1 Exogenic Processes - impact ejecta Scenario

The impact ejecta scenario is a model of particle ejection from the surface of an atmosphereless body due to impacts of micrometeoroids. Perpetual motion of Solar system bodies through the zodiacal cloud (IDPs and other dust populations) results in its continuous bombardment by a flux of impactors. If striking an atmosphereless body, these hypervelocity impacts cause an ejection of secondary material. The ejected mass may be considerably larger than the mass of the projectiles. A schematical sketch of this process is shown in Fig. 2.1. The ejected material is either re-accreted by the parent body or escapes its gravitational region of influence.

Dust creation by this cosmic erosion is most common throughout the Solar system. It applies to all atmosphereless bodies like planetary satellites (Paper A - C; Krivov et al., 2003; Krivov and Hamilton, 1997; Burns et al., 1984), asteroids (Hamilton and Burns, 1991, 1992), planets without an atmosphere like Mercury (Müller et al., 2002) or double dwarf planet Pluto - Charon (Thiessenhusen et al., 2002). The ejected grains form a dust cloud around the parent body and along its orbit which have already been detected by in situ measurements. Recent examples are: dust clouds around the Galilean satellites (Krüger et al., 2003) detected by the DDS on-board the Galileo spacecraft or similar clouds around satellites in the Saturnian system observed by the CDA of Cassini. These measurements bring valuable information about projectile families, ejection processes, spatial dust distribution and grain composition and allow for a comparison with theoretical models.

In this section we present a brief description of dust impact-ejection at the surface of an atmosphereless satellite. Owing to the complexity of this process, empirical models based on experimental data (Koschny and Grün, 2001a,b) are usually derived. A detailed review of different studies can be found in Krivov et al. (2003) and Paper C.

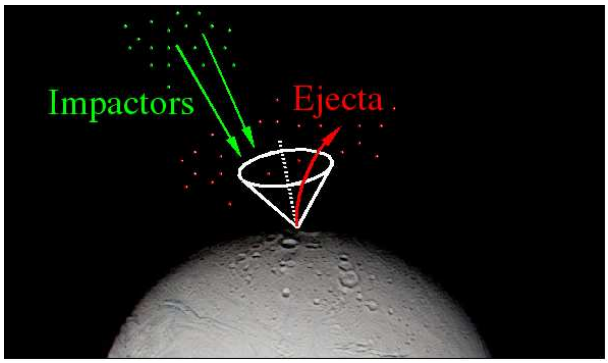


Figure 2.1:

Figure 2.2: Illustration of the impact ejecta mechanism. Impact of hypervelocity particles on the body surface causes ejection of secondary material. The amount and properties of the ejected debris depend on the parent body surface characteristics as well as the velocity and properties of the impactors.

The amount of ejecta clearly depends on the amount of impacting particles. The *mass flux of striking impactors* is defined as

$$F_{\rm imp}^{\infty} \;=\; \langle m_{\rm imp}\rangle n_{\rm imp}(r)\langle v_{\rm imp}\rangle(r)\;. \tag{2.1}$$

Here, $\langle m_{\rm imp}\rangle$ denotes an average mass of impactors, $n_{\rm imp}(r)$ and $\langle v_{\rm imp}\rangle(r)$ are their number density and average impact velocity at distance $r$ from the planet, respectively. The superscript $\infty$ refers to the unperturbed quantity

far from the planet's influence but in the same heliocentric distance. In case of a ejection of particles from a source body in a circumplanetary orbit by IDPs or another external population of impactors (e.g. Kuiper belt dust particles or interstellar dust population) the flux $F_{\rm imp}$ has to be corrected for the gravitational focusing effect. A planet attracts grains thereby increasing their velocity $v_{\rm imp}$ and the number density $n_{\rm imp}$ in the planets vicinity. In order to quantify the focusing effect at a distance $r$ of the satellite, the integrals of the two-body problem, energy and angular momentum, are applied to derive (see Paper C and references therein)

$$\frac{F_{\rm imp}}{F_{\rm imp}^{\infty}} \;=\; \frac{v_{\rm imp}}{v_{\rm imp}^{\infty}} \times \frac{n_{\rm imp}}{n_{\rm imp}^{\infty}} \;=\; \sqrt{1+\frac{2GM_{\rm p}}{r(v_{\rm imp}^{\infty})^2}} \times \frac{1}{2}\sqrt{1+\frac{2GM_{\rm p}}{r(v_{\rm imp}^{\infty})^2}}\left[1+\sqrt{1-\left(\frac{R_{\rm p}}{r}\right)^2}\right]. \tag{2.2}$$

Mass and radius of the planet are labeled as $M_{\rm p}$ and $R_{\rm p}$.

With this mass flux of impactors $F_{\rm imp}$, the *mass production rate* of ejecta can be calculated as

$$M^{+} \;=\; F_{\rm imp}\, Y\, S \;, \tag{2.3}$$

with the *total cross section of satellite* $S = \pi R^2$. The *yield* $Y$ is a ratio of ejected mass and mass of the projectile, characterising the efficiency of the impact in just one number. To estimate the yield function, experimental data obtained by Koschny and Grün (2001a) (Eq. (7) ibid)[2]are used. They investigated ice-silicate mixture targets with different silicate content $G_{\rm sil}$ (0 = pure water ice, 1 = pure silicate) and formulated the yield as a function of $m_{\rm imp}$ and $v_{\rm imp}$ (in SI units) as

$$Y \;=\; 2.85\times10^{-8}\times 0.0149^{G_{\rm sil}}\left(\frac{1-G_{\rm sil}}{927}+\frac{G_{\rm sil}}{2800}\right)^{-1} m_{\rm imp}^{0.23}\; v_{\rm imp}^{2.46}. \tag{2.4}$$

For very bright objects like Enceladus, Dione or Rhea covered by ice, $G_{\rm sil} = 0$ can safely be used. In contrast to that e.g. Phoebe or Martian moons Phobos and Deimos have a very dark surface, which mimics a pure silicate body and implies $G_{\rm sil} = 1$. However, the surface structure and composition of the studied bodies is usually only poorly known and the yield $Y$ is a source of large uncertainties.

In order to estimate the rate of ejected grains we assume the (cumulative) size distribution of ejecta being represented by a power law. With this, the total number of ejected grains with size larger than certain radius $s$ at a distance $r$ from a planet is given by

$$N^{+}(>s,r) \;=\; \frac{3-\gamma}{\gamma}\,\frac{F_{\rm imp}\,Y\,S}{m_{\rm max}}\left(\frac{s_{\rm max}}{s}\right)^{\gamma}. \tag{2.5}$$

As a plausible value of mass distribution slope $\gamma = 12/5$ is consistent with the exponent derived from Galileo data (Krüger et al., 2000). Nevertheless, the exact values of the parameters of all distributions are rather uncertain. The parameters $s_{\rm max}$ and $m_{\rm max}$ are the size and mass of the heaviest fragment, both related by the grain's bulk density (assuming a spherical shape of the particles). They are typically close to characteristic size and mass of the impactors (Krüger et al., 2000).

However, even if launched at the surface of a parent moon, not all dust grains will escape. A large fraction will fall back on the satellite (with mass $M$) but the grains with initial velocities larger than the three body escape velocity

$$v_{\rm esc} \;=\; \sqrt{2\,GM\left(\frac{1}{R_{\rm p}}-\frac{1}{h_{\rm Hill}}\right)}\;, \tag{2.6}$$

may escape the Hill sphere of gravitational influence of the parent moon with radius $h_{\rm Hill} \;=\; r\,\sqrt[3]{M_{\rm p}/\left[3(M_{\rm p}+M)\right]}$ and populate the circumplanetary environment. Therefore the velocities at the moment of ejection play an important role and it is important to specify them. Regardless of the mass of the ejecta, we adopt a power law for the *initial velocity distribution*

$$f_v(v) \;=\; \frac{\beta-1}{v_0}\left(\frac{v}{v_0}\right)^{-\beta} H[v-v_0]\;, \quad \text{normalised by} \quad \int_0^{\infty} f_v(v) \;=\; 1, \tag{2.7}$$

[2]Koschny and Grün (2001a) have a misprint in their Eq. (7). Evaluating their Eq. (5) and (6) results in Eq. (2.4)

where $H[v - v_0]$ denotes a Heaviside function. The parameters $v_0$ and $\beta$ are the minimal ejecta velocity ("cut-off of the distribution") and the distribution slope. The value of $\beta$ depends on the material properties of the target, characterised by $G_{\rm sil}$. For a water ice surface $\beta \approx 3$ is plausible and for regolith like one $\beta \approx 2$ is considered as deduced from impact lab experiments. The parameter $v_0$ can be estimated from the energy balance. The ratio of the kinetic energy of the ejecta $K_e$ and the impactors $K_i$ must be less than unity, since a considerable fraction of the energy is spend for deformation and heat during impact. The ratio $K_e/K_i$ varies from few percent to several tens of percent, (see Paper C; Krivov et al., 2003). For example, $K_e/K_i = 0.3$ (IDPs) and $K_e/K_i = 0.05$ (E ring impactors) have been used in Paper C.

Then, the number rate of ejected particles with sizes bigger than $s$ and velocities larger than $v_{\rm esc}$ contributing to the circumplanetary dust population is given by

$$N^+_{\rm esc}(> v_{\rm esc}, > s, r) \;=\; (v_0/v_{\rm esc})^{\beta-1}\, N^+(> s, r)\;. \tag{2.8}$$

Similarly, the total mass rate of grains with size bigger than $s$ leaving the parent body reads

$$M^+_{\rm esc}(> v_{\rm esc}, > s, r) \;=\; (v_0/v_{\rm esc})^{\beta-1}\, M^+(> s, r)\;. \tag{2.9}$$

Equations (2.8) and (2.9) give a cumulative number and mass rate escaping the surface of the parent body. These distributions generally have to be weighted to account for anisotropies of the ejecta flux at the surface of the parent moon. A simple example is the "windshield" effect caused by satellite motion - as the moon moves through the impactors cloud, there are more grains to hit the leading hemisphere (studied in detail by Sremčević et al., 2003). A similar approach was used also in Paper D, where an isolated source of ejecta on the surface of Enceladus was modelled and led to the identification of the signature of the active south polar source at Enceladus in the CDA data.

### 2.1.2 Endogenic Processes - (Cryo)Volcanism

There are just a few bodies in the Solar system that are known for ongoing geophysical activity such as volcanism, cryovolcanism or geyser eruptions. Apart from Earth and Venus, these are the Jovian moon Io, the Neptunian satellite Triton and as recently discovered, also the rather small Saturnian moon Enceladus (Porco et al., 2006). The processes observed on all three satellites have their own specifics but also one common aspect. All of them require an efficient internal source of energy so that the activity can be sustained. The most favourable mechanisms are the decay of radioactive elements known as radiogenic heating, and tidal heating caused by internal friction, where tidally induced deformation energy is dissipated (Kargel, 2006; Spencer et al., 2006). The latter mechanism is amplified for bodies locked in orbital resonance (Murray and Dermott, 1999) because of a steady increase of orbital eccentricity of the moon at this places.

The Voyager spacecrafts as well as Galileo discovered that Io is the most volcanically active body in the Solar System. Several active volcanoes (with temperatures up to 2,000 K), numerous lakes of molten sulfur and extensive long flows of molten sulphur or silicate spreading hundreds of kilometres have been found on the surface of Io (Geissler et al., 1999; Lopes et al., 2004). The energy for this activity probably derives from tidal interactions among Io, Jupiter, Europa and Ganymede. The three moons are locked into Laplace-resonant orbits. The gravitational interaction of Europa, Ganymede and Jupiter causes Io to "stretch" and "bend" by as much as 100 meters (Lopes and Williams, 2005), a process which generates enough heat through internal friction to sustain the ongoing volcanic activity. Some of Io's volcanic plumes have been measured rising over 300 km above the surface. With material ejected from the surface at $\sim 1\,{\rm km\,s^{-1}}$ the Io's volcanoes are a potent dust source in the Jovian system. Tiny (10 nm) dust particles ejected by Io's volcanic plumes and catapulted from Jupiter (velocities $> 200$ ${\rm km\,s^{-1}}$), denoted as "Jovian Dust Streams" were detected by several instruments in the interplanetary space (e.g. Graps et al., 2000; Krüger et al., 2003b,a).

Similar to Io, the tidal heating of Triton causes ongoing geysers-like eruptions spewing material several kilometers into the atmosphere of this satellite (Soderblom et al., 1990; Kirk et al., 1990). The eruptive material is probably liquid nitrogen, dust, or methane compounds from beneath the surface. Voyager 2 observed one of the

plumes rising 8 km above the surface and extending 140 km "downwind" before being deposited on Triton's surface. Additionally, the very specific cantaloupe terrain could have been caused by diapirism (the rising and falling of frozen nitrogen or other ices), by collapses, and by flooding caused by cryovolcanism.

The third active satellite known in the Solar system is the Saturnian moon Enceladus. This is a kind of mystery - the moon is rather small (diameter of about 500 km) and has a small orbital eccentricity which reduces the strength of tidal forces considerably. Severall instruments on-board spacecraft Cassini discovered unusual activity in the Enceladus south polar region during its flybys in 2005. It detected in the vicinity of south pole an elongated cracks dubbed "tiger stripes". These fractures were found to have increased temperature with respect to surrounding surface and to be a source of prominent dust and gas plumes. The exact mechanism of producing the jets is still enigmatic. Due to the low gravity of Enceladus the plumes extend hundreds or even thousands of kilometres in space (severall moon's radii) and leave the action sphere of the moon. Porco et al. (2006) proposed that these observed jets are geysers erupting from pressurised subsurface reservoirs of liquid water around zero degrees Celsius. To produce the eruption, the subsurface water has to be warmed, even boiled (Kargel, 2006). The most probable energy source warming the polar region is the tidal heating. This process associated with the eccentricity of Enceladus' orbit, forced by its 2:1 mean motion resonance with Dione was long believed to be the source of energy. However, this mechanism is too inefficient to initiate the ice melting (Wisdom, 2004). As touched above any successful application of this process has to pass the so-called "Mimas hurdle". This stems from the fact that Mimas is comparable in size, closer to Saturn and has a much larger orbital eccentricity - therefore the tidal heating should be by factor of 25 larger than heating in Enceladus. However, no geophysical activity have been observed at Mimas (Spencer et al., 2006). Several other mechanisms are still discussed (e.g. Nimmo and Pappalardo, 2006). The most promissing among them is a combination of the radiogenic heating and a spin-orbit secondary resonance (Wisdom, 2004; Porco et al., 2006) (both, depending on the Enceladus surface ice properties). Current Cassini measurements revealed that the dust ejected from Enceladus south pole is the major, source of dust maintaining the E ring. A detailed comparison of the contribution of impact ejecta mechanism and the south polar dust plumes is presented in Section 3.3, where the theoretical model is compared with the measurements of dust detector on-board Cassini.

## 2.2 Dust Dynamics

Once created at the surface of the satellite under consideration a dust grain is subject to various forces which significantly alter its trajectory. Apart from the gravity of the planet and its satellites many non-gravitational perturbations determine the journey of the dust grain until it finally terminates in one of the numerous sinks. The forces can be grouped into two classes: a deterministic, determined by well defined (mean) parameters (particle: size, charge, shape, field strengths) and stochastic fluctuations. The latter, in principle combines all unknowns of the system, adding a stochastic force-component of a different origin. For instance, especially for small grains a fluctuating surface potential may have a large impact on the motion inside the planet's magnetosphere. Unknown rotational states and irregular shapes of the particle further stochastically alter the radiation forces. In the subsequent sections we describe the main deterministic perturbation forces acting on the particle. Then the major stochastic processes are given and formulated quantitatively and a model of stochastic radiation pressure is presented.

### 2.2.1 Deterministics

The equation of motion of a dust grain with mass $m$ in a circumplanetary orbit in the frame centred at the planet reads

$$m\,\ddot{\vec{r}} = \vec{F}_{\mathrm{G}} + \vec{F}_{\mathrm{J2}} + \vec{F}_{\mathrm{RP}} + \vec{F}_{\mathrm{PR}} + \vec{F}_{\mathrm{L}} + \vec{F}_{\mathrm{PD}} + \vec{F}_{\mathrm{CD}} + \vec{F}_{\mathrm{3B}}\ , \tag{2.10}$$

where $\vec{r}$ denotes the radius vector of the particle. The forces on the right-hand side are: gravity of spherical planet ($F_{\mathrm{G}}$), perturbation of planetary oblateness ($F_{\mathrm{J2}}$), direct radiation pressure ($F_{\mathrm{RP}}$), Poynting-Robertson drag ($F_{\mathrm{PR}}$), Lorentz force ($F_{\mathrm{L}}$), direct plasma drag ($F_{\mathrm{PD}}$), Coulomb drag ($F_{\mathrm{CD}}$), gravitational influence of a third body like the Sun or a satellite ($F_{\mathrm{3B}}$). Depending on the specific application, the relative strength of the certain forces contributions may change or even additional forces (not listed here) may become important. In the following

sections we briefly discuss the introduced perturbations separately. For a more precise description we refer to the textbooks by Grün et al. (2001), Greenberg and Brahic (1984) or review articles by Horányi (1996) or Mann and Krivov (2000, unfortunately unpublished review), and the references therein.

#### 2.2.1.1 Gravity of Oblate Planet (G+J2)

The gravity of central planet dominates the dynamics of all bodies orbiting it, even the dust grains which are strongly perturbed by many other perturbations. A famous example are Saturn's main rings which are driven exclusively by gravity and dissipative collisions. With decreasing particle size, not only additional non-gravitational perturbations become significant but also more precise description of planet's gravitational potential is necessary. The latter is caused by the fact that due to the planets's rotation, its shape is not perfectly spherical but flattened on the poles. The gravitational potential of such rotational ellipsoid can be expanded into Legendre polynomial (e.g. Murray and Dermott, 1999) to yield

$$\vec{F}_{\mathrm{G+J2}} = mM_{\mathrm{p}}G\,\nabla\left(\frac{1}{r} - \frac{{R_{\mathrm{p}}}^2}{r^3}J_2P_2\left(\frac{z}{r}\right) - \frac{{R_{\mathrm{p}}}^4}{r^5}J_4P_4\left(\frac{z}{r}\right) - \ldots\right), \tag{2.11}$$

where the first term on the right-hand side of the equation represents the gravity of a spherical planet. The higher terms correspond to the planet's obliquity. The $P_2\left(\frac{z}{r}\right)$ and $P_4\left(\frac{z}{r}\right)$ coefficients are Legendre polynomials. The oblateness coefficients $J_2$ and $J_4$ (aka zonal harmonic coefficients) are dimensionless and specify the non-sphericity of the central body. For nearly all planets in our Solar system, higher coefficients ($J_i$, $i > 2$) are by few orders of magnitude smaller, thus usually neglected. For a general discussion on the effects of oblateness we refer to Kozai (1959).

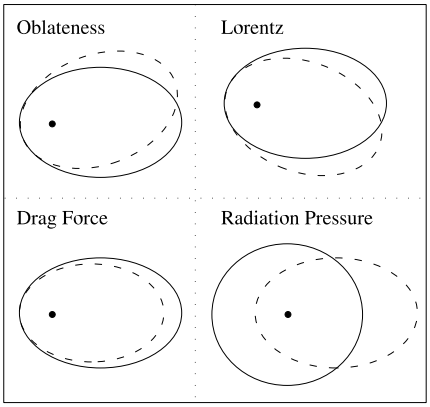


Figure 2.3: Sketches of orbital changes induced by four different perturbation forces: planetary oblateness, Lorentz force from a dipolar magnetic field, a drag force, and radiation pressure (continuous line - initial, dashed line - final). The orientation of the drift in case of Lorentz force depends on the sign of the particle's surface potential as well as the orientation of the magnetic field.

Planetary oblateness causes a conterclockwise[3] precession of the apsidal line of the orbital ellipse in space. While the orbit of a grain retains its size, shape and inclination ($\dot{a} = \dot{e} = di/dt \cong 0$) the apsidal line precesses with angular rate (see Fig. 2.3 for illustration)

$$\dot{\omega}_{\mathrm{J2}} = \frac{3}{2}\,\omega_k J_2 \left(\frac{R_{\mathrm{p}}}{a}\right)^2, \tag{2.12}$$

where $\omega_{\mathrm{J2}}$ is the longitude of pericenter of the grain, $\omega_k = \sqrt{GM_{\mathrm{p}}/a^3}$ the Kepler angular velocity, and $a$ the semimajor axis of the orbit.

[3] seen from the ecliptic North

#### 2.2.1.2 Radiative Effects (RP + PR + SH)

In general, any dust particle moving in the interplanetary space is exposed to Solar radiation. Since photons carry momentum, they affect the dynamics of the grain if being absorbed, emitted or scattered. This is especially important for small particles with a large ratio of surface area to mass (sizes from fractions up to tens of micrometers).

The force created by impinging photons on the dust grain can be written as (Burns et al., 1979; Gustafson, 1994; Mignard, 1984)

$$\vec{F}_{\mathrm{RP+PR}} = \pi s^2 \frac{Q_{\mathrm{pr}}}{c} F_{\odot} \left( \frac{1\mathrm{AU}}{a_{\mathrm{p}}} \right)^2 \left[ \left( 1 - \frac{1}{c} \vec{v} \cdot \vec{e}_{\odot} \right) \vec{e}_{\odot} - \frac{1}{c} \vec{v} \right], \tag{2.13}$$

where $\vec{v}$ is the velocity of the grain in an innertial frame fixed in the centre of the Sun, while $\vec{e}_{\odot}$ is a unit vector pointing radially outward from the Sun. The cross section of a dust grain with radius $s$ reads $\pi s^2$ and $c$ is the speed of the light. $Q_{\mathrm{pr}}$ denotes the radiation pressure efficiency coefficient and can be calculated by employing Mie theory of light scattering (Burns et al., 1979; Bohren and Huffman, 1983). It depends on the particle's shape, material properties, the wavelength of scattered light, and the index of refraction which in turn varies with wavelength and particle size. The Solar energy flux $F_{\odot}$ given at the Earth distance ($F_{\odot} = 1.36 \cdot 10^3$ J m$^{-2}s^{-1}$) has to be scaled according to the distance of the planet $a_{\mathrm{p}}$ by $(1\mathrm{AU}/a_{\mathrm{p}})^2$. The flux $F_{\odot}$ contains the total photon-energy emitted at the Sun's surface per unit area and time. It is interesting to note that this quantity implicitely contains the momentum per time carried by all photons which in fact characterise the force expressed by Eq. (2.13). The latter can be divided into two contributions - a direct radiation pressure force and the dissipative Poynting-Robertson drag.

**Direct Radiation Pressure (RP)**

The velocity independent constant component of Eq. 2.13, which is directed radially outward from the Sun is called *direct radiation pressure force* ($F_{\mathrm{RP}}$) and is usually treated separately. In heliocentric problem, since its dependence on particle distance from the Sun is the same as in case of gravity, the combined effect of both forces results in simple Keplerian motion around "effective Sun", with reduced mass $M_{\mathrm{eff}} = M_{\odot}(1-\beta)$, where $\beta = F_{\mathrm{RP}}/F_{\mathrm{G}}$. For a certain range of particle properties (e.g. submicron grain size or specific particle shape) the radiation pressure force may exceed the solar gravity ($\beta > 1$). Such grains, blown out from the Solar system following hyperbolic orbits are called β-meteoroids (Zook and Berg, 1975). In contrary to heliocentric case, a particle on circumplanetary orbit is periodically perturbed by Solar radiation force which is almost constant in magnitude but changes its orientation as the planet revolves the Sun and the grain orbits the planet. This problem cannot be solved by a simple reduction of the Solar mass. In this given planetary motion the direct radiation pressure does not influence the semimajor axis, but causes a periodical change of the grain's eccentricity and inclination (see Fig. 2.3) described in detail in Section 3.2. The amplitude of these oscillations is inversely proportional to the size of the grain and the period is driven by orbital period of the planet around Sun. For a certain grain size, the eccentricity is increased such that the grain collides with the central planet. This is a very effective mechanism influencing the size distribution of dust particles by removing particles exactly with certain size (e.g. in the Martian environment). Since the orbital period of the planet around the Sun is much longer than that of the dust grain in orbit around the planet, it is reasonable to assume that the Solar direction stays constant during the latter motion. With this simplification, a set of orbit-averaged differential equations, describing the evolution of the osculating elements, can be formulated (Burns et al., 1979; Chamberlain, 1979; Krivov et al., 1996; Horányi et al., 1992). This equations are used in Section 2.2.2 and 3.2 as well.

**Poynting-Robertson Drag (RP)**

The second part of Eq. 2.13 covers the velocity dependent terms in Eq. (2.13) defining the *Poynting-Robertson drag force* ($F_{\mathrm{PR}}$). This drag is caused by that part of the radiation pressure force, which is not perpendicular to a velocity vector of moving dust particle but has a small component opposite to the particle motion (due to the aberration effect). It is a dissipative force which continuously decreases the particle's angular momentum and orbital energy (Fig. 2.3). This leads to a gradual spiralling of the dust grain towards the central body within $10^3 - 10^5$ years (see Paper A - Eq. (2) and (3)) both in heliocentric as well as in the planetocentric case. Unlike other perturbations, drag forces invoke secular (monotonic) decrease, mainly of the orbital semimajor axis but also of eccentricity and inclination (Mignard, 1984).

**Influence of Planet's Shadow (SH)**

Circumplanetary dust populations usually comprise tori or rings whose constituents - the dust particles more or less frequently spend a fraction of each revolution in the planetary shadow. This is the case for all circumplanetary dust complexes in the Solar system, except for those of Uranus, because of the unusually large obliquity of the whole Uranian system. The radiation forces are vanishes during the time of the shadow passage of the dust particle.

The dynamical consequences of the body's passage through the planet's shadow were first studied in the early sixties of the last century. Predicting the dynamics of artificial satellites, scientists realized that the impact of the shadow of the planet cannot be neglected. The most pronounced effect was observed on the artificial satellite Echo 1. This 30 m balloon with 70 kg was an ideal example of particle for which radiation pressure plays an essential role although far from being micro-sized.

A particle orbiting a central planet stays inside the shadow for just a small fraction of its orbital period. For a particle in a circular orbit, lying in the same plane as the shadow, the loss and gain of energy during one orbital period caused by crossing the shadow ballance each other and average to zero. In the case of an elliptic, inclined orbit the symmetry will be broken and the balance of energy will not hold over one orbital period. The asymmetrical action of radiation pressure results in small periodic change of semimajor axis but it's influence is usually of minor importance for a particle located at a few planetary radii from planet (Mignard, 1984; Burns et al., 1979; Shapiro, 1963). Additionally to this effect, inside the planetary shadow also the plasma properties and particle charging process are abruptly changed (lack of photoemission). This, together with the periodical switching of the RP in the shadow result in rapid shifting of semimajor axis slightly inward and outward (Horányi et al., 1992; Mignard, 1984).

In fact, inside the shadow, radiative forces are suddenly "switched" off, i.e. mathematically the force comprise a step function - the strongest nonlinearity. The latter may cause a stochastic behaviour in particle dynamics. We want to notice that: according to our numerical results, a long-term influence of SH on an ensemble of individual particles ejected from the surface of Martian moon Deimos results in spatial spread of particle trajectories. The main influence was observed in case of semimajor axis, which standard deviation grows as a square root of time - equivalent to the system with an additive white noise.

**Non-sphericity of the Particle**

The grains are usually considered to be spherical. However, as shown in Fig. 1.2, the shape of a "real" dust grain is far from being spherical. This non-sphericity can significantly alter the impact of radiation pressure. As shown by e.g. Kimura et al. (2002) or Klacka et al. (2005), the dynamics, lifetimes as well as the resonance capture probability of non-spherical grains may considerably differ from that of spherical ones. In Section 2.2.2 and 3.2 we discuss the effect of radiation pressure on rotating non-spherical grains. We show that it leads to stochastic dispersion of the orbital elements of an ensemble of grains and consequently to spatial spread of the confined ensemble.

#### 2.2.1.3 Lorentz Force (L)

Grains immersed in the plasma environment of a planet are continuously bombarded by photons, electrons and ions. As a result, the grains acquire charge and their motion in a magnetic field (interplanetary or planetary) gives rise to the Lorentz force (Horányi, 1996)

$$\vec{F}_{\mathrm{L}} = Q\,\left[\vec{v}\times\vec{B}+\vec{E}\right]. \tag{2.14}$$

Here $Q$ denotes the electrical charge of a dust grain, $\vec{v}$ the velocity of the charged grain moving in the magnetic field $\vec{B}$ and electric field $\vec{E}$. Usually, instead of grain's charge $Q$, the particle's surface electrostatic potential $U$ with respect to infinity is used. The relation between these quantities is simply $Q = 4\pi\varepsilon_0 sU$ ($\varepsilon_0$ - permittivity of vacuum). As described later, the charge of a particle is a dynamical variable and together with the magnetic field properties is essential for the Lorentz force derivation. Since in Chapter 3 we will focus on the dusty rings (tori) around Mars and Saturn, we have to distinguish the dynamics of particles in interplanetary space around the planets

without (or negligibly small) magnetic field (Mars) and around giant planets with own, strong magnetic field (e.g. Jupiter or Saturn).

**Dust around Mars**

In this case the electromagnetic field is driven by the convective motion of the Solar wind. Usually, a model of spiral structure magnetic field (Parker, 1958) provides a fair approximation. The interplanetary magnetic field $\vec{B}$ is connected to an electric field $\vec{E} = -(\vec{v}_{sw} \times \vec{B})$, where $v_{sw} \approx 400\,\mathrm{km\,s^{-1}}$ is the velocity of the Solar wind near Mars (Horányi et al., 1991; Altobelli et al., 2003). Caused by the rotation of the Sun (equatorial period of 25.7 days), the polarity of the magnetic field varies with phase-space coordinates. As a particle moves through the fluctuating magnetic field, the Lorentz force rapidly changes its direction. On a long timescale this results in "Lorentz diffusion" (Morfill and Grün, 1979; Consolmagno, 1979; Spahn et al., 2003), i.e. a stochastic diffusion of orbital elements, namely semimajor axis, eccentricity, and especially inclination. The impact of this effect grows with decreasing grain size and is most pronounced for submicron or even micron-sized grains.

**Dust around Saturn**

The magnetic field near Saturn is governed by the planet's magnetosphere while the electric field is induced due to the rigid corotation of the magnetosphere with the planet $\vec{E} = (\vec{r} \times \vec{\omega}_\mathrm{p}) \times \vec{B}$, with $\omega_\mathrm{p}$ being the frequency of the planet's rotation (Horányi et al., 1992; Spahn et al., 1999; Richardson, 1995). For a particle orbiting Saturn in a circular orbit in the equatorial plane, the Lorentz force causes a precession of pericentre at an angular rate of

$$\dot{\omega}_\mathrm{L} = -2\frac{QB_0}{mc}\left(\frac{R_\mathrm{p}}{a}\right)^3 , \tag{2.15}$$

where $B_0$ is the magnetic strength of a dipole field at Saturn's surface (in CGS). Focusing on the Saturnian E ring, this precession is counterbalanced by the effects of the planetary oblateness by certain conditions. For micron-sized particles charged to about -5 V in the vicinity of Enceladus both effects cancel ($\dot{\omega}_\mathrm{L} - \dot{\omega}_\mathrm{J2} \cong 0$). This fact allows to built very large eccentricities and correspondingly a large radial extent of that ring. This dynamical balance could be one of the main mechanisms responsible for the global appearance of the E ring.

**Particle Charging**

The grain's charge acquired in plasma results from balance between number of electrons or ions captured or emitted from the surface by different mechanisms. Its time derivative is defined as

$$\dot{Q} = J_\mathrm{PEE} + J_\mathrm{e} + J_\mathrm{i} + J_\mathrm{SEE} , \tag{2.16}$$

where the terms on the right-hand side respresent charging currents defined as number of charged particles gained or lost per time, namely photoelectron emission $J_\mathrm{PEE}$, thermal collection of electrons $J_\mathrm{e}$ and ions $J_\mathrm{i}$, and secondary electron emission $J_\mathrm{SEE}$ (Mukai, 1981; Draine and Salpeter, 1979; Kimura and Mann, 1998; Horányi, 1996; Grün et al., 1984). Since the currents do not stay constant while the particles move in the plasma environment, the resulting equilibrium potential $U$ changes with time. Thus, the Eq. 2.16 must be solved simultaneously with the equations of motion. However, in order to simplify the dynamics a constant or approximate potential is often applied. Then, assuming $\dot{Q} = 0$ in Eq. 2.16, defines the surface equilibrium potential. In fact, this is often a reasonable assumption since the time-scales of charging are in most cases much smaller than the orbital periods. The charging of the grain depends strongly on the properties of plasma environment as well as the grain structure and size. Especially the choice of particle properties and material parameters is essential. In dependence on the chosen model of charge absorption and emission (Draine and Salpeter, 1979; Mukai, 1981; Weingartner and Draine, 2001; Willis et al., 1973) very different results may be obtained.

The resulting equilibrium potential in the interplanetary space during the average phase of the solar cycle is practically constant over a wide range of heliocentric distances and particle sizes and is roughly between +2 and +5 V (using a plasma model based on Köhnlein, 1996; Roatsch, 1988, and Hellwege, 1981 parameters). It is important to mention that in the vicinity of Mars, the usual structure of interplanetary magnetic field is perturbed. Mars, which does not have a strong $\vec{B}$ field acts as an obstacle to the Solar wind and causes a formation of a region where the plasma properties abruptly change. Comparable to water wake around a moving boat, a parabolically shaped bow shock is produced in the vicinity of Mars. Referring to Juhász and Horányi (1995) a potential of a

grain crossing this area can drastically change during one orbital period from usual couple of Volts up to -340 V. As already reported for shadow, such rapid changes in the particle dynamics may leads to diffusion of orbital elements.

In the Saturnian plasma environment, governed by its strong and complicated magnetosphere, the grain potential is a function of radial distance from the planet. Using the Richardson (1995) and Richardson et al. (1998) plasma model the resulting equilibrium potential of micron sized grain in the vicinity of Enceladus is approximately between -1 and -4 V (Dikarev, 1999; Horányi et al., 1992). Within the E ring, the grain potential grows with radial distance from the planet and at $\sim 7\ R_{\mathrm{Saturn}}$ it reaches a positive values. As discussed in Section 3.3 (Kempf et al., 2006), these theoretical estimates were recently confirmed by in situ measurement carried out by CDA.

#### 2.2.1.4 Plasma Drag (PD + CD)

The dust particle travelling through the plasma environment is steadily bombarded by ions and electrons. While the particle is getting charged, momentum transfer occurs both due to physical collisions and through long-range Coulomb interaction. Similarly to impinging photons, the absorbed or scattered ions and electrons exert a drag force which is a function of the relative speed between the dust grain and the one of plasma $(\vec{v}-\vec{u})$. The *direct plasma drag force* (PD) caused by the physical impacts between plasma particles and the grain is expressed as (Banaszkiewicz and Krivov, 1997; Dikarev, 1999; Grün et al., 1984)

$$F_{\mathrm{PD}} = \pi s^2 n_i\, m_i\, u_i^2 \left[ \left( M_i + \frac{1}{2M_i} \right) \frac{\exp(-M_i^2)}{\sqrt{\pi}} + \left( M_i^2 + 1 + \frac{1}{4M_i^2} \right) \mathrm{erf}(M_i) \right] . \tag{2.17}$$

This equation is valid under assumptions that the bulk energy of plasma ions is much larger than the potential of the surface charge. The direction of the drag force is antiparallel to the vector $\vec{w} = \vec{v} - \vec{u}$. The number density of considered ions with mass $m_i$ and moving with a thermal speed $u_i$ is given by $n_i$. The $M_i$ denotes the Mach number being the ratio of particle velocity relative to bulk of plasma $|\vec{w}|$ and ion thermal speed $u_i$.

The indirect momentum exchange with ions moving within the Debye sphere of the dust grain, the *Coulomb drag* (CD) reads (Northrop and Birmingham, 1990; Dikarev, 1999)

$$F_{\mathrm{CD}} = \frac{\sqrt{\pi} Q^2 e^2 n_i}{m_i w^2} \int_{-\infty}^{\infty} \frac{y}{|y|^3} \left(2yM_i - 1\right) \exp\left[-(y-M_i)^2\right] \ln \frac{1+(C\lambda_{\mathrm{D}})^2}{1+(Cs)^2} dy , \tag{2.18}$$

where $C = m_i u_i^2 y^2 / Q e$, with $e$ being the elementary charge (CGS units). The minimum debye length is defined by $\lambda_{\mathrm{D}} = \sqrt{kT_i/(4\pi n_i e^2)}$, where $k$ is the Boltzmann constant.

The relative importance of both components of the plasma drag depends on the conditions the grains are exposed. In the case of the Saturnian E ring, the dust grains move with supersonic speed with respect to the heavy ions which dominate the plasma ($w \gg u_i,\ \ M_i \gg 1$). Then, the Coulomb part of the force is negligible compared to the direct drag force (Morfill and Grün, 1979; Dikarev, 1999) and Eq. (2.18) can be approximated as

$$F_{\mathrm{PD}} = \pi s^2 n_i m_i w^2 . \tag{2.19}$$

Dynamicly, the action of plasma drag on the E ring dust particle increases its orbital energy and thus causes increase of the semimajor axis.

## 2.2.2 Stochastics

### 2.2.2.1 Sources of Stochasticity

There exist a variety of natural processes resulting in stochastic fluctuations. Among many other, the most prominent influence on circumplanetary dust dynamics has fluctuation of Lorentz force and radiation pressure.

The main sources of variable Lorentz force are: the fluctuations of the magnetic field and variation of a particle's charge due to change of incoming charge fluxes, sudden changes of the plasma environment due to inhomogeneity of magnetosphere (bow shock, magnetopause) etc. The impact of a fluctuating magnetic field on the dust dynamics in the Jovian environment was studied in detail by Spahn et al. (2003). There the stochastic Lorentz force acting on charged dust particles released from Galilean satellites was addressed. The authors showed that the stochastic magnetic field, modeled by an isotropical Gaussian noise give rise to a diffusion of the inclinations and eccentricities. The results of the analytical model and according numerical simulations have been compared with magnetic field data obtained by the magnetometer on-board the spacecraft Galileo. The resulting diffusion of eccentricity and inclination was found to be in the order of 10 % over the particle lifetime.

The chaotic oscillation of radiation pressure force is mainly caused by random variation of the Solar radiation flux or short lasting, episodic bursts caused by Solar flares or other high energetic features. The Solar flux also abruptly changes, if particles crosses a planetary shadow. Despite "external" changes of the radiation pressure itself, the individual and complex shape of the dust particle influences the radiation pressure via the grain's cross section. The time dependent change of the effective cross section furthermore adds a fluctuating dynamical component. In the subsequent sections we focus our study on investigation of stochastic radiation pressure. We study the dynamical consequences of steadily changing strength of RP due to change of the effective cross section of rotating non-spherical particles. However, the presented analytical model is general and can be used for any source of RP variations.

### 2.2.2.2 Stochasticity Induced by Particle Non-sphericity

As described above, the fluctuation of RP is a natural process having a different origin. In the following section we study dynamical consequences of steady, random variation of the force strength. The magnitude of the change strongly depends on the particular processed changing the RP properties. In our approach we create a model of rotating non-spherical particles. Their steady change of effective cross section effectively causes force fluctuation in this way reflecting the diversity of shapes of "real" particles in the ensemble created by arbitrary dust production mechanism.

For simplicity and in order to develop an analytical model, we consider particles influenced only by gravity of oblate planet and direct radiation pressure. It may be shown that for many dust complexes, this approximation is well justified. The equation of motion in the field of oblate body and exposed to the Solar radiation is determined by Eqs. (2.11) and (2.13). However, for our purpose we reformulate Eq. (2.13) in following form

$$\vec{F}_{\mathrm{RP}} = BS_r\vec{e}_{\odot}, \quad \text{with} \quad B = (Q_{\mathrm{pr}}/c)F_{\odot}\,(1\mathrm{AU}/a_{\mathrm{p}})^2\ , \tag{2.20}$$

where $B$ is the radiation pressure strength coefficient being a constant for a circumplanetary particles and $S_r$ denotes particle cross section ($S_r = \pi s^2$ for spherical grain).

Besides the forces acting on the particle the second key assumption of the model is the particle shape. In order to derive an expressions for the strength of the noise, we waive the idea of modelling properties of "real" dust particles (Fig. 1.2) for simplicity. Instead we start with the most simple but still relevant model reflecting the heterogeneity of particle shapes. We consider particles of two types - prolate (cigar-like shape - middle panel of Fig. 2.4) and oblate (rounded coin-like shape - right panel of Fig. 2.4) where the geometry drastically facilitates the analysis but still reflects basic characteristics. The shape of these two types of grains is produced by a rotation of a rectangle of length $2L$ with two semi-circles of radius $l < L$ adjoined to the shorter sides (left panel of Fig. 2.4) around two perpendicular axes. The only quantity characterising the shape of both particle classes is the aspect ratio $\alpha$ defined as the ratio of maximal and minimal size of the particle: $\alpha = L/l + 1$.

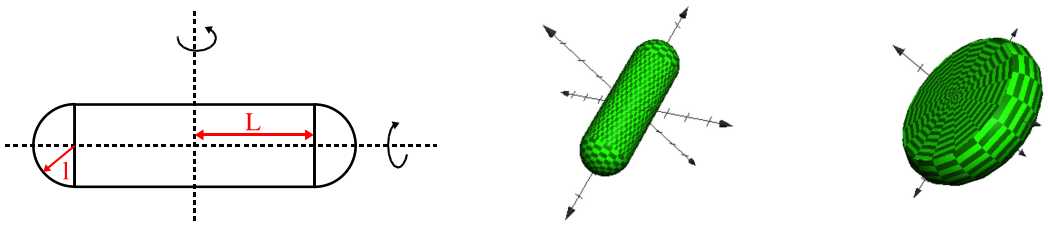


Figure 2.4: Illustration of the model particles obtained by rotation of the structure depicted in the left panel. Middle panel – a prolate particle, right panel – an oblate particle. The aspect ratio is generally defined as $\alpha = L/l + 1$.

Due to the permanent rotation at rate $\Omega_0$, the cross section of these dust grains exposed to Solar radiation is steadily changing, resulting effectively in variation of the radiation pressure and giving rise to the stochasticity of the perturbation. Therefore the cross section of the grain, representing the area of the grain projected on the plane perpendicular to the direction of the Solar radiation, is a time dependent function $S_r(t)$. Thus, the radiation pressure force (Eq. 2.20) with the time dependent $S_r(t)$, is a stochastic force with properties determined by the corresponding properties of the fluctuating variable $S_r(t)$. With these assumptions we separate the deterministic and stochastic part of the radiation pressure as follows

$$\vec{F}_{\rm RP} = F_{\rm RP}\,\vec{e}_\odot \;=\; B\,\langle S_r\rangle\,\vec{e}_\odot \;+\; B\,\zeta(t)\,\vec{e}_\odot, \qquad\qquad \langle\zeta(t)\rangle = 0\,. \tag{2.21}$$

The first term on the right-hand side is the deterministic component, related to the average cross section $\langle S_r\rangle$. The second term is the stochastic component fluctuating around its mean according to $\zeta(t) = S_r(t) - \langle S_r\rangle$. Here we assume that the radiation pressure is acting in radial direction from the Sun ($\vec{e}_\odot$) and neglect all the non-radial components. Additionally we consider that the variable $\zeta(t)$ may be treated as a stationary stochastic process with the time-correlation function

$$K(t',t) = \langle\zeta(t)\zeta(t')\rangle = K(|t'-t|) \tag{2.22}$$

depending only on the modulus of the time difference (see e.g. Resibois and de Leener, 1977; Brilliantov and Revokatov, 1996). Physically, $K(t)$ characterises the memory of the initial orientation of a particle and decreases with time having a maximum at $t = 0$. Resulting from properties of $\zeta(t)$ we can write

$$K(0) = \langle\zeta(t)^2\rangle = \langle S_r^2\rangle - \langle S_r\rangle^2\,, \tag{2.23}$$

where $K(0)$ denotes the difference between the averaged squared cross section of non-spherical particle $\langle S_r\rangle^2$ and the mean square average $\langle S_r^2\rangle$. The fluctuations $\zeta(t)$ and $\zeta(t')$ are almost uncorrelated with an increasing time difference $|t'-t|$. Especially, $K(|t'-t|) \to 0$ for $t \to \infty$.

The instant values of the function $\zeta(t)$ are determined by the instant grain orientation. Thus, choosing a particular model of orientational motion, $K(t)$ may be evaluated. The simplest model we can use is the free-rotation model (Brilliantov and Revokatov, 1996; Pierre and Steele, 1969), where the angular momentum of a grain is conserved. However, there exist several processes that could change the grain's angular momentum as e.g. collisions of grain with gas atoms or photons, emission/absorption of atoms, and photons related to Yarkovsky effect or torque by magnetic field. For both systems studied in this thesis, the Martian and Saturnian environment, the estimated change of angular momentum during the timespan of interest is negligible (see Paper B for more details).

We treat the system of free rotators as an ensemble with randomly distributed angular momenta and assume Gaussian distribution of angular velocities with the characteristic velocity $\Omega_0$. We can show that the time correlation function $K(t)$ depends on time only, through the product $\Omega_0 t$. Then we can write $K(t) = K(0)k(\Omega_0 t)$, with $k(x)$ being dimensionless function of the dimensionless argument.

The quantity which characterises the memory of a particle about its previous orientation is the correlation time of the stochastic variable $\zeta$. It can be estimated as $\sim 1/\Omega_0$. Since, according to our estimates, we expect the rotation frequency of the grains $\Omega_0$ to be very fast on the time-scale of the orbital motion, the simplest model of

δ-correlated white noise may be adopted (see also Spahn et al., 2003). Despite of its simplicity it already reflects the most prominent properties of the stochastic dynamics. Hence, the grain looses its memory very fast, we can write

$$K(t) \simeq 2K_0\delta(t)\,, \tag{2.24}$$

which holds with a high accuracy. That is, we can approximate the fluctuating variable $\zeta(t)$ by a δ-correlated (white) noise with the characteristic amplitude $\sqrt{2K_0}$. The constant $K_0$ can be estimated as

$$K_0 = \int_0^\infty K(t)dt = K(0)\int_0^\infty k(\Omega_0 t)dt = K(0)\left(\frac{\Omega_0}{A}\right)^{-1}. \tag{2.25}$$

As shown in detail in Paper B the constant A is of the order of unity. The value of the frequency $\Omega_0$ however remain very uncertain. Since there does not exist any observation for this value, it can cover a wide range, and will be treated as a parameter here.

Based on above assumptions we summarise the model of stochastic radiation pressure defined by Eq. (2.21) in the following way

$$\vec{F}_{\rm RP} \;=\; B\,\langle S_r\rangle\,\vec{e}_\odot \;+\; B\,\sqrt{2K_0}\;\xi(t)\,\vec{e}_\odot\,, \tag{2.26}$$

where $\xi(t)$ is given as white noise with zero mean and unit dispersion

$$\langle\xi(t)\rangle = 0\,, \qquad\qquad \langle\xi(t_1)\xi(t_2)\rangle = \delta(t_1-t_2). \tag{2.27}$$

The constant $K_0$ and the spin frequency $\Omega_0$ are of crucial importance. They define the strength of the stochastic component of radiation pressure and thus determine our model. Their derivation is presented in the next section.

**Quantifying of the Basic Parameters**

The time correlation function $K_0$ and spin frequency $\Omega_0$ characterise the fluctuation of radiation pressure and thus determine the stochasticity. In order to quantify these parameters, we will stick to estimates as described below. The time correlation parameter $K_0$ is obtained by evaluating Eq. (2.23) for $t' = t$ and sub-sequently Eq. (2.25). A detailed description of the first can be found in Appendix A of Paper B.

For *prolate* particles the projected area on the plane perpendicular to the solar radiation depends on the angle $\theta(t)$ between the symmetry axis of a particle and the direction of the radiation as

$$S_r(t) = 4Ll\sin\theta(t) + \pi l^2\,, \tag{2.28}$$

The average cross section then reads

$$\langle S_r(t)\rangle = 4Ll\langle\sin\theta(t)\rangle + \pi l^2\,, \tag{2.29}$$

and the mean square average of the particle cross section

$$\langle S_r(t)^2\rangle = 16L^2l^2\langle\sin^2\theta(t)\rangle + 8\pi Ll^3\langle\sin\theta(t)\rangle + \pi^2 l^4\,. \tag{2.30}$$

The particle axes of free rotators are isotropically distributed in space, giving

$$\langle\sin\theta(t)\rangle = \frac{\pi}{4}, \qquad\qquad \langle\sin^2\theta(t)\rangle = \frac{2}{3}, \tag{2.31}$$

Equation (2.23) is then written as

$$\begin{aligned} K(0) \;&=\; \frac{32}{3}L^2l^2 + 2\pi^2l^3L + \pi^2l^4 - \pi l\,(L+l) \\ &=\; L^2l^2\left(32/3-\pi^2\right) \;=\; 0.7971\,L^2l^2\,. \end{aligned} \tag{2.32}$$

An analogous analysis may be performed for *oblate* particle. Using the aspect ratio $\alpha = L/l + 1$ we can simplify expression for $\langle S_r\rangle$

$$\langle S_r\rangle = \pi l^2 \begin{cases} \alpha & \text{– prolate particles} \\ \frac{\alpha(\alpha+1)}{2} & \text{– oblate particles} \end{cases} \tag{2.33}$$

and summarise the time correlation parameter in a compact form:

$$K_0 = l^4 \Omega_0^{-1} \begin{cases} 0.7971\,(\alpha-1)^2 & \text{– prolate particles} \\ 0.8224\,\alpha^2(\alpha-1)^2 & \text{– oblate particles .} \end{cases} \tag{2.34}$$

It is relatively complicated to estimate the value of the second parameter $\Omega_0$. Since there are no direct measurements of this quantity and an exact derivation from basic principles is rather complicated, we will try for a simple but plausible estimate in the following.

The number density of most of the dust systems is relatively small and thus mutual collisions or impacts with other particles, like gas molecules or ions are extremely rare. It is unlikely that collisions determine the distribution of $\Omega_0$ of an ensemble of rotating dust grains. Therefore, we conclude that $\Omega_0$ of a dust grain is mainly determined by the initial mechanism of its creation.

Considering the impact ejecta mechanism, the collisions of hypervelocity micrometeoroids with the surface of the satellite create craters of diameter $D_{\rm crat}$. All the material in that crater is shattered and ejected into space with a characteristic speed $v_{\rm ej}$. Estimates of the angular velocity of the ejected particles may be performed for a rocky surface, and yields

$$\Omega_0 \sim \frac{v_{\rm ej}}{D_{\rm crat}}. \tag{2.35}$$

Assuming $v_{\rm ej}$ to be of the order of the escape velocity from the moon, $v_{\rm ej} \sim 5\,{\rm m\,s^{-1}}$, and $D_{\rm crat} \sim 2\times10^{-3}\,{\rm m}$ for a typical crater diameter, we estimate the characteristic frequency to be $\Omega_0 \approx 5\times10^3\,{\rm s^{-1}}$. The corresponding time scale of rotational motion is about $\Omega_0^{-1} \approx 10^{-3}\,{\rm s}$ and thus much smaller than the minimal orbital timescale (minimal particle's orbital period) in the Solar system. This furthermore justifies the application of the simple model of $\delta$-correlated white noise.

For the dust created by endogenic processes (geysers of volcanoes eruptions) we can assume that the eruption of dust is accompanied by that of a gas (sulfur in case of Io and water vapour in case of Enceladus). For simplicity, one may presume that during the eruption the dust grains are in near thermal equilibrium with the gas. After escaping from the parent body into space, they however, decouple from the gas. In this case the angular velocity of the grains is mainly determined by the gas temperature as

$$\Omega_0 \sim \sqrt{\frac{k_B T}{I}}\,. \tag{2.36}$$

Here, $k_B$ is the Boltzmann constant, $T$ the temperature of the gas, and $I$ the characteristic moment of inertia of a grain. Taking that the temperature of the gas varies from $10^2$ K to $10^3$ K[4], $\Omega_0$ ranges between 1-4 Hz for particles of size $\sim 10\,\mu$m and density $2.37\times10^3$ kg/m$^3$. This angular velocity also satisfies the requirement of fast rotation, which justifies the application of the white noise model.

#### 2.2.2.3 Analytical Solution of the Stochastic RP

In this section we analytically estimate the effects of the stochasticity using a linear analysis of the perturbation equations. We derive the mean and variance of eccentricity, inclination and semimajor axis of an ensemble of ejected particles. For a simplified analysis we use the equation of motion in terms of Lagrange orbital elements $h,k,p,q$ and the dimensionless time $\lambda$ as defined in Section 3.2.1, Paper A, B.

In Krivov et al. (1996) the dimensionless parameter $C$ is used to define the strength of the perturbing radiation pressure force. We model the stochastic behaviour of that force according to Eq. (2.21) and thus split this parameter into a deterministic $C_{\rm d}$ and the time dependent stochastic component $C_\xi(\lambda)$ as

$$C(\lambda) \equiv \frac{3}{2}\,\frac{F_{\rm RP}}{m n_\odot n_0 a_0} = C_{\rm d} + C_\xi(\lambda), \tag{2.37}$$

[4]The temperature in the eruption zone of Io is estimated as 1800 K and for Enceladus $\approx 300K$

where the $n_0, n_\odot$ are the initial mean motion of the grain and planet and $a_0$ is the initial semimajor axis of the grain. The fluctuating components $C_\xi$ is modelled by Gaussian white noise

$$\langle C_\xi(\lambda)\rangle = 0, \qquad \langle C_\xi(\lambda_1) C_\xi(\lambda_2)\rangle = \sigma^2\, \delta(\lambda_1 - \lambda_2). \tag{2.38}$$

Using Eqs. (2.26) and (2.37), the coefficients $C_\mathrm{d}$ and $\sigma^2$ can be expressed as

$$C_\mathrm{d} = \frac{3}{2}\frac{B\langle S_r\rangle}{m n_\odot n_0 a_0}, \qquad \sigma^2 = \frac{2\, {C_\mathrm{d}}^2\, K_0\, n_\odot}{\langle S_r\rangle^2}, \tag{2.39}$$

where the properties of stochastic variables (Eqs. (2.27) and (2.38)) have been applied. Since the parameters $C_\mathrm{d}$ and $\sigma^2$ depend on the amplitude of the time correlation function $K_0$ discussed in the previous section, they completely characterise the stochastic process. In general, the full Gauss perturbation equations (e.g. Burns, 1976) should be considered for the analysis. The orbit-averaged equations (Krivov et al., 1996) can omit certain terms which can give rise to an observable diffusion of elements. Nevertheless, in case of eccentricity even the simplified orbit-averaged analysis contains a zeroth order term which is sufficient to explain a diffusion of orbital elements.

The derivation of the mean and variance of the orbital elements subjected to a stochastic force is cumbersome although straightforward. Omitting technical details, we present a simplified description of the method and resulting expressions. For further details we refer to Paper B and its Appendix B. Hereafter, we denote the deterministic solution ($C_\xi = 0$) for a certain element $X$ as $X_\mathrm{d}$, the stochastic solution ($C_\mathrm{d} = 0$) as $X_\xi$, and the full solution as $X_\mathrm{t}$.

**Solution for Eccentricity**

Krivov et al. (1996) have derived simplified equations for eccentricity components $h$ and $k$. Neglecting the second order terms and dropping the inclination components in the orbit-averaged equations one obtains

$$\frac{dh}{d\lambda} = -C(\lambda)\cos\varepsilon\sin\lambda - k\omega, \qquad \frac{dk}{d\lambda} = +C(\lambda)\cos\lambda + h\omega. \tag{2.40}$$

Here $\varepsilon$ is the obliquity of a planet (for Mars $\varepsilon = 25^\circ$) and $\omega$ the oblateness parameter characterising the effect of planetary oblateness.

The purely deterministic solution $h_\mathrm{d}(\lambda)$ and $k_\mathrm{d}(\lambda)$ of the system of equations Eq. (2.40) for $C(\lambda) = C_\mathrm{d}$ was derived by Krivov et al. (1996). The solution of the pure stochastic case $C(\lambda) = C_\xi$, however, is given in Appendix B of Paper B. The complete solutions are the normally distributed elements $h_\mathrm{t}$ and $k_\mathrm{t}$ with mean

$$\langle h_\mathrm{t}(\lambda)\rangle = h_\mathrm{d}(\lambda), \qquad \langle k_\mathrm{t}(\lambda)\rangle = k_\mathrm{d}(\lambda), \tag{2.41}$$

and variance

$$\langle {h_\mathrm{t}}^2(\lambda)\rangle - \langle h_\mathrm{t}(\lambda)\rangle^2 \approx \langle {k_\mathrm{t}}^2(\lambda)\rangle - \langle k_\mathrm{t}(\lambda)\rangle^2 \approx \Lambda\lambda, \tag{2.42}$$

$$\text{where} \qquad \Lambda = \frac{1}{8}\sigma^2\left[3 + \cos(2\varepsilon)\right]. \tag{2.43}$$

Due to the nontrivial dependence of eccentricity on $h$ and $k$, the resulting eccentricity $e_\mathrm{t} = ({h_\mathrm{t}}^2 + {k_\mathrm{t}}^2)^{1/2}$ is not normally distributed. With this in mind the mean eccentricity reads

$$\langle e_\mathrm{t}(\lambda)\rangle \approx \sqrt{{e_\mathrm{d}}^2(\lambda) + \alpha_e \Lambda\lambda}\,. \tag{2.44}$$

The variance is given, for two limiting cases of strong and weak noise

$$\langle {e_\mathrm{t}}^2(\lambda)\rangle - \langle e_\mathrm{t}(\lambda)\rangle^2 \approx (2 - \alpha_e)\,\Lambda\lambda, \qquad \alpha_e = \begin{cases} 1/2, & \Lambda\lambda \ll {e_\mathrm{d}}^2 \\ \pi/2, & \Lambda\lambda \gg {e_\mathrm{d}}^2. \end{cases} \tag{2.45}$$

As we can see from Eq. (2.45) the standard deviation of eccentricity grows linearly with dimensionless time $\lambda$. In an ensemble of particles it yields a dispersion of eccentricities.

**Solution for Semimajor Axis**

For the semimajor axis, the orbit-averaged equations cannot be used anymore. The full perturbation equations have to be studied. In the deterministic case without Poynting-Robertson drag the semimajor axis keeps constant $a_\mathrm{d} = a_0$. In the stochastic case, this does not hold anymore. In our derivation we neglect the influence of planetary oblateness, $\omega = 0$, for simplicity. There are two reasons, which justify this assumption. First, the dependence of the purely deterministic solution $a_\mathrm{d}(\lambda)$ on $\omega$ is very weak. Second, we observe that the mean and variance of the eccentricity components $h_\xi$ and $k_\xi$ are not sensitive to $\omega$, contrary to their deterministic counterparts. The same can be demonstrated for the inclination elements $p$ and $q$.

With this we can use the Gauss perturbation equation for semimajor axis as given in Burns (1976)

$$\frac{d\,a}{d\,t} = \frac{2}{a\,n^2}\,\frac{F_\mathrm{RP}}{m}\,\vec{v}\cdot\vec{e}_\odot, \qquad n^2 = \frac{GM}{a^3}, \tag{2.46}$$

where $\vec{v}$ denotes the particle's velocity and $n$ its mean motion.

Calculating $\vec{v}\cdot\vec{e}_\odot$ and series expanding the result around $e_0, i_0 = 0$ we obtain

$$\vec{v}\cdot\vec{e}_\odot = -a\,n\,\left[\cos\varepsilon\sin\lambda\cos(\tilde{\omega}+\theta) - \cos\lambda\sin(\tilde{\omega}+\theta)\right] + \mathrm{O}(e) + \mathrm{O}(i), \tag{2.47}$$

where $\theta$ is the true anomaly. Clearly, in the purely deterministic case the orbit-average of this equation yields zero. Using the Stratonovich calculus we can derive the appropriate mean and mean square average of the scaled semimajor axis $\widetilde{a} = a/a_0$ as

$$\langle\widetilde{a}_\mathrm{t}^{-1}(\lambda)\rangle = 1 + 4\,\Lambda\lambda/9, \qquad \langle\widetilde{a}_\mathrm{t}^{-2}(\lambda)\rangle = 1 + 8\,\Lambda\lambda/3 + 16\,\Lambda^2\lambda^2/27, \tag{2.48}$$

and the resulting variance

$$\langle\widetilde{a}_\mathrm{t}^{-2}(\lambda)\rangle - \langle\widetilde{a}_\mathrm{t}^{-1}(\lambda)\rangle^2 = \frac{2}{9}\Lambda\lambda + \frac{32}{81}\Lambda^2\lambda^2\,. \tag{2.49}$$

**Solution for Inclination**

As shown in Krivov et al. (1996) the dynamics of particles close to the planet (e.g. Phobos, $\omega \approx 1$) and far from it (e.g. Deimos, $\omega \ll 1$) significantly differs. In sense of orbital elements, this difference is kept in dependence of $p$ and $q$ on $\omega$. For simplicity, we concentrate on the second case assuming $\omega \ll 1$. As in case of semimajor axis, the orbit-averaged equations of motion do not contain a zeroth order term which causes a noticeable diffusion. Therefore, these equations have to be replaced again by Gauss perturbation equations (e.g. Burns, 1976)

$$\mathrm{d}\vec{L}/\mathrm{d}t = \vec{r}\times F_\mathrm{RP}\vec{e}_\odot\,, \qquad \vec{L} = \vec{r}\times m\vec{v}, \qquad p = -L_y/L, \qquad q = L_x/L, \tag{2.50}$$

with angular momentum $\vec{L}$, where $L^2 = m^2 GM_\mathrm{p}\,a(1-e^2)$.

Approximating $a \approx a_0$, we obtain after lengthy but straightforward calculations

$$p_\mathrm{t}'(\lambda) = \frac{2}{3}\,C\,\sin\varepsilon\sin\lambda\sin(g+\theta) + \mathrm{O}_{1,p}(h,k,p,q), \tag{2.51}$$

$$q_\mathrm{t}'(\lambda) = \frac{2}{3}\,C\,\sin\varepsilon\sin\lambda\cos(g+\theta) + \mathrm{O}_{1,q}(h,k,p,q). \tag{2.52}$$

The method of calculating mean and variance of the inclination by using Eq. (2.51) and (2.52) as well as the relative importance of the zeroth and first-order terms is described in detail in Paper B. The inclination elements $p_\mathrm{t}$ and $q_\mathrm{t}$ are Gaussian, while for function of these elements $\sin i_\mathrm{t} = (p_\mathrm{t}^2 + q_\mathrm{t}^2)^{1/2}$ this is not true anymore as it has been for eccentricity. The average solution of $p_\mathrm{t}$ and $q_\mathrm{t}$ is

$$\langle p_\mathrm{t}(\lambda)\rangle \approx p_\mathrm{d}(\lambda), \qquad \langle q_\mathrm{t}(\lambda)\rangle \approx q_\mathrm{d}(\lambda), \tag{2.53}$$

where the standard deviations read

$$\langle {p_\mathrm{t}}^2(\lambda)\rangle - \langle p_\mathrm{t}(\lambda)\rangle^2 \;\approx\; \langle {q_\mathrm{t}}^2(\lambda)\rangle - \langle q_\mathrm{t}(\lambda)\rangle^2 \approx \Upsilon\,\lambda, \tag{2.54}$$

with

$$\Upsilon \equiv \frac{8\sin^2\varepsilon}{9(3+\cos 2\varepsilon)}\Lambda. \tag{2.55}$$

Similarly to eccentricity one obtains

$$\langle \sin i_{\rm t}(\lambda)\rangle \approx \sqrt{\sin^2 i_{\rm d}(\lambda) + \alpha_i\,\Upsilon\,\lambda}, \tag{2.56}$$

$$\langle \sin^2 i_{\rm t}(\lambda)\rangle - \langle \sin i_{\rm t}(\lambda)\rangle^2 \approx (2-\alpha_i)\,\Upsilon\,\lambda, \tag{2.57}$$

$$\alpha_i = \begin{cases} 1/2, & \Upsilon\lambda \ll \sin^2 i_{\rm d}, \\ \pi/2, & \Upsilon\lambda \gg \sin^2 i_{\rm d}. \end{cases} \tag{2.58}$$

## 2.3 Grain Lifetimes and Sinks

In order to complete the story of a particle's dynamical "life", the particle loss mechanisms and sinks have to be described. The lifetime of the particles is an important information which together with the dust production and particle dynamics allows to estimate the steady distribution of the studied dust populations. Before we specify the particular loss mechanisms we divide them in two principal groups. The first one consists of processes causing a gradual decrease of particle size as sublimation, evaporation or sputtering. Its role strongly depends on particle material composition and properties of a surrounding cosmic environment. The second group comprises the sudden particle loss due to collisions with other bodies (very often their own parent moon). The efficiency of this mechanism is determined by particle dynamics.

Dust grains in interplanetary space are, in general, exposed to the Solar radiation. This causes an increase of particle temperature and results in a gradual evaporation or sublimation of the material (Mukai et al., 2001). additionally, the grain immersed in a magnetosphere is eroded by flux of energetic ions, electrons, and UV photons referred to as sputtering. The sputtering rate strongly depends on particle material composition as well as properties of plasma, such as density, velocity and temperature (may vary enormously throughout various regions). The consequence of sputtering is almost negligible for a solid, e.g silicate particle (Leinert and Grün, 1990), but crucial for icy grains as the ones maintaining the Saturnian E ring (Grün et al., 1984). Recently, Jurac et al. (2001) proposed that $1\,\mu$m icy grains in the E ring vanish by sputtering in 50 years, which is much shorter than previously estimated sputtering lifetimes ($10^3$ years, Haff et al., 1983), while smaller grains disappear more rapidly in years ($\sim 0.1\,\mu$m) or even months ($\sim 0.01\,\mu$m). Juhász and Horányi (2002) approximated this results by the equation $s(t) = s_0\,[1 - t/(50\,s_0)]$, where $s_0$ denotes the initial particle size. However, these results have to be reconsidered by an analysis of new Cassini data in the future.

The second mechanism, the particle collisions, is the main loss mechanism in the Solar system. The particles that are created in the planetary system and move in the same region as the parent satellites orbit the planet, will sooner or later collide with the moons, dense rings or central planet. Additionally, they may be destroyed by mutual grain-grain collisions. In contrast to particle creation, due to the high-speed interplanetary impacts, the recolliding particles are usually not energetic enough to be a substantial source of secondary ejecta. However, alternative models also exist. Since the considered target objects are very often the original parent bodies, it in fact gives rise to a chain of sources and sinks. This, so-called self-sustainment scenario, where the reaccreted particles generate a substantial amount of secondary material (in many cases triggered by flux of external impactors), was speculated for e.g. Martian dust tori (Sasaki, 1995, 1996) or Saturn's E ring (Hamilton and Burns, 1994).

Apart from gravitational perturbations which considerably alter the grain's trajectory, for instance in close encounters, there is a variety of perturbation forces, discussed above, influencing significantly the particle orbit and finally lead to a collisions. As described in section 2.2.1.2 any particle exposed to Solar radiation experiences a radiation pressure force. The direct radiation pressure force causes under certain conditions an increase of grains eccentricity, finally leading to collisions with the planet or in the case of Saturn, with the main rings. Depending on the particle size and shape, the effects of the indirect component, the Poynting-Robertson drag, causes a gradual spiralling of grains towards the central body. Another drag force, the plasma drag may either cause an orbital collaps (e.g. Jovian ring particles) or orbital expansion (Saturn's E ring). This permanent transport may on one hand allow the particle to escape from the vicinity of the parent body (being the main sink) but on the other

hand it may increase its collisional probability with other sinks (e.g. other satellites, central planet, dense rings). Corresponding particle lifetimes with respect to these processes were estimated by e.g. Burns et al. (1984) or Burns et al. (2001).

To estimate the lifetimes quantitatively, we may calculate the grain's $e$-folding lifetimes against collisions with planetary satellite ($T_{\rm moon}$ - being infinity if not crossing the moons orbit). We use Öpik's (1976) formula

$$T_{\rm moon} = {\omega_{\rm moon}}^{-1} \approx \pi \sqrt{\sin^2 i + \sin^2 i_{\rm moon}} \left(\frac{a_{\rm moon}}{R_{\rm moon}}\right)^2 \left(\frac{u}{u_{\rm r}}\right) P, \tag{2.59}$$

where $\omega_{\rm moon}$ is the corresponding collisional frequency, $i$ and $i_{\rm moon}$ are the inclinations of the grain's and moon's orbit, $R_{\rm moon}$ and $a_{\rm moon}$ the satellite radius and semimajor axis and $P$ is the orbital period of the particle. $u$ is the average grain velocity relative to the moon and $u_{\rm r}$ is its radial component - both defined by:

$$u = \sqrt{3 - \frac{1}{A} - 2\sqrt{A(1-e^2)}\cos i} \quad \text{and} \quad u_{\rm r} = \sqrt{2 - \frac{1}{A} - A(1-e^2)}. \tag{2.60}$$

Here $A \equiv a/a_{\rm moon}$ denotes the dimensionless semimajor axis of the particle orbit. The ratio $u/u_{\rm r}$ only weakly depends on the orbital elements, including eccentricity. For $A \approx 1$ and small $i$, the ratio $u/u_{\rm r}$ is of the order of unity (Hamilton and Burns, 1994; Krivov and Hamilton, 1997).

Eqs. (2.59) and (2.60) can be used to calculate instantaneous lifetimes agains collision with any satellite $T_{\rm moon}(t)$ corresponding to particle's $a(t)$, $e(t)$, $i(t)$. Introducing the obvious relation for the collision frequencies $\omega = \omega_1 + \omega_2 + \ldots$ and periods $T^{-1} = T_1^{-1} + T_2^{-1} + \ldots$, the collision lifetimes against collision with several moons can be calculated as

$$T_{\rm impact}^{-1} = T_{\rm moon1}^{-1} + T_{\rm moon2}^{-1} + \ldots \ . \tag{2.61}$$

The time-dependent $T_{\rm impact}(t)$ has an "instantaneous" meaning: it is the lifetime one would expect, if at the moment $t$ the particle's orbital elements $a(t)$, $e(t)$, $i(t)$ were "frozen".

Similarly, the particle lifetime against mutual collisions of equal-sized partices is (Paper A)

$$T_{\rm coll} = {\omega_{\rm coll}}^{-1} \approx (n S_r v_{\rm imp})^{-1}, \tag{2.62}$$

where $n$ is here the number density of particles, $v_{imp} \approx v_0 \sqrt{e_{mean}^2 + i_{mean}^2}$ the mean relative (mutual) velocity between them ($v_0$ is the orbital velocity of the parent moon), and $S_r = 2\pi s^2$ the collisional cross section. The approximate value of the number density is

$$n \approx N^+ T / V \ , \tag{2.63}$$

where $N^+$ is the dust production rate in the considered size interval and $T$ the mean lifetime against both impacts with the moons and grain-grain collisions. The quantity $V$ is the volume of the torus around the orbit of the parent moon (e.g. Martian moons tori or Enceladus torus)

$$V \approx 8\pi a_0^3 e_{\rm max} i_{\rm max}, \tag{2.64}$$

with $a_0$ being the initial semimajor axis of the grain (parent moon orbit), $e_{max}$ and $i_{max}$ typical amplitudes of oscillations of eccentricity and inclination.

Equations (2.62)–(2.64) result in

$$T_{\rm coll} \approx \frac{8\pi a_0^3 e_{max} i_{max}}{N^+ T S_r v_{imp}} \ , \tag{2.65}$$

giving mean lifetime against mutual collisions and collisions with planetary moons as:

$$\frac{1}{T} \approx \frac{1}{T_{\rm impact}} + \frac{N^+ T S_r v_{\rm imp}}{8\pi a_0^3 e_{\rm max} i_{\rm max}}. \tag{2.66}$$

Except of $N^+$ which is mainly determined by the particle production mechanism, all quantities in Eq. (2.66) are determined by the grain dynamics and are rather well determined. Using Eq. (2.66) we may derive the mean lifetimes of dust particles of different size. Additionally, as shown in section 3.2.2.4 it allows to estimate the fraction of remaining particles and in dependence on the dust production efficiency also the resulting particle spatial density and the corresponding optical depth $\tau$. The importance of all mentioned particle loss mechanisms and sinks strongly depends on the exact configuration and current state of the dust grain and therefore has to be studied individually for each considered dust system.

## 2.4 Brief Summary

The main aim of the model presented in this chapter was to describe the "life" of dust particles orbiting an arbitrary planet. In order to provide a steady state description of any dust population, the creation, dynamical evolution and the final extinction of a particle ensemble has to be studied together. First we described two major dust production mechanisms in the Solar system:

- **Exogenic impact ejecta process** - production of dust at atmosphereless bodies by hypervelocity impacts of micrometeoroids.
- **Endogenic processes** producing dust and gas plumes at the planetary satellites by geyser eruptions, volcanic/cryovolcanic activity, mechanisms which has to be triggered by efficient source of energy.

The ejected particles are influenced by ensemble of perturbation forces. Dividing the forces into two principal groups, we introduced:

- **Deterministic forces** - gravity of oblate planet, direct radiation pressure, Poynting-Robertson drag, Lorentz force, and plasma drag determined by well defined properties of particles and surrounding fields.
- **Stochastic fluctuations** - stochastic fluctuations of acting forces or particle properties as variation of radiation pressure and Lorentz force or steady change of particle charge and cross section due to rotation of non-spherical grain.

Finally we described severall processes limiting particle lifetime as gradual decrease of particle size by sputtering or particle collisions. We derived particle lifetimes against collisions with planetary moons and mutual grain-grain collisions.

# Chapter 3

# Applications

The configuration of the dust complex in a given planetary environment is largely determined by the particles' creation, dynamical "life", and "death" (Chapter 2). In this chapter we present two specific applications, namely the Martian dust tori and Saturn's E ring. We start with a comparison of the impact ejecta efficiency at the satellites of Mars and Saturn (Section 3.1). In Section 3.2 we study the (deterministic and stochastic) aspects of the long-term dynamics of dust particles ejected from Deimos, focus on the influence of Poynting-Robertson drag and the corresponding change of global properties of the Deimos dust torus. Then, the dynamical consequences of radiation pressure are examined in terms of a stochastic model. Finally, in Section 3.3 we investigate the effect of different dust production mechanisms at Enceladus. Comparing the data recorded by the CDA during the Enceladus E11 flyby with simulations, we identify a strong dust source in the south polar region of the satellite. We determine the contribution of this source relative to dust produced by micro-meteoroid impacts.

## 3.1 impact ejecta Dust Production at Mars and Saturn

The empirical model for the impact ejecta mechanism presented in Section 2.1.1 allows to estimate the amount of material ejected from the surface of an atmosphereless body due to impacts of a given flux of micrometeoroids. In this section, we estimate the dust production from the Martian moons Phobos and Deimos and the large Saturnian E ring moons by impacting IDPs. Other impactor families are not considered here, but we refer to Paper C for a detailed comparison of ejecta produced at Saturnian moons by the E ring particles and IDPs. The resulting mass and number production rates as well as satellite and impactor properties are summarised in Table. 3.1.

The mass flux and velocities of IDPs at Mars and Saturn, estimated from the models of Grün et al. (1985) and Divine (1993) give a motivation for the parameters. In our study, we assume IDP particles with a typical mass of $10^{-8}\,\mathrm{kg}$ and size $s_{\max} = 100\,\mu\mathrm{m}$. The choice of the maximal ejecta velocity is $v_{\max} = 3{,}000\,m\,\mathrm{s}^{-1}$.

For the flux of impactors at Mars we adopt values used by Krivov et al. (2006)

$$F_{\mathrm{imp}}^{\infty} \;\approx\; 1\times10^{-15}\mathrm{kg\ m^{-2}\,s^{-1}} \quad \text{and} \quad v_{\mathrm{imp}}^{\infty} = 15\times10^{3}\,\mathrm{m\,s^{-1}}\,. \tag{3.1}$$

Due to the relatively small mass of Mars, gravitational focusing is small and we neglected a corresponding change of the impactor mass flux and velocity. As shown in Table 3.1 the correction factor $n_{\mathrm{imp}}/n_{\mathrm{imp}}^{\infty}$ and $v_{\mathrm{imp}}/v_{\mathrm{imp}}^{\infty}$ differ from unity by one percent at most. Due to the low albedo of Phobos and Deimos we may consider the surface to be pure silicate ($G_{\mathrm{sil}} = 1$) giving a yield for both satellites, $Y \;\approx\; 300$. Then, the total mass production rate is $M^{+} \approx 1.3\times10^{-4}\mathrm{kg\,s^{-1}}$ for Phobos and $4\times10^{-5}\mathrm{kg\,s^{-1}}$ for Deimos.

Previous studies of the Martian dust complex have shown that the dynamics and lifetimes of the grains strongly depend on the particle size (next section, Paper A). After the loss of spacecraft Nozomi unfortunately no in situ data of the dust tori will be available. The next opportunity for a detection of the putative dust tori of Mars will

be observation from Earth during the ring plane crossing in December 2007 (Krivov et al., 2006). According to our modelling, smaller particles are produced at much higher rates, and the lifetimes against impacts to the martian moons decrease with increasing particle size (Paper A). Therefore the optical depth in the dust belt is dominated by particles somewhat larger than the critical radii as defined in the next section. For this reason we estimate the dust production just for a "partial torus", for a narrow size range [20,30] $\mu$m for Phobos and [10,15] $\mu$m for Deimos. The resulting number of grains per unit time leaving the surface of the moons in these size ranges (Eq. 2.5) is $N^+ \approx 10^5\,\mathrm{s}^{-1}$ for Phobos and $N^+ \approx 10^6\,\mathrm{s}^{-1}$ for Deimos (the larger cross section of Phobos almost compensates the smaller production due to the larger grain sizes). Since the escape velocity $v_{\mathrm{esc}}$ of both satellites is very small ($\lesssim 10\,\mathrm{m\,s}^{-1}$), almost all of the ejected particles escape the moons' gravity and we may approximate $M^+(> v_{\mathrm{esc}}) = M^+$, $N^+(> v_{\mathrm{esc}}) = N^+$. Our results are in good agreement with values obtained by Krivov et al. (2006).

Table 3.1: Parameters and IDP fluxes for satellites of Mars and Saturn. The asterix symbol ($*$) denotes values for the grains in size interval [20,30] $\mu$m (Phobos) and [10,15] $\mu$m (Deimos), respectively. 2B|3B - refers to the 2-body and 3-body escape velocity, respectively.

| Parameters<br>$F^{\infty}_{\mathrm{imp}}[\mathrm{kg\,m^{-2}\,s^{-1}}]$<br>$v^{\infty}_{\mathrm{imp}}[\mathrm{m\,s^{-1}}]$ | Eq. | Mars<br>$1\times10^{-15}$<br>$15\times10^{3}$ | | Saturn<br>$1.8\times10^{-16}$<br>$9.5\times10^{3}$ | | |
|---|---|---|---|---|---|---|
| Satellite | | Phobos | Deimos | Enceladus | Dione | Rhea |
| $Distance[10^6\,\mathrm{m}]$ | | 9.4 | 23.5 | 238 | 377 | 527 |
| $Radius[10^3\,\mathrm{m}]$ | | 11.2 | 6.2 | 252 | 562 | 764 |
| $Geom.\,Albedo$ | | 0.071 | 0.068 | 1.0 | 0.6 | 0.6 |
| $G_{\mathrm{sil}}$ | (2.4) | 1 | 1 | 0 | 0 | 0 |
| $K_e/K_i$ | (C - 7) | - | - | 0.3 | 0.3 | 0.3 |
| $\beta$ | (2.7) | - | - | 3 | 3 | 3 |
| $v_{\mathrm{imp}}/v^{\infty}_{\mathrm{imp}}$ | (C - 14) | 1.020 | 1.008 | 2.13 | 1.80 | 1.61 |
| $n_{\mathrm{imp}}/n^{\infty}_{\mathrm{imp}}$ | (C - 14) | 0.983 | 1.002 | 2.01 | 1.74 | 1.58 |
| $F_{\mathrm{imp}}/F^{\infty}_{\mathrm{imp}}$ | (2.2) | 1.003 | 1.010 | 4.28 | 3.13 | 2.55 |
| $v_{\mathrm{imp}}[10^3\,\mathrm{m\ s^{-1}}]$ | (C - 14) | 15.3 | 15.1 | 20.2 | 17.1 | 15.3 |
| $F_{\mathrm{imp}}[10^{-15}\,\mathrm{kg\,m^{-2}\,s^{-1}}]$ | (2.2) | 1.003 | 1.01 | 0.77 | 0.56 | 0.46 |
| $Y$ | (2.4) | 338 | 328 | 15,000 | 10,000 | 7500 |
| $v_0[\mathrm{m\ s^{-1}}]$ | (C - 7) | - | - | 29.84 | 31.18 | 32.07 |
| $v_{\mathrm{esc}}[\mathrm{m\ s^{-1}}]$ (2B\|3B) | (2.6) | 11.3\|6.5 | 6.9\|6 | 239\|205 | 510\|464 | 635\|592 |
| $M^+[\mathrm{kg\ s^{-1}}]$ | (2.3) | $1.3\times10^{-4}$ | $4\times10^{-5}$ | 2.3 | 5.5 | 6.3 |
| $N^+[\mathrm{s^{-1}}]$ | (2.5) | $10^5*$ | $10^6*$ | $3.6\times10^{12}$ | $8.7\times10^{12}$ | $1.0\times10^{13}$ |
| $M^+(> v_{\mathrm{esc}})[\mathrm{kg\ s^{-1}}]$ | (2.9) | - | - | 0.049 | 0.025 | 0.019 |
| $N^+(> v_{\mathrm{esc}})[\mathrm{s^{-1}}]$ | (2.9) | - | - | $7.7\times10^{10}$ | $3.9\times10^{10}$ | $2.9\times10^{10}$ |

For Saturn's E ring region we consider properties of the satellite surfaces and IDPs as given in Paper C, Krivov et al. (2003), and Sremčević et al. (2003). The following flux and velocities of IDPs at Saturn are used (Table 3.1)

$$F^{\infty}_{\mathrm{imp}} \;\approx\; 1.8\times10^{-16}\mathrm{kg\ m^{-2}\,s^{-1}} \quad \text{and} \quad v^{\infty}_{\mathrm{imp}} = 9.5\times10^{3}\,\mathrm{m\,s^{-1}}\,. \tag{3.2}$$

In contrast to the Martian system, the gravitational focusing at Saturn plays important role. For example, the flux $F_{\mathrm{imp}}$ near Enceladus is about 4 times larger than the unperturbed $F^{\infty}_{\mathrm{imp}}$. The importance of gravitational focusing decreases with increasing distance from the planet. Thus, as the yield $Y$ strongly depends on the velocity of the impactors, it is also function of distance from the planet. Moreover, the total mass of particles escaping a satellite depends on the mass and size of the moon. On the one hand, the moon surface serving as a target for impactors is proportional to $R^2$. On the other hand, with increasing mass of the moon it gets harder for the grains to escape. Because both tendencies compete, there exists an optimal moon size for which the ejection mechanism is most efficient. As an example, even if $Y$ and $F_{\mathrm{imp}}$ for Enceladus is bigger than for Dione, the $M^+$ for Dione is larger. Here the larger size (cross section) of Dione is decisive. On the other hand the larger mass of Dione

makes $M^+(> v_{\rm esc})$ smaller than the corresponding value for Enceladus. To compare both planetary systems, we may conclude that, naturally, due to much bigger size of the Saturnian moons, the resulting $N^+$ is by several orders of magnitude higher than $N^+$ for Phobos and Deimos.

A more general model for planetary dust environments should include also other impactor families than IDPs. This could be interstellar dust particles or dust created by episodic events as the dust brought by active comets like Shomaker Levy 9 impacting Jupiter (Krivov et al., 2002). Moreover the ejected particles themselves create dust tori or rings, and re-impacts on the moons may abundantly eject dust particles. Both in the Martian (Sasaki, 1995, 1996) and in the Saturnian environment (Hamilton and Burns, 1994), this mechanism was discussed, possibly leading to self-sustaining dust tori. A recent comparison of the relative influence of IDPs and E ring particles (ERPs) for different Saturnian moons is described in detail in Paper C.

## 3.2 Martian Dust Complex: The Deimos Torus

The existence of a dust complex around Mars was first suggested by Steven Soter in 1971 (Soter, 1971). He proposed that Mars is encircled by a disk or torus of dust particles originating from the Martian satellites. As Phobos and Deimos are exposed to the steady flux of interplanetary micrometeoroids, these hypervelocity impacts would produce secondary material (Section 2.1.1) which should generate ethereal dust tori along the orbits of the satellites. Despite relatively robust theoretical predictions (see Krivov and Hamilton, 1997; Krivov et al., 2006, for overview on previous work) these tori still escape direct observational confirmation. These negative results pose a challenge for further theoretical study.

The dynamics of ejected particles is subject to gravity, radiation pressure, Lorentz force, and thus, may be very complex. The strength of the various perturbation forces differs in the dependence on grain size and position relative to Mars. According to Krivov (1994) there exist several populations of particles that exhibit fundamentally different dynamics. The largest ejected grains, larger than 1 mm (Population 0), are mainly governed by the gravity of Mars. They form a relatively narrow disc along the orbit of the moons. Since these particles are rapidly lost due to the collisions with the parent moons, their number densities and lifetimes are fairly small, on the order of $\sim 1$ Martian year. The next population of smaller particles in the size range between tens to hundreds of microns (Population I) has lifetimes between tens of years (Phobos' ejecta) and a few thousand up to tens of thousands of years (Deimos). Since they are small enough to be noticeably affected by non-gravitational perturbing forces, such as direct radiation pressure and Poynting-Robertson drag, they may form extended tori variable in size and asymmetrically orientated with respect to Mars (Krivov and Hamilton, 1997). They comprise the main component of the entire dust complex and are the main target of our study. The most efficient loss mechanism for this population is the reaccretion by Phobos and Deimos as well as mutual grain-grain collisions (Paper A). As described in Section 2.2.1 the combined influence of J2 and RP causes periodic oscillations of eccentricity and inclination of individual particles. Since the maximal eccentricity is inversely proportional to the particle size (Krivov et al., 1996), there exists a critical grain size $s_{\rm crit}$ ($\approx 10$ $\mu$m) below which the particles hit Mars at their pericenter in less than one year (Population II). Yet smaller submicron grains (Population III) are strongly affected by fast fluctuations of the solar wind and the Martian plasma environment. They are removed from the Martian system within 10-100 days and may form a highly variable subtle halo around Mars (Horányi et al., 1990, 1991).

In the present study we address the dynamics of the longest living particles ejected from Deimos, i.e. Population I, which are expected to dominate the dust environment at Mars (Juhász and Horányi, 1995). The motion of the dust under action of the two strongest perturbations, J2 and RP, at Mars has been intensively studied (Krivov et al., 1996; Hamilton, 1996; Ishimoto, 1996; Krivov and Hamilton, 1997; Howard et al., 2003). The other perturbative forces as e.g. Poynting-Robertson drag or electro-magnetic forces, are small, and thus, are usually neglected in the size range we consider. However, if considering particles with extremely long lifetimes of tens of thousands of years, as Deimos Population I, weak forces may become significant for the particle dynamics.

We divide our study into two parts. In the first part we develop a model of the dynamics of Deimos' particles governed by gravity of oblate Mars, direct radiation pressure and Poynting-Robertson drag (Paper A). We particularly concentrate on the long-term influence of Poynting-Robertson drag which was never included in previous models. We quantify its long-term influence on the structure and spatial geometry of the torus. Further, we estimate

the lifetime of particles with respect to collisions with the moons and grain-grain collisions. In the second part, motivated by the negative results of the attempts to detect the Martian tori, we investigate a further mechanism that may decrease tori optical depth. Namely, the rotation of non-spherical particles causes a change of the effective particle cross section and leads to highly variable strength of the RP force. For an ensemble of particles we model this effect as a stochastic force. Performing a set of numerical simulations we compare the results with theoretical predictions presented in Section 2.2.2. The effect leads to a diffusion of orbital elements which depletes optical depth $\tau$.

### 3.2.1 Orbit-averaged Equations

The motion of particles under the influence of the gravity of oblate Mars, direct radiation pressure, and Poynting-Robertson drag as formulated in Section 2.2.1 is analytically not treatable. Thus, we numerically integrate the equations of motion (2.10). Since we address the long-term dynamics, direct numerical integration requires prohibitively long computing times. A faster alternative is to study the orbit-averaged equations of motion.

The system of orbit-averaged perturbation equations of particle motion under the combined influence of J2, RP, and PR reads (PaperA)

$$\frac{da}{d\lambda_\odot} = -Da \tag{3.3}$$

$$\begin{aligned}\frac{dh}{d\lambda_\odot} &= -k\omega\frac{5I^2-2I-1}{2E^4} - \frac{C}{E(1+I)}\{[p-Hh]q\cos\lambda_\odot \\ &+ [E^2(1+I)-p(p-Hh)]\cos\varepsilon\sin\lambda_\odot \\ &+ [E^2(1+I)p-IKk]\sin\varepsilon\sin\lambda_\odot\}\end{aligned} \tag{3.4}$$

$$\begin{aligned}\frac{dk}{d\lambda_\odot} &= h\omega\frac{5I^2-2I-1}{2E^4} + \frac{C}{E(1+I)}\{[q-Hk]p\cos\varepsilon\sin\lambda_\odot \\ &+ [E^2(1+I)-q(q-Hk)]\cos\lambda_\odot \\ &- [E^2(1+I)q-IKh]\sin\varepsilon\sin\lambda_\odot\}\end{aligned} \tag{3.5}$$

$$\begin{aligned}\frac{dp}{d\lambda_\odot} &= q\omega\frac{I}{E^4} + \frac{C}{E(1+I)}[Hp-(1+I)h]\times \\ &\times [(p\cos\varepsilon - I\sin\varepsilon)\sin\lambda_\odot - q\cos\lambda_\odot]\end{aligned} \tag{3.6}$$

$$\begin{aligned}\frac{dq}{d\lambda_\odot} &= -p\omega\frac{I}{E^4} + \frac{C}{E(1+I)}[Hq-(1+I)k]\times \\ &\times [(p\cos\varepsilon - I\sin\varepsilon)\sin\lambda_\odot - q\cos\lambda_\odot],\end{aligned} \tag{3.7}$$

where the Lagrange orbital elements $h,k,p,q$ are defined by

$$h = e\cos\tilde{\omega}, \quad k = e\sin\tilde{\omega}, \quad p = \sin i\cos\Omega, \quad q = \sin i\sin\Omega. \tag{3.8}$$

Here $\tilde{\omega}\equiv\Omega+g$ denotes the longitude of pericenter and $e$, $i$, $\Omega$, and $g$ are eccentricity, inclination, longitude of the ascending node, and the argument of the pericenter, respectively. As independent variable the longitude of the Sun $\lambda$ is used, leading to a dimensionless formulation. Neglecting the eccentricity of Mars, $\lambda$ is a linear function of time

$$\lambda = \lambda_{\odot 0} + n_\odot t, \qquad n_\odot = \sqrt{GM_\odot/a_\mathrm{p}^3}, \tag{3.9}$$

where $n_\odot$ is the mean motion of the planet and $\lambda_{\odot 0}$ is the initial solar longitude at the moment of ejection ($t_0 = 0$).

The parameters coupling Eqs. (3.3) – (3.7) are defined as

$$D = \frac{3}{8}\frac{1}{n_\odot}F_\odot\left(\frac{1\mathrm{AU}}{a_\mathrm{p}}\right)^2\frac{Q_\mathrm{pr}}{c^2\rho s}\left(5+\cos^2 i\right), \tag{3.10}$$

$$E = \sqrt{1-e^2} = \sqrt{1-h^2-k^2}, \qquad H = hp + kq, \tag{3.11}$$

$$I = \cos i = \sqrt{1-p^2-q^2}, \qquad K = hq - kp, \tag{3.12}$$

The factor $D$ characterises the decrease of semimajor axis $\dot{a}/a = Dn_\odot$ due to PR drag (Burns et al., 1979). Replacing $\cos^2 i$ with unity, the decay of semimajor axis is exponential $a = a_0 \exp(-Dn_\odot t)$. The parameter $\varepsilon$ denotes the obliquity of Mars ($\varepsilon = 25^\circ$) and $\rho$ the material density of the dust grain. The dimensionless parameters $C$ and $\omega$ characterise the strength of radiation pressure and oblateness (as defined in Krivov et al., 1996). These variables are functions of semimajor axis:

$$C(a) = C_0 \left(\frac{a}{a_0}\right)^{\frac{1}{2}}, \qquad \omega(a) = \omega_0 \left(\frac{a}{a_0}\right)^{-\frac{7}{2}}, \tag{3.13}$$

with $C_0 \equiv C(a_0)$ and $\omega_0 \equiv \omega_0(a_0)$. Assuming a grain density of $\rho = 2.37\,\mathrm{g\ cm^{-3}}$, $C_0$ and $\omega_0$ can be expressed for Phobos and Deimos ejecta as:

$$C_0 = 4.10\,\frac{Q_{\mathrm{pr}}(s)}{s[\mu\mathrm{m}]} \quad \text{(Phobos)} \qquad C_0 = 6.49\,\frac{Q_{\mathrm{pr}}(s)}{s[\mu\mathrm{m}]} \quad \text{(Deimos)} \tag{3.14}$$

$$\omega_0 = 0.829 \quad \text{(Phobos)}, \qquad \omega_0 = 0.0335 \quad \text{(Deimos)}. \tag{3.15}$$

As seen from Eqs. (3.10) and (3.13), the parameters D, C, and $\omega$ are a functions of the orbital elements and therefore couple the equations (3.3 – 3.7). The parameter $D$ has a weak dependence on inclination, which we take into account in the numerical integration. Both, $C$ and $\omega$ are functions of semimajor axis.

For the numerical integration of the orbit-averaged perturbation equations (Eqs. (3.3) – (3.7)) in Lagrange orbital elements as well as Newtons Equation (2.10) in phase-space coordinates, we use an integrator based on Everhart's (1985) method with adaptive choice of the integration step.

### 3.2.2 Deterministic Solution of the Photo-Gravitational Problem (J2 + RP + PR)

#### 3.2.2.1 Radiation Pressure and Planetary Oblateness

The dynamics of a grain in the beginning of its orbital evolution is mainly perturbed by direct RP (Krivov et al., 1996; Hamilton and Krivov, 1996; Burns et al., 2001), the indirect component of radiation pressure (PR) becomes important only at long time scales. In this subsection we study the effect or RP alone, investigating PR in the following subsection separately.

Since direct radiation pressure is a conservative force and does not affect the total energy of the grain, the semimajor axis of a dust particle remains constant. However, its orbital eccentricity oscillates with a period near Mars' orbital period (1 Martian year = 1.88 years, hereafter denoted by M.y.) and an amplitude depending on the strength of radiation pressure $C$:

$$e_{\max} = 2C/(1+C^2)\,, \tag{3.16}$$

provided that the obliquity $\varepsilon$ is small, meaning that the particle orbit basically lies in the ecliptic plane so that solar radiation is parallel to the orbital plane. The orbital inclination also oscillates, but with a longer period (tens of M.y. for 10 $\mu$m grains).

Equation (3.16) also sets the critical threshold of $C$ for which the maximal eccentricity is so large that particle collides with Mars ($e_{\max} = 1 - R_{\mathrm{p}}/a_0$, for Deimos $e_{\max} = 0.855$). In the same sense it also defines the critical size of particles $s_{\mathrm{crit}}$, which distinguishes between Deimos Population II and long living Population I. Evaluating Eqs. (3.15) and (3.16) this implies a critical radius $s_{\mathrm{crit}} = 5\,\mu$m. However, numerical test integrations with additional forces yield a slightly higher value of approximately 7 $\mu$m. Naturally, since the production rate of smaller particles is higher, we can expect that grains with size just above the critical value $s_{\mathrm{crit}}$ will dominate the Population I. For this reason we focus on particle sizes from 7 up to 30 $\mu$m. In this section, we consider spherical grains consisting of silicate (for parameters, see Kimura et al., 1997; Krivov et al., 1998). The bulk density of this material is

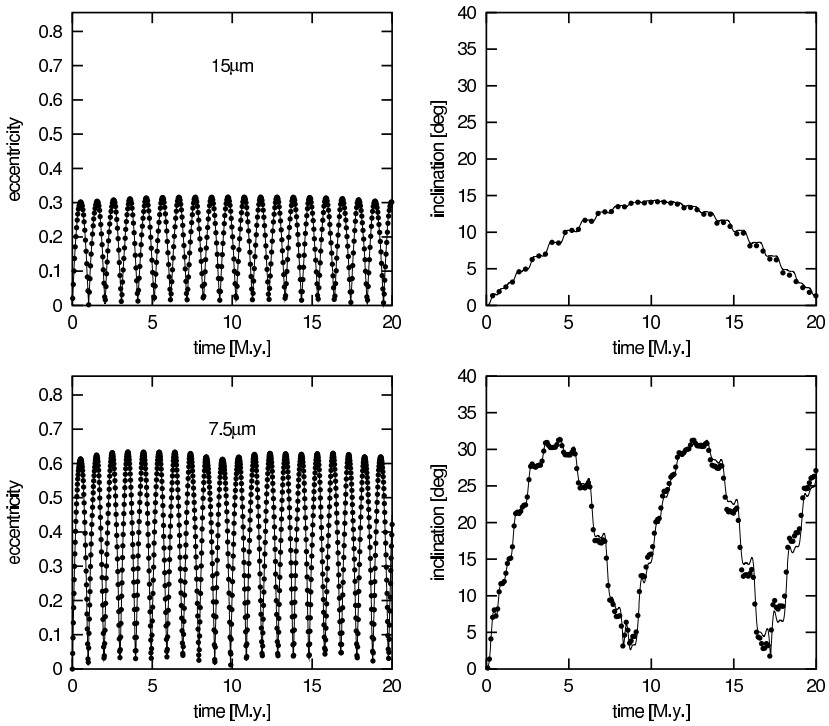


Figure 3.1: Dynamical evolution of 15 $\mu$m (top) and 7.5 $\mu$m Deimos ejecta (bottom) subject to radiation pressure and planetary oblateness. Points: integration of Newtons equations (2.10), solid lines: integration of orbit-averaged Eqs. (3.3)–(3.7). The range of the eccentricity axis corresponds to the critical eccentricity 0.855, for which the pericenters of orbits touch the Martian surface.

$\rho = 2.37\,\mathrm{g\,cm^{-3}}$ and the radiation pressure efficiency $Q_{\mathrm{pr}}$ is calculated depending on the grain size as shown in Paper A (Table 1 ibid).

Taking into account planetary oblateness together with direct radiation pressure permits a more accurate description of the problem. Figure. 3.1[1] depicts the evolution of eccentricity and inclination of particles launched from Deimos' surface with radii of 7.5 and 15 $\mu$m. Numerical integration of orbit-averaged equations in Lagrange elements (the solid line) and direct integration of Newtons equation of motion for the phase-space coordinates (points), show that the Eqs. (3.4 – 3.7) provide good accuracy. The eccentricity exhibit a slow low-amplitude modulation with the period of the inclination oscillation (about 20 M.y. for $s = 15\,\mu$m and 8 M.y. for $s = 7.5\,\mu$m). The amplitude is about one or two percent of $e_{max}$.

The system of equations (3.4)–(3.7), can be simplified by neglecting the terms of order $e^2$, $i^2$, $C\,i$ and assuming that $\omega$ is small (Krivov et al., 1996). Than an approximate analytic expression for the oscillation periods of $e$ and $i$ and their amplitudes can be found. For the eccetricity these are:

$$e_{max} \approx \frac{2C(\cos\varepsilon + \omega)}{1-\omega^2}, \qquad T_e \approx 1/(1-\omega), \tag{3.17}$$

and for the inclination:

$$i_{max} \approx \arcsin\frac{2d}{\nu}, \qquad T_i \approx \frac{1}{\nu}, \tag{3.18}$$

where

$$d = \frac{C^2}{2}\,\frac{1+\omega\cos\varepsilon}{1-\omega^2}\sin\varepsilon, \qquad \text{and} \qquad \nu = \omega + \frac{C^2}{2}\,\frac{\cos\varepsilon+\omega}{1-\omega^2}. \tag{3.19}$$

[1]There is typo in Paper A. Their Fig. 1 depicts the dynamics of a grain under influence of J2 and RP and not just RP as stated. However, the overall dynamics is similar in both cases. The main change is in the period and amplitude of inclination.

#### 3.2.2.2 Poynting-Robertson Drag

We will show in this section, that PR plays a crucial role for the dynamics of the long-living particles. Adding the PR in the equations results in orbital dissipation, thus in a gradual decrease of semimajor axis. Since the orbit-averaged equations are coupled and the parameters $C$ and $\omega$ change with time (see Paper A - Fig. 2 for their long-term variation), the change of semimajor axis also influence other orbital elements. Fig. 3.2 shows the progressive change of amplitudes and periods of eccentricity and inclination obtained from analytical Eqs. (3.17) - (3.18) and by numerical integration of Eqs. (3.3)–(3.7). The correspondence between theory (lines) and simulation (points) is quite satisfactory except for $i_{\max}$. A similar formula for $i_{\max}$ derived by Hamilton (1996) (his $2i_{\text{forced}}$) gives almost the same results. In contrast to the amplitudes and period of eccentricity, which remain almost constant, both inclination quantities steadily decrease with time. As the semimajor axis decreases, the particles

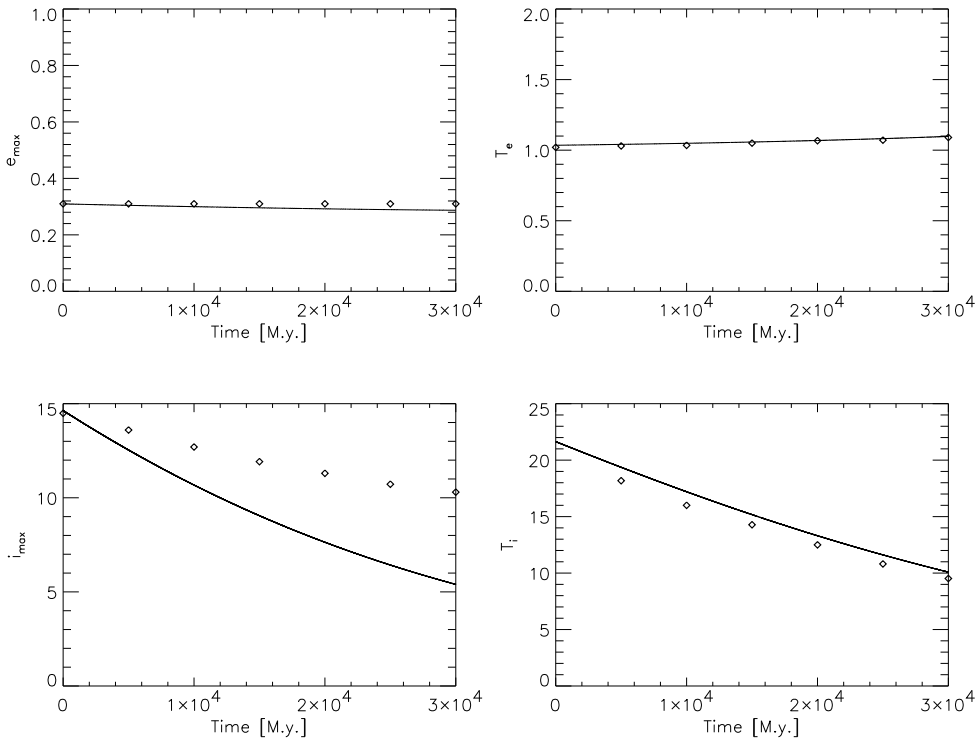


Figure 3.2: Time evolution of amplitudes and periods of eccentricity and inclination derived for 15 $\mu$m Deimos ejecta subject to J2, RP and PR. Lines correspond to the theoretical estimates (Eqs. (3.17) - (3.18)) and dots to the numerical solution of orbit-averaged equations of motion (Eqs. (3.3)–(3.7)).

slowly drift inwards and will reach the regime where both perturbations, J2 and also RP become simultaneously important for the dynamics ($C$ decreases and $\omega$ increase with time). This resembles a grains ejected from Phobos for which the analytical treatment is more complicated (Krivov et al., 1996; Ishimoto, 1996; Hamilton, 1996; Hamilton and Krivov, 1996).

To investigate the long-term influence of PR we numerically integrate the orbit-averaged equations (Eqs. (3.3) – (3.7)). The resulting time variation of semimajor axis, eccentricity and inclination is shown in Fig. 3.3 for a 15 $\mu$m (left panel) and 7.5 $\mu$m (right panel) grain. The grains have been ejected from Deimos at Martian autumn equinox ($\lambda_\odot = 180^\circ$) on a circular orbit lying in the equatorial plane ($e_0 = i_0 = 0$). The decrease of the semimajor-axis $a$ due to the drag can be clearly recognized. The time dependence of the eccentricity and inclination amplitudes corresponds quantitatively to analytical predictions (Fig. 3.2 - nearly constant $e_{\max}$, gradual decrease of $i_{\max}$).

The abrupt change in the dynamics of the 7.5 $\mu$m grain after approximately 21,000 M.y. in Fig. 3.3 is a sign of reaching a chaotic regime. We do not present a detailed analysis of this phenomenon here, but refer to Paper A

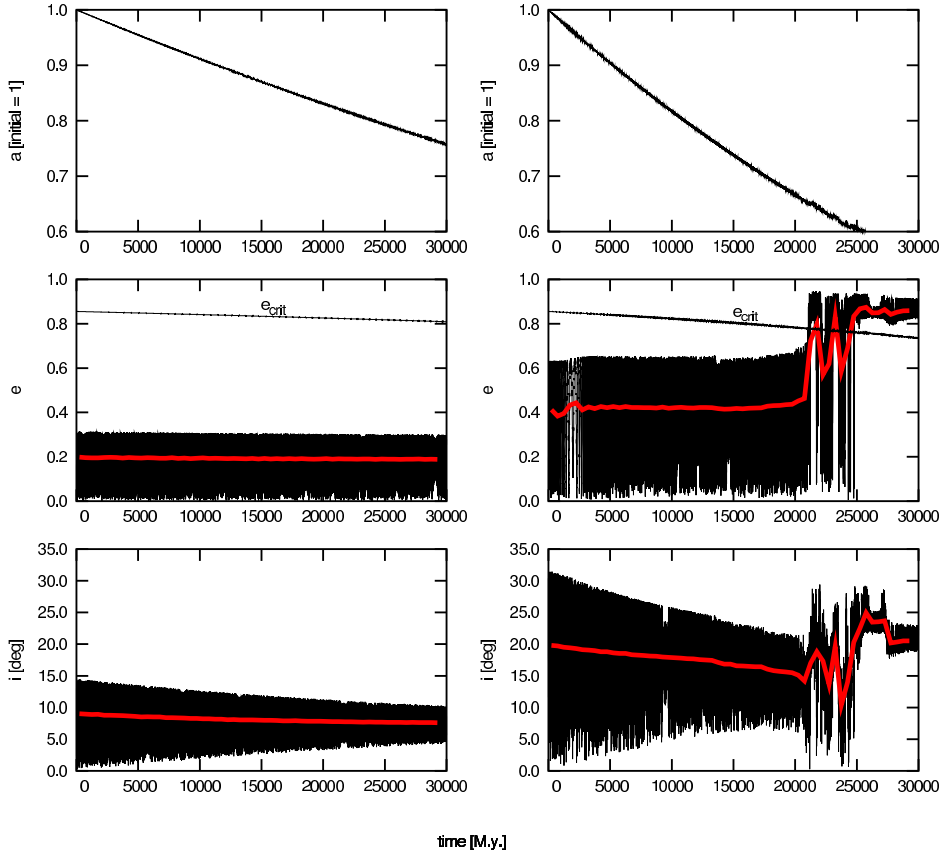


Figure 3.3: Influence of J2, RP and PR on the dynamics of 15 $\mu$m (left) and 7.5 $\mu$m (right) grains ejected from Deimos into a circular orbit. The time evolution of semimajor axis, eccentricity and inclination was obtained by numerical integration of Eqs. (3.3)–(3.7). The additional thin line in the eccentricity plot corresponds to $e_{crit}$ —the critical value of eccentricity of a particle to collide with Mars at the pericenter of the orbit. The thick gray solid line corresponds to averaged values of the eccentricity and inclination.

where the effect is studied. This sudden change of the eccentricity and inclination just occurs at the time point where the particle reaches a saddle separatrix of the underlying dynamical problem. The smaller the grain is, the earlier it reaches this phase. The trajectory flips from the libration to the circulation regime (Hamilton and Krivov, 1996). From this point on any, an arbitrarily small change in the initial conditions or any small perturbation will lead to a quantitatively different trajectory. Additionally, the grain eccentricity rise above the critical value and the grain is rapidly lost by collision with Mars. As outlined in Paper A this peculiar behaviour is a classical saddle separatrix chaos and was already identified for Phobos ejecta under the perturbations of J2 and RP, however, for much larger grains of hundreds of $\mu$m in size (Krivov et al., 1996; Hamilton and Krivov, 1996).

#### 3.2.2.3 Impact of PR Drag on the Deimos Torus Geometry

With the same method as in previous section we numerically simulated the dynamics of the Deimos Population I particles (grains $> 11\,\mu$m) to construct a snapshot of the particle configuration. In order to catch the main features of the torus geometry we transformed the instantaneous values of osculating elements complemented with a random value of the mean anomaly into Cartesian coordinates and projected them into 3 different planes (Fig. 3.4). The configuration is pictured at two distinct time epochs: right after the ejection of grains and after 30,000 M.y. of orbital evolution. All snapshots are produced for one and the same Martian season, the autumn equinox ($\lambda_\odot = 180^\circ$). For comparison, also the Phobos torus created by short living particles is displayed.

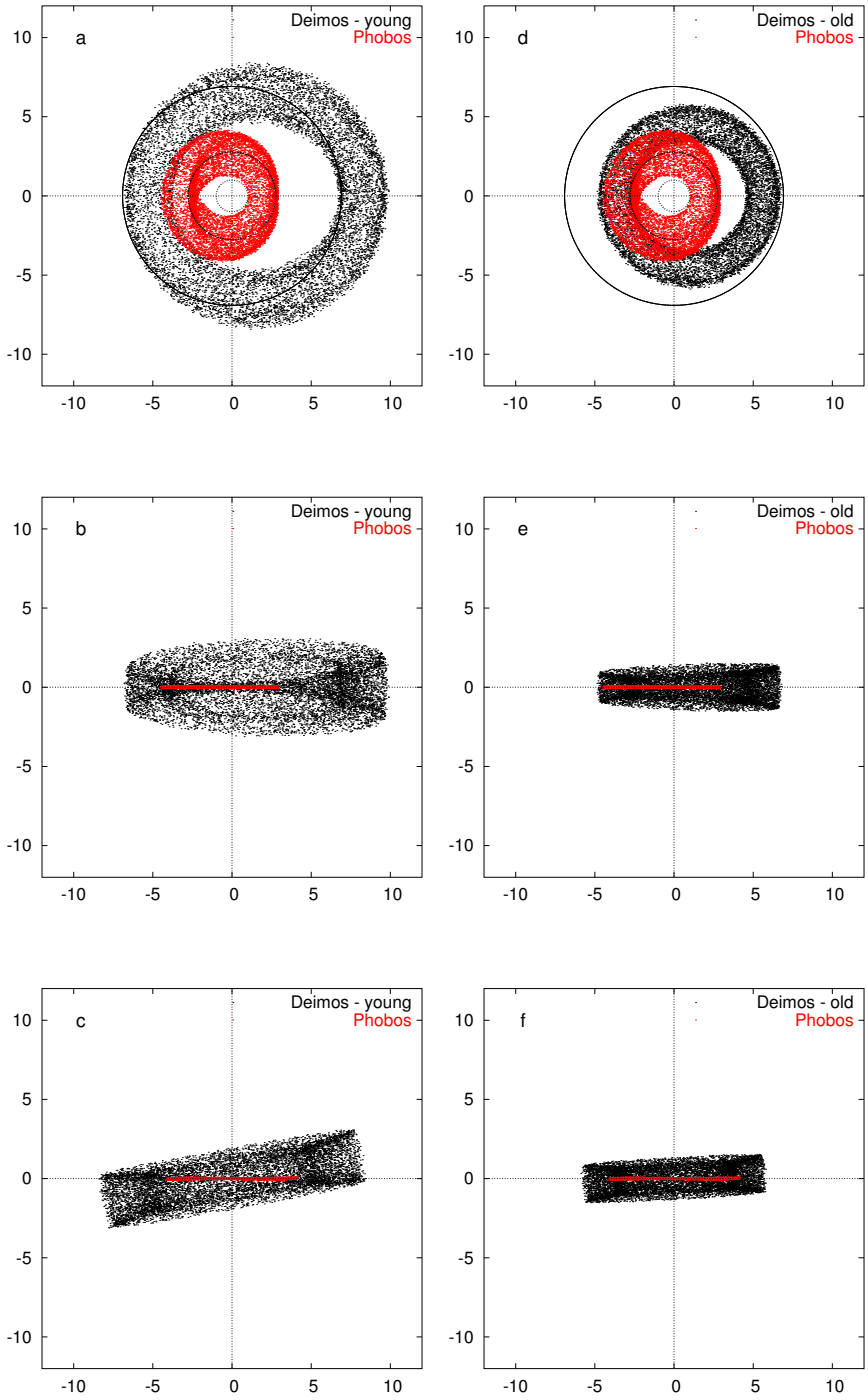


Figure 3.4: Snapshots of a Deimos torus formed by 11 $\mu$m particles under the influence of J2, RP and PR. Left: 'young' particles in the beginning of the orbital evolution; right: 'old' particles after $3 \times 10^4$ M.y. Top to bottom: $XY$, $XZ$, $YZ$ projections of the equatorial equinoctial particle coordinates. All snapshots are given for the Martian autumn equinox (the Sun is in direction of the negative $OX$ axis). Coordinates are in the units of Mars' radii $R_M$. The Phobos torus of like-sized particles is overplotted on all panels (inner thin ring-like configuration). In the upper panels, the small inner circle represents Mars and the two outer circles are the orbits of Phobos and Deimos.

The torus geometry exhibits several evident gradual changes with time

1. a gradual contraction of the torus
2. decrease of the torus displacement and azimuthal symmetrisation (Figs. 3.4 a, b versus d, e);
3. flattening of the torus (Figs. 3.4 b–c versus e–f);
4. decrease of the torus tilt (Fig. 3.4 c versus f).

Comparing with the Phobos torus, we see that both tori gradually start to overlap and the Deimos particles mix with those from Phobos. Results of even longer simulations (50,000 years) show that the azimuthal structure of both tori becomes almost indistinguishable. However, even if the semimajor axis and eccentricities of the Deimos grains become comparable with the Phobos grains when switching to the "Phobos regime", the inclinations remain larger ($\sim 10^\circ$ - see Fig. 3.3). In this sense the Deimos particles "remember" their source, even if being in the "Phobos regime".

The displayed tori can be interpretted as a mono-sized dust configuration which is produced by an individual impact of a large meteorite producing a single size particle population shortly after the collision or later after 30,000 M.y. To illustrate the "real" distribution of the dust in the Martian system, a by far more complex analysis would be necessary. At first, the continuous production of particles in micrometeoroid impacts has to be taken into account. There, a appropriate size and mass distribution of particles escaping from both moons should be considered. Snapshots like those depicted in Fig. 3.4 should be summed up with weight proportional to the absolute numbers of particles remaining in the system at the moment of observation. As the number of particles ejected simultaneously will decay with time, "older" populations will get lower weights than "younger" ones. However, we may conclude that the signature of the PR dynamics sketched in Fig. 3.4 will be visible in any representation. This means that the steady-state Deimos torus should be smaller in size, spatially more symmetric and less inclined to the equatorial plane, in comparison to the torus predicted in earlier studies represented by the left panel of Fig. 3.4.

#### 3.2.2.4 Particle Lifetimes

In this section we discuss the balance of particle creation, the dynamical "life" and main loss mechanisms making up the fate of the Deimos torus. Since sublimation or sputtering are ineffective for rocky particles at heliocentric distance of Mars (Leinert and Grün, 1990), the main loss mechanism is collisions of grains with other bodies. Here we estimate the particle lifetimes against collision with Phobos and Deimos and other dust particles.

**Collisions with Phobos and Deimos**

We start with the description of gradual changes of a particle orbit (ejected from Deimos) in the Martian system due to PR for different-sized ejecta. Figure 3.5 shows the time evolution of pericentric and apocentric distances calculated for the instantaneous osculating elements, characterising the region which a particle of given size may reach. For comparison, the position of Phobos and Deimos as well as the surface of Mars are shown. The evolution of three different particle sizes is derived. For the smallest grains ($7.5\,\mu$m), the initial amplitude of oscillation of eccentricity is so high that the grain crosses not only Deimos' orbit but also the orbit of Phobos. This naturally increases the loss probability of the grain. The motion of intermediate sized grains ($11\,\mu$m) is characterised by two phases in time. In the beginning the grains do not reach the orbit of Phobos. In the course of PR evolution, both pericentric and apocentric distances decrease until at $t \approx 26,000$ M.y. the apocentre drifts inside the Deimos orbit, stopping further reaccretion of ejecta by this moon. However, at the same time the pericentric distance shrinks down to the orbit of Phobos, so that the particles become Phobos-crossers. For even bigger grains ($30\,\mu$m) the eccentricity is small enough that there exist intermediate period of time when the grain moves "safely" within both orbits and none of the moons acts as a sink. The larger the grain, the smaller the $e_{\max}$ and the slower the decay of $a$ due to PR and thus the period of a "safe survival" of the particle between both moons increases with grain radius. Therefore, one would expect to find long-lived particles in this size range.

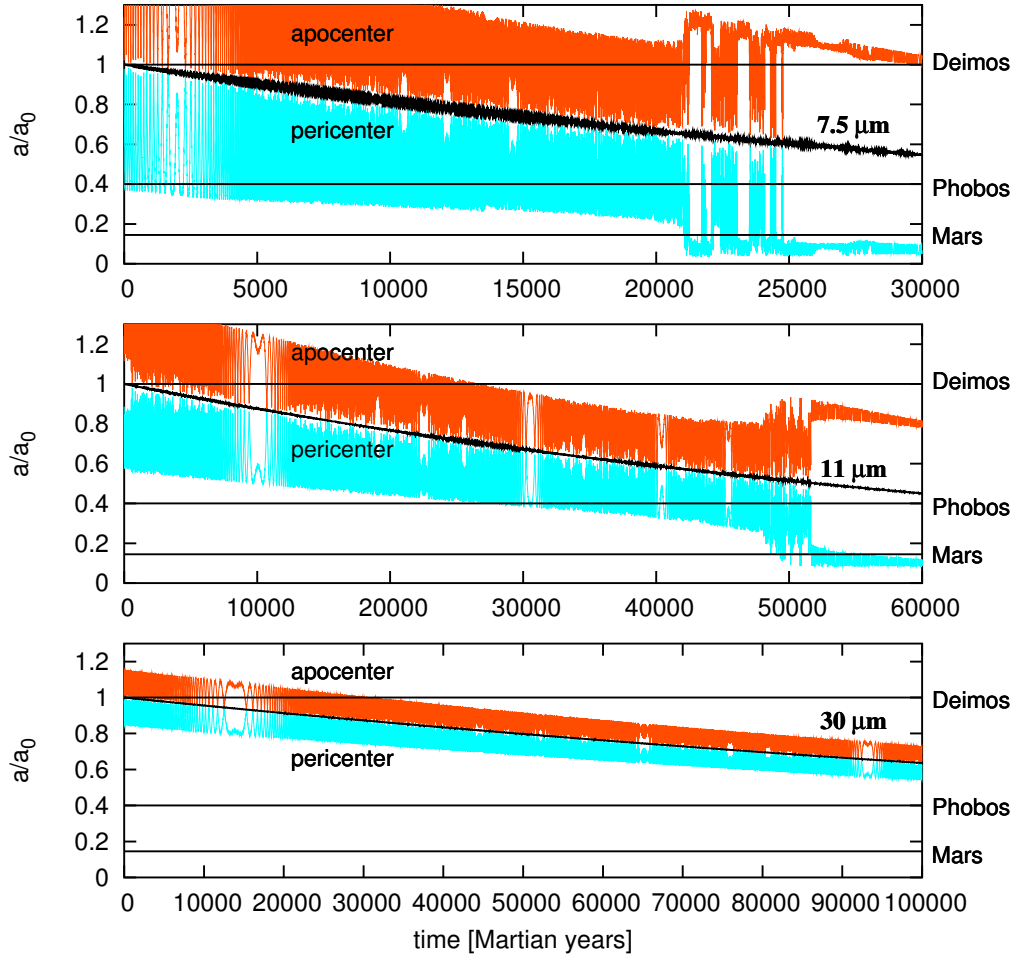


Figure 3.5: The instantaneous pericentric distance (light blue) and apocentric distance (red) calculated for Deimos particles with radii 7.5 $\mu$m (top), 11 $\mu$m (middle) and 30 $\mu$m (bottom). The distances are scaled to the semimajor axis of the Deimos orbit. Horizontal straight lines mark orbital radii of Deimos, Phobos and the surface of Mars.

Using the model described in Section 2.3 we can calculate the particle $e$-folding lifetimes against collisions with Phobos $T_{\rm PH}$ and Deimos $T_{\rm DE}$ (Eqs. 2.59 - 2.61). Then we can calculate the fraction $f$ of surviving particles as a function of time. We simultaneously integrated the Eqs. (3.3) – (3.7) with the quasi kinetic equation

$$\frac{df(t)}{dt} = -T_{\rm impact}^{-1}(t)\, f(t) = -\omega_{\rm c}(t)\, f(t)\,, \tag{3.20}$$

where $\omega_{\rm c}$ is an average frequency of collisions with any of the moons. Assuming $f(0) = 1$ to be an initial condition.

Results of this analysis for different particle sizes are shown in Fig. 3.6. This plot confirms the trend anticipated in Fig. 3.5. For grains smaller than 11 $\mu$m, which are continuosly crossing orbits of both moons, $f(t)$ decreases rapidly with time. For intermediate sized grains we observe a plateau in the $f(t)$ curve which corresponds to region where grains orbit in between Phobos and Deimos. It drops if particles cross the Phobos orbit.

However, since we did not take into account the real number of ejected particles and its surviving fraction, this representation may be misleading. Consequently we calculate the steady-state number of grains for each grain radius. Denoting by $N^+(s)$ the constant dust production rate from the Deimos surface in a unit size interval around $s$ we obtain

$$N_{\rm ss}(s) = N^+(s) \int_0^\infty f(s,t)\, dt, \tag{3.21}$$

where we have added $s$ as an argument of $f$. Figure 3.7 shows the resulting steady-state number of grains as a function of size for $N^+ \equiv 1$. It shows a peak for sizes around $\approx 13\,\mu$m, as the result of two competitive effects.

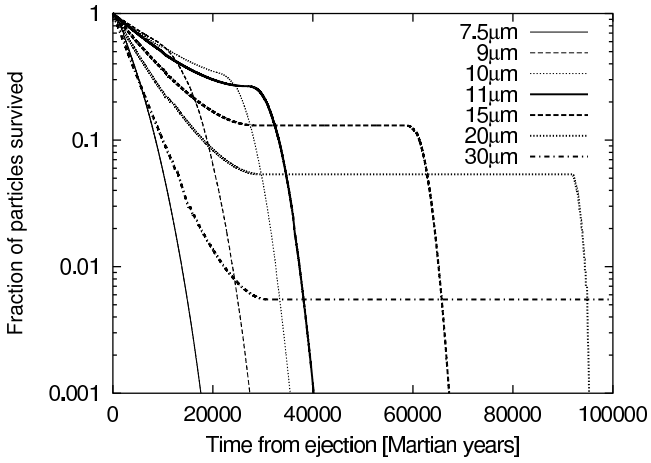


Figure 3.6: Fraction of particles surviving collisions with Deimos and Phobos. The plateau corresponds to the regime when the entire particle orbit lies between the orbits of Phobos and Deimos.

First, starting from $11\,\mu$m, the duration of the safe stage of the particle evolution increases with particle size, corresponding to an elongation of the the plateau in Fig. 3.6. Second, the bigger the particles are, the less effective is the PR drift and the longer the particles stay in the "dangerous region" crossing the Deimos orbit. It means that the fraction of grains that are not removed by Deimos before reaching that stage decreases with radius, i.e. the level of the plateau in Fig. 3.6 becomes smaller with grain size.

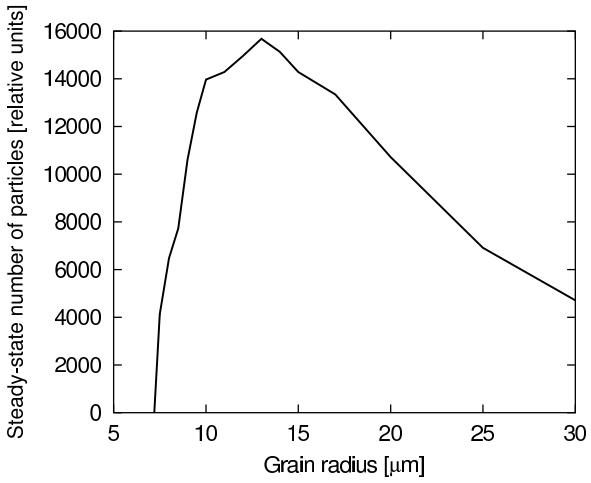


Figure 3.7: Steady-state number of particles as a function of their size. The numbers are relative, assuming that the production rate per unit radius interval is the same for all radii. Absolute numbers can be obtained by multiplying the depicted function by the expected production rate $N^+$ as a function of size.

To obtain the actual steady-state number of particles we have to multiply the solution of the integral shown in Fig. 3.7 by the actual $N^+(s)$ distribution. Realistically, smaller particles are produced with higher probability than the larger ones. As a result we will obtain an even sharper peak at nearly the same size. Therefore the particles between 10 and $15\,\mu$m are expected to dominate the number density of the Deimos torus. One can show that they will dominate the cross section of dust in the torus as well and thus, also its optical depth $\tau$.

The curve in Fig. 3.7 also allows an additional interpretation. Because $N^+$ is a dimensional quantity ($N^+ = 1$ M.y.$^{-1}$ was taken in Fig. 3.7), the same curve can be interpreted as a mean lifetime of a particles of given size. The maximum corresponds to $\approx 16,000$ M.y. This mean lifetime should not be mixed with the maximum possible lifetime of the grains - a quantity which can be estimated from Fig. 3.6. We can see that about 13% of $15\,\mu$m-sized grains stay in orbits for $\approx 6 \times 10^4$ M.y. and 5% of $20\,\mu$m-sized particles are lost only after $\approx 1 \times 10^5$ M.y. The

lifetimes of those long-lived grains are however, likely to be limited by other mechanisms. Potential mechanisms are collisions with interplanetary or interstellar grains (in order of $10^6$ M.y. – Grün et al., 1985), or mutual collisions.

**Mutual collisions**

Here we disccuss the effect of mutual collisions on the lifetimes of the grains ejected from Deimos. For a quantitative estimate we apply the model presented in Section 2.3 (Eqs. 2.62 - 2.65). Since, as shown above, the most dominant population (highest number density) of the Deimos torus consists of particles with sizes $10\,\mu\text{m} \leq s \leq 15\,\mu\text{m}$, these grains have the shortest collisional lifetimes with respect to mutual collisions. Thus, for the sake of simple estimates, we consider Deimos torus composed only of particles in this size range. For $s \approx 10\,\mu$m, we take $e_{\text{mean}} \approx i_{\text{mean}} \approx 0.3$ rad to get $v_{\text{imp}} \sim 0.8\,\text{km}\,\text{s}^{-1}$, $e_{\text{max}} \approx i_{\text{max}} \approx 0.4$ rad, and $T_{\text{impact}} \approx 15,000$ M.y. (Fig. 3.7). The dust production rate $N^+$ is mainly determined by properties of the dust production mechanism which is relatively uncertain. In Section 3.1 we estimated, for the considered size interval ($10\,\mu\text{m} \leq s \leq 15\,\mu\text{m}$), a value $N^+ \sim 10^{6\pm1}\,\text{s}^{-1}$, which corresponds to value derived by Krivov and Hamilton (1997). Then Eq. (2.66) can be solved for $T$ and the desired $T_{coll}$ is then determined by Eq. (2.65). To compare the theory with observations, the edge-on optical depth $\tau_{\parallel}$ can be estimated as (Krivov and Hamilton, 1997)

$$\tau_{\parallel} \approx \frac{N^+ T S_r v_{imp}}{8 a_0^2 i_{max}}. \tag{3.22}$$

For a lower limit of estimated dust production rate $N^+ = 10^5\,\text{s}^{-1}$, mutual collisions are infrequent and the dominant loss mechanism is impacts with the moons: we find $T_{coll} = 30,000$ M.y., which is larger than $T_{impact} = 15,000$ M.y. The "combined" lifetime is $T = 10,000$ M.y., and $\tau_{\parallel} \approx 2 \times 10^{-8}$. On the other hand taking the higher dust production rate $N^+ = 10^7\,\text{s}^{-1}$, we obtain $T_{coll} = 1900$ M.y. Here, $T = 1600$ M.y., and $\tau_{\parallel} \approx 4 \times 10^{-7}$.

At this point we have to stress that the actual optical depth should be somewhat higher, since the contribution of particles with other sizes than the considered size interval is not considered. Still, the expected optical depth should be below the recent observational limit $\tau_{\parallel} < 10^{-6}$ (Showalter et al., 2006). Therefore the proposed observational campaign during the Martian opposition in December 2007, when significantly better precission will be obtained is the main opportunity for direct detection of the Martian Tori (see Krivov et al., 2006, for detail).

### 3.2.3 Stochastic Influence of Radiation Pressure

The attempts to observe the Martian dust complex, ended with negative results up to now. Despite of the fairly large uncertainty in the flux of IDPs there is little doubt about the impact ejecta mechanism principle. For instance have impact ejecta generated dust clouds been observed in in situ measurements around the Galilean Moons (Krüger et al., 2003). This motivates us to reconsider the dynamics of dust particles and to identify a mechanisms leading in further depleting of optical depth of the tori. Therefore, we apply our general model of stochastic diffusion described in Section 2.2.2 to the dynamics of Population I, which is expected to be the most dominant in the Martian system (Juhász and Horányi, 1995). The long lifetimes of these particles allow even weak perturbations to alter noticeably the tori characteristics. In this study we investigate the effect of stochastic radiation pressure force. Stochastic perturbations have never been addressed in the context of the Martian dust complex. As in our theoretical study (Section 2.2.2.2) we focus on RP fluctuations induced by permanent rotation of non-spherical particle and compare the results of analytical theory (Section 2.2.2.3) with the performed simulations.

As shown in Section 2.2.2, this problem can be modeled by splitting the radiation pressure force in deterministic and stochastic component. The deterministic component corresponds to radiation pressure acting on a spherical grain with the average cross section defined by Eq. (2.33). The stochastic component is modelled by appropriately scaled Gaussian white noise. Than the radiation pressure force can be written in form:

$$\vec{F}_{\text{RP}} \;=\; B\,\langle S_r \rangle\,\vec{e}_{\odot} \;+\; B\,\sqrt{2K_0}\;\xi(t)\,\vec{e}_{\odot}\,, \tag{3.23}$$

where $\xi(t)$ is given as white noise with zero mean and unit dispersion

$$\langle \xi(t) \rangle = 0\,, \qquad\qquad \langle \xi(t_1)\xi(t_2) \rangle = \delta(t_1 - t_2). \tag{3.24}$$

In order to study the dynamics of a grain under the influence of the central gravity of oblate Mars (Eq. (2.11)) and stochastic radiation pressure (Eq. (3.23)), we numerically integrate the particle's equation of motion. We use Everhart's (1985) integration scheme with a constant integration step of $\Delta t = 500\,\mathrm{s}$. At each integration step the calculated coordinates and velocities were converted into the osculating orbital elements and stored. The method is similar to that used by Spahn et al. (2003). At each integration step a random Gaussian variable with zero mean and unit variance was generated. It was then scaled by a numerical factor $\kappa$ and added to the deterministic part of the radiation pressure. This numerical scheme, the so called "exact propagator", is described in detail in Mannella (2000) and in Mannella and Palleschi (1989). With the factor $\kappa$ defined as

$$\kappa = B\frac{1}{\Delta t}\sqrt{2K_0\Delta t} \tag{3.25}$$

this scheme yields an accuracy of the order of the integration time step $\Delta t$. In this approach, the factor $\kappa$ is the main parameter defining the strength of the stochastic noise. It is a function of the basic parameters of the stochastic model $K_0$ and consequently also $\Omega_0$. The preceding factor $1/\Delta t$ on the right-hand side of Eq. (3.25) has to be included, since we are adding a stochastic force into the integration routine for the deterministic part (see Mannella, 2000, for detail). The main reason for the application of the factor given in Eq. (3.25) is that the spread of the stochastic variable is not linear in time. To exclude any artificial effects caused by the choice of the integrator, we independently checked the results with a different stochastic integrator (Milstein et al., 2002) yielding a good agreement.

The initial setup of the most important stochastic parameters like $K_0$ and $\Omega_0$ as well as the main particle properties (shape, material, bulk density, $Q_{\mathrm{pr}}$, ...) is of crucial importance for the resulting particle dynamics. As shown in Section 2.2.2.3, all orbital elements show a diffusive behaviour with effective diffusion coefficients proportional to the dimensionless coefficient $\Lambda(K_0,\Omega_0)$ - Eq. (2.43). This coefficient sensitively depends on the particle's rotation frequency $\Omega_0$ and effective size $s_{\mathrm{eff}}$. The effective particle radius $s_{\mathrm{eff}}$ is connected to the grain's minimal size $l$ and aspect ration $\lambda$ as $s_{\mathrm{eff}} = l\sqrt{[\alpha(\alpha+1)]/2}$, allowing easy comparison between non-spherical and spherical particles. Fig 3.8 depicts the variation of the effective diffusion coefficient $\Lambda$ as a function of grain size $s_{\mathrm{eff}}$ and rotational frequency $\Omega_0$. Here, the dust grain was taken to be oblate with aspect ratio $\alpha = 5$, material bulk density $\rho = 2.37 \times 10^3\,\mathrm{kg\,m^{-3}}$, and the factor $Q_{\mathrm{pr}}$ depending on grain size as described in Paper A. The grain is considered to be on Deimos orbit (23480 km), which implies that $\varepsilon = 25^\circ$ and $\omega = 0.0335$ (see Krivov et al., 1996, for details). Depending on $\Omega_0$ and grain size, the stochastics may even dominate the dynamics.

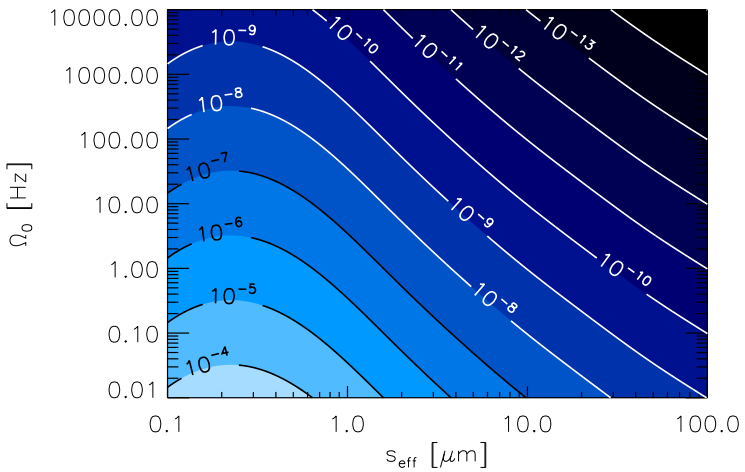


Figure 3.8: Variation of the dimensionless diffusion coefficient $\Lambda$ (Eq. (2.43)) with respect to the particle rotational frequency $\Omega_0$ and effective size $s_{\mathrm{eff}}$. The grain is considered to be oblate with an aspect ratio $\alpha = 5$ and to consist of silicate with a material density $\rho = 2.37 \times 10^3\,\mathrm{kg\,m^{-3}}$. The variation of $Q_{\mathrm{pr}}$ with particle size is responsible for maxima near $s_{\mathrm{eff}} = 0.2\,\mu\mathrm{m}$.

In our simulations of the putative Martian tori we consider an ensemble of particles ejected from Deimos with the same properties (material, shape, $\rho$, $Q_{\mathrm{pr}}$) as used for Fig. 3.8. The initial orbit of *all* grains is *identical*, and

coincides with the *circular orbit* of Deimos ($a_0 = 23480$ km, $i_0 = e_0 = 0$). We tested a wide range of parameters, such as $s_{\rm eff}, \alpha$ and $\Omega_0$. Here we present the results for two different particle sizes ($s_{\rm eff} = 15\,\mu$m($Q_{\rm pr} = 0.385$) and $s_{\rm eff} = 40\,\mu$m($Q_{\rm pr} = 0.372$)) and two extreme values of the rotational frequency ($\Omega_0 = 5 \times 10^3\,{\rm s}^{-1}$ and $\Omega_0 = 1.5 \times 10^{-2}\,{\rm s}^{-1}$ (see Section 2.2.2.2 for details). Since we focus on comparison of the simulation results with the predictions of the analytical theory, we choose a relatively short total integration time, of 3,000 Martian. However, during this integration interval, all the main features of stochastic dynamics can be observed. For each set of parameters we simulate an ensemble of particles (250 different realizations). In terms of a stochastic context each grain trajectory refers to a different realization of the stochastic process induced by fluctuations in radiation pressure.

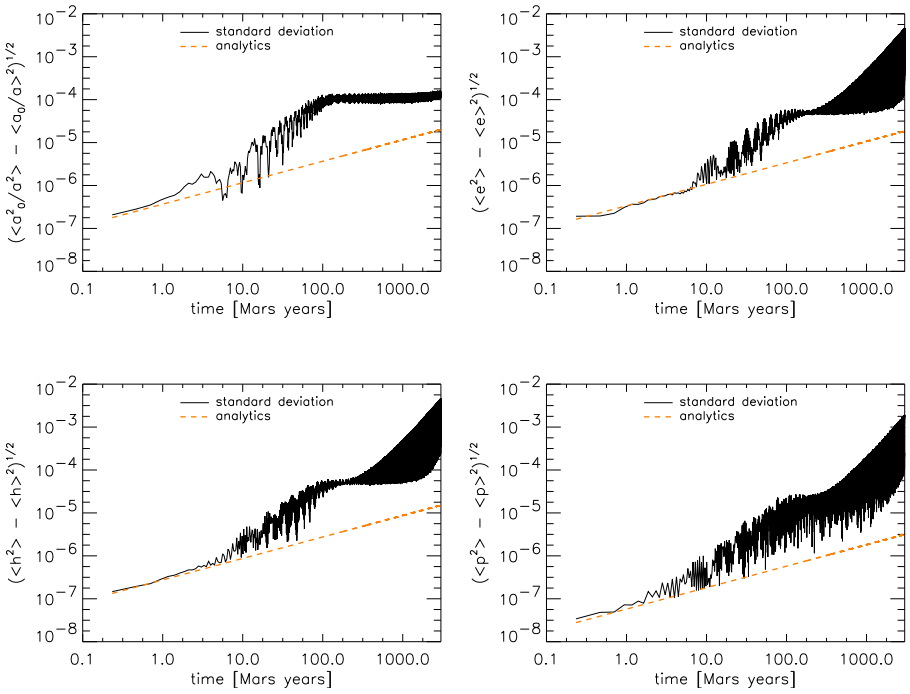


Figure 3.9: The standard deviations of normalised inverse semimajor axis $a_0/a$, eccentricity $e$, and Lagrangian elements $h = e\cos\tilde{\omega}$ and $p = \sin i \cos\Omega$ for an ensemble of 250 particles. The time dependence of the orbital elements $k = e\sin\tilde{\omega}$ and $q = \sin i \sin\Omega$ (not shown) is almost identical to that of $h$ and $p$ respectively. Parameters of the grains are: $s_{\rm eff} = 40$ $\mu$m, the aspect ratio $\alpha = 5$, and the rotation frequency $\Omega_0 = 5 \times 10^3$ s$^{-1}$. The dashed line depicts the analytical estimates. The integration time is 3,000 M.y.

The stochastic perturbation causes a dispersion of the orbital elements and consequently a spatial spread of trajectories. For an ensemble of particles the time evolution of the standard deviation of the osculating elements is shown in Fig. 3.9 – 3.11. The analytical predictions are plotted along for a comparison. The corresponding values of characteristic parameters $\sigma^2$, $\Lambda$, $\Upsilon$, $C_d$ defined in Chapter 2 for given grain size and $\Omega_0$ are listed in Paper B (Table 1 ibid).

Comparison of Fig. 3.9 and 3.10 demonstrates that the dispersion of smaller grains is more strongly influenced by fluctuation of RP. Similarly, variation of $\Omega_0$ (Figs. 3.10 and 3.11) has strong impact on the spatial spread of trajectories. While for large $\Omega_0$ the spread is relatively weak (Figs. 3.9 and 3.10), in case of slow rotation (Fig. 3.11) a significant variation of the orbital elements, up to 10% during the first 1,000 years, is observed.

At the initial stage of the ensemble evolution (a few Martian years) the agreement between the numerical simulations and the analytical results is good. The length of agreement is dependent on the set of chosen parameters. As seen in Fig. 3.11 for slow rotators, the agreement is kept for much longer time. A considerable deviation is developed later. This is a consequence of the neglect of nonlinear terms in the analytical solution, which become

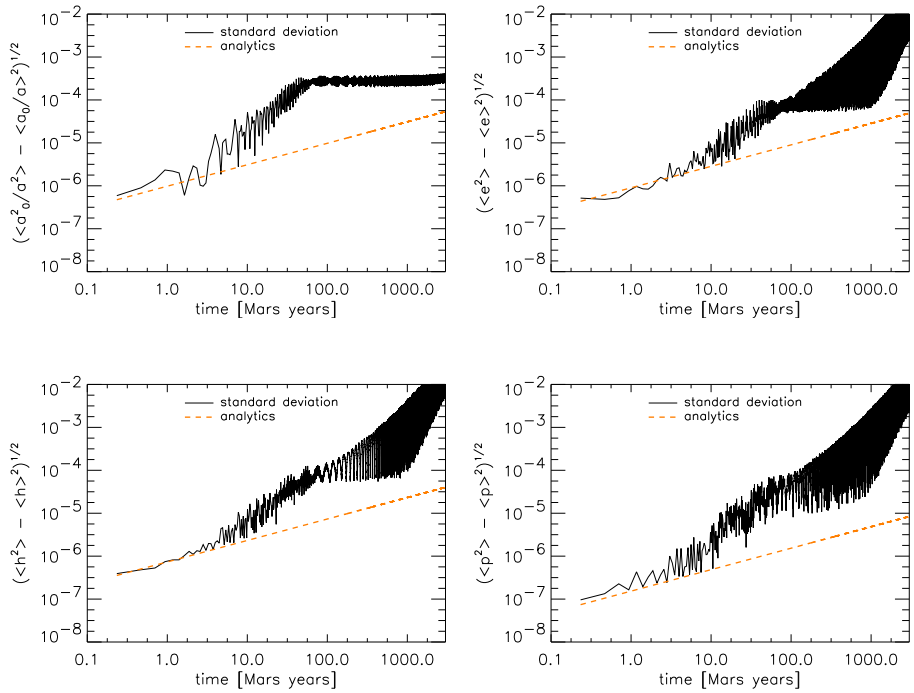


Figure 3.10: Results for similar integrations as presented in Fig. 3.9, but for a particle size $s_{\rm eff} = 15$ $\mu$m.

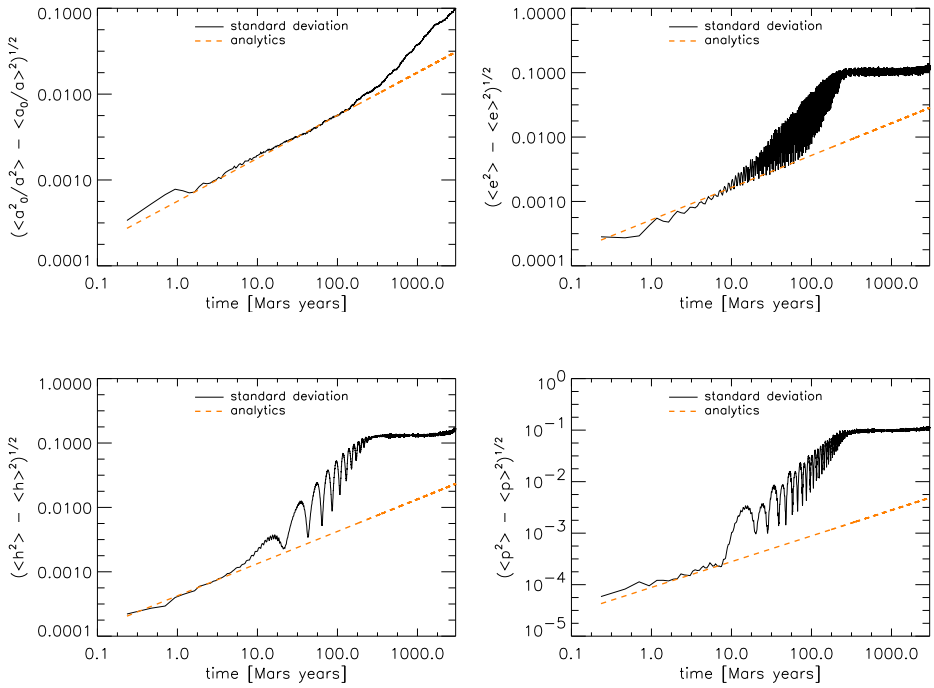


Figure 3.11: Results for similar integrations as presented in Fig. 3.9, but for particle size $s_{\rm eff} = 15$ $\mu$m and $\Omega_0 = 1.5 \times 10^{-2}\,{\rm s}^{-1}$.

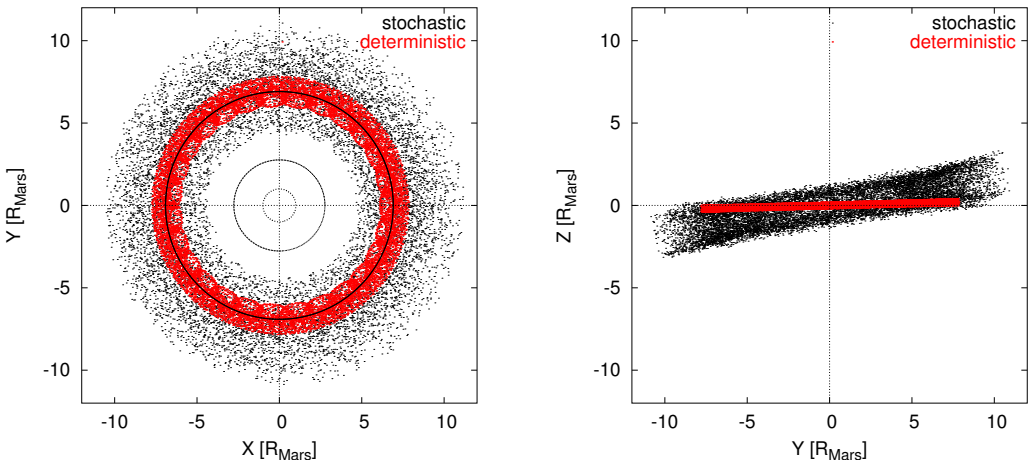


Figure 3.12: Comparison of stochastic (black) and deterministic (red) dynamics of 15 $\mu$m particle under the influence of J2 and direct radiation pressure. In the stochastic case simulations are performed for an oblate particle with $\alpha = 5$, $\Omega_0 = 1.5 \times 10^{-2}$ s$^{-1}$. Coordinates are in units of Mars' radii $R_{\rm Mars}$. The thin black circles on the XY projection correspond, respectively, to Mars' surface, and Phobos' and Deimos' orbits. The plot depicts the single particle spatial evolution for the first 3,000 M.y. of orbital evolution.

important with increasing time. Although our analytical theory fails at large times, it provides a lower boundary estimate for the stochastic effects of interest. In other words, due to the omitted nonlinear terms, the actually expected standard deviation of the orbital elements is always larger than that predicted by the analytical theory. Another interesting effect, evident from Figs. 3.9 - 3.11 is the temporary saturation of the standard deviation of orbital elements and alternation of their regime of growth. This saturation is probably caused by originally small nonlinear terms neglected in our linearised model but present in the complete numerical solution.

The effect of stochasticity on the particle dynamics is illustrated in Fig. 3.12. It depicts the XY and YZ projection of particle trajectories in the equatorial equinoctial coordinate system centred on Mars with and without stochastic force. The figure shows the respective tori around Deimos' orbit created by a single 15 $\mu$m grain under influence of gravity of oblate Mars and the direct radiation pressure. No particular Martian season is chosen here, as in Section 3.2.2.3, therefore the configuration represents an average over the Martian seasons. That means that all instant positions of a single particle stored at constant time intervals during the first 3,000 M.y. of orbital evolution are plotted. The initial orbit in both cases coinsides with the orbit of Deimos ($i_0 = e_0 = 0$). The parameters of the stochastic force and the particle properties are identical to the ones used in Fig. 3.11 (oblate 15 $\mu$m grain, $\alpha = 5$, $\Omega_0 = 1.5 \times 10^{-2}$ s$^{-1}$). Stochasticity causes a large spatial spread of trajectories compared to the deterministic case. For an ensemble of particles this dispersion should even be more pronounced. From another point of view, this plot can be considered as the comparison of the dynamics of strictly spherical and non-spherical particles.

In order to quantify the total influence of the stochastic radiation pressure, one needs to simulate longer integration times of the order of particle lifetimes. The available computer time did not allow a systematic study of the long-term evolution at the time of this study, since the stochastic integrations are extremely demanding. However, results can be used to estimate the quantitative change of the torus topology and spatial properties. Further, the decrease of the optical depth important for observation, of the whole system could be estimated in the future. However, this task would require a separate study which is out of the scope of this thesis. Finally, we wish to stress that the developed theory can be applied to any circumplanetary dust system.

### 3.2.4 Summary

We have studied the dynamics of dust particles ejected from Deimos that are subject to Solar radiation pressure and planetary gravity, including corrections due to oblateness. The long lifetimes of the micron-sized ejecta (up to $\sim 10^5$ years) imply that even a weak perturbations as the indirect component of radiation pressure (Poynting-Robertson drag) or its stochastic fluctuations induced by the rotation of non-spherical particles may have a significant contribution.

In the first, deterministic part of the chapter we focused on the long-term impact of Poynting-Robertson drag on particle dynamics and the overall properties of a Deimos torus. We performed a detailed analysis of lifetimes of different-sized particles and studied the structural change of the torus due to PR. We found that the dissipation of orbital energy, caused by the drag force resulting in a gradual decrease of particle semimajor axis, basically does not affect the eccentricity oscillations, but causes an adiabatic decrease of amplitude and period of oscillations in orbital inclination. We found a peculiar behaviour of the smallest particles of the considered dust Population ($\approx 5-10\,\mu$m) which may reach a chaotic regime, resulting in unpredictable dynamics. Particles with slightly bigger sizes ($\approx 10-15\,\mu$m) are expected to dominate the Deimos torus. Their gradual spiralling toward Mars affects the structure of the predicted torus as well as their lifetimes. Due to the PR drag, the Deimos torus shrinks in size and becomes more symmetric in shape and less inclined than the previously predicted asymmetric torus. These grains are most likely removed in collisions with Phobos and Deimos or by mutual collisions.

In the second part of the chapter, the influence of the non-sphericity (or individuality) of the dust particles has been analysed. We found that the random modulation of particle cross section caused by rotation of a non-spherical grain may be a source of stochasticity in the system. We modelled the particles by simplified figures of rotation and treated the system of particles as an ensemble of free rotators. We calculated the time-correlation function determined by a characteristic angular velocity. Consequently, the radiation pressure force can be represented as a sum of a deterministic and a random component. The latter is modelled as Gaussian white noise with zero mean, giving rise to stochastic diffusion. In a set of numerical simulations we found that stochasticity leads to diffusion of orbital elements of an ensemble of particles. This corresponds to spatial spread of the initially confined ensemble, resulting in a decrease of particle number density. We compared the results with theoretical predictions presented in Section 2.2.2.3. Our theory is in good agreement with simulations for the initial phase of the time evolution, while due to the simplifying assumptions, the difference between analytics and simulations grows with time. However, our analytical solution may be used to estimate a low boundary of the time-dependent standard deviation of the orbital elements. The effect of the stochastic radiation pressure may significantly deplete the number density of the Deimos Torus.

## 3.3 Enceladus Dust Plumes

In Section 2.1 we presented two fundamental mechanisms of dust production at atmosphereless satellites, the exogenic impact ejecta process (Section 2.1.1) and endogenic geyser eruptions (Section 2.1.2). Since any body in the Solar system is exposed to a steady flux of impactors (e.g. IDPs or interstellar) producing secondary ejecta, the first process is the major dust production mechanism in the Solar system. However, for several objects which are geophysically active, additional sources of dust particles are significant. As recently discovered the Saturnian moon Enceladus is a potent source of dust particles that are produced in geyser eruptions at the south pole of the satellite. In this section we focus on the study of dust produced at Enceladus and compare the relative contribution of both processes. We present a model of the dust population in the Enceladus vicinity built by particles freshly ejected from the surface. Finally, we compare the predictions with measurements of the CDA obtained during the flyby of Enceladus on 14th July 2005 (E11).

### 3.3.1 The Cassini Observation

In the pre-Cassini era the main sources of information on the Saturn system were Pioneer, Voyager data, and Earth-based observations. The observation of the Saturnian moon Enceladus by Cassini experiments brought many

surprises. Enceladus, the sixth largest moon of Saturn with a radius of 252.1 km (Porco et al., 2006), was found out to be one of the most spectacular icy moons in the Solar system. Enceladus is immersed in Saturn's E ring, a wide and diffuse blue ring of fine particles with peak size between 0.3 and 3 $\mu$m (Nicholson et al., 1996). The short dynamical lifetimes of E ring dust requires a steady replenishment of the material. Enceladus has long been suspected to be the main source of the ring, because of the sharply peaked optical depth and the lowest vertical extend of the ring near the moons's orbit.

Two mechanisms, which are in principle able to contribute to the E ring dust complex have been proposed. The first mechanism is the impact ejecta process, successfully explaining the dust-clouds around the Jovian moons (Krivov et al., 2003; Sremčević et al., 2003; Sremčević et al., 2005). In this scenario, interplanetary dust particles and also E ring particles strike Enceladus and other moons inside the E ring, producing secondary debris, which sustains the ring. An alternative dust production process has been discussed in view of Voyager images from Saturn flybys. The high albedo and overall inhomogeneity of the craters distribution indicating a high rate of resurfacing and the narrow particle size distribution of the ring, led to the hypothesis of surface activity (geysers) or ice volcanism on Enceladus' surface (e.g. Haff et al., 1983; Showalter et al., 1991; Pang et al., 1984). Activity, which was searched for by Cassini (Porco et al., 2006).

In 2005 the Cassini had three close encounters with Enceladus, in February (E3), March (E4), and July (E11). During the first two flybys, at relatively high altitude (1,000 and 500 km above the surface), some of the Cassini instruments detected anomalous geophysical activity at the satellite. Therefore, the trajectory of the third flyby (E11) was adjusted to be deep inside Enceladus' Hill sphere ($h_{\text{Hill}} = 948$ km), only 168 km above the surface.

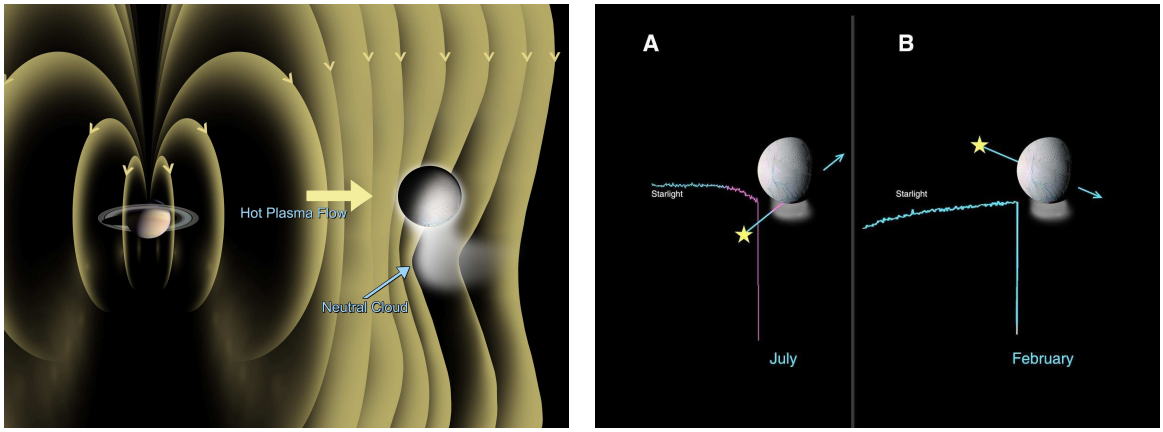


(a) (b)

Figure 3.13: (a) - Artist concept demonstrating the detection of a dynamic atmosphere on Enceladus by Cassini magnetometer. (b) - Gradual decrease of star brightness during a stellar occultation observed by UVIS indicates existence of water vapour atmosphere above the Enceladus' South pole. (Planetary Photojournal, JPL, PIA06432, PIA03552)

Data from the Cassini magnetometer, obtained during the two first flybys, were interpreted in terms of tenuous atmosphere around Enceladus bending the magnetic field of Saturn. The magnetometer data suggested a localised gas outflow from Enceladus' South pole (Fig. 3.13(a)). Variations in the data suggests that the outgassing rate varies on a time scale of days or weeks (Dougherty et al., 2006).

The Cassini Ultraviolet Imaging Spectrograph (UVIS), was designed to observe stellar occultations. While observing the passage of the star Bellatrix behind Enceladus (crossing the region above Enceladus' South pole), the starlight dimmed (pinkish part of the intensity curve) close to Enceladus (left panel of Fig. 3.13(b)). This effect can be explained by a thin atmosphere gradually obscuring the starlight (Hansen et al., 2006). The change of the star's spectrum indicates the presence of water vapour in the atmosphere. As the star re-emerged from behind Enceladus, no dimming of the starlight was observed, indicating an anisotropic outflow of gas from the satellite.

Other observations (right panel of Fig. 3.13(b)) with different orientation of the star passage (not crossing the South pole region) clearly supports the existence of localised source on Enceladus' South pole.

After the first two flybys, which couldn't image the south polar region due to flyby geometry, this region was expected to be cold (left panel of Fig. 3.14(a)), similar to the whole surface. This is expected from exceptionally high albedo of Enceladus' surface which reflects almost 80% of the sunlight. Moreover the poles are naturally expected to be colder than the equator. These expectations were turned upside down by the observation of Cassini's infrared spectrometer. The right panel of Fig. 3.14(a) shows the image taken by Cassini's Composite InfraRed Spectrometer (CIRS) during the third flyby. It shows infrared radiation (heat) from the South pole of Enceladus. The warm spot centred at the pole manifests internal heat leaking from the icy surface (Spencer et al., 2006).

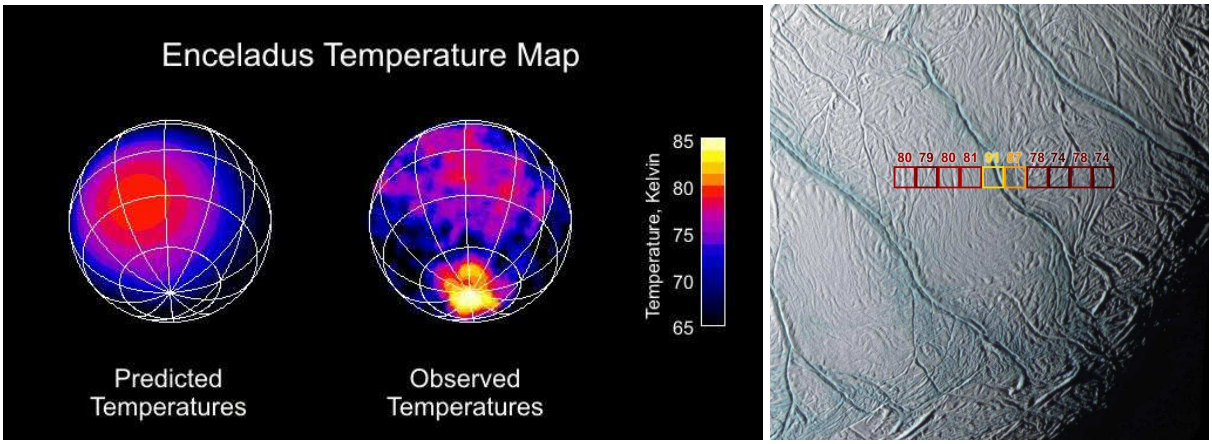


(a) (b)

Figure 3.14: (a) - Temperature map of Enceladus observed by CIRS. The right panel depicts the warm south polar region observed during E11 flyby. (b) - High resolution scan of surface temperature by CIRS above the south polar region. The highest temperature coincides with the "tiger stripe" features observed by ISS. (Planetary Photojournal, JPL, PIA06432, PIA06433)

A more precise scan of the average surface temperature of this region overlaid to a picture obtained by the imaging team (Imaging Science Subsystem - ISS) is shown in Fig. 3.14(b). The colour of each square (6 km across), and the number above it, denote the average temperature of the surface within the field of view recorded by CIRS. The image reveals that the highest temperature coincides with the elongated cracks dubbed "tiger stripes". Precise measurements exhibit that a relatively small area around the fractures has substantially higher temperature (114 – 157 K - Spencer et al., 2006) than the average surface. This high temperaure cannot be explained by Solar heating of the surface. This favours the theory of an additional heat source beneath the "tiger stripe" region. The mechanism of Enceladus' heating is still subject to open debate.

High resolution images obtained by ISS during the third flyby allowed a detailed study of the south polar terrain. For instance, the surface was found to be free of impact craters, most notably the south pole exhibits several prominent 130 km long fractures, the "tiger stripes". Morover, Enceladus' surface has the largest range in crater number density among all Saturnian moons, which is a sign of long lasting and probably ongoing geologic activity. The lowest crater density is found at the south pole, where no crater is larger than 1 km. This indicates that the region is younger than 500,000 years (Porco et al., 2006). Even more spectacular, the ISS cameras reveal a plume of dust (Fig. 3.15), escaping from the warm south polar region. The dust jets are similar to Yellowstone geyser eruptions lifting a big amount of material. The source region in the images appears to coincide with the "tiger stripes".

In addition to the these remote observations, the CDA subsystem, the High Rate Detector (HRD) registered impacts of micron-sized particles during the flybys. The impact rate measured by the dust detector during the E11 flyby increased steadily, when approaching the satellite but peaked about one minute before closest approach

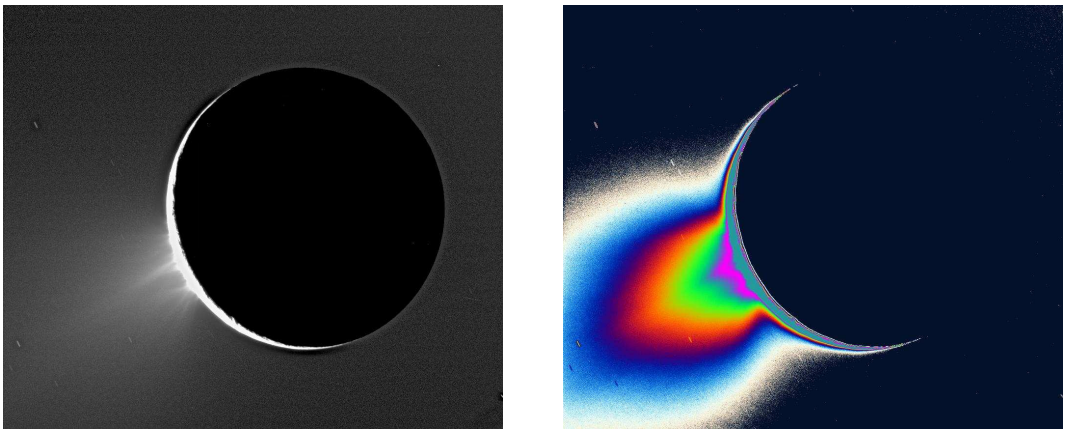

(a) (b)

Figure 3.15: (a) - Discrete plumes of icy material sprayed from the South pole region of Saturn's moon Enceladus observed backlit by the sun above the limb of the moon (looking approximately broadside at the "tiger stripes"). (b) - This image was enhanced and colour-coded in order to make faint signals in the plume more apparent and to emphasise the enormous extent of the fainter, larger-scale component of the plume. (Planetary Photojournal, JPL, PIA07758, PIA07758)

(CA) of the spacecraft to the moon (Paper D). Similarly, the Cassini Ion and Neutral Mass Spectrometer (INMS) detected water gas, showing also a peak rate before the closest approach, but with a smaller offset of -30 s (Waite et al., 2006). As shown in the following section, a dust cloud generated by micrometeoroid impacts (impact ejecta) would clearly produce an impact rate peaking directly at closest approach. However, since the spacecraft approached Enceladus from south (CA at a latitude of $\sim 25°$S - see Fig. 1 of Waite et al., 2006), the shift of peak rate supports the theory of a dust and gas source at the South pole. The time difference between the peaks of HRD and INMS indicates a decoupling of gas and dust shortly after release from the moons' surface. Comparing the measurements with theoretical models of dust creation allows to estimate the relative contribution of different production mechanisms, and identify the dominant source of the E ring.

### 3.3.2 Dust Ejecta Model

High energetic collisions of micrometeoroids ejecting material from Enceladus were for a long time considered to be the main source of the E ring (e.g. Hamilton and Burns, 1994; Spahn et al., 1999). The surprising detection of the high temperature regions at the south pole of Enceladus and the observed dust plumes escaping from the "tiger stripes" support the hypothesis of geyser eruptions being the source maintaining the E ring. In this section we compare both source mechanisms with measurements during the E11 flyby.

#### 3.3.2.1 Isotropic impact ejecta

Using the mechanism described in detail in Section 2.1.1 and applied to Martian dust tori in Section 3.1, we have modelled a distribution of dust around Enceladus created by impacts of dust particles ejecting secondary debris. For Enceladus, two families of impactors are relevant. These are the interplanetary dust particles and the E ring particles themselves (their relative importance is discussed in Paper C). The trajectory of the E11 flyby crossed the Hill sphere of gravitational influence of the moon. We numerically simulate the full three-body problem, tracing the trajectories of 1 million particles launched *isotropically*[2] *from the moon's surface* with initial conditions

[2]Due to e.g. the "windshield" effect or preferenced direction of impactors' flow, the impact ejecta production is not perfectly isotropical. However, such choice of starting directions is a reasonable approximation in order to simplify the analysis.

plausible for the impact ejecta mechanism (see Paper E for comparison of 2D and 3D results). The starting points were chosen uniformly over the surface of the moon. Since we study dynamics of freshly ejected particles in the vicinity of Enceladus we neglect other forces than Enceladus' and Saturn's gravity. The dynamics of dust particles governed by gravity is independent of their mass and size. Therefore, we do not need to distinguish different particle sizes. The sizes distribution in the vicinity of the moon, stems from the particle size distribution considered for the particle creation process. Other perturbations as radiation pressure, planetary oblateness and Lorentz force influence the long-term dynamics of the particles, eventually forming the E ring background. The

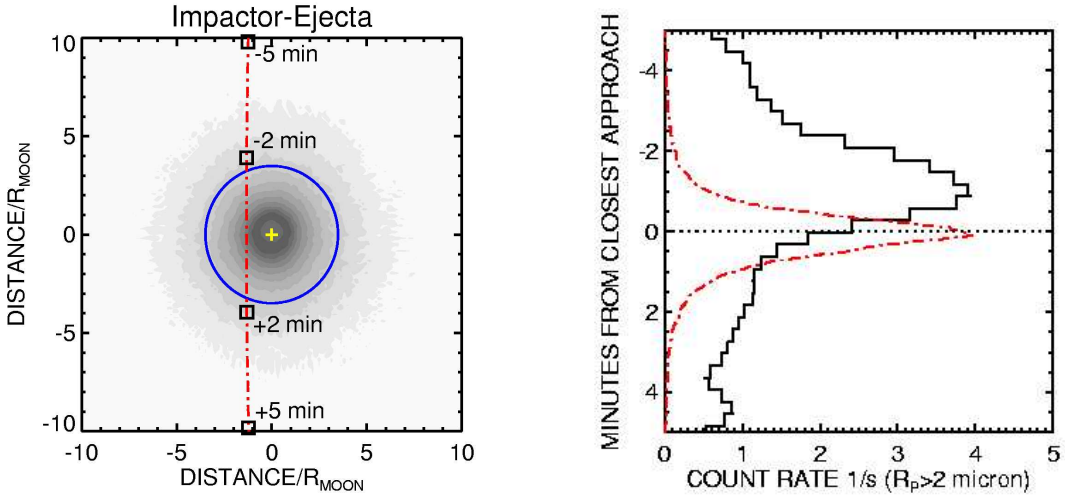


Figure 3.16: Left panel: Particle number density in the plane of the Cassini trajectory estimated from simulations of the impact ejecta process. Darker shades refer to higher density. The initial isotropic distribution of ejecta leads to nearly spherically symmetric dust cloud. The blue circle denotes the intersection of the Hill sphere of gravitational influence (948 km) with the plane of Cassini's trajectory. The yellow cross is the normal projection of the moon's centre to this plane. The red dash-dotted line is the spacecraft trajectory. Right panel: Predicted count rate computed along the trajectory (red dashed-dotted line) normalised to the peak rate measured by HRD during E11 flyby (histogram). No offset with respect to closest approach is observed.

initial velocities were chosen according to a power law distribution (Eq. 2.7) with a slope $\beta = 3$ in the range $0.15\ v_{esc} < v < 2\ v_{esc}$. The starting directions are uniformly distributed in a cone of semi-opening angle of 25° normal to the surface at the starting location (see Paper E). As shown in Fig. 3.16 the impact ejecta mechanism produces a nearly spherically symmetric configuration of dust. This implies that a signal detected by HRD during the flyby is expected to be symmetric with respect to closest approach if the cloud is impact ejecta generated, in contrast to the observations during the E11 flyby.

#### 3.3.2.2 Localised South Pole Source

The alternative model is motivated by the observation of the south polar venting and the hot spot by Cassini instruments described above. In order to simulate localised dust production, the starting positions of the ejected grains were started uniformly in a circular area of an angular diameter of 30° *centred at the South pole*. This is the approximate size of the warm region (Spencer et al., 2006). Using otherwise the same initial conditions as in the impact ejecta case we again trace the dynamics of ejected grains and calculate the spatial distribution of dust in the vicinity of Enceladus.

In contrast to the impact ejecta process, the localised source at the South pole leads to a asymmetric cloud, with higher densities above the South pole (Fig. 3.17). Consequently, the simulated impact count rate on the E11 flyby trajectory peaks prior to closest approach. These results are consistent with the HRD measurements.

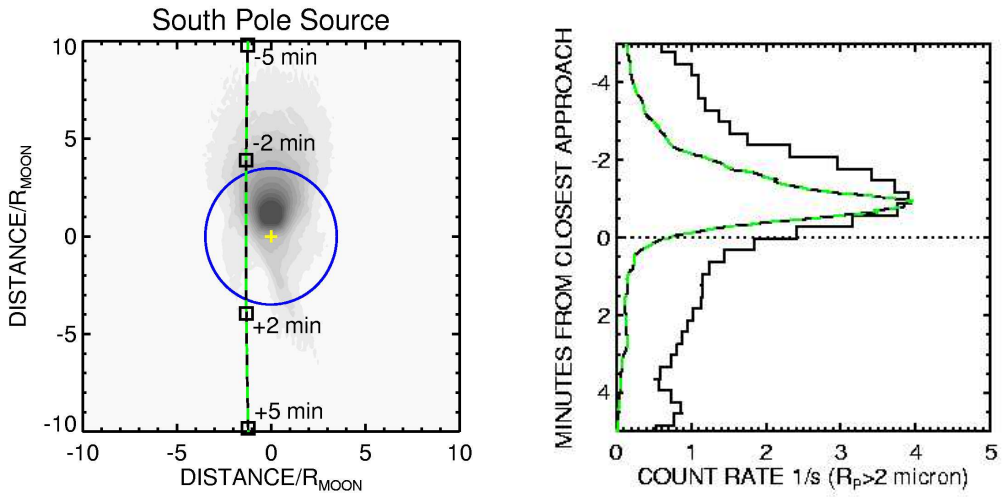


Figure 3.17: Asymmetric dust cloud created by dust ejecta from the South pole. The offset of peak count rate from CA is well reproduces. The green dashed line depicts the trajectory of Cassini. See Fig. 3.16 for further description.

The fact, that in this case the adopted initial conditions of the impact ejecta model actually reproduce the observations implies, that the peak offset is not affected by the details of the ejection process, if the production is restricted to the South pole (Paper E).

### 3.3.3 Comparison of Theory and Observation

In situ measurements of the dust population during the Enceladus flyby deep inside the moon's Hill sphere offer a unique opportunity to identify the source of the dust ejected from Enceladus surface and may answer the open question of the E ring origin. The High Rate Detector of the CDA consists of two thin (28 $\mu$m and 6 $\mu$m) polyvenylidene fluoride sensors with cross sections of 50 cm$^2$ and 10 cm$^2$, respectively. An impact of a hypervelocity dust particle changes the polarisation of the sensor material, resulting in a short, sharp signal. The HRD allows to record impacts in regions with high particle density (e.g. in the vicinity of Enceladus) where the more sensitive impact ionisation detector of the CDA is saturated. The registered impact rate can be as high as $10^4$ s$^{-1}$. Here we concentrate on the data obtained by the 50 cm$^2$ sensor which is sensitive to dust grains with radius larger than 2 $\mu$m. The absolute value of observed count rate allows to estimate the dust production rate at Enceladus.

In addition to the south polar source and impact ejecta dust, the E ring background naturally contributes to the signal recorder by HRD. This background can be estimated from long-term simulatrions of particles that are subject to gravity of oblate Saturn, radiation pressure, Lorentz force and plasma drag (Section 2.2.1). The equations of motion has been solved numerically for grains smaller than 5 $\mu$m. In view of the sensitivity of the HRD-detector, only grains larger than 2 $\mu$m were considered for the estimate. Their trajectories were followed until they hit Enceladus, other E ring moons, Saturn or the main rings. The background produces a count rate, which is about 5 times smaller than that of freshly ejected particles. The contributions of the freshly ejected particles originating from the Enceladus' south-pole source and impact ejecta process have been appropriately scaled and combined with the E ring background to give the total model rate expected at the Cassini HRD during the E11 flyby.

In order to estimate quantitatively the relative contribution of both sources of freshly ejected particles at Enceladus, we combine their contribution in a way that no secondary peak develops due to the impact ejecta dust in the total rate at the closest approach and together with the E ring background they mimic the data of HRD (Fig. 3.18). In this way we estimate $5 \times 10^{12}$ particles s$^{-1}$ larger than 2 $\mu$m ejected from the south-pole source escaping Enceladus' gravity and similarly $10^{12}$ particles s$^{-1}$ maximally produced by the impact ejecta mechanism. This

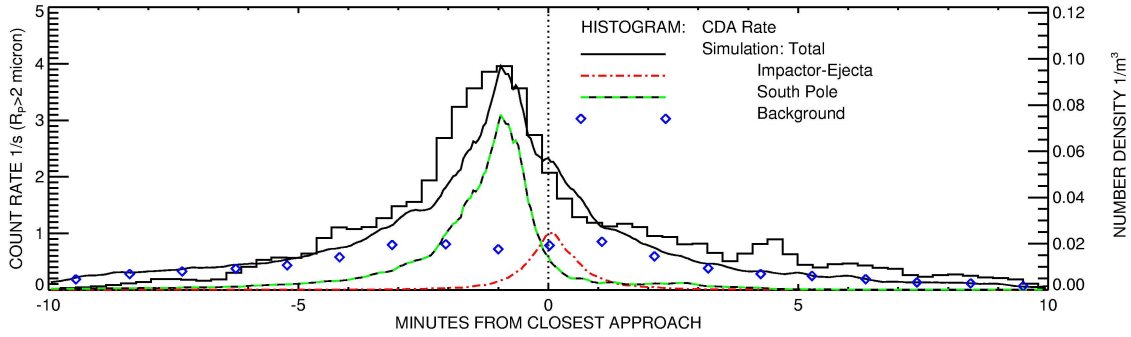


Figure 3.18: Comparison of CDA data with the simulations. The count rate observed by HRD (histogram) measured during the E11 flyby is compared with the count rate computed along the spacecraft trajectory from the simulation of the E ring background (blue diamonds) and the one from impact ejecta process (red) and south-pole source (green) normalised to the observed peak rate. The relative contribution of impact ejecta process to that of the South pole source is chosen in such a way that no secondary peak develops in the combined rate near the closest approach.

corresponds to an escaping mass of $0.2\,\mathrm{kg.s^{-1}}$, assuming all particles to be $2\mu$m sized. For an extended size distribution this rate may increase to a few kilograms per second.

We investigated the influence of the particle source location on the rate profile observed with HRD by simulating a grid of 2600 sources, distributed over the moon's surface. From each of these sources we traced the dynamics of 50,000 particles started for simplicity with initial conditions for the impact ejecta mechanism. We derive the time offset of the peak impact rate to the closest approach for E11 trajectory for each source. These results are presented on the contour map of offset times plotted over a base map of the south polar region from ISS (Fig. 3.19). In this way we were able to constrain those regions leading to -1 min offset. We find that the regions producing -60 s offset from closest approach cover just a small fraction of Enceladus' surface, including the south polar cap. Identifying the region of the "tiger stripes" as the major dust production area, the offset of the HRD-rate peak in the range of -70 sec up to -50 sec has been reproduced.

### 3.3.4 Summary

As demonstrated by our analysis and simulation of the CDA data obtained during the E11 flyby, the geysers at the Enceladus' South pole are most likely the dominant particle source of Saturn's E ring, .

Based on our numerical simulations of the dust environment around Enceladus we can conclude that the asymmetric signature observed in HRD signal during the E11 flyby is consistent with a locally enhanced dust production in the South pole region of Enceladus. An ejection of particles by impacts of hypervelocity micrometeoroids alone cannot explain the observed data. Consequently, the south polar venting is presumably the main mechanism maintaining the existence of Saturn's E-ring.

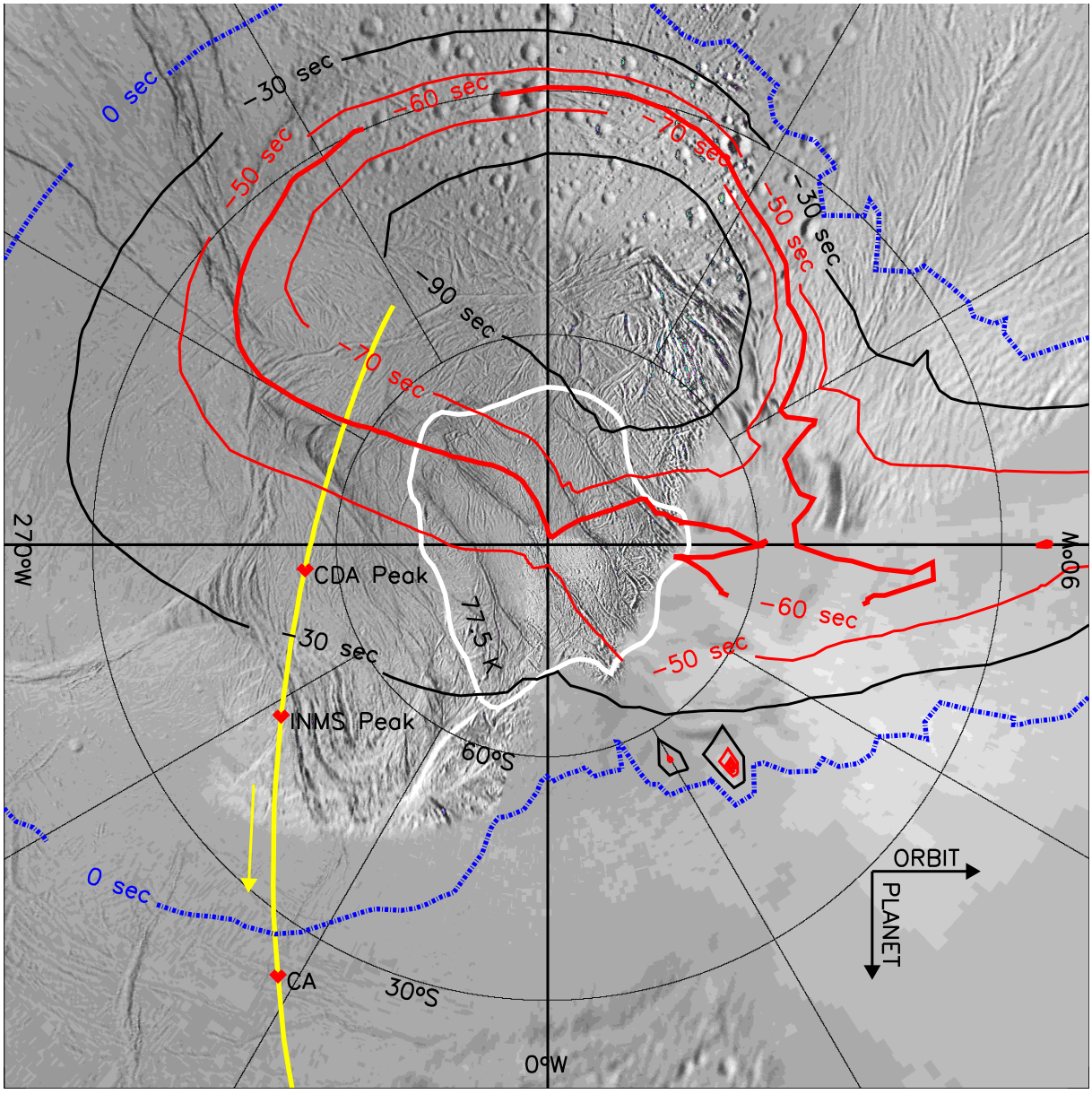


Figure 3.19: The contours of expected time offset of count rate peak from closest approach for a localised dust sources on Enceladus' south polar region. For each source the particle count rate along the Cassini trajectory was computed. The contours are plotted above an ISS base map of the South pole. The position of sources creating a -60 s offset of the maximal count rate observed by CDA during the flyby are plotted as a thick red line. The white line around the pole denotes the 77.5 K isotherm from CIRS (Spencer et al., 2006). The thick yellow line denotes the projection of Cassini trajectory on the Enceladus' surface with the points of closest approach and the maxima of CDA (−50 s) and INMS (−30 s).

# Chapter 4

# Summary and Conclusions

The cosmic dust is an important and vital component of any stellar system. Many bodies (stars, planets, moons, asteroids) are known, or expected to have dust envelopes, rings or tori around them or along their orbits. The main aim of this thesis has been:

**I. Development of a general model of circumplanetary dust dynamics.**

**II. Application of the model to particular dust systems.**

- Martian dust complex: The Deimos torus.
- Enceladus dust plumes.

## 4.1 Model of Particle Life

In order to build a model of a dust population, particle creation, dynamics and extinction has to be simultaneously incorporated. In this thesis we have concentrated on two main dust production processes:

- **Exogenic impact ejecta process.** Any body in a planetary system is steadily exposed to flux of micrometeoroids from zodiacal cloud, ring particles or interstellar grains. If colliding on atmosphereless bodies, these hypervelocity impacts eject substantial amount of secondary material. This is the major dust production mechanism in the Solar system. We have developed a general impact ejecta model, which allows to quantify the importance of this process at any body it concerns.
- **Endogenic geophysical processes producing dust on planetary satellites.** There were geysers or volcanoes, powered by either tidal heating of radiogenic process, observed on severall bodies in Solar system (Io, Enceladus, Triton). In the same manner severall instruments on-board Cassini spacecraft have indicated a geophysical activity in the south polar region of Enceladus - extended plumes of dust and gas. Developing models of dust surrounding Enceladus we may identify the dominant dust source at Enceladus and find the main mechanism sustaining the E ring.

Once ejected, the particles are subject to many perturbation forces, which may significantly alter their dynamics. Additionally to the description of the main perturbations, we study influence of stochastic fluctuations of this forces resulting in stochastic behaviour of particle ensemble. In particular:

- **Deterministic forces** - Well defined forces for fixed particle properties and surrounding fields. We have considered gravity of oblate planet, direct radiation pressure, Poynting-Robertson drag, Lorentz force, and plasma drag and described their dynamical consequences.

- **Stochastic fluctuations** - We studied a dynamical influence of fast fluctuations of radiation pressure force, which was never addressed before. Implementing this as a stochastic component in the equation of motion we have derived a comprehensive analytical model. In order to estimate the effect of RP fluctuations, among many possible mechanisms we have considered rotation of non-spherical particles causing change of grain's effective cross section. In this case, the particle's shape and its spin are fundamental quantities determining the stochasticity. According to our estimates, particles perform a very fast rotation compared to the orbital frequency. As a result, the evolution of the orbital elements of particles' ensemble clearly shows a diffusion. Explicit expressions for the effective diffusion coefficients, which characterise the growth of the standard deviations of the orbital elements, have been also derived.

At last, in order to complete the model, the final stage of particle life has to be described - its termination by different processes as particle sublimation, sputtering, or collisions with other bodies. Since the sputtering is mainly important for ice grains, the collisions of grains with planetary satellites, dense rings or mutually with other dust particles are usually the main loss mechanism. We focused on derivation of particle lifetimes against collisions with planetary moons and other dust grains.

## 4.2 Applications

**Martian Dust Complex: the Deimos torus**

We considered dynamics of dust ejected from Martian moon Deimos by impact ejecta process forming an asymmetric torus around the orbit of the moon. We concentrated on the longest living population of particles with radii larger than $\approx 7\,\mu$m. The long lifetimes of this ejecta (up to $\sim 10^5$ years) imply that even weak perturbations as the indirect component of radiation pressure (Poynting-Robertson drag) or stochastic fluctuations may noticeably alter the tori characteristics.

The Poynting-Robertson drag (PR) is a dissipative force causing gradual decrease of grains' semimajor axis. Its long-term influence significantly affects particle dynamics and causes structural changes of the Deimos torus. We have studied the combined action of the gravity of oblate Mars, direct radiation pressure and Poynting-Robertson drag and found:

- Ejecta of sizes of $\approx 5-10\,\mu$m in radius may reach a chaotic regime resulting in unpredictable dynamics. The peculiar behaviour is related to motion in the vicinity of saddle separatrix of the underlying dynamical problem
- Providing a better estimates of lifetimes of different sized Deimos ejecta we found that collisions of particles with Martian moons and mutual grain-grain collisions may be equally important. Particle in size range $\approx 10-15\,\mu$m are expected to dominate the Deimos torus.
- Long term action of PR results in changes of Deimos torus structure. Namely we have found a gradual contraction of the torus, decrease of the torus displacement and its spatial symmetrisation, flattening of the torus, decrease of the torus tilt.

These effects of the stochastic component of the radiation pressure force may be summarised:

- Diffusion of orbital elements of ensemble of particle has been found.
- The analytical theory gives a low boundary estimate of the stochastic diffusion. Its correspondence to the numerical results is very good in the beginning of particle's orbital evolution. Later the nonlinear terms omitted in analytical theory, enter the dynamics.

- For a slow rotating ($\Omega_0 = 1.5 \times 10^{-2}$ Hz), 15 $\mu$m particles a dispersion of orbital elements by factor of 10 % in 3,000 Martian years was found. This implies a spread in order of tens of percent per grain's lifetime.
- The spatial dispersion of ensemble trajectories results in decrease of particle number density and drop of optical depth of the tori.

**Enceladus Dust Plumes**

The dust environment around Saturn's moon Enceladus was studied, in combination with data measured by Cassini dust detector during the flyby of the moon in July 2005. The detector measured a population of micron-sized particles with impact rate maximum occurring 1 minute before the closest approach of the spacecraft to the moon. This asymmetric signature has been modeled by two populations of dust particles. First by impact ejecta dust particles isotropically ejected from whole surface. Second by localised dust source around Enceladus south pole. This has been also motivated by observations of other Cassini instruments, which discovered high surface temperature and prominent dust plumes at the south polar region. We have found:

- Particles ejected isotropically from Enceladus surface by impact ejecta process create nearly spherically symmetric configuration of dust, which does not correspond to the measurements. Thus, impact ejecta cannot explain the measured data.
- The locally enhanced dust production in the south polar region of Enceladus leads to asymmetric dust cloud, which reproduces the offset of measured count rate peak fairly well.
- Comparison of the combined contribution of fresh ejected particles and E ring background with dust detector measuremets allows to relate the strength of both dust sources. We estimate $5 \times 10^{12}$ particles $s^{-1}$ ejected from the south-pole source and escaping the Enceladus gravity and $10^{12}$ particles $s^{-1}$ (less than 20%) produced by the impact ejecta mechanism (for particle sizes $> 2\mu$m).
- The south polar venting is most likely the dominant dust source maintaining the whole E ring dust complex.

## 4.3 Limitations & Outlook

The main uncertainties of the model stem from the simplifying assumptions or from lack of precise measurements of the properties of studied objects. In case of the semi-empirical impact ejecta model, the main source of inaccuracy are the uncertainty of incoming flux properties, material composition of the satellites and ejecta and its distribution. However, there is just little doubt about this principle, and the free parameters of the model can be determined by comparison of in situ observations with theoretical predictions. In case of Enceladus, the exact mechanism of particle creation and its growth in the vents at Enceladus' south pole as well as its distribution after ejection still remains an open question. Furthermore the enigma, where does this rather small satellite obtains its internal energy from is also unsolved. The future flyby of Enceladus in 2008, deeper in the Hill sphere ($< 100$ km above the surface) should bring valuable informations quantifying the models.

Our studies raised several questions which should be studied in the future. In the case of Martian dust populations, several improvements of the Phobos and Deimos tori model could be carried out. Integrating the contribution of particles with different sizes, continuously ejected from both moons, and considering their specific dynamics and lifetimes, a generalised steady-state model of the tori must be developed. Additionally the stochastic diffusion of the tori presented in this thesis should be studied together with additional perturbations. Quantifying the contribution of another sources of stochasticity, the resulting change of spatial configuration as well as the drop of tori optical depth of the tori should be determined. Longer simulations, in order of particle lifetimes have to be performed. Converting particle number density in light intensity, the change of tori observability could be quantified (e.g. Krivov et al., 2006).

# Acknowledgments

This work would not have been possible without help of many people. Particularly I want to express my thanks to:

My supervisors Prof Frank Spahn and Prof Alexander V. Krivov for the opportunity to work on this interesting topic, for their scientific guidance and friendly approach. I especially acknowledge the support of Prof Frank Spahn during writing this work.

Prof Dr Jürgen Kurths for his support during my years in the AGNLD department.

Dr Jürgen Schmidt, Dr Nicole Albers, Dr Nikolai V. Brilliantov, Dr Miodrag Sremčević, Lucia Zemanová for corrections of the manuscript.

Dr Nicole Albers, Dr Nikolai V. Brilliantov, Marcel Hörning, Prof Alexander V. Krivov, Dr Jürgen Schmidt, Martin Seiß, Dr Miodrag Sremčević, and Prof Frank Spahn for the friendly atmosphere in the office and usefull and inspiring discussions during our "Ring-Seminars".

Dr Miodrag Sremčević, Martin Seiß and especially Dr Nicole Albers for their help through the labyrinth of offices.

Jörg-Uwe Tessmer for the technical support and maintenance of the "AGNLD computer pool".

Birgit Voigt for her help in the office and friendly advices.

And last, but definitely not least, I would like to thank my wife, my family, and friends for all their love, support and patience.

This work was supported by the DEUTSCHE FORSCHUNGSGEMEINSCHAFT (DFG), grant number *Kr 2164/1-3*.

# Bibliography


Altobelli, N., Kempf, S., Landgraf, M., Srama, R., Dikarev, V., Krüger, H., Moragas-Klostermeyer, G., and Grün, E. (2003). Cassini between Venus and Earth: Detection of interstellar dust. *Journal of Geophysical Research (Space Physics)*, 108:7–1.

Baggaley, W. J. (2000). Advanced Meteor Orbit Radar observations of interstellar meteoroids. *Journal of Geophysical Research*, 105:10353–10362.

Baguhl, M., Grun, E., Hamilton, D. P., Linkert, G., Riemann, R., and Staubach, P. (1995). The flux of interstellar dust observed by ULYSSES and Galileo. *Space Science Reviews*, 72:471–476.

Banaszkiewicz, M. and Krivov, A. V. (1997). Hyperion as a Dust Source in the Saturnian System. *Icarus*, 129:289–303.

Bohren, C. F. and Huffman, D. R. (1983). *Absorption and Scattering of Light by Small Particles*. Wiley and Sons: New York – Chichester – Brisbane – Toronto – Singapore.

Brilliantov, N. V. and Revokatov, O. P. (1996). *Molecular Motion in Disordered Media*. Moscow University Press, Moscow. (in russian).

Burns, J. A. (1976). Elementary derivation of the perturbation equations of celestial mechanics. *American Journal of Physics*, 44:944–949.

Burns, J. A., Hamilton, D. P., and Showalter, M. R. (2001). Dusty Rings and Circumplanetary Dust: Observations and Simple Physics. In Grün, E., Gustafson, B. A. S., Dermott, S., and Fechtig, H., editors, *Interplanetary dust*, pages 641–725. Berlin : Springer.

Burns, J. A., Lamy, P. L., and Soter, S. (1979). Radiation forces on small particles in the Solar System. *Icarus*, 40:1–48.

Burns, J. A., Showalter, M. R., and Morfill, G. E. (1984). The ethereal rings of Jupiter and Saturn. In Greenberg, R. and Brahic, A., editors, *Planetary Rings*, pages 200–272. University of Arizona Press, Tucson, Arizona.

Chamberlain, J. W. (1979). Depletion of satellite atoms in a collisionless exosphere by radiation pressure. *Icarus*, 39:286–294.

Consolmagno, G. J. (1979). Lorentz scattering of interplanetary dust. *Icarus*, 38:398–410.

Dikarev, V. V. (1999). Dynamics of particles in Saturn's E ring: effects of charge variations and the plasma drag force. *Astronomy and Astrophysics* , 346:1011–1019.

Dikarev, V. V. and Grün, E. (2002). New information recovered from the Pioneer 11 meteoroid experiment data. *Astronomy and Astrophysics*, 383:302–308.

Divine, N. (1993). Five populations of interplanetary meteoroids. *Journal of Geophysical Research*, 98:17029–17048.

Dougherty, M. K., Khurana, K. K., Neubauer, F. M., Russell, C. T., Saur, J., Leisner, J. S., and Burton, M. E. (2006). Identification of a Dynamic Atmosphere at Enceladus with the Cassini Magnetometer. *Science*, 311:1406–1409.

Draine, B. T. and Salpeter, E. E. (1979). On the physics of dust grain in hot gas. *Astrophysical Journal*, 231:77–94.

Everhart, E. (1985). An efficient integrator that uses Gauss-Radau spacing. In Carusi, A. and Valsecchi, G. B., editors, *Dynamics of Comets: Their Origin and Evolution*, pages 185–202. Dordrecht, Reidel.

Feibelman, W. A. (1967). Concerning the "D" ring of Saturn. *Nature*, 214:793–794. basic paper about the E ring discovery.

Geissler, P. E., McEwen, A. S., Ip, W., Belton, M. J. S., Johnson, T. V., Smyth, W. H., and Ingersoll, A. P. (1999). Galileo Imaging of Atmospheric Emissions from Io. *Science*, 285:870–874.

Graps, A. L., Grün, E., Svedhem, H., Krüger, H., Horányi, M., Heck, A., and Lammers, S. (2000). Io as a source of the jovian dust streams. *Nature*, 405:48–50.

Greenberg, R. and Brahic, A., editors (1984). *Planetary Rings*. University of Arizona Press, Tucson, Arizona.

Grün, E. (2002). Dust Astronomy. *Bulletin of the American Astronomical Society*, 34:885.

Grün, E., Fechtig, H., Hanner, M. S., Kissel, J., Lindblad, B., Linkert, D., Maas, D., Morfill, G. E., and Zook, H. A. (1992a). The Galileo Dust Detector. *Space Science Reviews*, 60:317–340.

Grün, E., Fechtig, H., Kissel, J., Linkert, D., Maas, D., McDonnell, J. A. M., Morfill, G. E., Schwehm, G., Zook, H. A., and Giese, R. H. (1992b). The Ulysses dust experiment. *Astronomy and Astrophysics Supplement Series*, 92:411–423.

Grün, E., Gustafson, B., Mann, I., Baguhl, M., Morfill, G. E., Staubach, P., Taylor, A., and Zook, H. A. (1994). Interstellar dust in the heliosphere. *Astronomy and Astrophysics* , 286:915–924.

Grün, E., Gustafson, B. A. S., Dermott, S., and Fechtig, H. (2001). *Interplanetary dust*. Berlin : Springer.

Grün, E., Morfill, G. E., and Mendis, D. A. (1984). Dust-magnetosphere interactions. In Greenberg, R. and Brahic, A., editors, *Planetary Rings*, pages 275–332. The University of Arizona Press.

Grün, E., Zook, H. A., Baguhl, M., Balogh, A., Bame, S. J., Fechtig, H., Forsyth, R., Hanner, M. S., Horányi, M., Kissel, J., Lindblad, B.-A., Linkert, D., Linkert, G., Mann, I., McDonnell, J. A. M., Morfill, G. E., Phillips, J. L., Polanskey, C., Schwehm, G., Siddique, N., Staubach, P., Svestka, J., and Taylor, A. (1993). Discovery of Jovian dust streams and interstellar grains by the ULYSSES spacecraft. *Nature*, 362:428–430.

Grün, E., Zook, H. A., Fechtig, H., and Giese, R. H. (1985). Collisional balance of the meteoritic complex. *Icarus*, 62:244–272.

Gustafson, B. A. S. (1994). Physics of Zodiacal Dust. *Annual Review of Earth and Planetary Sciences*, 22:553–595.

Haff, P. K., Siscoe, G. L., and Eviatar, A. (1983). Ring and plasma - The enigmae of Enceladus. *Icarus*, 56:426–438.

Hamilton, D. P. (1996). The asymmetric time-variable rings of Mars. *Icarus*, 119:153–172.

Hamilton, D. P. and Burns, J. A. (1991). Orbital stability zones about asteroids. *Icarus*, 92:118–131.

Hamilton, D. P. and Burns, J. A. (1992). Orbital stability zones about asteroids. II - The destabilizing effects of eccentric orbits and of solar radiation. *Icarus*, 96:43–64.

Hamilton, D. P. and Burns, J. A. (1994). Origin of Saturn's E Ring: Self-Sustained, Naturally. *Science*, 264:550–553.

Hamilton, D. P. and Krivov, A. V. (1996). Circumplanetary dust dynamics: Effects of solar gravity, radiation pressure, planetary oblateness, and electromagnetism. *Icarus*, 123:503–523.

Hansen, C. J., Esposito, L., Stewart, A. I. F., Colwell, J., Hendrix, A., Pryor, W., Shemansky, D., and West, R. (2006). Enceladus' Water Vapor Plume. *Science*, 311:1422–1425.

Hellwege, K.-H., editor (1981). *Landolt-Börnstein*. Springer-Verlag Berlin, Heidelberg, New York.

Horányi, M. (1996). Charged Dust Dynamics in the Solar System. *Annual review of astronomy and astrophysics*, 34:383–418.

Horányi, M., Burns, J. A., and Hamilton, D. P. (1992). The dynamics of Saturn's E ring particles. *Icarus*, 97:248–259.

Horányi, M., Burns, J. A., Tátrallyay, M., and Luhmann, J. G. (1990). Toward understanding the fate of dust lost from the Martian satellites. *Geophysical Research Letters*, 17:853–856.

Horányi, M., Tátrallyay, M., Juhász, A., and Luhmann, J. G. (1991). The dynamics of submicron-sized dust particles lost from Phobos. *Journal of Geophysical Research*, 96:11,283–11,290.

Howard, J. E., Krivov, A. V., and Spahn, F. (2003). Transverse halo orbits about Mars? *Geophysical Research Letters*, 30(13):1680.

Humes, D. H., Alvarez, J. M., O'Neal, R. L., and Kinard (1974). The interplanetary and near-Jupiter meteoroid environment. *Journal of Geophysical Research*, 79:3677–3684.

Ishimoto, H. (1996). Formation of Phobos/Deimos dust rings. *Icarus*, 122:153–165.

Juhász, A. and Horányi, M. (2002). Saturn's E ring: A dynamical approach. *Journal of Geophysical Research (Space Physics)*, 107.

Juhász, A. and Horányi, M. (1995). Dust torus around Mars. *Journal of Geophysical Research*, 100:3277–3284.

Jurac, S., Johnson, R. E., and Richardson, J. D. (2001). Saturn's E Ring and Production of the Neutral Torus. *Icarus*, 149:384–396.

Kalas, P., Larwood, J., Smith, B. A., and Schultz, A. (2000). Rings in the Planetesimal Disk of β Pictoris. *Astrophysical Journal Letters* , 530:L133–L137.

Kargel, J. S. (2006). Enceladus: Cosmic Gymnast, Volatile Miniworld. *Science*, 311:1389–1391.

Kempf, S., Beckmann, U., Srama, R., Horanyi, M., Auer, S., and Grün, E. (2006). The electrostatic potential of E ring particles. *Planetary and Space Science*, 54:999–1006.

Kimura, H., Ishimoto, H., and Mukai, T. (1997). A study on solar dust ring formation based on fractal dust models. *Astronomy and Astrophysics* , 326:263–270.

Kimura, H. and Mann, I. (1998). The Electric Charging of Interstellar Dust in the Solar System and Consequences for Its Dynamics. *Astrophysical Journal*, 499:454–462.

Kimura, H., Okamoto, H., and Mukai, T. (2002). Radiation Pressure and the Poynting-Robertson Effect for Fluffy Dust Particles. *Icarus*, 157:349–361.

Kirk, R. L., Brown, R. H., and Soderblom, L. A. (1990). Subsurface energy storage and transport for solar-powered geysers on Triton. *Science*, 250:424–429.

Klacka, J., Kocifaj, M., and Pástor, P. (2005). Motion of dust near exterior resonances with planet. *Journal of Physics Conference Series*, 6:126–131.

Köhnlein, W. (1996). Radial dependence of solar wind parameters in the ecliptic (1.1 $R_\odot$ – 61 AU). *Solar Physics*, 169:209–213.

Koschny, D. and Grün, E. (2001a). Impacts into Ice-Silicate Mixtures: Crater Morphologies, Volumes, Depth-to-Diameter Ratios, and Yield. *Icarus*, 154:391–401.

Koschny, D. and Grün, E. (2001b). Impacts into Ice-Silicate Mixtures: Ejecta Mass and Size Distributions. *Icarus*, 154:402–411.

Kozai, Y. (1959). The motion of a close earth satellite. *Astronomical Journal*, 64:367–377.

Krivov, A. V. (1994). On the dust belts of Mars. *Astronomy and Astrophysics* , 291:657–663.

Krivov, A. V., Feofilov, A. G., and Dikarev, V. V. (2006). Search for the putative dust belts of Mars: The late 2007 opportunity. *Planetary and Space Science*, 54:871–878.

Krivov, A. V. and Hamilton, D. P. (1997). Martian dust belts: Waiting for discovery. *Icarus*, 128:335–353.

Krivov, A. V., Kimura, H., and Mann, I. (1998). Dynamics of dust near the Sun. *Icarus*, 134:311–327.

Krivov, A. V., Krivova, N. A., Solanki, S. K., and Titov, V. B. (2004). Towards understanding the β Pictoris dust stream. *Astronomy and Astrophysics* , 417:341–352.

Krivov, A. V., Krueger, H., Horányi, M., and Spahn, F. (2002). SL9 Dust in the Jovian System? *Bulletin of the American Astronomical Society*, 34:884.

Krivov, A. V., Sokolov, L. L., and Dikarev, V. V. (1996). Dynamics of Mars-orbiting dust: Effects of light pressure and planetary oblateness. *Celestial Mechanics*, 63:313–339.

Krivov, A. V., Sremčević, M., Spahn, F., Dikarev, V. V., and Kholshevnikov, K. V. (2003). Impact-generated dust clouds around planetary satellites: spherically symmetric case. *Planetary and Space Science*, 51:251–269.

Krüger, H., Geissler, P., Horányi, M., Graps, A. L., Kempf, S., Srama, R., Moragas-Klostermeyer, G., Moissl, R., Johnson, T. V., and Grün, E. (2003a). Jovian dust streams: A monitor of Io's volcanic plume activity. *Geophysical Research Letters*, 30(21).

Krüger, H., Horányi, M., and Grün, E. (2003b). Jovian dust streams: Probes of the Io plasma torus. *Geophysical Research Letters*, 30:30–1.

Krüger, H., Krivov, A. V., and Grün, E. (2000). A dust cloud of Ganymede maintained by hypervelocity impacts of interplanetary micrometeoroids. *Planetary and Space Science*, 48:1457–1471.

Krüger, H., Krivov, A. V., Sremčević, M., and Grün, E. (2003). Impact-generated dust clouds surrounding the Galilean moons. *Icarus*, 164:170–187.

Landgraf, M., Baggaley, W. J., Grün, E., Krüger, H., and Linkert, G. (2000). Aspects of the mass distribution of interstellar dust grains in the solar system from in situ measurements. *Journal of Geophysical Research*, 105:10343–10352.

Leinert, C. and Grün, E. (1990). Interplanetary dust. In Schwenn, R. and Marsch, E., editors, *Physics if the Inner Heliosphere. I. Large-Scale Phenomena*, pages 207–275. Springer-Verlag.

Lopes, R. M. C., Kamp, L. W., Smythe, W. D., Mouginis-Mark, P., Kargel, J., Radebaugh, J., Turtle, E. P., Perry, J., Williams, D. A., Carlson, R. W., and Douté, S. (2004). Lava lakes on Io: observations of Io's volcanic activity from Galileo NIMS during the 2001 fly-bys. *Icarus*, 169:140–174.

Lopes, R. M. C. and Williams, D. A. (2005). Io after Galileo. *Reports of Progress in Physics*, 68:303–340.

Makuch, M., Brilliantov, N. V., Sremčević, M., Spahn, F., and Krivov, A. V. (2006). Stochastic circumplanetary dynamics of rotating non-spherical dust particles. *Planetary and Space Science*, 54:855–870.

Makuch, M., Krivov, A. V., and Spahn, F. (2005). Long-term dynamical evolution of dusty ejecta from Deimos. *Planetary and Space Science*, 53:357–369.

Mann, I. and Krivov, A. V. (2000). Sources, sinks, and evolution of interplanetary dust. *Unpublished review*.

Mannella, R. (2000). A gentle introduction to the integration of stochastic differential equations. In Freund, J. A. and Pöschel, T., editors, *Stochastic Processes in Physics, Chemistry, and Biology*, pages 353–364. Dordrecht, Springer.

Mannella, R. and Palleschi, V. (1989). Fast and precise algorithm for computer simulation of stochastic differential equations. *PRA*, 40:3381–3386.

Mignard, F. (1984). Effects of radiation forces on dust particles in planetary rings. In Greenberg, R. and Brahic, A., editors, *Planetary Rings*, pages 333–366. University of Arizona Press, Tucson, Arizona.

Milstein, G. N., Repin, Y. M., and Tretyakov, M. V. (2002). Symplectic Integration of Hamiltonian Systems with Additive Noise. *SIAM Journal on Numerical Analysis*, 39:2066–2088.

Morfill, G. E. and Grün, E. (1979). The motion of charged dust particles in interplanetary space. I - The zodiacal dust cloud. II - Interstellar grains. *Planetary and Space Science*, 27:1269–1292.

Mukai, T. (1981). On the charge distribution of interplanetary grains. *Astronomy and Astrophysics* , 99(1):1–6.

Mukai, T., Blum, J., Nakamura, A. M., Johnson, R., and Havnes, O. (2001). Physical processes on Interplanetary dust. In Grün, E., Gustafson, B. A. S., Dermott, S., and Fechtig, H., editors, *Interplanetary dust*, pages 445–507. Berlin : Springer.

Müller, M., Green, S. F., McBride, N., Koschny, D., Zarnecki, J. C., and Bentley, M. S. (2002). Estimation of the dust flux near Mercury. *Planetary and Space Science*, 50:1101–1115.

Murdin, P. (2001). Encyclopedia of astronomy and astrophysics. *Encyclopedia of Astronomy and Astrophysics*.

Murray, C. D. and Dermott, S. F. (1999). *Solar System Dynamics*. Cambridge Univ. Press.

Nicholson, P. D., Showalter, M. R., Dones, L., French, R. G., Larson, S. M., Lissauer, J. J., McGhee, C. A., Sicardy, B., Seitzer, P., and Danielson, G. E. (1996). Observations of Saturn's ring-plane crossing in August and November. *Science*, 272:509–516.

Nimmo, F. and Pappalardo, R. T. (2006). Diapir-induced reorientation of Saturn's moon Enceladus. *Nature*, 441:614–616.

Northrop, T. G. and Birmingham, T. J. (1990). Plasma drag on a dust grain due to Coulomb collisions. *Planetary and Space Science*, 38:319–326.

Öpik, E. J. (1976). *Interplanetary Encounters: Close Range Gravitational Interactions*. New York, Elsevier.

Pang, K. D., Voge, C. C., Rhoads, J. W., and Ajello, J. M. (1984). The E ring of Saturn and satellite Enceladus. *Journal of Geophysical Research*, 89:9459–9470. the volcanic activity is also proposed.

Parker, E. N. (1958). The perturbation of interplanetary dust grains by the solar wind. *Astrophysical Journal*, 128:664–676.

Pierre, A. G. S. and Steele, W. A. (1969). Time correlations and conditional distribution functions for classical ensembles of free rotors. *Phys. Rev.*, 184(1):172–186.

Porco, C. C., Helfenstein, P., Thomas, P. C., Ingersoll, A. P., Wisdom, J., West, R., Neukum, G., Denk, T., Wagner, R., Roatsch, T., Kieffer, S., Turtle, E., McEwen, A., Johnson, T. V., Rathbun, J., Veverka, J., Wilson, D., Perry, J., Spitale, J., Brahic, A., Burns, J. A., DelGenio, A. D., Dones, L., Murray, C. D., and Squyres, S. (2006). Cassini Observes the Active South Pole of Enceladus. *Science*, 311:1393–1401.

Resibois, P. and de Leener, M. (1977). *Classical Kinetic Theory of Fluids*. Wiley & Sons, New York.

Richardson, J. D. (1995). An extended plasma model for Saturn. *Geophysical Research Letters*, 22:1177–1180.

Richardson, J. D., Eviatar, A., McGrath, M. A., and Vasyliunas, V. M. (1998). OH in Saturn's Magnetosphere: Observations and Implications. *Bulletin of the American Astronomical Society*, 30:1449–+.

Roatsch, T., editor (1988). *Data of the Planetary System*. Akademie-Verlag Berlin.

Sasaki, S. (1995). Surface Properties of Phobos/Deimos and Formation of Self-Sustained Martian Dust Torus. In *Lunar and Planetary Institute Conference Abstracts*, pages 1219–1220.

Sasaki, S. (1996). Martian Self-Sustaining Dust Torus. In Gustafson, B. A. S. and Hanner, M. S., editors, *ASP Conf. Ser. 104: IAU Colloq. 150: Physics, Chemistry, and Dynamics of Interplanetary Dust*, pages 187–190.

Shapiro, I. I. (1963). The prediction of satellites orbits. In Roy, M., editor, *Dynamics of satellites*, pages 257–312. Springer, Berlin.

Showalter, M. R., Cuzzi, J. N., and Larson, S. M. (1991). Structure and particle properties of Saturn's E ring. *Icarus*, 94:451–473.

Showalter, M. R., Hamilton, D. P., and Nicholson, P. D. (2006). A deep search for Martian dust rings and inner moons using the Hubble Space Telescope. *Planetary and Space Science*, 54:844–854.

Soderblom, L. A., Becker, T. L., Kieffer, S. W., Brown, R. H., Hansen, C. J., and Johnson, T. V. (1990). Triton's geyser-like plumes - Discovery and basic characterization. *Science*, 250:410–415.

Soter, S. (1971). The dust belts of Mars. *Report of Center for Radiophysics and Space Research No. 462*.

Spahn, F., Albers, N., Hörning, M., Kempf, S., Krivov, A. V., Makuch, M., Schmidt, J., Seiß, M., and Miodrag Sremčević (2006a). E ring dust sources: Implications from Cassini's dust measurements. *Planetary and Space Science*, 54:1024–1032.

Spahn, F., Krivov, A. V., Sremčević, M., Schwarz, U., and Kurths, J. (2003). Stochastic forces in circumplanetary dust dynamics. *Journal of Geophysical Research (Planets)*, 108:5021.

Spahn, F., Schmidt, J., Albers, N., Hörning, M., Makuch, M., Seiß, M., Kempf, S., Srama, R., Dikarev, V., Helfert, S., Moragas-Klostermeyer, G., Krivov, A. V., Sremčević, M., Tuzzolino, A. J., Economou, T., and Grün, E. (2006b). Cassini Dust Measurements at Enceladus and Implications for the Origin of the E Ring. *Science*, 311:1416–1418.

Spahn, F., Thiessenhusen, K.-U., Colwell, J. E., Srama, R., and Grün, E. (1999). Dynamics of dust ejected from Enceladus: Application to the Cassini–Enceladus encounter. *Journal of Geophysical Research*, 104:24,111–24,120.

Spencer, J. R., Pearl, J. C., Segura, M., Flasar, F. M., Mamoutkine, A., Romani, P., Buratti, B. J., Hendrix, A. R., Spilker, L. J., and Lopes, R. M. C. (2006). Cassini Encounters Enceladus: Background and the Discovery of a South Polar Hot Spot. *Science*, 311:1401–1405.

Srama, R., Ahrens, T. J., Altobelli, N., Auer, S., Bradley, J. G., Burton, M., Dikarev, V. V., Economou, T., Fechtig, H., Görlich, M., Grande, M., Graps, A., Grün, E., Havnes, O., Helfert, S., Horanyi, M., Igenbergs, E., Jessberger, E. K., Johnson, T. V., Kempf, S., Krivov, A. V., Krüger, H., Mocker-Ahlreep, A., Moragas-Klostermeyer, G., Lamy, P., Landgraf, M., Linkert, D., Linkert, G., Lura, F., McDonnell, J. A. M., Möhlmann, D., Morfill, G. E., Müller, M., Roy, M., Schäfer, G., Schlotzhauer, G., Schwehm, G. H., Spahn, F., Stübig, M., Svestka, J., Tschernjawski, V., Tuzzolino, A. J., Wäsch, R., and Zook, H. A. (2004). The Cassini Cosmic Dust Analyzer. *Space Science Reviews*, 114:465–518.

Srama, R. and Grün, E. (1997). The dust sensor for Cassini. *Advances in Space Research*, 20:1467–1470.

Sremčević, M., Krivov, A. V., Krüger, H., and Spahn, F. (2005). Impact-generated dust clouds around planetary satellites: model versus Galileo data. *Planetary and Space Science*, 53:625–641.

Sremčević, M., Krivov, A. V., and Spahn, F. (2003). Impact-generated dust clouds around planetary satellites: asymmetry effects. *Planetary and Space Science*, 51:455–471.

Taylor, A. D., Baggaley, W. J., and Steel, D. I. (1996). Discovery of interstellar dust entering the Earth's atmosphere. *Nature*, 380:323–325.

Thiessenhusen, K.-U., Krivov, A. V., Krüger, H., and Grün, E. (2002). A dust cloud around Pluto and Charon. *Planetary and Space Science*, 50:79–87.

Waite, J. H., Combi, M. R., Ip, W.-H., Cravens, T. E., McNutt, R. L., Kasprzak, W., Yelle, R., Luhmann, J., Niemann, H., Gell, D., Magee, B., Fletcher, G., Lunine, J., and Tseng, W.-L. (2006). Cassini Ion and Neutral Mass Spectrometer: Enceladus Plume Composition and Structure. *Science*, 311:1419–1422.

Weingartner, J. C. and Draine, B. T. (2001). Photoelectric Emission from Interstellar Dust: Grain Charging and Gas Heating. *Astrophysical Journal Supplement Series* , 134:263–281.

Willis, R. F., Feuerbacher, B., and Fitton, B. (1973). Optical and Photoemission Properties of Graphic Grains (presented by R. F. Willis). In *IAU Symp. 52: Interstellar Dust and Related Topics*, pages 303–309.

Wisdom, J. (2004). Spin-Orbit Secondary Resonance Dynamics of Enceladus. *Astronomical Journal*, 128:484–491.

Zook, H. A. and Berg, O. E. (1975). A source for hyperbolic cosmic dust particles. *Planetary and Space Science*, 23:183–203.

# Appendix A

# Long-term Dynamical Evolution of Dusty Ejecta from Deimos

MAKUCH M., KRIVOV A. V., AND SPAHN F. (2005).
Long-term Dynamical Evolution of Dusty Ejecta from Deimos. **Planetary and Space Science**, 53:357-369.
doi: 10.1016/j.pss.2004.09.063

Available online at www.sciencedirect.com
SCIENCE DIRECT®
Planetary and Space Science 53 (2005) 357–369
Planetary and Space Science
www.elsevier.com/locate/pss

# Long-term dynamical evolution of dusty ejecta from Deimos

Martin Makuch*, Alexander V. Krivov, Frank Spahn

*Institute of Physics, Nonlinear Dynamics Group, University of Potsdam, Am Neuen Palais 10, Bldg. 19, 14469 Potsdam, Germany*

Received 2 June 2004; received in revised form 2 September 2004; accepted 16 September 2004
Available online 22 December 2004

**Abstract**

We re-assess expected properties of the presumed dust belt of Mars formed by impact ejecta from Deimos. Previous studies have shown that dynamics of Deimos particles are dominated by two perturbing forces: radiation pressure (RP) and Mars' oblateness (J2). At the same time, they have demonstrated that lifetimes of particles, especially of grains about ten of micrometers in size, may reach more than $10^4$ years. On such timescales, the Poynting–Robertson drag (PR) becomes important. Here we provide a study of the dynamics under the combined action of all three perturbing forces. We show that a PR decay of the semimajor axes leads to an adiabatic decrease of amplitudes and periods of oscillations in orbital inclinations predicted in the framework of the underlying RP + J2 problem. Furthermore, we show that smallest of the long-lived Deimos grains (radius $\approx$ 5–10 μm) may reach a chaotic regime, resulting in unpredictable and abrupt changes of their dynamics. The particles just above that size ($\approx$ 10–15 μm) should be the most abundant in the Deimos torus. Our dynamical analysis, combined with a more accurate study of the particle lifetimes, provides corrections to earlier predictions about the dimensions and geometry of the Deimos torus. In addition to a population, appreciably inclined and shifted towards the Sun, the torus should contain a more contracted, less asymmetric, and less tilted component between the orbits of Phobos and Deimos.


*PACS:* 96.30.Gc; 94.10.Nh; 96.30.Wr

*Keywords:* Mars; Deimos; Ejecta; Dynamics; Radiation pressure; Poynting–Robertson drag

## 1. Introduction

Like all bodies in the Solar system, the tiny Martian moons Phobos and Deimos are continuously bombarded by interplanetary micrometeoroids. Due to these hypervelocity impacts secondary material is ejected from the surface of the bodies. The mass of the ejecta is several orders of magnitude greater than the mass of projectiles. The velocities of the ejected debris are typically tens of meters per second, which is comparable with, or greater than, the escape velocity from the satellite surface. Escaping particles should generate ethereal dust tori along the orbits of the parent satellites (first suggested by Soter, 1971). These putative dust tori, which still escape direct detection (see Showalter et al., 2001, for the most recent attempt), were theoretically studied by many authors (see Krivov and Hamilton, 1997 for detail overview of previous work).

The dynamics of the ejecta are very complex, being controlled by a large array of perturbing forces. These include gravity of the oblate Mars, solar radiation pressure, Lorentz force, and others. Relative importance of a particular perturbation depends mainly on the size of the grains and their position in the Martian system. As the ejecta dynamics depend on the grain size, different-sized ejecta of both moons form several populations with quite distinct properties. Using the terminology of Krivov (1996), Population 0 consists of

*Corresponding author. Tel.: +49 331 9771 390; fax: +49 331 9771 142.
*E-mail address:* makuch@agnld.uni-potsdam.de (M. Makuch).

0032-0633/$ - see front matter © 2004 Elsevier Ltd. All rights reserved.
doi:10.1016/j.pss.2004.09.063

the largest grains with radii $\gtrsim 1$ mm. Since non-gravitational perturbations on the macroscopic grains are weak, they stay within confined tori along the moons' orbits, the size of which is determined by the initial ejection velocity distribution (Kholshevnikov et al., 1993). As these particles rapidly re-accrete on the parent moon, their lifetimes and related number densities are very low. Population I contains smaller particles with radii from hundreds down to qtens of microns and lifetimes between tens of years (Phobos) and *tens of thousands of years* (Deimos). These should form extended asymmetric tori and represent the dominant component of the entire dust complex. Their major loss mechanism is still re-accretion by the parent moon. Combined influence of the solar radiation pressure and Mars oblateness causes periodic oscillations of eccentricity and inclination. Below a certain critical radius $s_{\mathrm{crit}}$ ($\sim 10\,\mu$m, see Krivov et al., 1996), the amplitude of the eccentricity oscillations becomes so high that the particles collide with Mars at the pericenter of their orbits in less than 1 year, so they are present with low number densities. These grains are classified as Population II. Tiniest, submicron-sized fragments (Population III) are strongly influenced by electromagnetic forces and solar wind. They are swiftly swept out from the vicinity of Mars in 10–100 days and form an extended, highly variable halo around Martian system (Horányi et al., 1990, 1991). However, a small fraction of the submicron-sized grains ejected from Martian moons at larger speeds can reach stable orbits transverse to the ecliptic plane with lifetimes exceeding 1000 years (Howard et al., 2003).

The aim of this work is to analyse long-term dynamical evolution of the Deimos particles of Population I, which are expected to dominate the dust environment at Mars (Juhász and Horányi, 1995). The dynamics of grains governed by two strongest perturbations, solar radiation pressure (RP) and planetary oblateness (J2), were studied both analytically and numerically in detail before (Krivov et al., 1996; Hamilton, 1996; Ishimoto, 1996; Krivov and Hamilton, 1997). However, the Poynting–Robertson effect (PR), which becomes important over extremely long lifetimes of tens of thousands of years, has never been included in previous models of dust at Mars. This paper provides a study of the dynamics under the combined influence of all three perturbing forces: RP, J2, and PR.

Section 2 discusses equations of motion, which are then used in Section 3 to study the dynamical evolution of different-sized ejecta from Deimos. Section 4 focuses on lifetimes of the grains in Martian system. The results are used in Section 5 to find out the expected structure of the Deimos torus and to compare it with the Phobos one. Section 6 lists our conclusions.

## 2. Equations of motion

### 2.1. Equations of motion in coordinates

The most straightforward way to study the dynamics is numerical integration of the equation of motion of a particle under the influence of all three perturbing forces:

$$m\ddot{\vec{r}} = \vec{F}_{\mathrm{GR}} + \vec{F}_{\mathrm{J2}} + \vec{F}_{\mathrm{RP}} + \vec{F}_{\mathrm{PR}}, \tag{1}$$

where the right-hand side terms represent the gravitational force of the spherical Mars $\vec{F}_{\mathrm{GR}}$, oblateness of the planet $\vec{F}_{\mathrm{J2}}$, direct radiation pressure $\vec{F}_{\mathrm{RP}}$ and Poynting–Robertson drag $\vec{F}_{\mathrm{PR}}$. We used a code based on the Everhart's (1985) method with the automatic choice of step size. The integration interval was chosen in very broad range from $\sim 10^3$ up to $\sim 10^5$ Martian years (1.88 years; henceforth denoted by [M.y.]) depending on conditions and purpose of the simulation. The design of our integration code allows us to follow a set of trajectories with different initial data, which can be chosen with a large degree of flexibility.

### 2.2. Orbit-averaged equations in orbital elements

Since we are interested in long-term dynamics, direct numerical integrations described above would imply very long computing times. An alternative would be to numerically integrate orbit-averaged equations of motion in orbital elements, which we describe in this section.

We start with a brief description of the PR effect. The PR force $\vec{F}_{\mathrm{PR}}$ is a component of the radiation pressure force and is usually treated separately from the direct radiation pressure $\vec{F}_{\mathrm{RP}}$. Since it is a dissipative force, acting in opposite direction to the particle velocity, the grains gradually lose orbital energy and angular momentum. This results in a decrease of semimajor axis $a$ with time which, in the orbit-averaged approximation, is given by (Burns et al., 1979):

$$\frac{\dot{a}}{a} = Dn_{\odot} \tag{2}$$

with

$$D = \frac{3}{8}\left(\frac{1}{n_{\odot}}\right)\left(\frac{S_0}{R_{\mathrm{M}}^2}\right)\left(\frac{Q_{\mathrm{pr}}}{c^2 \varrho s}\right)(5+\cos^2 i). \tag{3}$$

Here, $S_0 = 1.36 \times 10^6\,\mathrm{erg\,cm^{-2}}$ is the solar constant, $R_{\mathrm{M}}$ the heliocentric distance of Mars in AU, $n_{\odot}$ the mean motion of Sun, $i$ the inclination of the particle orbit, $c$ the speed of light, $\varrho$ and $s$ are density and radius of the particle. $Q_{\mathrm{pr}}$ is the radiation pressure efficiency factor depending on the grain radius $s$. Replacing $\cos^2 i$ with unity, Eq. (2) implies an exponential decay of the semimajor axis: $a = a_0 \exp(-Dn_{\odot}t)$, where $a_0$ is the initial semimajor axis.

In the orbit-averaged approximation, the PR force does not affect the eccentricity of a planetocentric orbit (Burns et al., 1979)—in contrast to heliocentric motion, which circularises under the action of PR. The changes in other orbital elements are small and can be ignored.

Following Krivov et al. (1996) we express the equations of motion of a particle in terms of Lagrange elements $h$, $k$, $p$, $q$, defined as

$$h = e\cos\tilde{\omega}, \quad k = e\sin\tilde{\omega},$$
$$p = \sin i\cos\Omega, \quad q = \sin i\sin\Omega, \tag{4}$$

where $\tilde{\omega} \equiv \Omega + g$ is the longitude of pericenter and $e, \Omega, g$ are eccentricity, longitude of node and argument of pericenter, respectively. As an independent variable, we use the longitude of the Sun $\lambda_\odot$, which makes the equations of motion dimensionless. Neglecting the eccentricity of Martian orbit, $\lambda_\odot$ is a linear function of time:

$$\lambda_\odot = \lambda_{\odot 0} + n_\odot t, \tag{5}$$

where $\lambda_{\odot 0}$ is the initial solar longitude at the moment of ejection ($t = 0$) or, more exactly, when a particle reaches the boundary of the moon's action sphere.

The orbit-averaged equations of motion under RP and J2 were derived by Krivov et al. (1996). They can be generalised to include the PR effect by adding Eq. (2), rewritten in the same variables. The resulting system reads:

$$\frac{da}{d\lambda_\odot} = -Da, \tag{6}$$

$$\begin{aligned}\frac{dh}{d\lambda_\odot} = &-k\omega\frac{5I^2-2I-1}{2E^4}\\ &-\frac{C}{E(1+I)}\{[p-Hh]q\cos\lambda_\odot\\ &+[E^2(1+I)-p(p-Hh)]\cos\varepsilon\sin\lambda_\odot\\ &+[E^2(1+I)p-IKk]\sin\varepsilon\sin\lambda_\odot\},\end{aligned} \tag{7}$$

$$\begin{aligned}\frac{dk}{d\lambda_\odot} = &\,h\omega\frac{5I^2-2I-1}{2E^4}\\ &+\frac{C}{E(1+I)}\{[q-Hk]p\cos\varepsilon\sin\lambda_\odot\\ &+[E^2(1+I)-q(q-Hk)]\cos\lambda_\odot\\ &-[E^2(1+I)q-IKh]\sin\varepsilon\sin\lambda_\odot\},\end{aligned} \tag{8}$$

$$\begin{aligned}\frac{dp}{d\lambda_\odot} = &\,q\omega\frac{I}{E^4}+\frac{C}{E(1+I)}[Hp-(1+I)h]\\ &\times[(p\cos\varepsilon - I\sin\varepsilon)\sin\lambda_\odot - q\cos\lambda_\odot],\end{aligned} \tag{9}$$

$$\begin{aligned}\frac{dq}{d\lambda_\odot} = &-p\omega\frac{I}{E^4}+\frac{C}{E(1+I)}[Hq-(1+I)k]\\ &\times[(p\cos\varepsilon - I\sin\varepsilon)\sin\lambda_\odot - q\cos\lambda_\odot],\end{aligned} \tag{10}$$

with

$$E = \sqrt{1-e^2} = \sqrt{1-h^2-k^2},$$
$$I = \cos i = \sqrt{1-p^2-q^2},$$
$$H = hp + kq,$$
$$K = hq - kp, \tag{11}$$

where $\varepsilon$ denotes the obliquity of Mars (25°), and $C$ and $\omega$ are dimensionless parameters that characterise the strength of the radiation pressure and oblateness (see Krivov et al., 1996, for an exact definition).

Eqs. (6)–(11) are coupled through the parameters $D$, $C$ and $\omega$. The first of them has a weak dependence on the inclination $i$ (see Eq. (3)), which we take into account in numerical integrations. The other parameters, $C$ and $\omega$, are functions of semimajor axis:

$$C(a) = C_0\left(\frac{a}{a_0}\right)^{1/2}, \quad \omega(a) = \omega_0\left(\frac{a}{a_0}\right)^{-7/2}, \tag{12}$$

where $C_0 \equiv C(a_0)$ and $\omega_0 \equiv \omega_0(a_0)$. Assuming a grain density of $\varrho = 2.37\,\mathrm{g\,cm^{-3}}$, $C_0$ and $\omega_0$ can be expressed as

$$C_0 = 4.10\frac{Q_{\mathrm{pr}}(s)}{s[\mu\mathrm{m}]}\ \text{(Phobos' ejecta)},$$
$$C_0 = 6.49\frac{Q_{\mathrm{pr}}(s)}{s[\mu\mathrm{m}]}\ \text{(Deimos' ejecta)} \tag{13}$$

and

$$\omega_0 = 0.829\ \text{(Phobos' ejecta)},$$
$$\omega_0 = 0.0335\ \text{(Deimos' ejecta)}. \tag{14}$$

Like equations in coordinates (1), the equations in elements, Eqs. (6)–(11), were integrated by the Everhart routine with the automatic choice of step size. Since these integrations are by about two orders of magnitude faster, we use them as the main tool to study the dynamics in this paper. Of course, the results were thoroughly tested against those coming from Eqs. (1). Examples of that comparison will be given in subsequent sections.

## 3. Grain dynamics

Before we pass on to a discussion of the particle dynamics, we shall specify the dependence of the radiation pressure forces on the particle sizes. Throughout the paper, we use compact spherical grains made of one of the silicates, a dielectric material with less absorption in visible light (for its parameters, see Kimura et al., 1997; Krivov et al., 1998). The radiation pressure efficiency $Q_{\mathrm{pr}}$ as a function of particle's radius is given in Table 1. The bulk density of this material is $\varrho = 2.37\,\mathrm{g\,cm^{-3}}$. We note that, since grains with the same ratio of $Q_{\mathrm{pr}}/(s\varrho)$ experience the same acceleration by radiation pressure, the results can be easily scaled to

different values of the radiation pressure factor $Q_{pr}$ and material density $\varrho$. As an example, an 8 μm grain ($Q_{pr} = 0.41$, $\varrho = 2.37\,g\,cm^{-3}$) in this paper corresponds to a 23 μm grain in Krivov et al. (1996) who adopted $Q_{pr} = 1$ and $\varrho = 2\,g\,cm^{-3}$.

### 3.1. Radiation pressure alone

On timescales up to hundreds of years, i.e. before the semimajor axes of the Deimos ejecta have been lowered by the PR effect considerably, their dynamics are dominated by radiation pressure (e.g., Krivov et al., 1996; Hamilton and Krivov, 1996). It causes the orbital eccentricity to oscillate with a period close to 1 M.y. and an amplitude depending on the radiation pressure strength:

$$e_{max} = 2C/(1 + C^2), \tag{15}$$

provided that the obliquity $\varepsilon$ is small. The inclination experiences periodic changes of a longer period (tens of M.y. for $\sim 10\,\mu m$ particles), with both period and amplitude depending on $C$ and hence on the grain size. This is illustrated by Fig. 1 that depicts the evolution of both orbital elements for Deimos particles with two specific radii, 15 and 7.5 μm. Plotted are results obtained by both methods described in previous sections: integration of orbit-averaged equations in Lagrangian elements (Eqs. (6)–(11), lines) and, for comparison, by direct numerical integration of the equations in coordinates (Eq. (1), points). The plots show that Eqs. (6)–(11) provide an excellent accuracy.

Table 1
Radiation pressure efficiency of the material adopted in the calculations of the radiation pressure force

| $s$[μm] | 5 | 6 | 7 | 8 | 10 | 15 | 20 | 30 |
|---|---|---|---|---|---|---|---|---|
| $Q_{pr}$ | 0.442 | 0.433 | 0.426 | 0.411 | 0.400 | 0.385 | 0.378 | 0.374 |

The eccentricity panels in Fig. 1 also reveal a slight modulation of the eccentricity oscillation by the variation of the inclination. This second period in the eccentricity is equal to the "main" period in the inclination (about 20 M.y. for $s = 15\,\mu m$ and 8 M.y. for $s = 7.5\,\mu m$). The amplitude is about one or two percent of $e_{max}$.

Eq. (15) determines the critical value of $C$, and therefore of the particle size, for which $e_{max} = 1 - R/a_0 = 0.855$ ($R$ is the Mars radius) and the pericenter of orbit reaches the Mars surface. Eqs. (15) and (13) yield $s_{crit} \approx 5\,\mu m$. With test numerical integrations of (1), in which we included additional forces and effects (ellipticity of Mars' orbit, planetary shadow), we checked that the "realistic" critical size is somewhat larger, $\approx 7\,\mu m$. Since smaller particles are produced at the moon surface at higher rates than

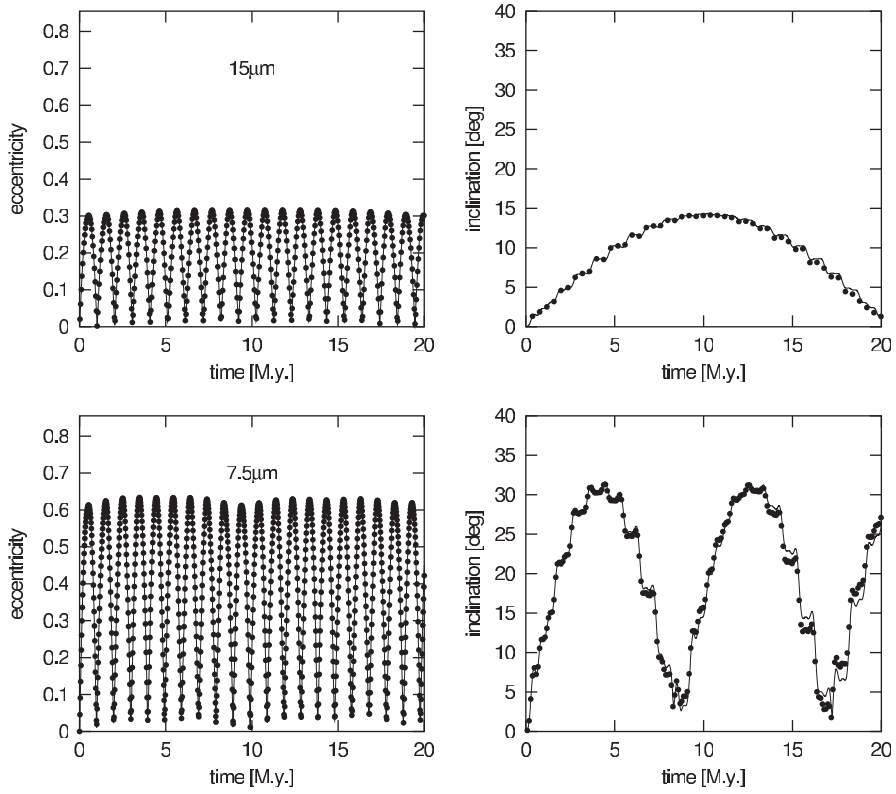


Fig. 1. Dynamical evolution of 15 μm (top) and 7.5 μm Deimos ejecta (bottom) under the radiation pressure. Points: integrations of Eq. (1), solid lines: integrations of Eqs. (6)–(11). Left: eccentricity, right: inclination. The upper edge of the eccentricity panels corresponds to the critical eccentricity 0.855, for which the pericenters of orbits touch the Martian surface.

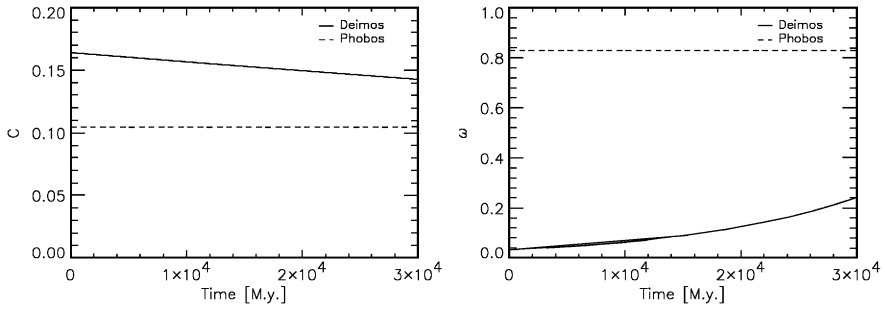


Fig. 2. Time evolution of the radiative ($C$) and oblateness ($\omega$) parameters for a 15 μm Deimos particle. Horizontal dashed lines are the parameters of a like-sized Phobos grain.

larger ones, grains just above this critical size are expected to dominate the Population I. This explains the "working range" of sizes considered in this paper: from $\approx 7$ up to $\approx 30\,\mu$m.

### 3.2. Radiation pressure and planetary oblateness

A more accurate description of the dynamics can be achieved by taking into account the oblateness of Mars, parameterised by the force parameter $\omega$. From the system of Eqs. (7)–(11), neglecting the terms of order $e^2$, $i^2$ and $\sin i$ and assuming that $\omega$ is small, Krivov et al. (1996) found approximate analytic expressions for the periods of oscillation of $e$ and $i$ and their amplitudes. The amplitude and period of oscillations of eccentricity are

$$e_{\max} \approx \frac{2C(\cos\varepsilon + \omega)}{1-\omega^2}, \tag{16}$$

$$T_e \approx 1/(1-\omega). \tag{17}$$

The amplitude and period of oscillations of the inclination are

$$i_{\max} \approx \arcsin\frac{2d}{v}, \tag{18}$$

$$T_i \approx \frac{1}{v}, \tag{19}$$

where

$$d = \frac{C^2}{2}\frac{1+\omega\cos\varepsilon}{1-\omega^2}\sin\varepsilon \quad \text{and}$$
$$v = \omega + \frac{C^2}{2}\frac{\cos\varepsilon+\omega}{1-\omega^2}. \tag{20}$$

### 3.3. Radiation pressure, planetary oblateness and Poynting–Robertson drag

We now add the PR force into the model. With the PR effect at work, a decrease of the semimajor axis makes "constants" $C$ and $\omega$ (Eq. (12)) functions of time. The time evolution of $C$ and $\omega$ for a 15 μm Deimos particle is depicted in Fig. 2. Using then (16)–(17) and (18)–(19), we calculated the long-term time evolution of the amplitudes and periods of oscillations in eccentricity and inclination (Fig. 3, lines). While for eccentricity the amplitude and period stay nearly constant, for inclination both quantities experience a moderate decrease with time. This falls in a qualitative agreement with numerical integrations of Eqs. (6)–(11) (Fig. 3, points). A quantitative agreement is good for all quantities except for $i_{\max}$. The discrepancy is caused by simplifying assumptions made by Krivov et al. (1996) in their derivation of Eq. (18). Note that another analytic formula for $i_{\max}$ obtained by Hamilton (1996) (his $2i_{\text{forced}}$) gives nearly the same result as Eq. (18).

Closer to Mars the radiation pressure parameter $C$ decreases and the oblateness parameter $\omega$ increases. Thus, both perturbing forces become simultaneously important for the dynamics of particles. This is the case for ejecta from Phobos, which makes their dynamics much more complicated (e.g., Krivov et al., 1996; Ishimoto, 1996; Hamilton, 1996; Hamilton and Krivov, 1996). One of the central ideas of this study is that the inclusion of the PR dissipation causes the Deimos particles to gradually migrate inward. Consequently, we expect that, after sufficient time, the Deimos particles switch into the "Phobos regime". Accordingly, in the subsequent sections, we follow the orbital evolution of the Deimos particles over time spans long enough for the orbits to shrink appreciably.

### 3.4. Gradual orbit modifications

Numerical integration of orbit-averaged 3D equations of motion (6)–(11) performed with zero initial eccentricities and inclinations over longer timescales gives the results shown in Fig. 4. Panels illustrate the time evolution of the semimajor axis, eccentricity and inclination of the same particles as in Fig. 1: with radii 15 μm (left) and 7.5 μm (right) ejected from Deimos in Martian autumn equinox ($\lambda_\odot = 180°$). In Fig. 4 (top) the decrease of semimajor axis can be easily recognised. As expected from analytic estimates (see Fig. 3), the amplitude of the eccentricity oscillations stays nearly

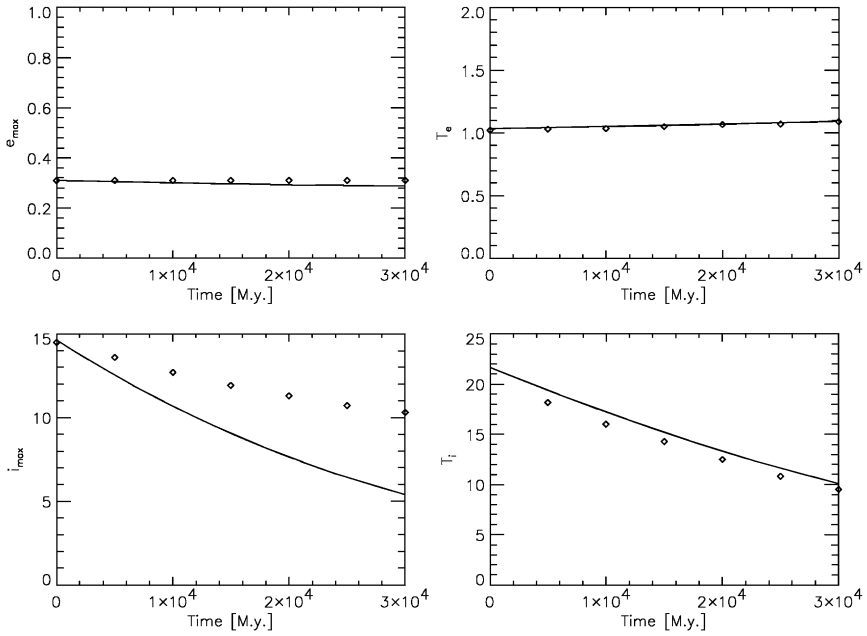


Fig. 3. Time evolution of the amplitude and period of eccentricity and inclination of the 15 μm Deimos ejecta.

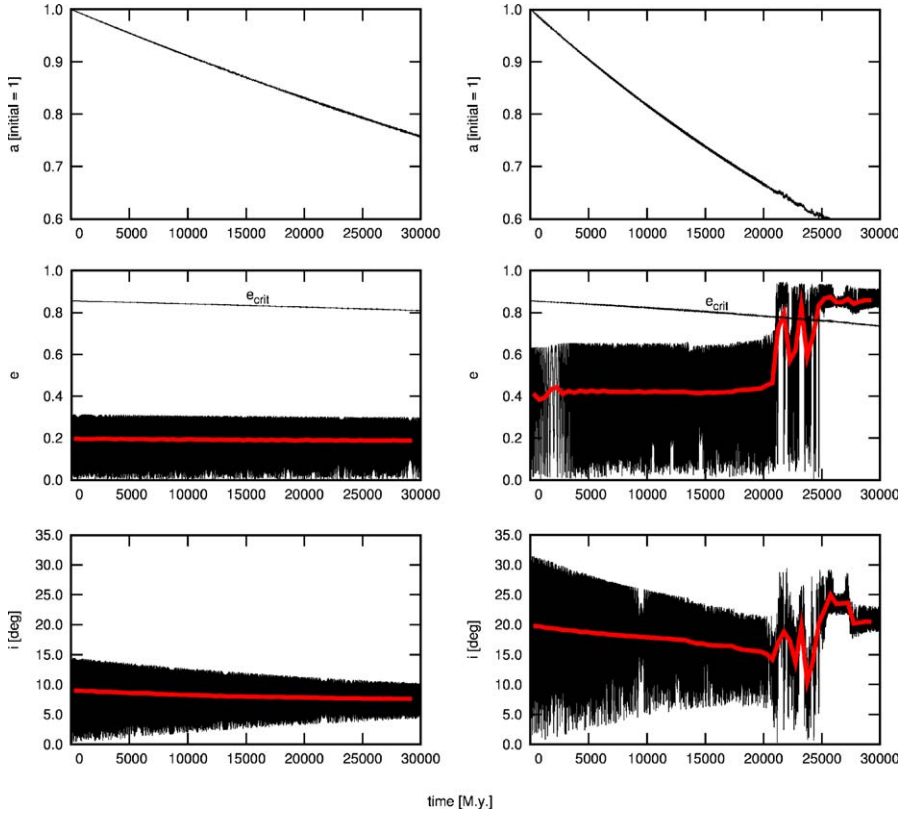


Fig. 4. Time evolution of orbital elements of 15 μm (left) and 7.5 μm (right) grains ejected into the circular Deimos orbit under the influence of radiation pressure, oblateness of Mars, and the PR effect. The curves were obtained by numerical integration of Eqs. (6)–(11). The additional thin line in the eccentricity plot corresponds to $e_{crit}$—the critical value of eccentricity of a particle, such that the particle collides with Mars in the pericenter of the orbit. The thick grey solid line in the middle and bottom panels corresponds to averaged values of the eccentricity and inclination.

constant (Fig. 4, middle), whereas the inclination shows a gradual decrease of amplitude (Fig. 4, bottom). All these trends are stronger for smaller grains. The sudden change in the dynamics of the 7.5 μm grain after about 21 000 M.y., which strongly attracts attention in Fig. 4, is discussed in detail in the next section.

### 3.5. Abrupt orbit modifications and chaos

In Fig. 5 we show dynamical evolution of different-sized Deimos ejecta under the influence of radiation pressure, Mars' oblateness, and the Poynting–Robertson drag over a long time span. Instead of analysing gradual changes of periods and amplitudes in $e$ and $i$, we now focus on the evolution of the mean values of elements. Therefore, we plot time-average values of the orbital elements $a_{\mathrm{mean}}$, $e_{\mathrm{mean}}$, $i_{\mathrm{mean}}$ over adjacent time intervals of 500 M.y. Shown are orbital histories of particles with zero initial $e$ and $i$ of three sizes: 15 (thick solid), 10 (thick dashed), and 7.5 μm (thick dotted lines).

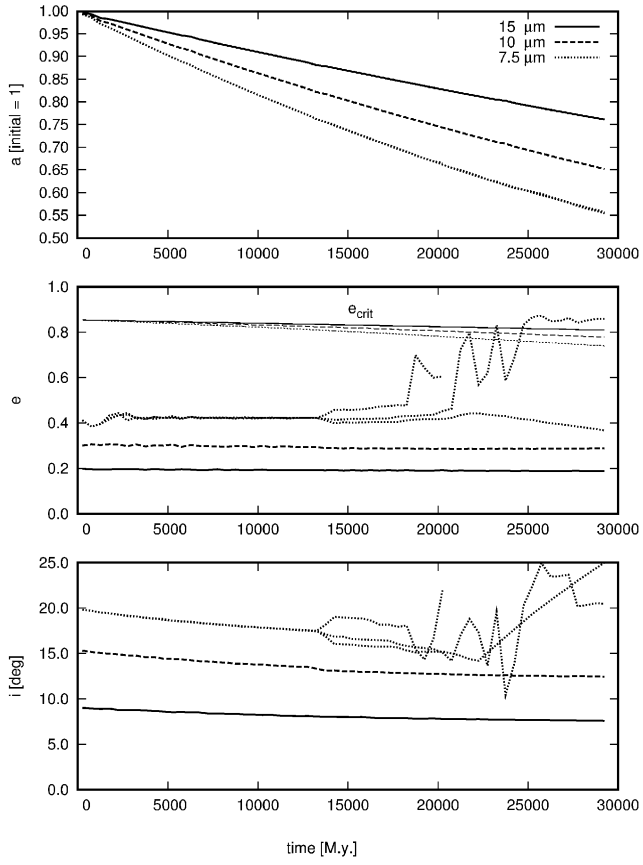


Fig. 5. Dynamical evolution of different-sized Deimos ejecta under the radiation pressure, Mars' oblateness and the PR drag over a long time span. From top to bottom: semimajor axes, eccentricities, and inclinations. The curves represent time-average values of the orbital elements over adjacent time intervals of 500 M.y. Shown are orbital histories of particles of three sizes: 15 (thick solid), 10 (thick dashed), and 7.5 μm (thick dotted lines). On the middle panel, we overplot the critical eccentricity for which the pericenter is at the planetary surface. Since it depends on the (size-dependent) value of the semimajor axis, we plot the critical eccentricity of the particles of a certain size with a thin line of the same style (solid, dashed, or dotted) as the one used to depict the orbital elements. For smallest radius, 7.5 μm, we launched 3 particles with slightly different initial values of the solar longitude: $\lambda_\odot = 180°$, 181°, and 182°. At a certain instant of time, the three curves drastically diverge. This is a saddle separatrix chaos discussed in the text.

For the two larger sizes, we only see a nearly constant mean $e$ (which is larger for smaller particles), and a gradually decreasing mean $i$ (larger values and faster decrease for smaller particles). This is consistent with the analysis given in the previous section.

For smallest radius, 7.5 μm, however, sudden changes start to occur after $\approx 13\,000$ M.y. of their orbital evolution. We launched 3 particles with slightly different initial values of the solar longitude: $\lambda_\odot = 180°$, 181°, and 182°. At a certain instant of time, three curves drastically diverge. An exact moment when it happens varies from one particle to another (see figure). The same effect would result from a change in *any* of the initial data, even by an *arbitrarily small* amount. All this is indicative for chaos, the appearance of which needs to be explained. Before we proceed with that analysis, we note that, after the particle has achieved the chaotic regime, the eccentricity reaches the critical value, and the grain is lost at the Martian surface. Particles smaller than 7.5 μm, but still above the critical radius, reveal the same behaviour (not shown in the figure). The smaller the grain, the sooner it lands in chaos.

To explain the phenomenon, it is useful to analyse phase portraits of the dynamical system. Krivov et al. (1996) and Hamilton and Krivov (1996) studied a simplified 2D problem (neglecting Mars' obliquity $\varepsilon$ and setting inclination $i$ to zero), which is integrable, allowing an exhaustive analytic treatment. As variables, they used eccentricity $e$ and solar angle $\phi_\odot \equiv \tilde{\omega} - \lambda_\odot$. The latter variable measures the angle between the planetocentric directions toward orbit's pericenter and the Sun. They constructed phase portraits in the $e - \phi_\odot$ plane and investigated the location and properties of fixed points. Fig. 6 depicts such phase portraits for Deimos ejecta with the same sizes as in Fig. 5, found from numerical integrations of Eqs. (6)–(11). The orbits of larger, 15 and 10 μm grains (left) are close to circles surrounding a fixed point (local maximum, $P_3$ in the notation of Hamilton and Krivov (1996)) located on the $e\cos\phi_\odot$ axis (cf. Fig. 3 of Hamilton and Krivov (1996)). The trajectory of a smaller, 7.5 μm particle, reveals a more complicated structure, including the circle just described and an additional outer circle (right). A "bridge" between both circles is associated with another fixed point, a saddle $P_4$, also located on the $e\cos\phi_\odot$ axis.

To explain the behaviour of the 7.5 μm-sized grain, we computed phase portraits in the simplified 2D problem analytically by means of the Hamilton and Krivov (1996) formulas. Fig. 7 plots a family of trajectories of 7.5 μm-sized Deimos grains starting from slightly different points around $e = 0$. Three panels correspond to different values of semimajor axis $a/a_0$ (1.0, 0.7, and 0.6) and therefore to different stages of the dynamical evolution. As semimajor axis decreases ($C$ decreases, $\omega$ increases), $P_3$ migrates only slowly to the left, while the

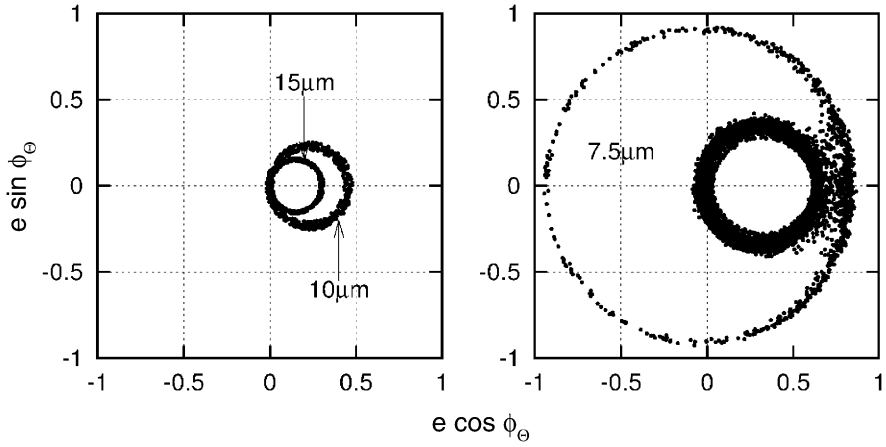


Fig. 6. Polar plot of eccentricity $e$ versus solar angle $\phi_\odot \equiv \tilde{\omega} - \lambda_\odot$ for Deimos particles with radii 15 and 10 μm (left) and 7.5 μm (right).

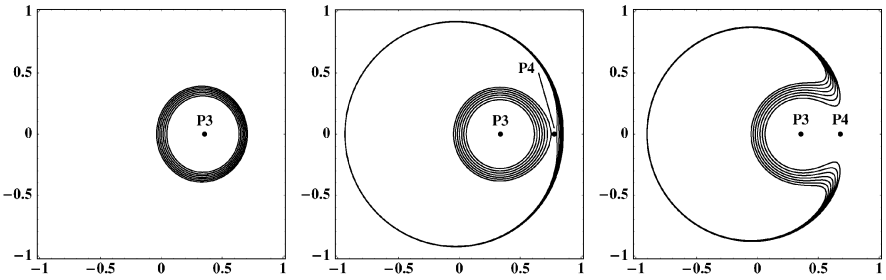


Fig. 7. A family of trajectories of 7.5 μm-sized Deimos grains starting with different initial eccentricities close to zero, calculated analytically from a simplified 2D problem. The axes are the same as in Fig. 6. Panels from left to right correspond to diminishing values of semimajor axis $a/a_0$ (1.0, 0.7, and 0.6) and therefore to different stages of the dynamical evolution. Cf. Fig. 6 (right).

saddle $P_4$ approaches from the right much faster. When $a/a_0 = 0.7$ ($P_3 = [0.34, 0]$ and $P_4 = [0.78, 0]$), the $e_0 = 0$ trajectory reaches the separatrix associated with saddle. As this happens, the trajectory flips from the libration regime (inner circle, solar angle librates about zero) to the circulation regime (outer circle, solar angle takes all values between 0° and 360°).

Thus, some of the trajectories with $e_0$ close to zero pass by the saddle from the left and follow inner circles. Others go to the right of $P_4$ and swerve to a large outer circle. Still, the integrable 2D system depicted in Fig. 7 does not contain any chaos: every trajectory belongs to one regime or another. However, adding the third dimension ($\varepsilon \neq 0$, $i \neq 0$ in Eqs. (6)–(11)) makes the system non-integrable and can cause unpredictable switches between both regimes along one and the same trajectory. The same effect can be triggered by small perturbations imposed on a trajectory. Thus the peculiar behaviour of smaller ejecta is a classical saddle separatrix chaos. A similar behaviour was identified earlier in the dynamics of the Phobos ejecta under radiation pressure and Mars' oblateness (without the PR effect), however at much larger grain sizes of hundreds μm (Krivov et al., 1996; Hamilton and Krivov, 1996).

## 4. Lifetimes of particles in the Deimos torus

### 4.1. Impacts with Deimos and Phobos

The main loss mechanism for the Deimos ejecta is collision with the parent body, Deimos, as well as with the other satellite—Phobos. In Fig. 8 we show the evolution of pericentric and apocentric distances of different-sized Deimos grains. For the smallest size, 7.5 μm, the amplitude of the eccentricity oscillations is high enough for the grain to cross not only the Deimos orbit, but also the orbit of Phobos from the very beginning. Thus both moons act as sinks, efficiently removing the particles. The orbit of the medium-sized grain (11 μm) initially crosses only the Deimos orbit. In the course of the PR evolution, both pericentric and apocentric distances decrease until the apocentre crosses the Deimos orbit at $t \approx 26\,000$ M.y., stopping further re-accretion of the ejecta by this moon. However, at the

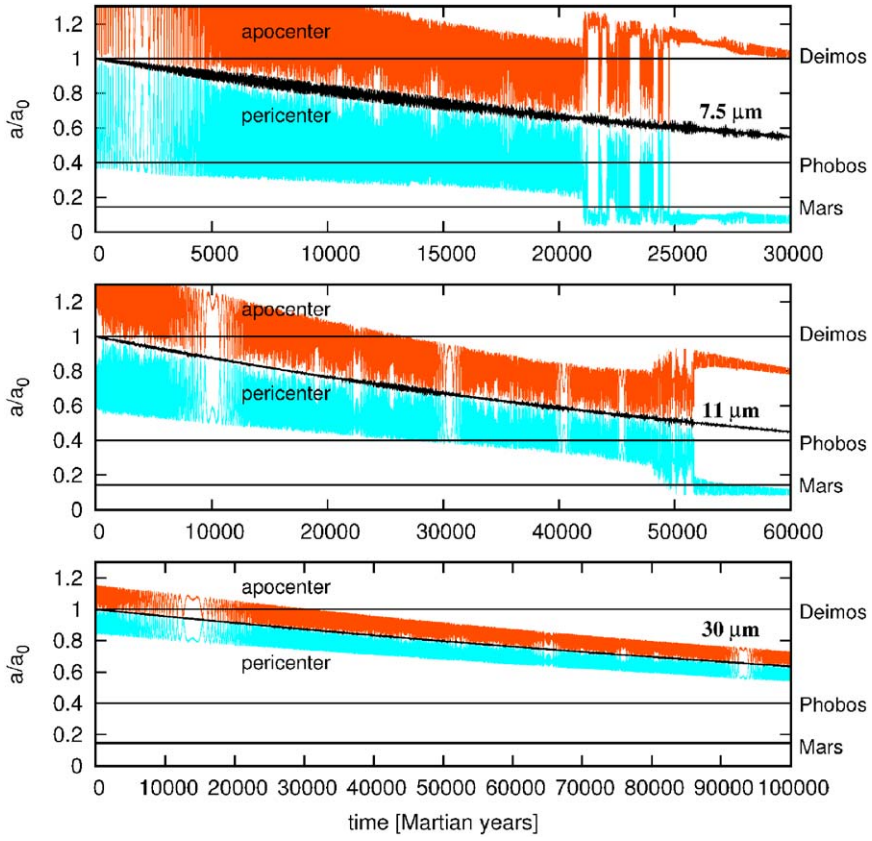


Fig. 8. Time evolution of instantaneous pericentric distance (light grey) and apocentric distance (dark grey) of Deimos particles with radii 7.5 μm (top), 11 μm (middle) and 30 μm (bottom). The distances are scaled to the semimajor axis of the Deimos orbit. Horizontal straight lines mark orbital radii of Deimos, Phobos and the surface of Mars.

same moment the pericentric distance shrinks to the size of the Phobos orbit; it is now Phobos that eliminates the particles. For larger particles, the latter event occurs later than the former. During some period of time, the whole orbit of a grain lies between the orbits of Phobos and Deimos, crossing neither of them. The larger the grain, the slower the PR evolution, the smaller the $e_{\max}$ and therefore the longer the time span when the particle safely orbits Mars between both satellites. Therefore, one would expect to find long-lived particles in this size regime.

To make quantitative estimates, we consider $e$-folding lifetimes against collisions with both moons—Phobos $T_{\rm p}$ and Deimos $T_{\rm d}$; each of them having an infinitely large value when the grain orbits do not intersect the orbit of the respective satellite. For each of the two moons, we can use Öpik's (1976) formula

$$T_{\rm moon} \approx \pi \sqrt{\sin^2 i + \sin^2 i_{\rm moon}} \left(\frac{a_{\rm moon}}{R_{\rm moon}}\right)^2 \left(\frac{u}{u_{\rm r}}\right) P, \qquad (21)$$

where $i$ is mean inclination of particle's orbit, $i_{\rm moon}$ is that of moon's orbit (both being measured from Mars' equatorial plane); $R_{\rm moon}$ and $a_{\rm moon}$ are the satellite radius and semimajor axis of its orbit; $u$ is the average grain velocity relative to the moon; $u_{\rm r}$ is the radial component of $u$ and $P$ is the orbital period of the particles. Further,

$$u = \sqrt{3 - \frac{1}{A} - 2\sqrt{A(1-e^2)}\cos i} \quad \text{and}$$
$$u_{\rm r} = \sqrt{2 - \frac{1}{A} - A(1-e^2)}, \qquad (22)$$

with $A \equiv a/a_{\rm moon}$ being the dimensionless semimajor axis of the particle orbit. The ratio $u/u_{\rm r}$ weakly depends on the orbital elements, including eccentricity and, for $A \approx 1$ and small $i$, is of the order of unity (Hamilton and Burns, 1994; Krivov and Hamilton, 1997).

The collisional lifetimes were then calculated as follows. As before, we numerically integrated Eqs. (6)–(11) over a sufficiently long interval for a considered particle size. Instantaneous values of the orbital elements $a$, $e$, $i$ were used in Eqs. (21)–(22) to compute separately $T_{\rm p}(t)$ and $T_{\rm d}(t)$. The collisional lifetime against collisions with both moons was then evaluated as $T_{\rm impact}^{-1} = T_{\rm p}^{-1} + T_{\rm d}^{-1}$. Because orbital elements entering Eqs. (21) and (22) change with time, $T_{\rm impact}$ will be a function of time as well. Thus, $T_{\rm impact}(t)$ has an "instantaneous" meaning: it is the lifetime one would

expect, if at the moment $t$ the particle's orbital elements $a(t)$, $e(t)$, $i(t)$ were "frozen". For the same grain sizes, we then calculated the fraction $f$ of surviving particles, as a function of time. This was done by simultaneously integrating, together with Eqs. (6)–(11), the differential equation

$$\frac{\mathrm{d}f(t)}{\mathrm{d}t} = -T^{-1}_{\mathrm{impact}}(t)f(t), \tag{23}$$

assuming $f(0) = 1$ as an initial condition. Fig. 9 depicts the results, which we can interprete with the aid of Fig. 8. Particles with radii below 11 μm are removed by both Deimos and Phobos, and so $f(t)$ decreases rapidly. Curves for larger particles contain flat portions, whose length increases with radius. Each "plateau" corresponds to a period when the entire orbit lies between the orbits of Deimos and Phobos. It drops when a particle becomes a Phobos-crosser.

With the function $f(t)$, it is easy to calculate a steady-state number of grains for each grain radius. Denoting by $N^+(s)$ the dust production rate from the Deimos surface in a unit size interval around $s$ and assuming $N^+(s)$ to be constant in time, we have

$$N_{\mathrm{ss}}(s) = N^+(s)\int_0^\infty f(s,t)\,\mathrm{d}t, \tag{24}$$

where we have added $s$ as an argument of $f$. The resulting curve for $N^+ \equiv 1$ (i.e. the integral in Eq. (24)) is plotted in Fig. 10, showing a strong maximum around $\approx 13$ μm. The position of the maximum results from a trade-off between two effects. On the one hand, starting from 11 μm, the duration of the "safe" stage of the particle evolution increases with its size. Accordingly, the "plateau" in Fig. 9 gets longer. On the other hand, a fraction of grains that are not removed by Deimos before they reach that stage decreases with radius—the level of the "plateau" in Fig. 9 gets smaller with particle's size.

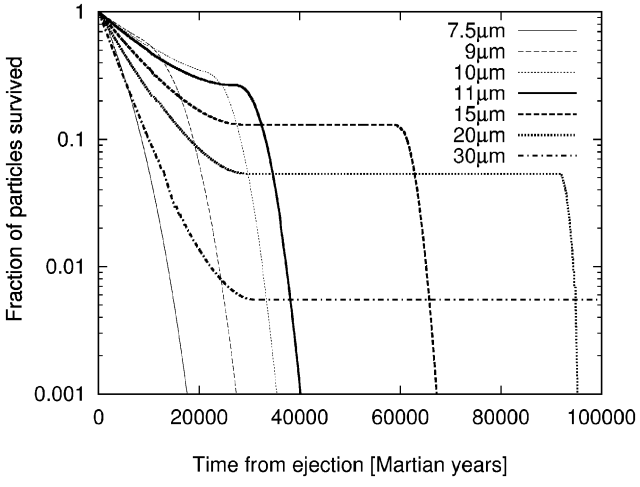


Fig. 9. Fraction of particles surviving collisions with Deimos and Phobos.

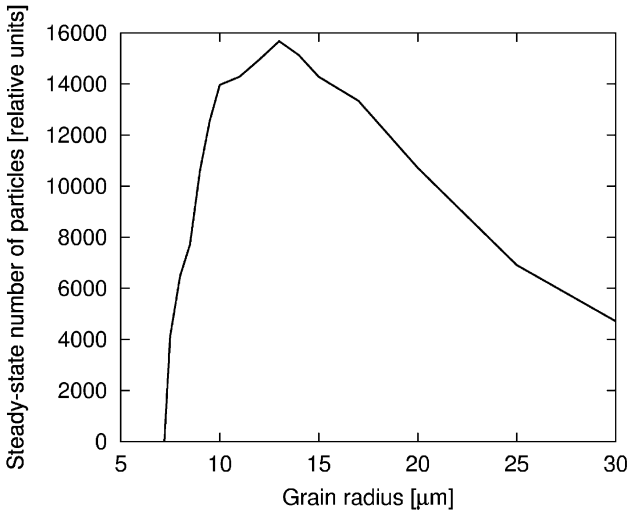


Fig. 10. Steady-state number of particles as a function of their size. The numbers are relative, assuming that the production rate per unit radius interval is the same for all radii. Absolute numbers can be obtained by multiplying the depicted function by the expected production rate as a function of size.

In reality, smaller particles must be produced at much higher rates than bigger ones, so that $N^+(s)$ is approximately a power law with the exponent close to $-3.5$ (Krivov and Hamilton, 1997). Multiplication of the integral by this distribution would give even sharper peak at nearly the same size. Thus, particles with $s \approx 10$–$15$ μm are expected to dominate the number density of the Deimos torus. One can show that they will dominate the cross section of dust in the torus as well. These particles, "hanging" in the region between the orbits of Deimos and Phobos, are large enough to pose serious threat for a spacecraft; see Section 4.2 for estimates. This should be kept in mind in space mission planning.

Note that $N^+$ is a dimensional quantity; in plotting $N_{\mathrm{ss}}$ in Fig. 10, we have set $N^+ = 1\,\mathrm{M.y.}^{-1}$. Therefore, the same curve can also be interpreted as a mean lifetime of different-sized particles in Martian years. The maximum corresponds to $\approx 16\,000$ M.y. This mean lifetime is not to be mixed with the maximum possible lifetime of the grains. Fig. 9 shows, for instance, that about 13% of 15 μm-sized grains stay in orbits for $\approx 6 \times 10^4$ M.y. and 5% of 20 μm-sized particles are lost only after $\approx 1 \times 10^5$ M.y.

### 4.2. Mutual collisions

We now look at possible loss mechanisms of grains other than impacts with Mars and its two moons. Sublimation and sputtering could be efficient for pure icy particles (Leinert and Grün, 1990), but are not important for the regolith grains. Lifetimes of 10 μm-sized particles against collisions with interplanetary grains are of the order of $10^6$ M.y. (Grün et al., 1985).

The only potentially important additional sink is mutual collisions of the torus particles.

As grains with $s \sim 10$–$15\,\mu m$ have much larger number densities in the Deimos torus than the others, these grains have the shortest collisional lifetime, and the latter is largely determined by their collisions with themselves. Thus, for the sake of simple estimates, we consider a "partial" Deimos torus, composed solely by particles in the size range $10\,\mu m \leqslant s \leqslant 15\,\mu m$. The lifetime against mutual collisions is

$$T_{coll} \approx (n\sigma v_{imp})^{-1}. \quad (25)$$

Here, $n$ is the number density of the particles, $v_{imp} \approx v_0\sqrt{e_{mean}^2 + i_{mean}^2}$ the mean relative velocity between them ($v_0$ is the Deimos orbital velocity), and $\sigma = 2\pi s^2$ the collisional cross section. The number density is approximately given by

$$n \approx N^+ T/V, \quad (26)$$

where now $N^+$ is the production rate of 10–15 μm dust from the surface, $T$ is the mean lifetime against both impacts with the moons and grain–grain collisions, and $V$ is the torus volume:

$$V \approx 8\pi a_0^3 e_{max} i_{max}, \quad (27)$$

with $a_0$ being the radius of the Deimos orbit, $e_{max}$ and $i_{max}$ typical amplitudes of oscillations of eccentricity and inclination. Eqs. (25)–(27) yield

$$T_{coll} \approx \frac{8\pi a_0^3 e_{max} i_{max}}{N^+ T \sigma v_{imp}}. \quad (28)$$

Taking into account an obvious relation $T^{-1} = T_{impact}^{-1} + T_{coll}^{-1}$, we find

$$\frac{1}{T} \approx \frac{1}{T_{impact}} + \frac{N^+ T \sigma v_{imp}}{8\pi a_0^3 e_{max} i_{max}}. \quad (29)$$

All quantities in Eq. (29) except for $N^+$ are determined by the dynamics. From the results of previous sections for $s \approx 10\,\mu m$, we take $e_{mean} \approx i_{mean} \approx 0.3$ rad (Figs. 4–5) to get $v_{imp} \approx 0.8\,km\,s^{-1}$, $e_{max} \approx i_{max} \approx 0.4$ rad, and $T_{impact} \approx 15\,000$ M.y. (Fig. 10). In contrast, $N^+$ is determined by the dust production mechanism from the satellite surface. Previous estimates (see e.g. Krivov and Hamilton, 1997) gave values $N^+ \sim 10^{6\pm1}\,s^{-1}$ for $10\,\mu m \leqslant s \leqslant 15\,\mu m$.

For any value of $N^+$, Eq. (29) can be solved for $T$, and accordingly $T_{coll}$ can be found from Eq. (28). We can also estimate the geometrical edge-on optical depth of the torus (Krivov and Hamilton, 1997)

$$\tau_{||} \approx \frac{N^+ T \sigma v_{imp}}{8 a_0^2 i_{max}}. \quad (30)$$

For a lower dust production rate $N^+ = 10^5\,s^{-1}$, mutual collisions are less important than impacts with the moons: we find $T_{coll} = 30\,000$ M.y., which is larger than $T_{impact} = 15\,000$ M.y. The "combined" lifetime is $T = 10\,000$ M.y., and $\tau_{||} \approx 2 \times 10^{-8}$. However, for a higher dust production rate $N^+ = 10^7\,s^{-1}$, $T_{coll}$ is much shorter than $T_{impact}$ : $T_{coll} = 1900$ M.y. In this case, $T = 1600$ M.y., and $\tau_{||} \approx 4 \times 10^{-7}$. Actual optical depth should be somewhat higher, due to contributions made by particles $s > 15\,\mu m$. Still, the expected optical depth is below the current observational limit $\tau_{||} < 10^{-6}$ (Showalter et al., 2001).

It is easy to estimate a meteoric hazard for a spacecraft. Assume it to orbit Mars within the Deimos torus. The dust flux, i.e. the number of impacts per unit area per unit time, is simply $nv_{imp}$. For $N^+ = 10^5$–$10^7\,s^{-1}$, one should expect $10^2$–$10^3$ impacts of 10 μm-sized grains per $1\,m^2$ during one orbital revolution around Mars.

We finally make one concluding remark. The dynamical effects considered in Section 3 are only possible because for particles with radii somewhat above $s_{crit}$ the lifetime against accretion by Deimos is comparable to the PR drift time. We have just found that the lifetime against mutual collisions is of the same order of magnitude, too! All this is a pure coincidence: were the size of the Deimos and Phobos orbits, or the size of Deimos itself, different from the actual values, that would no longer be true.

## 5. Structure of the Deimos torus

The same numerical integrations were used to construct snapshots of the Deimos torus. To this end, we simply converted instantaneous values of the osculating elements, complemented with a random value of the mean anomaly, into Cartesian coordinates.

The results are depicted in Fig. 11. It shows snapshots of the torus of 11 μm grains at two different time epochs: for 'young' particles soon after ejection (left panels) and for 'old' particles after $3 \times 10^4$ M.y. of the orbital evolution (right panels). In each case, the torus is shown in three different projections. All snapshots are constructed for one and the same Martian season (autumn equinox, $\lambda_\odot = 180^\circ$).

We see that long-term influence of perturbing forces results in a gradual change of the torus geometry with time. The following effects take place:

(1) A gradual contraction of the torus (Figs. 11a–c versus d–f);
(2) decrease of the torus displacement and azimuthal symmetrisation of the torus (Figs. 11a–b versus d–e);
(3) flattening of the torus (Figs. 11b–c versus e–f);
(4) decrease of the torus tilt (Fig. 11c versus f).

In the same figure, we overplot the snapshots of the Phobos torus of like-sized, 11 μm-particles. Both tori start to progressively overlap and the particles of Phobos

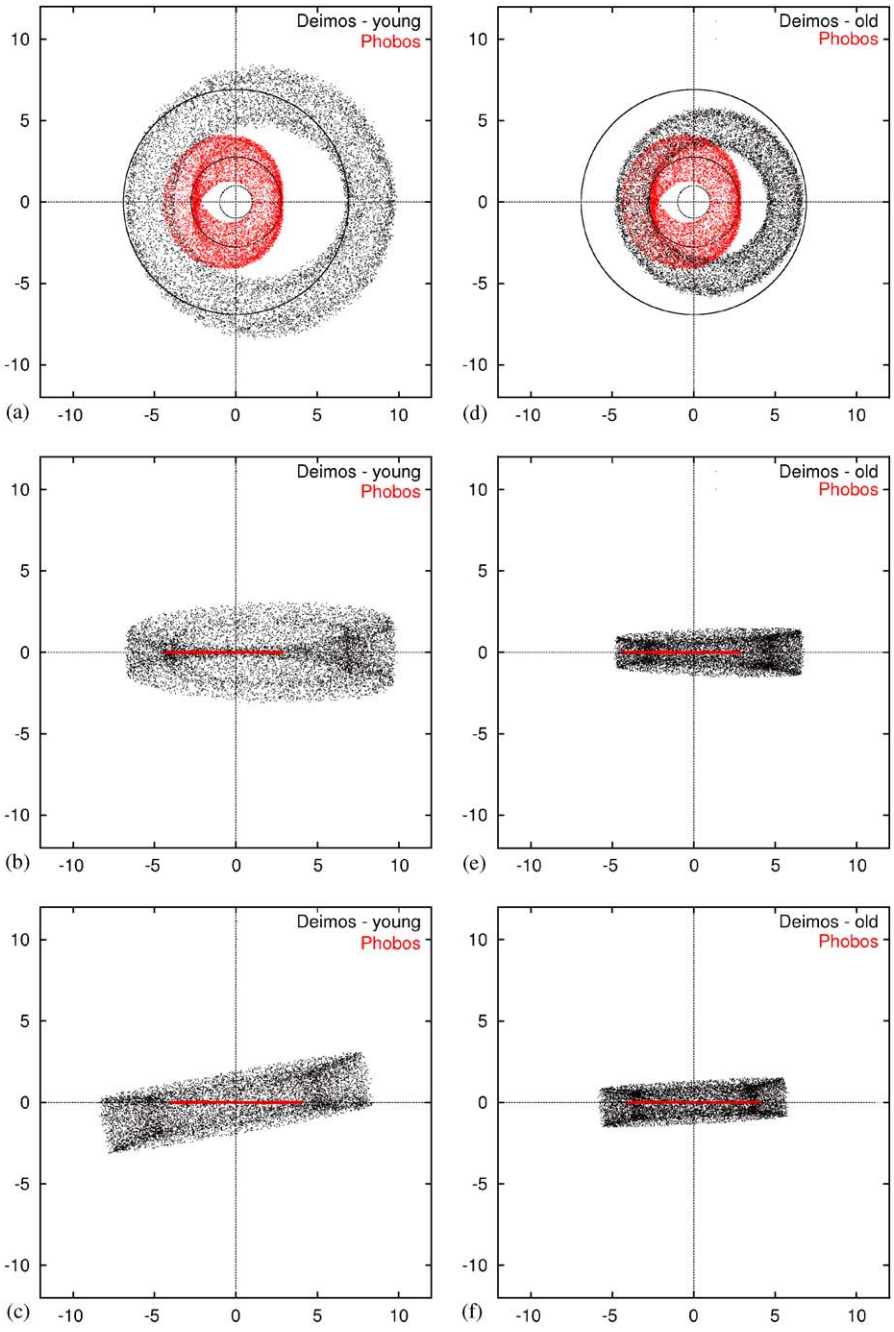


Fig. 11. Snapshots of the Deimos torus formed by 11 μm particles under the influence of the J2, RP and PR forces. Left: 'young' particles in the beginning of evolution; right: 'old' particles after $3 \times 10^4$ M.y. Top to bottom: $XY$, $XZ$, $YZ$ projections of the equatorial equinoctial coordinate system centred on Mars. All snapshots are given for the Martian autumn equinox (the Sun is on the negative $OX$ axis). Coordinates are in the units of Mars' radii $R_M$. The Phobos torus of like-sized particles is overplotted on all panels (inner thin ring-like configuration). In the upper panels, small inner circle represents Mars and two outer circles are the orbits of Phobos and Deimos.

and Deimos increasingly mix. After 50 000 M.y. (not shown in the figure), the azimuthal projections of both tori would become nearly indistinguishable. Still, the Deimos torus remains much thicker than the Phobos one, which is easy to explain. Although evolved Deimos particles acquire semimajor axes and eccentricities close to those of Phobos grains, the Deimos particles arrive at the "Phobos regime" with larger orbital inclinations of $\sim 10^\circ$ (see Fig. 4) than the Phobos grains have. In this sense, even in the "Phobos regime", the Deimos ejecta "remember" their dynamical history.

The scatter plots shown in each column of Fig. 11 represent instantaneous configuration of dust ejected at the same instant of time, 0 M.y. or 30 000 M.y. ago. They can be interpreted as a real configuration produced by an individual impact of a large meteorite onto the

Deimos surface. A "steady-state" Deimos torus sustained by a continuous flux of micrometeorites consists of particles that were injected into the system at different moments of time in the past. Therefore, snapshots like those depicted in Fig. 11 should be summed up with weights proportional to the absolute numbers of particles remaining in the system at the moment of observation. As the population of particles ejected simultaneously will be decaying with time, "older" populations will get lower weights than "younger" ones. We argue, however, that the resulting steady-state torus will bear clear signatures of the PR dynamics, being smaller in size, more symmetric, and more aligned to the equatorial plane than the "classical" torus predicted in earlier studies and shown in the left panels of Fig. 11.

## 6. Conclusions

In this paper, we have considered dynamics of dusty ejecta from Deimos under the combined action of three perturbing forces: solar RP, Mars' J2, and the PR force. Inclusion of the latter force into the model is new and is justified by long lifetimes of the Deimos grains, up to $\sim 10^5$ years. We have also provided better estimates of the lifetimes of different-sized Deimos ejecta and analysed spatial structure of the presumed Deimos torus. Our main conclusions are as follows:

1. The PR decay of the semimajor axes does not affect the oscillations of the orbital eccentricity, but causes an adiabatic decrease of amplitudes and periods of oscillations in orbital inclinations predicted in the framework of the underlying RP + J2 problem.

2. Smallest of the long-lived Deimos grains (radius $\approx 5$–$10\,\mu$m) may reach a chaotic regime, resulting in unpredictable and abrupt changes of their dynamics. Chaos is associated with the motion in the vicinity of a saddle separatrix of the underlying dynamical system.

3. The particles just above that size ($\approx 10$–$15\,\mu$m) are expected to dominate the Deimos torus. Impacts with both martian moons and mutual collisions can be equally important in limiting the lifetimes of these particles. Their PR drift and gradual changes in the dynamics should be reflected by the torus structure. In addition to a population, appreciably inclined and shifted towards the Sun, the torus should contain a more contracted, less asymmetric, and less tilted component interior to the orbit of Deimos.

## Acknowledgements

We thank Antal Juhász and an anonymous referee for useful and speedy reviews of this work. We are grateful to Miodrag Sremčević for sharing with us his skills in using the IDL and Mathematica® packages. Helpful discussions with James E. Howard are appreciated. This research was funded by Deutsche Forschungsgemeinschaft (DFG), project KR 2164/1-1. Part of the work was also supported by Deutsches Zentrum für Luft- und Raumfahrt (DLR), project 50 OH 0003.

## References

Burns, J.A., Lamy, P.L., Soter, S., 1979. Radiation forces on small particles in the Solar System. Icarus 40, 1–48.

Everhart, E., 1985. An efficient integrator that uses Gauss-Radau spacing. In: Carusi, A., Valsecchi, G.B. (Eds.), Dynamics of Comets: their Origin and Evolution. Dordrecht, Reidel, pp. 185–202.

Grün, E., Zook, H.A., Fechtig, H., Giese, R.H., 1985. Collisional balance of the meteoritic complex. Icarus 62, 244–272.

Hamilton, D.P., 1996. The asymmetric time-variable rings of Mars. Icarus 119, 153–172.

Hamilton, D.P., Burns, J.A., 1994. Origin of Saturn's E ring: self-sustained, naturally. Science 264, 550–553.

Hamilton, D.P., Krivov, A.V., 1996. Circumplanetary dust dynamics: effects of solar gravity, radiation pressure, planetary oblateness, and electromagnetism. Icarus 123, 503–523.

Horányi, M., Burns, J.A., Tátrallyay, M., Luhmann, J.G., 1990. Toward understanding the fate of dust lost from the Martian satellites. Geophys. Res. Lett. 17, 853–856.

Horányi, M., Tátrallyay, M., Juhász, A., Luhmann, J.G., 1991. The dynamics of submicron-sized dust particles lost from Phobos. J. Geophys. Res. 96, 11,283–11,290.

Howard, J.E., Krivov, A.V., Spahn, F., 2003. Transverse halo orbits about Mars? Geophys. Res. Lett. 30, No. 13.

Ishimoto, H., 1996. Formation of Phobos/Deimos dust rings. Icarus 122, 153–165.

Juhász, A., Horányi, M., 1995. Dust torus around Mars. J. Geophys. Res. 100, 3277–3284.

Kholshevnikov, K.V., Krivov, A.V., Sokolov, L.L., Titov, V.B., 1993. The dust torus around Phobos orbit. Icarus 105, 351–362.

Kimura, H., Ishimoto, H., Mukai, T., 1997. A study on solar dust ring formation based on fractal dust models. Astron. Astrophys. 326, 263–270.

Krivov, A.V., 1996. On the dust belts of Mars. Astron. Astrophys. 291, 657–663.

Krivov, A.V., Hamilton, D.P., 1997. Martian dust belts: waiting for discovery. Icarus 128, 335–353.

Krivov, A.V., Sokolov, L.L., Dikarev, V.V., 1996. Dynamics of Mars-orbiting dust: effects of light pressure and planetary oblateness. *Celestial Mechanics* Dynamical Astron. 63, 313–339.

Krivov, A.V., Kimura, H., Mann, I., 1998. Dynamics of dust near the Sun. Icarus 134, 311–327.

Leinert, C., Grün, E., 1990. Interplanetary dust. In: Schwenn, R., Marsch, E. (Eds.), Physics of the Inner Heliosphere. I. Large-Scale Phenomena. Springer, Berlin, pp. 207–275.

Öpik, E.J., 1976. Interplanetary Encounters: Close Range Gravitational Interactions. Elsevier, New York.

Showalter, M.R., Hamilton, D.P., Nicholson, P.D., 2001. A search for martian dust rings. Bull. Am. Astron. Soc. 33, 1095.

Soter, S., 1971. The dust belts of Mars. Report of Center for Radiophysics and Space Research, vol. 462.

# Appendix B

# Stochastic Circumplanetary Dynamics of Rotating Non-spherical Dust Particles

MAKUCH M., BRILLIANTOV N. V., SREMČEVIĆ, M., SPAHN, F., KRIVOV, A. V. (2006).
Stochastic Circumplanetary Dynamics of Rotating Non-spherical Dust Particles. **Planetary and Space Science**, 54:855-870.

Available online at www.sciencedirect.com
SCIENCE DIRECT
Planetary and Space Science 54 (2006) 855–870
Planetary and Space Science
www.elsevier.com/locate/pss

# Stochastic circumplanetary dynamics of rotating non-spherical dust particles

Martin Makuch[a,*], Nikolai V. Brilliantov[a], Miodrag Sremčević[b], Frank Spahn[a], Alexander V. Krivov[c]

[a]Institute of Physics, University of Potsdam, Am Neuen Palais 10, Bldg. 19, 14469 Potsdam, Germany
[b]Laboratory of Atmospheric and Space Physics, University of Colorado, Boulder, USA
[c]Astrophysical Institute and University Observatory, Friedrich Schiller University, Jena, Germany

Received 22 November 2005; accepted 4 May 2006
Available online 11 July 2006

**Abstract**

We develop a model of stochastic radiation pressure for rotating non-spherical particles and apply the model to circumplanetary dynamics of dust grains. The stochastic properties of the radiation pressure are related to the ensemble-averaged characteristics of the rotating particles, which are given in terms of the rotational time-correlation function of a grain. We investigate the model analytically and show that an ensemble of particle trajectories demonstrates a diffusion-like behaviour. The analytical results are compared with numerical simulations, performed for the motion of the dusty ejecta from Deimos in orbit around Mars. We find that the theoretical predictions are in a good agreement with the simulation results. The agreement however deteriorates at later time, when the impact of non-linear terms, neglected in the analytic approach, becomes significant. Our results indicate that the stochastic modulation of the radiation pressure can play an important role in the circumplanetary dynamics of dust and may in case of some dusty systems noticeably alter an optical depth.


*PACS:* 96.30.Gc; 94.10.Nh; 02.50.Ey; 96.30.Wr

*Keywords:* Mars; Deimos; Ejecta; Stochastics; Radiation pressure

## 1. Introduction

Dust belts and rings formed by small dust grains orbiting planets are an important component of the solar system. Examples are the E-ring of Saturn, inner dust rings of Jupiter (Burns et al., 1984), tenuous dust rings between the orbits of Jovian satellites Europe, Ganymede and Callisto (Krivov et al., 2002), dust bands of Uranus (Esposito et al., 1991). It is also expected that ejecta from Phobos and Deimos give rise to the dust belts of Mars, whose existence is not yet confirmed (Krivov et al., 2006).

For the dust particles, whose size ranges from approximately 0.01–100 μm, many non-gravitational perturbations, such as direct radiation pressure (e.g. Burns et al., 1979), Lorentz force (Horányi et al., 1991), Poynting–Robertson force (e.g. Makuch et al., 2005) or plasma drag (e.g. Dikarev, 1999) may play a key role in determining their dynamics. Due to the physical nature of these forces they necessarily contain not only an average deterministic component, but also a stochastic component, which may be of different origin. The influence of the stochastic part of the Lorenz force due to the fluctuating magnetic field has been studied in detail by Spahn et al. (2003). Here, we address the stochastic component of the radiation pressure caused by spinning of non-spherical particles. If a non-spherical particle changes its orientation in space, its cross-section with respect to the impinging solar radiation varies accordingly. This causes a variation of the radiation pressure, i.e. a time modulation of the force acting on the particle. For an ensemble of dust particles the modulated force may be represented as a sum of a deterministic mean

*Corresponding author. Tel.: +49 331 9771390; fax: +49 331 9771142.
*E-mail address:* makuch@agnld.uni-potsdam.de (M. Makuch).

0032-0633/$ - see front matter © 2006 Elsevier Ltd. All rights reserved.
doi:10.1016/j.pss.2006.05.006

force and a fluctuating random force. Knowing the properties of this stochastic force one can analyse how it influences the particle dynamics.

In the present study we develop a model of the stochastic radiation pressure due to the rotational motion of non-spherical grains and analyse its impact on the circumplanetary motion. We elaborate an analytical approach for the general case and perform numerical simulations for the particular case of the circum-Martian dynamics of dust particles. The latter seems to be one of the most promising application of the new approach, since the previous theories, based on the deterministic models failed to explain the negative result of the current attempts to detect the Martian dust tori.

The paper is organized as follows. In Section 2 the general equation of motion is formulated and the necessary notations are introduced. In Section 3 we address the role of particle rotation, formulate the stochastic radiation pressure model, and implement it into the equation of motion. In this section we also present a simplified analytical analysis of the circumplanetary stochastic motion. In Section 4 an extended analytical solution to this problem is given. Section 5 applies the general theory to the circum-Martian dust dynamics. We perform comprehensive numerical investigations and compare the simulation results with the theoretical predictions. In Section 6 we summarize our findings. Some computation details are given in the Appendix.

## 2. Equation of motion

In order to model the circumplanetary particle dynamics it is necessary to consider a set of different forces. The impact of planetary oblateness, the deterministic part of direct radiation pressure, and Poynting–Robertson drag has been studied in context of circum-Martian motion by Makuch et al. (2005). Here, however, we focus on the stochastic perturbation of the radiation pressure due to rotation of non-spherical particles. Generally, the equation of motion of a dust particle, for the set of perturbations addressed here, may be written as follows:

$$m\ddot{\vec{r}} = -mGM\nabla\left(\frac{1}{r}+\frac{R^2}{r^3}J_2P_2(\vec{r})\right)+BS_r\vec{e}_\odot. \quad (1)$$

The first term on the right-hand side represents the gravity of an oblate planet (e.g. Mars) and the second one direct radiation pressure. Here, $r$ denotes the radius vector of the particle in planetocentric coordinates, $M$ and $R$ mass and equatorial radius of the planet and $m$ is the mass of the dust grain. $J_2$ is the oblateness coefficient ($J_2 = 1.96\times10^{-3}$ for Mars) and $P_2(\vec{r})$ is the Legendre's polynomial. Factor $B = (Q_{\rm pr}/c)F_\odot(\mathrm{AU}/a_{\rm plan})^2$ characterizes the strength of radiation pressure with the constant $Q_{\rm pr}$ being the radiation pressure efficiency and with the solar energy flux $F_\odot$ at the Earth distance ($F_\odot = 1.36\times10^3\,\mathrm{J\,m^{-2}\,s^{-1}}$) scaled to the distance of the planet $a_{\rm plan}$ by the ratio $(\mathrm{AU}/a_{\rm plan})^2$, $c$ is the speed of light and $S_r = \pi s^2$ the particle cross-section (see e.g. Krivov et al., 1996; Krivov and Jurewicz, 1999). The unit vector $\vec{e}_\odot$ points radially outward from the Sun.

In the numerical analysis of the particle dynamics we directly apply Eq. (1) in its Newtonian form, that is, in the Cartesian coordinates. In this case the Everhart's (1985) method with a constant time step has been employed. A detailed description of the numerical implementation will be given in Section 5.

As shown in the subsequent sections, the perturbation force in Eq. (5) is the stochastic force. Hence the above equation is a stochastic differential equation, which requires a special numerical treatment, discussed in detail in Section 5. In particular, a constant time step is necessary. This significantly reduces the efficiency of the numerical scheme and makes the simulations very time-consuming.

## 3. Stochastic model for the radiation pressure

### 3.1. Fluctuations of radiation pressure due to rotation of non-spherical particles

To describe the dynamics of dust grains a simplified assumption about the particles' shape is usually adopted. Particles are assumed to be spheres of radius $s$ with a unique and constant cross-section $S_r$. However, as it was deduced from the measurements of interplanetary dust, collected in the Earth's stratosphere, "real" grains may be far from being spherical. Particles have a complicated morphology and may be hardly characterized by only one parameter $s$. Moreover, they continuously spin. Therefore, the particle's cross-section exposed to the solar radiation permanently alters with time. This causes fluctuations of the radiation pressure and thus affects the dynamics of the grains.

To analyse directly the influence of the fluctuating radiation pressure we use equations of motion taking into account a time-dependent particle cross-section $S_r(t)$. Function $S_r(t)$ describes the cross-section. It is obtained by projecting the body boundaries onto a plane perpendicular to the direction of the solar radiation. As already mentioned, the time dependence of the cross-section stems from the non-sphericity of particles and their permanent spinning. Henceforth, we will treat Eq. (1) with time-dependent $S_r(t)$ as an equation, which describes an ensemble of spinning particles with different angular velocities and orientations. This means that we will treat Eq. (1) as a stochastic differential equation. The properties of the stochastic radiation pressure force are determined by the corresponding properties of the fluctuating variable $S_r(t)$. We assume that the rotation of the grains around their centre of mass is not affected by the orbital motion.

Hence we can represent the radiation pressure as a sum of a deterministic part, related to the average cross-section $\langle S_r\rangle$, and a stochastic part fluctuating around its mean according to $\zeta(t) = S_r(t) - \langle S_r\rangle$. Thus, we write the radiation pressure force as

$$\vec{F}_{\rm rp} = F_{\rm rp}\vec{e}_\odot = B\langle S_r\rangle\vec{e}_\odot + B\zeta(t)\vec{e}_\odot, \quad \langle\zeta(t)\rangle = 0. \quad (2)$$

Here we assume that the radiation pressure force acts only in the radial direction defined by $\vec{e}_\odot$ and neglect the contribution of non-radial components. We also assume that the variable $\zeta(t)$ may be treated as a stationary stochastic process with the time-correlation function

$$K(t',t) = \langle \zeta(t)\zeta(t') \rangle = K(|t'-t|) \tag{3}$$

depending on the modulus of the time difference (see e.g. Resibois and de Leener, 1977; Brilliantov and Revokatov, 1996). Physically, $K(t)$ characterizes the memory of the initial orientation of a particle. Naturally, it decays as time grows. This function has a maximum at $t=0$, which, according to the definition of $\zeta(t)$ reads

$$K(0) = \langle \zeta(t)^2 \rangle = \langle S_r^2 \rangle - \langle S_r \rangle^2. \tag{4}$$

With increasing time difference $|t'-t|$, the fluctuations $\zeta(t)$ and $\zeta(t')$ become almost uncorrelated and $K(|t'-t|)$ decays to zero, that is, $K(t\to\infty)=0$. If the rotation frequency of the grains is very fast on the timescale of the orbital motion, the simplest model of $\delta$-correlated white noise may be adopted (Spahn et al., 2003). This already reflects the most prominent properties of the stochastic dynamics.

Since $\zeta(t)$ is determined by the grain orientation, the function $K(t)$ is directly related to the time-correlation function of the particle orientation. Choosing a model of orientational motion, $K(t)$ may be evaluated. The simplest orientation model is a free-rotation model, where the angular momentum of a grain is conserved (Brilliantov and Revokatov, 1996; Pierre and Steele, 1969). A grain can change its angular momentum in several processes—due to collisions with gas atoms or cosmic ray particles, by adsorption/emission of photons, and adsorption/ejection of atoms (Purcell, 1979). The adsorption/emission of photons is related to the Yarkovsky effect (e.g. Spitale and Greenberg, 2001; Skoglov, 2002; Vokrouhlicky and Capek, 2002), while the adsorption/ejection of atoms refers to the so-called photophoresis (e.g. Krauss and Wurm, 2005).

The influence of the direct Yarkovsky effect is negligible, since the temperature gradient, responsible for the effect cannot noticeably develop for quickly rotating and relatively small grains. The reflection/adsorbtion of the solar radiation by the irregular shaped particle may, in principle, cause a random torque (e.g. Vokrouhlicky and Capek, 2002). However, it is expected that this effect could be noticeable only for large and slowly rotating bodies and is negligible for small grains performing a fast rotation. For the typical case of Martian tori, the properties of the near-Martian interplanetary space (Roatsch, 1988) imply that one can neglect collisions with a dilute gas or cosmic rays particles and correspondingly also the effect of photophoresis. We assume that these effects may be also neglected for the other systems addressed in our study. Finally, a torque may arise if a charged grain rotates in a magnetic field (Purcell, 1979). Using the expected angular velocity of grains, $\sim 10^{-1}-10^{3}$ Hz (see the estimates below) and the charge of the particles (Juhász and Horányi, 1995) together with the magnitude of the magnetic field (Juhász and Horányi, 1995), the corresponding torques can be found. Simple estimates then show that particles of the typical size of $\sim 10\,\mu$m subjected to this torque perform a precession with the precession frequency $\sim 10^{-11}-10^{-8}$ Hz when the magnetic field strength corresponds to the Martian or Saturnian environment. Therefore, in what follows we neglect for simplicity this slow precession.

Based on the above analysis we adopt here the free-rotators model for the dust particles. Hence, we treat the system of grains as an ensemble of freely rotating grains with randomly distributed angular momenta. Calculations of the time-correlation function $K(t)$ for this model are rather technical and we therefore present here only the qualitative analysis. Some additional discussion is given in Appendix A.

In order to formulate the model we adopt the following assumptions: First, we assume that particles are symmetric tops with two characteristic lengths, $L_\parallel$, which is parallel to the symmetry axis and $L_\perp$, which is perpendicular to that axis. Second, for an angular velocity distribution of the grains we adopt Gaussian distribution with the characteristic velocity $\Omega_0$ (see Appendix A for more detail). Then the analysis shows that the time-correlation function $K(t)$ depends on time only through the product $\Omega_0 t$, i.e. it may be written as $K(t) = K(0)k(\Omega_0 t)$, where $k(x)$ is a dimensionless function of the dimensionless argument. This result follows also from the dimension reasoning. Third, we consider particles of a simplified form—the figures of rotation. These are obtained by spinning the rectangle of size $2L \times 2l$, with two adjoined semicircles of radius $l<L$ (Fig. 1). Rotating this figure around the axis which passes through its centre and directed along the larger, $2L$-side of the rectangle, yields a *prolate* sphero-cylinder with $L_\parallel = 2L+2l$ and $L_\perp = 2l$. Rotation around the axis that passes through its centre and directed along the shorter $2l$-side yields an *oblate*, disc-shaped particle, with $L_\parallel = 2l$ and $L_\perp = 2L+2l$. Using these models for the particle shapes drastically simplifies the analysis, still reflecting their basic characteristics.

As it will be shown below, the characteristic time of the orbital motion of the dust particles (the orbital period) is much larger than the correlation time of the stochastic variable $\zeta$, estimated as $\sim 1/\Omega_0$. In other words, on the timescale of orbital motion, the grains immediately loose their memory about the previous orientation. Mathematically, this statement formulated as an approximation reads

$$K(t) \simeq 2K_0\delta(t), \tag{5}$$

which holds with a high accuracy. Hence, we approximate the fluctuating variable $\zeta(t)$ by a $\delta$-correlated (white) noise with an amplitude $\sqrt{2K_0}$. The constant $K_0$ may be derived from the relation

$$\begin{aligned} K_0 &= \int_0^\infty K(t)\,\mathrm{d}t = K(0)\int_0^\infty k(\Omega_0 t)\,\mathrm{d}t \\ &= K(0)\Omega_0^{-1}A = K(0)\left(\frac{\Omega_0}{A}\right)^{-1}, \end{aligned} \tag{6}$$

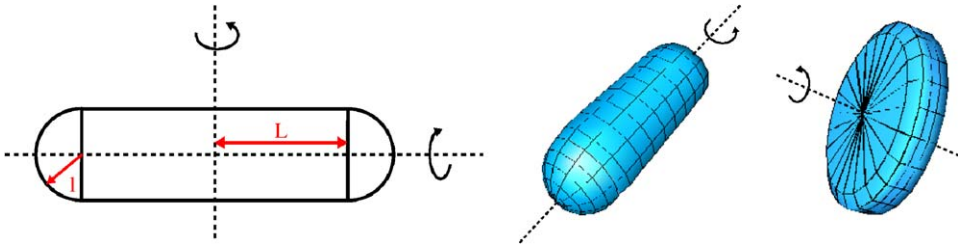


Fig. 1. The particles are assumed to be figures of rotation: middle—prolate particles with $L_{\parallel} = 2L + 2l$ and $L_{\perp} = 2l$, right—oblate particles, with $L_{\parallel} = 2l$ and $L_{\perp} = 2L + 2l$. In both cases, the aspect ratio is equal to $\alpha = L/l$.

where the property of the $\delta$-function and the definition of the dimensionless function $k$ is used. As it is shown in Appendix A, the constant $A$ in Eq. (6) is of the order of unity. Since the rotation frequency $\Omega_0$ is not experimentally known and may be estimated only with a large uncertainty, it suffices to apply the simplifying assumption, $A = 1$. Alternatively, the parameter $\Omega_0$ in what follows may be treated as the ratio $\Omega_0/A$, since as it is seen from Eq. (6), the value of $K_0$ depends only on this ratio.

With the above assumptions we arrive at the following stochastic model for the radiation pressure force:

$$\vec{F}_{\rm rp} = F_{\rm rp}\vec{e}_{\odot} = B\langle S_r\rangle\vec{e}_{\odot} + B\sqrt{2K_0}\,\xi(t)\vec{e}_{\odot}, \tag{7}$$

where $\xi(t)$ denotes white noise with zero mean and unit dispersion

$$\langle\xi(t)\rangle = 0, \quad \langle\xi(t_1)\xi(t_2)\rangle = \delta(t_1 - t_2). \tag{8}$$

In order to proceed either analytically or numerically we need to find the quantities $K_0$ and $\Omega_0$, which will be done in next section.

### 3.2. Basic parameters of the grain's orientational time-correlation function

#### 3.2.1. Amplitude of the time-correlation function

For *prolate* particles the projection area on the plane perpendicular to the solar radiation depends on the angle $\theta(t)$ between the symmetry axis of a particle and the direction of the radiation as

$$S_r(t) = 4Ll\sin\theta(t) + \pi l^2, \tag{9}$$

so that the mean-square average value of this quantity reads,

$$\langle S_r(t)^2\rangle = 16L^2l^2\langle\sin^2\theta(t)\rangle + 8\pi Ll^3\langle\sin\theta(t)\rangle + \pi^2l^4. \tag{10}$$

For free rotators, the distribution of the particle axes in space is assumed to be spherically symmetric, giving

$$\langle\sin\theta(t)\rangle = \frac{\pi}{4}, \quad \langle\sin^2\theta(t)\rangle = \frac{2}{3}, \tag{11}$$

and finally

$$K(0) = \langle S_r^2\rangle - \langle S_r\rangle^2 = L^2l^2(\tfrac{32}{3} - \pi^2) = 0.7971L^2l^2. \tag{12}$$

For *oblate* particles similar calculations may be performed. Introducing the aspect ratio, $\alpha = L/l + 1$, as the ratio of maximal to minimal size of the particle, we write the expressions for $K_0$ and $\langle S_r\rangle$ for both types of particles in a compact form

$$\langle S_r\rangle = \pi l^2\begin{cases}\alpha & \text{prolate particles,}\\ \dfrac{\alpha(\alpha+1)}{2} & \text{oblate particles,}\end{cases} \tag{13}$$

and

$$K_0 = l^4\Omega_0^{-1}\begin{cases}0.7971(\alpha-1)^2 & \text{prolate particles,}\\ 0.8224\alpha^2(\alpha-1)^2 & \text{oblate particles.}\end{cases} \tag{14}$$

#### 3.2.2. Characteristic rotation frequency

We assume that the system of dust particles is very rarified, so that the collisions between grains or collisions of the grains with other particles, such as gas molecules, ions, etc. are extremely rare and cannot support any "thermal" distribution of the angular velocity in an ensemble of rotating grains. Hence the rotation frequency of the grains is determined by the mechanisms of their creation. There could be several mechanisms, among which the impact-ejecta one is the most important.

According to the presently accepted theoretical model of the impact-ejecta process, the hypervelocity impacts of interplanetary dust particles cause an ejection of secondary material. The total mass of ejected grains is several orders of magnitude higher than the mass of impactors. The velocities of ejecta are of the order of, or higher than, the escape velocity of the parent bodies (approximately $1-10\,\mathrm{m/s}$). The tiny grains which successfully leave the action sphere of the parent bodies finally create dust complexes surrounding the bodies or their orbits.

When a fast particle (micrometeoroid) collides with a surface of a satellite it creates a crater on the surface of diameter $D_{\rm crat}$. All the material of the surface initially located in the crater is crashed into small pieces which are ejected into space with the characteristic velocity $v_{\rm ej}$. Estimates of the angular velocity of the ejected particles may be performed for the case of a rocky surface (Brilliantov et al., 2006), which yields the following result:

$$\Omega_0 \sim \frac{v_{\rm ej}}{D_{\rm crat}}. \tag{15}$$

Using $v_{\rm ej} = 5\,\mathrm{m/s}$ for a typical ejection velocity and $D_{\rm crat} = 20\times10^{-4}\,\mathrm{m}$, for a typical crater diameter we

estimate the characteristic frequency as $\Omega_0 \approx 5 \times 10^3\,\mathrm{s}^{-1}$. The corresponding timescale of the rotation motion, ($\Omega_0^{-1} \approx 10^{-3}$ s) is much smaller than the orbital timescale which is of the order of $\sim 10^5$ s, if one uses the ejection from Deimos as an example. This justifies the application of the simple model of $\delta$-correlated white noise.

Another possible mechanism of particle creation may be the eruption of dust due to volcanic (or cryovolcanic) activity at some celestial bodies. One can mention the Jupiter satellite Io as an example. The eruption of dust is accompanied by that of a gas (sulphur, in the case of Io). One can assume that during the eruption the dust grains are in a transient thermal equilibrium with the gas. They decouple however from the gas after escaping from the body into space. In this case the angular velocity of the grains is determined by the temperature of the gas:

$$\Omega_0 \sim \sqrt{\frac{k_\mathrm{B} T}{I}}, \tag{16}$$

where $k_\mathrm{B}$ is the Boltzmann constant, $T$ is the temperature of the gas and $I$ is the characteristic moment of inertia of a grain. Assuming that the temperature of the gas ranges from $10^2$ to $10^3$ K (the temperature in the eruption zone of Io is estimated as 1800 K) we obtain that $\Omega_0$ varies in the interval 1–4 Hz for particles of size $\sim 10\,\mu$m and density $2.37 \times 10^3\,\mathrm{kg/m^3}$. This value of the angular velocity satisfies the requirement of fast rotation, which makes the application of the white noise model valid.

### 3.3. Role of stochasticity in the dust dynamics: simplified analysis

Before starting comprehensive analytical or numerical study of the impact of the stochastic radiation pressure on the circumplanetary dynamics, it is worth to perform simplified analysis, choosing a simple model.

Consider a particle moving around a planet on a circular orbit with zero inclination. The perturbation equation for the semimajor axis $a$ reads (e.g. Burns, 1976):

$$\frac{\mathrm{d}a}{\mathrm{d}t} = \frac{2a^2}{GM}\frac{\dot{E}}{m}. \tag{17}$$

Here the constants $G$, $m$ and $M$ have been defined previously, and $\dot{E}$ denotes the rate of change of the particle energy due to the perturbation of the radiation pressure force. Using Eq. (2) we write

$$\dot{E} = \vec{F}_\mathrm{rp} \cdot \vec{v} = F_\mathrm{rp}(\vec{v} \cdot \vec{e}_\odot), \tag{18}$$

where $\vec{v}$ is the velocity of the particle, which is on the circular orbit constant. That is $v = na$, with $n = \sqrt{MG/a^3}$ being the mean orbital motion of the particle. Moreover, choosing the direction to the Sun, $\vec{e}_\odot$ along the $x$-axis, we write

$$\vec{v} \cdot \vec{e}_\odot = v_x = -v \sin nt = -na \sin nt. \tag{19}$$

Hence, we obtain,

$$\frac{\mathrm{d}a}{\mathrm{d}t} = -\frac{2}{mn^2 a} F_\mathrm{rp} na \sin nt \simeq -\frac{2}{mn_0} F_\mathrm{rp} \sin n_0 t, \tag{20}$$

where in the last equation we for simplicity approximate the mean motion $n$ by its initial value $n_0$. The solution to Eq. (20) may be written as

$$a(t) = a_0 - \int_0^t \frac{2}{mn_0} F_\mathrm{rp}(t') \sin n_0 t'\,\mathrm{d}t', \tag{21}$$

where $a_0$ is the initial value of the semimajor axis and $F_\mathrm{rp}(t)$ depends on time via the stochastic component $B\sqrt{2K_0}\xi(t)$, see Eq. (2). The ensemble average of $a$ then reads

$$\langle a \rangle = a_0 - \int_0^t \frac{2}{mn_0} \langle F_\mathrm{rp}(t') \rangle \sin n_0 t', \tag{22}$$

which implies the following time-dependent fluctuation of this orbital element:

$$\begin{aligned} \delta a(t) = a(t) - \langle a \rangle &= -\int_0^t \frac{2}{mn_0} [F_\mathrm{rp} - \langle F_\mathrm{rp} \rangle] \sin n_0 t'\,\mathrm{d}t' \\ &= -\int_0^t \frac{2}{mn_0} B\sqrt{2K_0}\xi(t') \sin n_0 t'\,\mathrm{d}t'. \end{aligned} \tag{23}$$

In Eq. (23) we use (2) and take into account that $\langle F_\mathrm{rp} \rangle = B\langle S_r \rangle$. Correspondingly, the reduced standard deviation of the element depends on time as

$$\begin{aligned} \frac{\langle (\delta a)^2 \rangle}{a_0^2} &= \frac{8B^2K_0}{m^2 n_0^2 a_0^2} \int_0^t \mathrm{d}t' \int_0^t \mathrm{d}t'' \langle \xi(t')\xi(t'') \rangle \sin n_0 t' \sin n_0 t'' \\ &= \frac{8B^2K_0}{m^2 n_0^2 a_0^2} \int_0^t \sin^2 n_0 t'\,\mathrm{d}t' \\ &= \frac{4B^2K_0}{m^2 n_0^2 a_0^2} \left( t + \frac{1}{2n_0} \cos 2n_0 t \right), \end{aligned} \tag{24}$$

where we take into account the property of the white noise, $\langle \xi(t')\xi(t'') \rangle = \delta(t' - t'')$. For the time addressed here, $n_0 t \gg 1$, which corresponds to many rotation periods of the particle around the planet, one can neglect the oscillating terms in the last equation, which yields the diffusion-like equation for the standard deviation,

$$\frac{\langle (\delta a)^2 \rangle}{a_0^2} = Dt \tag{25}$$

with the effective "diffusion coefficient"

$$\begin{aligned} D &= \frac{4B^2K_0}{m^2 n_0^2 a_0^2} \\ &= \frac{4B^2 l^4}{m^2 \Omega_0} \frac{a_0}{GM} \begin{cases} 0.7971(\alpha - 1)^2 & \text{prolate particles,} \\ 0.8224\alpha^2(\alpha - 1)^2 & \text{oblate particles,} \end{cases} \end{aligned} \tag{26}$$

where Eq. (14) for $K_0$ has been used. As it follows from Eqs. (25) and (26) the standard deviation of the semimajor axis for an ensemble of particles grows with time. The rate of its growth strongly depends on the particle's size $l$ and the aspect ratio $\alpha$. It is also interesting to note that $D$ depends inversely on the average

rotation frequency $\Omega_0$, that is, the diffusion coefficient is smaller if particles rotate fast. Another important feature of the above relation is the dependence on the semimajor axis $a_0$ and the planet mass $M$. For particles orbiting around a light planet (small $M$) on an extended orbit (large $a_0$) the diffusion coefficient may be very large.

Let us make some estimates for this quantity for an oblate grain orbiting Mars on the Deimos or Phobos orbit. For better comparison with previous studies we define an effective radius ($s_{\rm eff}$) of spherical grain with the cross-section equal to $\langle S_r\rangle$ of an *oblate* particle. Denoting the minimal particle radius $l$ as $s_{\min}$ we obtain the relation $s_{\rm eff}=s_{\min}\sqrt{\alpha(\alpha+1)/2}$. Correspondingly the mass of a particle is $m=\rho_g\pi s_{\min}^3(2\alpha^2+\pi\alpha)$, where $\rho_g=2.37\times 10^3\,{\rm kg/m^3}$ is the bulk density of the grain. For the aspect ratio of particles we choose $\alpha=5$ and the radiation pressure efficiency $Q_{\rm pr}$ is calculated in the same manner as described in Section 5.

Referring for the discussion of the astrophysical relevance to Section 5, we obtain for a grain with $s_{\rm eff}=0.5\,\mu{\rm m}$ rotating with the angular velocity 0.01 Hz the diffusion coefficient $D=3.31\times 10^{-11}\,{\rm s^{-1}}$ for Deimos ejecta and $D=1.32\times 10^{-11}\,{\rm s^{-1}}$ for Phobos one. With this diffusion coefficient the standard deviation of the semi-major axis increases up to 14% of its initial value during 10 Martian years (8.8% for Phobos). For astrophysically more relevant time interval corresponding to mean particle lifetime of one Martian year we get change of 4.4% (2.8% for Phobos). Similarly, for particles with size $s_{\rm eff}=10\,\mu{\rm m}$ rotating with the same frequency from the longest-living Martian population, the diffusion coefficient is $D=1.99\times 10^{-14}\,{\rm s^{-1}}$. This corresponds to the increase of the standard deviation up to 11% during 10 000 Martian years.

The more rigorous analysis given in Section 4 yields essentially the same order-of-magnitude values for the diffusion coefficient.[1]

## 4. Analytical solution for the stochastic equation of motion

The goal of this section is to analytically estimate effects of the stochastic radiation pressure using linear analysis of the perturbation equations. To this aim we will first introduce a non-singular orbital elements and dimensionless parameters that characterize the strength of radiation pressure and oblateness. Then we proceed calculating the distribution functions, mean and variances of eccentricity, inclination and semimajor axis of ejected particles. The employed calculations are rather technical, and an example of calculations for the case of eccentricity is presented in Appendix B.

[1]In Section 4 we use the dimensionless time $\lambda=n_\odot t$, where $n_\odot$ is the mean motion of the planet, and, respectively, the dimensionless diffusion coefficient $\Lambda$. Hence, the diffusion coefficient $D$ of Section 3 is to be compared with $\Lambda n_\odot$.

### 4.1. Orbital elements and force parameters

Following Krivov et al. (1996), we introduce the non-singular orbital elements

$$h=e\cos\tilde\omega,\quad k=e\sin\tilde\omega,\quad p=\sin i\cos\Omega,\quad q=\sin i\sin\Omega, \tag{27}$$

where $\tilde\omega\equiv\Omega+g$ is the longitude of pericentre and $e,i,\Omega$, and $g$ are eccentricity, inclination, longitude of the node, and the argument of the pericentre, respectively (see Appendix B). As an independent variable, we use the longitude of the Sun $\lambda$ leading to dimensionless equations of motion. Neglecting the eccentricity of the planet orbit, $\lambda$ is a linear function of time

$$\lambda=\lambda_{\odot 0}+n_\odot t,\quad n_\odot=\sqrt{GM_\odot/a_{\rm plan}^3}, \tag{28}$$

where $n_\odot$ is the mean motion of the planet and $\lambda_{\odot 0}$ is the initial solar longitude at the moment of ejection ($t_0=0$).

For the further analysis it is convenient to introduce dimensionless force parameters. The radiation pressure is expressed with the coefficient $C$ as (Krivov et al., 1996)

$$C(\lambda)\equiv\frac{3}{2}\frac{F_{\rm rp}}{mn_\odot n_0 a_0}=C_{\rm d}+C_\xi(\lambda), \tag{29}$$

where the radiation pressure force $F_{\rm rp}$ has been defined in Eq. (2) and $n_0$ denotes the initial mean motion of the grain $n_0^2=GM/a_0^3$. $C_{\rm d}$ is the deterministic component of $C$ and $C_\xi$ is the fluctuating part, modelled as a Gaussian white noise

$$\langle C_\xi(\lambda)\rangle=0,\quad \langle C_\xi(\lambda_1)C_\xi(\lambda_2)\rangle=\sigma^2\delta(\lambda_1-\lambda_2). \tag{30}$$

Taking Eq. (7) into account for the stochastic radiation pressure and comparing it with Eq. (29) we express $C_{\rm d}$ and $\sigma^2$ as

$$C_{\rm d}=\frac{3}{2}\frac{B\langle S_r\rangle}{mn_\odot n_0 a_0},\quad \sigma^2=\frac{2C_{\rm d}^2K_0n_\odot}{\langle S_r\rangle^2}, \tag{31}$$

where Eqs. (8) and (30) have been used. The quantities defined in Eq. (31) make a direct link to the terms defined in the previous section.

In what follows we will denote the complete solution for a variable $X$ ($X$ is a certain orbital element) as $X_{\rm t}$, while $X_\xi$ denotes the solution with $C_{\rm d}=0$ and $X_{\rm d}$ the purely deterministic solution with $C_\xi=0$. Correspondingly, for the derivatives with respect to the dimensionless time $\lambda$ we will use the notation ${\rm d}X/{\rm d}\lambda\equiv X'$.

### 4.2. General solution for eccentricity

Although the general equations of the motion for the orbital elements are coupled (see Appendix B), it has been demonstrated by Krivov et al. (1996) that for eccentricity components $k$ and $h$ much simpler equations may be obtained. Namely, it is sufficient to consider only the first-order terms in the orbit averaged equations and to ignore inclination components $p$ and $q$ which are significantly

smaller (cf. Eq. (39) in Krivov et al., 1996),

$$h' = -C\cos\varepsilon\sin\lambda - k\omega, \quad k' = +C\cos\lambda + h\omega, \tag{32}$$

where $\varepsilon$ is the obliquity of a planet ($\varepsilon = 25^\circ$ for Mars). In general, one needs to consider the full Gauss perturbation equations (e.g. Burns, 1976), since the orbit averaging procedure might disregard certain terms which can give rise to a noticeable diffusion, as it will be demonstrated for the semimajor axis and inclination. However, the presented Eqs. (32) contain the zeroth-order term which is sufficient to explain diffusion of $h$ and $k$.

The solution $h_\mathrm{d}(\lambda)$ and $k_\mathrm{d}(\lambda)$ to the system (32) for the deterministic case, $C = C_\mathrm{d}$, is known (see Krivov et al., 1996). Eqs. (32) for the purely stochastic case $C = C_\xi$, may be solved with the same reasoning as for the previously given simplified analysis (see Appendix B for detail). The solutions are the normally distributed elements $h_\mathrm{t}$ and $k_\mathrm{t}$ with mean

$$\langle h_\mathrm{t}(\lambda)\rangle = h_\mathrm{d}(\lambda), \quad \langle k_\mathrm{t}(\lambda)\rangle = k_\mathrm{d}(\lambda), \tag{33}$$

and variance

$$\langle h_\mathrm{t}^2(\lambda)\rangle - \langle h_\mathrm{t}(\lambda)\rangle^2 \approx \langle k_\mathrm{t}^2(\lambda)\rangle - \langle k_\mathrm{t}(\lambda)\rangle^2 \approx \Lambda\lambda, \tag{34}$$

$$\Lambda = \tfrac{1}{8}\sigma^2\,[3 + \cos(2\varepsilon)]. \tag{35}$$

The resulting eccentricity $e_\mathrm{t} = (h_\mathrm{t}^2 + k_\mathrm{t}^2)^{1/2}$ is not normally distributed. Its mean is

$$\langle e_\mathrm{t}(\lambda)\rangle \approx \sqrt{e_\mathrm{d}^2(\lambda) + \alpha_e\Lambda\lambda}, \tag{36}$$

and the variance reads for the limiting cases of strong and weak noise:

$$\langle e_\mathrm{t}^2(\lambda)\rangle - \langle e_\mathrm{t}(\lambda)\rangle^2 \approx (2 - \alpha_e)\Lambda\lambda, \tag{37}$$

$$\alpha_e = \begin{cases} 1/2, & \Lambda\lambda \ll e_\mathrm{d}^2, \\ \pi/2, & \Lambda\lambda \gg e_\mathrm{d}^2. \end{cases} \tag{38}$$

As it is clearly seen from Eq. (37), the standard deviation of the eccentricity linearly increases with the dimensionless time $\lambda$. In other words, the evolution of this orbital element for an ensemble of grain demonstrates the diffusional behaviour.

### 4.3. Solution for the semimajor axis

In addition to the simplified analysis of Section 3 we wish to present here the corresponding rigorous analysis of the semimajor axis evolution. First, we note that although it remains constant $a_\mathrm{d}(\lambda) \approx a_0$ in the purely deterministic case without the Poynting–Robertson force, this does not hold if an additional stochastic component is present. Unfortunately, in this case it is not possible to use the orbit-averaged equations, but the full perturbation equation for the semimajor axis has to be studied (e.g. Burns, 1976)

$$\frac{\mathrm{d}a}{\mathrm{d}t} = \frac{2}{an^2}\frac{F_\mathrm{rp}}{m}\vec{v}\cdot\vec{e}_\odot, \quad n^2 = \frac{GM}{a^3}, \tag{39}$$

where, as previously, $\vec{v}$ is the particle's velocity and $n$ is the mean motion of the particle. In Eq. (39) we ignored the oblateness of the planet, assuming $\omega \approx 0$, since both the deterministic solution $a_\mathrm{d}(\lambda)$ and moments of $h_\xi$ and $k_\xi$, as well as $p_\xi$ and $q_\xi$, are not very sensitive to $\omega$.

Calculating $\vec{v}\cdot\vec{e}_\odot$ and expanding the result around $e_0, i_0 = 0$ we obtain

$$\begin{aligned}\vec{v}\cdot\vec{e}_\odot = & -an[\cos\varepsilon\sin\lambda\cos(\tilde{\omega}+\theta) \\ & - \cos\lambda\sin(\tilde{\omega}+\theta)] + \mathrm{O}(e) + \mathrm{O}(i),\end{aligned} \tag{40}$$

where $\theta$ is the true anomaly. Clearly, in the purely deterministic case the orbit average of this equation yields zero. Starting from Eq. (39), introducing the scaled semimajor axis $\tilde{a} = a/a_0$, dimensionless time $\lambda$, we further obtain

$$\tilde{a}'(\lambda) = -\tfrac{4}{3}C\tilde{a}^{3/2}[\cos\varepsilon\sin\lambda\cos(\tilde{\omega}+\theta) - \cos\lambda\sin(\tilde{\omega}+\theta)], \tag{41}$$

The equation for $\tilde{a}$ is an equation with multiplicative noise and in terms of Stratonovich calculus, separation of variables yields the result

$$\begin{aligned}\tilde{a}_\mathrm{t}^{-1/2}(\lambda) - 1 = \frac{2}{3}\int_0^\lambda & [\cos\varepsilon\sin x\cos f(x) \\ & - \cos x\sin f(x)]C_\xi(x)\,\mathrm{d}x.\end{aligned} \tag{42}$$

The integrand contains the oscillatory function $f(x) = \tilde{\omega}(x) + \theta(x)$ which is a fast variable and hence, for $\lambda \gg 1$ may be accurately approximated by a uniform distribution. Since $C_\xi(x)$ is Gaussian, the resulting integral in the last equation is also Gaussian with zero mean and with variance equal to $4\Lambda\lambda/9$. Thus, we obtain

$$\begin{aligned}&\langle\tilde{a}_\mathrm{t}^{-1}(\lambda)\rangle = 1 + 4\Lambda\lambda/9, \\ &\langle\tilde{a}_\mathrm{t}^{-2}(\lambda)\rangle = 1 + 8\Lambda\lambda/3 + 16\Lambda^2\lambda^2/27\end{aligned} \tag{43}$$

or

$$\langle\tilde{a}_\mathrm{t}^{-2}(\lambda)\rangle - \langle\tilde{a}_\mathrm{t}^{-1}(\lambda)\rangle^2 = \tfrac{2}{9}\Lambda\lambda + \tfrac{32}{81}\Lambda^2\lambda^2. \tag{44}$$

Hence in a linear approximation the coefficient $\Lambda$ in Eq. (44) plays a role of the diffusion constant for the dimensionless time $\lambda$. To compare the obtained result with the conclusion of the simplified analysis of Section 3, we notice that $\tilde{a}_\mathrm{t} = 1 + \delta a/a_0$ and that

$$\langle\tilde{a}_\mathrm{t}^{-2}(\lambda)\rangle - \langle\tilde{a}_\mathrm{t}^{-1}(\lambda)\rangle^2 = 2\frac{\langle(\delta a)^2\rangle}{a_0^2} = 2\Lambda\lambda/9, \tag{45}$$

where all non-linear terms have been omitted. Applying the definitions of $\lambda$ and $\Lambda$, Eqs. (28) and (35), it is easy to show that the diffusion coefficient $D$ of the simplified analysis, Eq. (26), coincides (up to a numerical prefactor) with the dimensionless coefficient $\Lambda$, if the dimensionless time is used.

### 4.4. General solution for inclination

It is known that the inclination components $p$ and $q$ in case of $\omega \ll 1$ (which corresponds to the case of Deimos ejecta for the circum-Martian motion), and $\omega \approx 1$ (which corresponds to the Phobos ejecta) have a different behaviour (Krivov et al., 1996). For simplicity in what follows we assume that $\omega \ll 1$.

In order to analyse the evolution of the inclination in the general case it is not enough to use orbit-averaged equations since they lack zeroth-order terms, which cause a noticeable diffusion. Following Burns (1976), we write the perturbation equation as

$$\mathrm{d}\vec{L}/\mathrm{d}t = \vec{r} \times F_{\mathrm{rp}}\vec{e}_{\odot}, \quad \vec{L} = \vec{r} \times m\vec{v}, \quad p = -L_y/L, \quad q = L_x/L, \tag{46}$$

with the angular momentum $\vec{L}$, where $L^2 = m^2 GMa(1-e^2)$.

Using an approximation $a \approx a_0$, we obtain after long but straightforward calculations

$$p'_{\mathrm{t}}(\lambda) = \tfrac{2}{3}C \sin\varepsilon \sin\lambda \sin(g+\theta) + \mathrm{O}_{1,p}(h,k,p,q), \tag{47}$$

$$q'_{\mathrm{t}}(\lambda) = \tfrac{2}{3}C \sin\varepsilon \sin\lambda \cos(g+\theta) + \mathrm{O}_{1,q}(h,k,p,q). \tag{48}$$

For the constant $C = C_{\mathrm{d}}$ the above zero-order terms can be neglected since their average over the orbit vanishes. These, however, give rise to a substantial diffusion when $C = C_{\mathrm{d}} + C_{\xi}(\lambda)$. It is possible to improve Eqs. (47) and (48) by adding first-order terms $\mathrm{O}_{1,p/q}$ from, for instance, orbit-averaged equations by Krivov et al. (1996), while still keeping the equations linear and thus analytically solvable. However, solutions of such more general equations are extremely cumbersome and do not add any important secular term to the moments of $p_{\mathrm{t}}$ and $q_{\mathrm{t}}$ (though the more general equations are needed for an accurate analytical estimate of $p_{\mathrm{d}}$ and $q_{\mathrm{d}}$ as demonstrated by Krivov et al., 1996).

Calculation of the moments of the inclination components from Eqs. (47) and (48) can be done in a very similar manner as presented for the eccentricity case (Appendix B). The inclination elements $p_{\mathrm{t}}$ and $q_{\mathrm{t}}$ are normally distributed, while $\sin i_{\mathrm{t}} = (p_{\mathrm{t}}^2 + q_{\mathrm{t}}^2)^{1/2}$ is not Gaussian. Their average read

$$\langle p_{\mathrm{t}}(\lambda)\rangle \approx p_{\mathrm{d}}(\lambda), \quad \langle q_{\mathrm{t}}(\lambda)\rangle \approx q_{\mathrm{d}}(\lambda), \tag{49}$$

and the standard deviations are

$$\langle p_{\mathrm{t}}^2(\lambda)\rangle - \langle p_{\mathrm{t}}(\lambda)\rangle^2 \approx \langle q_{\mathrm{t}}^2(\lambda)\rangle - \langle q_{\mathrm{t}}(\lambda)\rangle^2 \approx \Upsilon\Lambda, \tag{50}$$

where

$$\Upsilon \equiv \frac{8\sin^2\varepsilon}{9(3+\cos 2\varepsilon)}\Lambda. \tag{51}$$

Similarly

$$\langle \sin i_{\mathrm{t}}(\lambda)\rangle \approx \sqrt{\sin^2 i_{\mathrm{d}}(\lambda) + \alpha_i \Upsilon\Lambda}, \tag{52}$$

$$\langle \sin^2 i_{\mathrm{t}}(\lambda)\rangle - \langle \sin i_{\mathrm{t}}(\lambda)\rangle^2 \approx (2-\alpha_i)\Upsilon\Lambda, \tag{53}$$

$$\alpha_i = \begin{cases} 1/2, & \Upsilon\Lambda \ll \sin^2 i_{\mathrm{d}}, \\ \pi/2, & \Upsilon\Lambda \gg \sin^2 i_{\mathrm{d}}. \end{cases} \tag{54}$$

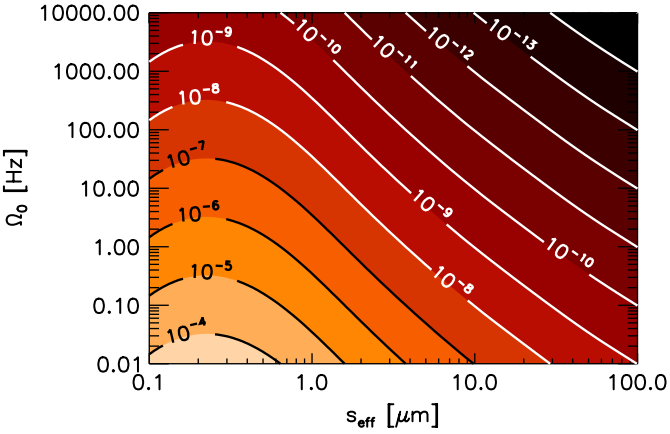


Fig. 2. Dependence of dimensionless diffusion coefficient $\Lambda$ defined by Eq. (35) on the particle effective radius $s_{\mathrm{eff}}$ and the rotation velocity $\Omega_0$. The calculations are done for an oblate silicate grain placed on the Deimos orbit. The bulk density of the grain is $\varrho_g = 2.37 \times 10^3\,\mathrm{kg/m^3}$, the aspect ratio is $\alpha = 5$ and the radiation pressure efficiency coefficient $Q_{\mathrm{pr}}$ was calculated for each grain size as described by Makuch et al. (2005). The non-monotonous behaviour of $\Lambda$ stems from that of the coefficient $Q_{\mathrm{pr}}$.

Here, we again encounter the diffusional behaviour of the orbital elements.

### 4.5. Diffusive behaviour of the orbital elements

As we have demonstrated above, all the orbital elements show a diffusive behaviour with the effective diffusive coefficients. These coefficients are proportional with the coefficient of the order of unity to the "basic" dimensionless coefficient $\Lambda$ (see Eqs. (35), (37), (44), (50), (53)). The coefficient $\Lambda$ sensitively depends on the particle's size $s_{\mathrm{eff}}$ and the rotational frequency $\Omega_0$, as is illustrated in Fig. 2, where $\alpha = 5$ and the other parameters were taken for the circum-Martian motion on the Deimos orbit. In particular, we use $\varepsilon = 25^\circ$, $\omega = 0.0335$ (for details see Krivov et al., 1996), $\rho_g = 2.37\,\mathrm{g\,cm^{-3}}$ and $Q_{\mathrm{pr}}$ was calculated according to the grain effective radius as discussed by Makuch et al. (2005). As it follows from Fig. 2, the coefficient $\Lambda$ varies by 10 orders of magnitude in the range of astrophysically relevant values for $s_{\mathrm{eff}}$ and $\Omega_0$. The non-monotonous behaviour of $\Lambda$ stems from that of the radiation pressure efficiency coefficient $Q_{\mathrm{pr}}$ (Makuch et al., 2005).

As it will be shown below, the analytical theory for the diffusion coefficients gives the lower boundary for this value, hence Fig. 2 may be used to estimate the impact of the stochastic radiation pressure. Note that the results of the plot may also be used for a rough estimate of the low boundary of the effect for a general circumplanetary motion, after the proper rescaling of the distance of the planet from the Sun $a_{\mathrm{plan}}$ (scales as $a_{\mathrm{plan}}^{-4}$), the mass of the planet $M$ (scales as $M^{-1}$) and the semimajor axis (scales as $a_0$).

## 5. Numerical simulations: application for the circum-Martian dynamics

To check the predictions of the analytical theory we perform a set of numerical simulations for the particular case of circumplanetary dynamics. Namely, in what follows we focus on the circum-Martian motion of dust ejected from Deimos. Choosing the grain size we take into account its astrophysical relevance. Namely, according to the classification by Krivov (1994) there exist several groups of particles with quite different dynamics. The biggest ejecta fragments, larger than approximately 1 mm (denoted as Population 0), are only subject to the gravity of the oblate planet. They create narrow tori along the moons' orbits. Since these particles are rapidly lost due to collisions with the parent moons, their lifetimes and corresponding number densities are very small. Smaller grains, which sizes range from tens to hundreds of micrometers form Population I and are small enough to be noticeably affected by non-gravitational perturbing forces, such as direct radiation pressure and Poynting–Robertson effect. The lifetimes of these grains are between tens of years (Phobos' ejecta) and tens of thousands years (Deimos). They form extended asymmetric tori and are expected to be the main component of the Martian dust environment. The most important loss mechanism of these dust particles is the re-accretion by the parent moon as well as the mutual collisions as shown in the recent study by Makuch et al. (2005). The combined influence of planetary oblateness and radiation pressure causes periodic oscillations of eccentricity and inclination. Since the maximal eccentricity is inversely proportional to the particle size (Krivov et al., 1996), there exist a critical grain size $s_{\rm crit}$ ($\approx 10\,\mu$m) below which the particles hit Mars at the pericentre of their orbit in less than one year. These micron-sized grains form Population II. Still smaller, submicron-sized particles (Population III) are strongly affected by fast fluctuations of the solar wind and plasma environment. They are swept out from the vicinity of Mars within 10–100 days and form a highly variable subtle halo around Mars (Horányi et al., 1990, 1991).

Based on rather robust theoretical predictions there were a couple of attempts to detect the Martian dust tori (see Krivov et al., 2006 for a review). However, none of them have been successful up to now. We are motivated by these negative results to reconsider the dynamics of dust particles and to find a mechanism changing the predicted optical properties of the tori. Therefore, in the present study we apply our general theory to describe the dynamics of Population I, which is expected to be the most dominant in the Martian system (Juhász and Horányi, 1995). The long lifetimes of these particles implies that even weak perturbations may cause a significant change of the tori characteristics. The dynamics of the tori particles under the influence of planetary oblateness (J2), direct radiation pressure (RP), and Poynting–Robertson drag (PR) was studied in detail (Krivov et al., 1996; Hamilton, 1996; Ishimoto, 1996; Krivov and Hamilton, 1997; Makuch et al., 2005). However, any impact of stochastic perturbations has never been addressed before in the context of this problem.

To model the stochastic dynamics of these particles we consider an ensemble of oblate grains with the bulk density of $2.37\times10^3\,{\rm kg/m^3}$ corresponding to silicate. Assuming ergodicity, the dynamics of a single grain mimics the evolution of the whole ensemble. We have tested a wide range of parameters $s_{\rm min}$, $\alpha$, and $\Omega_0$, which characterize the properties of the grains. As has been already mentioned, the radiation pressure efficiency coefficient $Q_{\rm pr}$ was calculated according to the approach presented by Makuch et al. (2005). The initial elements were identical for all ejected particles. The starting position was a circular orbit lying in the equatorial plane with a semimajor axis $a$ equal to that of Deimos (23 480 km).

To trace the dynamics of the ejected grains we numerically integrated Eq. (1) of planetocentric particles subject to gravity of oblate Mars and stochastic radiation pressure force (2). We used the constant integration time step $\Delta t = 500$ s. At each integration step the calculated coordinates and velocities were converted into the osculating orbital elements and stored. As described previously, the radiation pressure force consists of two components. The first, deterministic part is the direct radiation pressure. It acts on a particle with the average cross-section defined by Eq. (13). The second, stochastic part was modelled by a Gaussian white noise. The method of modelling of the stochastic component is similar to that used by Spahn et al. (2003). At each integration step a random Gaussian variable with zero mean and unit variance was generated. Than it was scaled by a numerical factor $\kappa$ and added to the deterministic part of the radiation pressure. This numerical scheme, so-called "exact propagator", is described in detail in Mannella (2000) and in Mannella and Palleschi (1989). With the factor $\kappa$ defined as

$$\kappa = B\frac{1}{\Delta t}\sqrt{2K_0\Delta t} \tag{55}$$

this numerical scheme yields the accuracy of the order of the integration time step $\Delta t$. We want to stress here that the factor $\kappa$ in Eq. (55) reflects the amplitude of the noise, which is inversely proportional to the square root of the rotation frequency (see definition of $K_0$, Eq. (14)). Note also that the preceding factor $1/\Delta t$ in the right-hand side of Eq. (55) comes into play since we add the stochastic radiation pressure into the integration routine for the deterministic part (see Mannella, 2000, for the detail). We additionally checked our numerical results on shorter timescales (up to hundreds of M.y.) using another stochastic integrator (Milstein et al., 2002).

Here we present the results of numerical simulations for two different particle sizes with the effective radius $s_{\rm eff}$ of 15 and 40 μm. As it has been already noted the minimal particle radius can be calculated for oblate particles from the relation, $l = s_{\rm min} = s_{\rm eff}\sqrt{2/\alpha(\alpha+1)}$. Since our main

goal is to compare the simulation results with the predictions of the analytical theory, we chose a relatively short integration time of less than 3000 Martian years. The results of longer simulations with larger variety of particle sizes, shape, and spin properties will be presented elsewhere. In each run we performed a series of realizations of the stochastic radiation pressure, i.e. a set of individual orbits with identical initial orbits has been simulated. In our simulations we studied the oblate particles with the aspect ratio $\alpha = 5$. The radiation pressure coefficient of $Q_{pr} = 0.385$ ($s_{eff} = 15\,\mu m$) and $Q_{pr} = 0.372$ ($s_{eff} = 40\,\mu m$) was used (see Table 1).

We expect that for the case of circum-Martian motion the angular velocity of the grains is determined by the ejection mechanism, for which our simple model yields $\Omega_0 = 5 \times 10^3\,s^{-1}$ (see Section 3.2). Therefore in simulations we mainly use this value of $\Omega_0$. However, some unaccounted processes during the dust creation may not be excluded, which imply the other magnitude of $\Omega_0$. Hence for the case of $s_{eff} = 15\,\mu m$ we also use $\Omega_0 = 1.5 \times 10^{-2}\,s^{-1}$ as an alternative value of the rotation frequency.

As it follows from our studies, the permanent action of the stochastic perturbation causes a spatial spread of particle trajectories. The spread itself can be characterized by a standard deviation of the osculating elements. The time dependence of the standard deviation of the orbital elements of the ensemble of 200 and more particles with the effective radii $s_{eff} = 40$ and $15\,\mu m$ are shown in Figs. 3–5. The predictions of the analytical theory are also plotted along with the numerical results. The corresponding

Table 1
Numerical values of the constants characterizing the diffusion of orbital elements derived from the analytical predictions, for a given particle size and aspect ratio $\alpha = 5$

| $s_{eff}$ (μm) | $Q_{pr}$ | $\Omega_0$ (Hz) | $\sigma^2$ | $C_d$ | $\Lambda$ | $\Upsilon$ |
|---|---|---|---|---|---|---|
| 40 | 0.372 | $5 \times 10^3$ | $2.3 \times 10^{-14}$ | 0.061 | $1.0 \times 10^{-14}$ | $4.5 \times 10^{-16}$ |
| 15 | 0.385 | $5 \times 10^3$ | $1.8 \times 10^{-13}$ | 0.166 | $8.0 \times 10^{-14}$ | $3.5 \times 10^{-15}$ |
| 15 | 0.385 | $1.5 \times 10^{-2}$ | $5.8 \times 10^{-8}$ | 0.166 | $2.7 \times 10^{-8}$ | $1.2 \times 10^{-9}$ |

Direct comparison with the numerical simulations is depicted in Figs. 3–5.

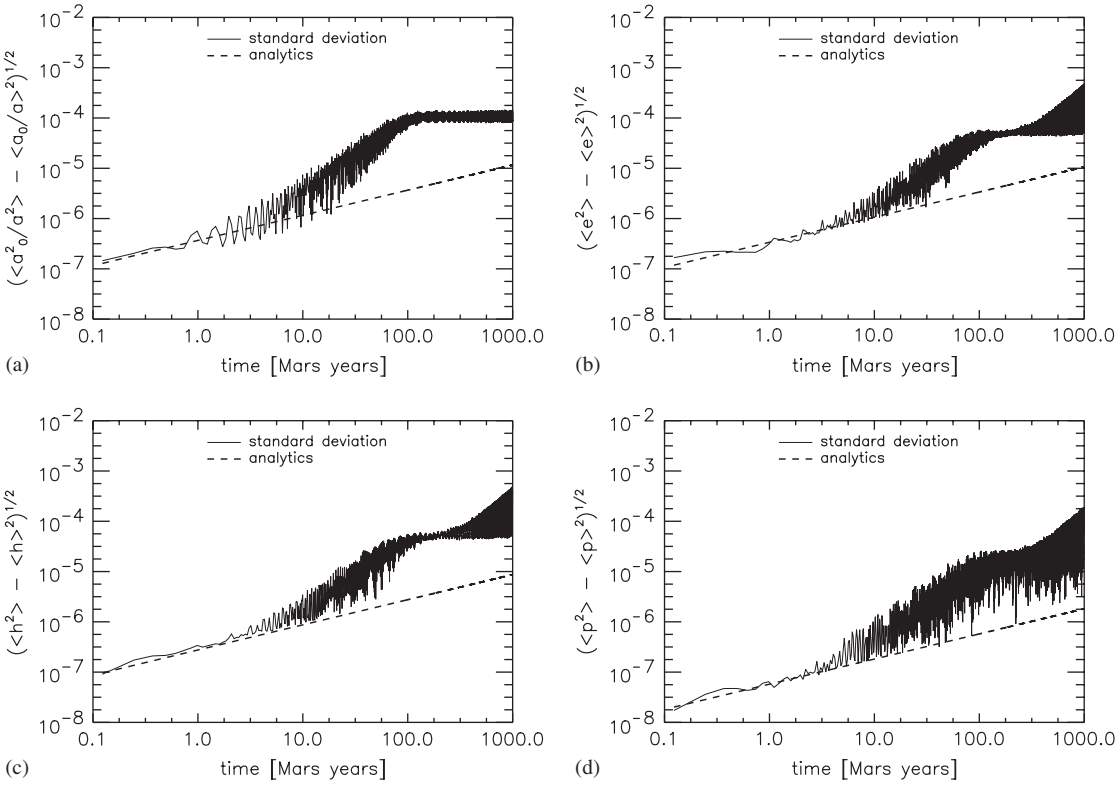


Fig. 3. The standard deviations of: (a) normalized inverse semimajor axis; (b) eccentricity; (c) Lagrangian element $h = e\cos\tilde{\omega}$; and (d) Lagrangian element $p = \sin i \cos\Omega$ for an ensemble of 200 particles. The time dependence of the orbital elements $k$ and $q$ is almost identical to that of $h$ and $p$, respectively, and hence is not shown. Parameters of the grains are: $s_{eff} = 40\,\mu m$, the aspect ratio $\alpha = 5$, and the rotation frequency $\Omega_0 = 5 \times 10^3\,s^{-1}$. The dashed line depicts the analytical estimates.

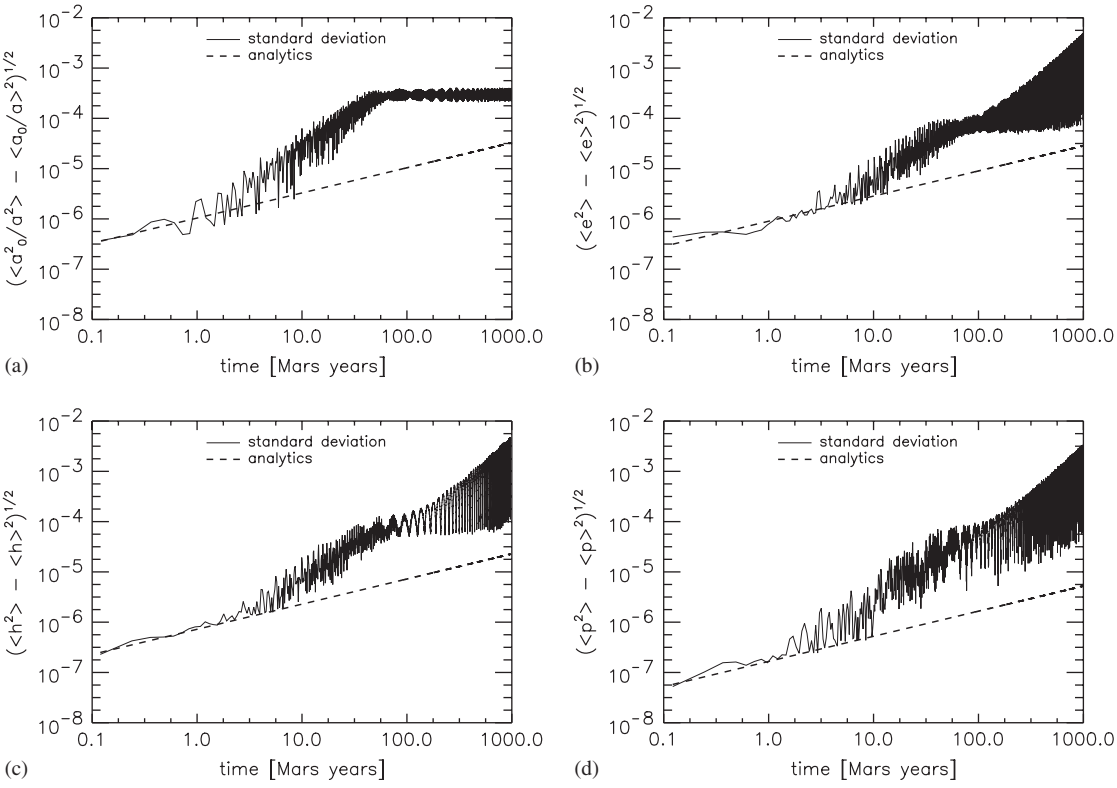


Fig. 4. The same as Fig. 3, but for particle size $s_{\mathrm{eff}} = 15\,\mu\mathrm{m}$.

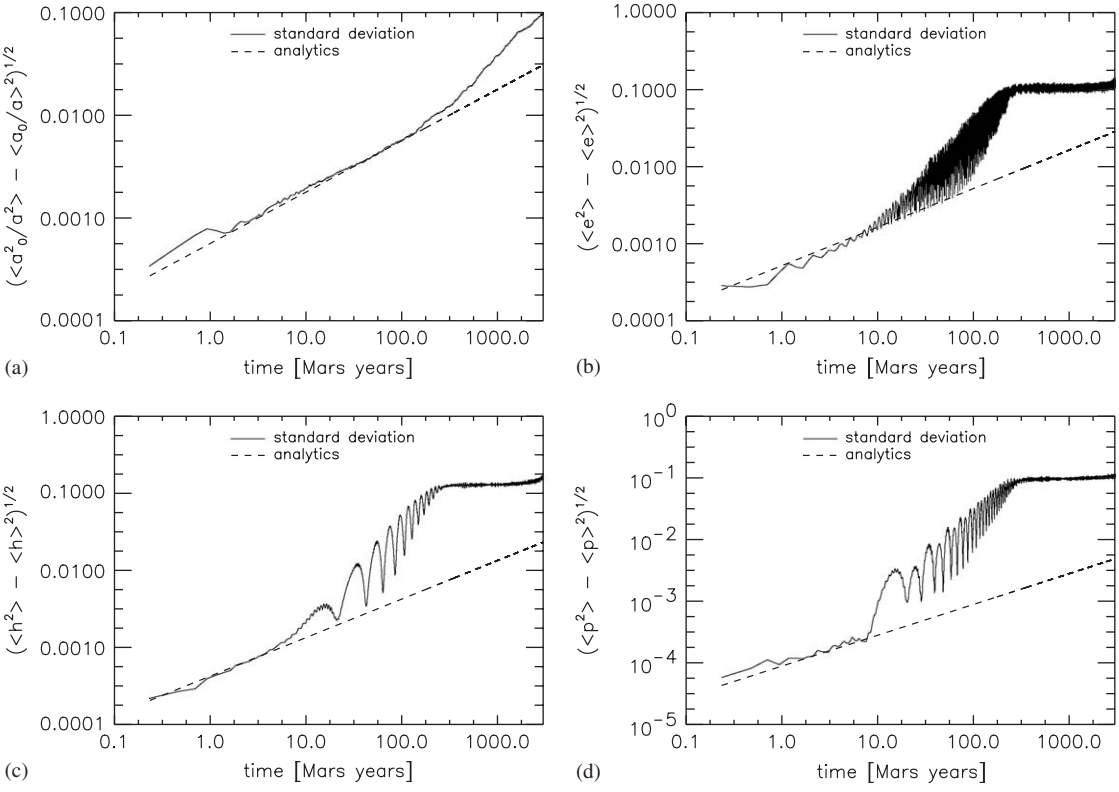


Fig. 5. The same as Fig. 3, but for particle size $s_{\mathrm{eff}} = 15\,\mu\mathrm{m}$ and $\Omega_0 = 1.5 \times 10^{-2}$.

analytical values of $\sigma^2$, diffusion coefficients $\Lambda$, $\Upsilon$, and the deterministic component of radiation pressure $C_d$ for a used grain size and $\Omega_0$ are given in Table 1.

Comparing the numerical results for the both grain sizes, Figs. 3 and 4, it is evident that the dispersion of the elements depends on the particle size: the grains with smaller size are more sensitive to the influence of a stochastic radiation pressure and the corresponding dispersion of trajectories is higher. Moreover, from Figs. 4 and 5 it may also be seen that the spatial spread of the trajectories crucially depends on the rotational frequency $\Omega_0$. While for the large $\Omega_0$ the spread is relatively weak (Figs. 3 and 4), for the case of slow rotation (Fig. 5) a significant variation of the orbital elements, up to 10% during the first 1000 years, is observed.

The agreement between the analytical predictions and simulation results is good at the beginning of the ensemble evolution. Later, however, a noticeable deviation of the theory from the numerical results is observed. This may be attributed to the neglected non-linear terms, becoming important in course of time. At this point we face the limitation of our theory due to initial assumptions taken in order to proceed such complex problem. These are e.g. the condition of mutual independence of the elements or limitations of the linear theory. Comparing the plots for different grain sizes one can notice that the accuracy of the theory crucially depends on the deterministic coefficient $C_d$, which is inversely proportional to the size of the grains.

We wish to stress that although our analytical theory fails at later times, it presumably gives the low boundary estimate for the effect of interest. In other words, due to the omitted non-linear terms, the actual standard deviation of the orbital elements is always larger than that predicted by the analytical theory. The other interesting effects which may be attributed to the omitted non-linear terms are the apparent saturation of the standard deviation of the orbital elements (Figs. 3a and 4a) and alternation of their regime of growth (Figs. 3b and 4b). The latter effect lacks presently an explanation, while the former one may be interprete as follows: the detailed analysis (Brilliantov et al., 2006) shows that the form of simplified Gauss perturbation equations after their linearization is similar to that of the *damped* stochastic oscillator. The standard deviation of the amplitude of the latter system saturates after an initial linear growth with time. In our analytical approach which, is aimed to obtain the estimates of the effective diffusion coefficients, we omit for simplicity very small terms, responsible for the damping. Hence our theory corresponds to the *undamped* stochastic oscillator which lacks the saturation, whereas the numerical study successfully reproduces the saturation effect.

## 6. Conclusions

We analyse the role of stochastic perturbations in the circumplanetary motion of dust particles. We address one of the most important sources of the stochasticity in this system—the random modulation of the radiation pressure force by the rotation motion of non-spherical particles. We formulate the model of the stochastic radiation pressure based on this effect. We consider particles of a simplified form, that is, we assume the particles to be the figures of rotation. These may be characterized by two dimensions, one parallel to the symmetry axis and the other one, perpendicular to this axis. Such simplified model allows to express the stochastic properties of the fluctuating radiation pressure in terms of the rotational time-correlation function of rotating grains. In order to calculate the time-correlation function we adopt a model of freely rotating particles, whose dependence on time is determined by a characteristic angular velocity. According to our estimates, the particles perform a very fast rotation around their centre of mass on the timescale of the orbital motion. This allows to represent the radiation pressure force as a sum of a deterministic component, which refers to the average cross-section of the spinning particles and a random component, modelled as a Gaussian white noise with zero mean. The dispersion of the noise is expressed in terms of the time integral of the orientational time-correlation function. We estimate the characteristic rotation frequency for two different mechanisms of particle creation, one due to the impact-ejection mechanism by hypervelocity impacts of interplanetary particles and the other one due to volcanic eruption of a dust–gas mixture.

We performed numerical and analytical studies of the formulated model of the stochastic radiation pressure. In the analytical treatment we expanded the equations of motion around the initial orbit and kept terms up to the second order in this expansion. To treat the stochastic terms in the simplified equations we applied Stratonovich calculus and obtain the solution to these stochastic differential equations. Using the properties of the Gaussian white noise we derived expressions for the average and square average of the orbital elements for the ensemble of non-spherical particles. Our results clearly demonstrate the diffusion-like behaviour of these quantities. We also find explicit expressions for the effective diffusion coefficients which characterize the growth rate of the standard deviations of the orbital elements.

The analytical results have been compared with results of extensive numerical simulations with the parameters corresponding to the motion on the Deimos orbit around Mars. We observe that the predictions of our theory are in a very good agreement with the simulation results for the initial period of the system evolution. The agreement however worsens at later times due to the increasing impact of the non-linear terms neglected in the theoretical approach. We conclude that our analytical theory may be used for an estimate of the low boundary of the time-dependent standard deviation of the orbital elements. Since the simulation of orbital motion with stochastic forces is extremely time consuming, all numerical runs have been performed only for a restricted interval of time, less than 3000 Martian years. Nevertheless, even for this, relatively

short time, the effect of the stochastic radiation pressure has been found to be significant.

Therefore, the results of our study lead us to the conclusion that the stochasticity of the radiation pressure force due to the rotation of non-spherical particles plays a significant role in the orbital dynamics of dust grains and may be crucial in determining the density distribution of dusty systems, especially the Martian dust tori.


## Acknowledgements

We thank Nicole Albers for her careful corrections of this manuscript and together with Jürgen Schmidt for useful comments and stimulating discussions. This research was funded by Deutsche Forschungsgemeinschaft (DFG), projects Kr 2164/1-3 (M.M.) and Sp 384/18-1 (N.V.B.). M.S. was supported by Cassini UVIS project.


## Appendix A. Time-correlation function of rotation motion

In this section the details of the evaluation of the time-correlation function $K(t)$ are discussed for the case of *prolate* particles. Using Eq. (9) we write the average cross-section as

$$\langle S_r\rangle = 4Ll\langle\sin\theta(t)\rangle + \pi l^2 = \pi l(L+l) \tag{A.1}$$

and, respectively, fluctuation as

$$\xi(t) = S(t) - \langle S\rangle = 4Ll\left(\sin\theta(t) - \frac{\pi}{4}\right), \tag{A.2}$$

where we take into account that the angle $\theta$ is uniformly distributed over the sphere with the density $1/4\pi$:

$$\langle\sin\theta(t)\rangle = \int_0^{\pi}\sin\theta\,\mathrm{d}\theta\int_0^{2\pi}\mathrm{d}\varphi\,\frac{1}{4\pi}\sin\theta = \frac{\pi}{4}. \tag{A.3}$$

Similarly, for the uniform distribution $\langle\sin^2\theta(t)\rangle = \frac{2}{3}$. Hence, the time-correlation function $K(t)$ may be written as

$$\langle\xi(0)\xi(t)\rangle = L^2l^2(\tfrac{32}{3} - \pi^2)k(t) = K(0)k(t), \tag{A.4}$$

with the normalized time-correlation function

$$k(t) = \frac{\langle\sin\theta(0)\sin\theta(t)\rangle - \langle\sin\theta\rangle^2}{(32/3-\pi^2)}, \tag{A.5}$$

so that $k(0) = 1$. We wish to note that the free-rotators model for the orientational motion is used to obtain *qualitative* estimates. This simplest model is not, however, a self-averaging model: although $\langle\xi\rangle = 0$, the asymptotic value of the time-correlation function for this model at $t\to\infty$ does not vanish, $\langle\xi(0)\xi(\infty)\rangle \neq 0$ (see e.g. Binder and Heermann, 1983, for more precise definition). This property of the ensemble of free rotators has been already pointed out by Pierre and Steele (1969). Still, one can exploit this model, either subtracting from $k(t)$ its asymptotic value, $k(t)\to k(t)-k(\infty)$, or using the *model function*, according to the rule, suggested by Pierre and Steele (1969):

$$k(t) \approx \mathrm{e}^{-\varkappa t^2/2}, \quad \varkappa = -\frac{\mathrm{d}^2}{\mathrm{d}t^2}k(t)\bigg|_{t=0}. \tag{A.6}$$

This Gaussian model function satisfies the basic requirements for the time-correlation functions, $\mathrm{d}k(t)/\mathrm{d}t = 0$ at $t = 0$ and $k(\infty) = 0$ (see e.g. Brilliantov and Revokatov, 1996). It has been also shown by Pierre and Steele (1969) that it mimics rather satisfactory the actual correlation function $k(t)$.

To find $k(t)$ one needs to know how $\sin\theta(t)$ depends on time for an individual particle and then perform the ensemble averaging. Since there is no external torque exerted on the particles, this is completely kinematical problem. According to the elementary mechanics (e.g. Landau and Lifshitz, 1965) the motion of such particles corresponds to the motion of a free symmetric top. That is, the angular momentum of the particle $\vec{M}$ is kept fixed, while the body performs two superimposed rotations: it rotates around its symmetry axis and the symmetry axis itself precesses around the vector $\vec{M}$, with the angular velocity $\Omega_{\mathrm{pr}}$ (see Fig. 6). The rotation around the symmetry axis does not change the angle $\theta$ and hence can be neglected; $\theta$ is, however, affected by the precession.

Let the components of the inertia tensor in its principal axes, $x'$, $y'$, $z'$, be $I_1 = I_2 = I_\perp$ and $I_3 = I_\parallel$ (the symmetry axis is directed along $z'$-axis), and the components of the angular velocity be $\Omega_1$, $\Omega_2$, and $\Omega_3$, then the angular momentum reads as

$$M = \sqrt{(I_\perp\Omega_1)^2 + (I_\perp\Omega_2)^2 + (I_\parallel\Omega_3)^2}. \tag{A.7}$$

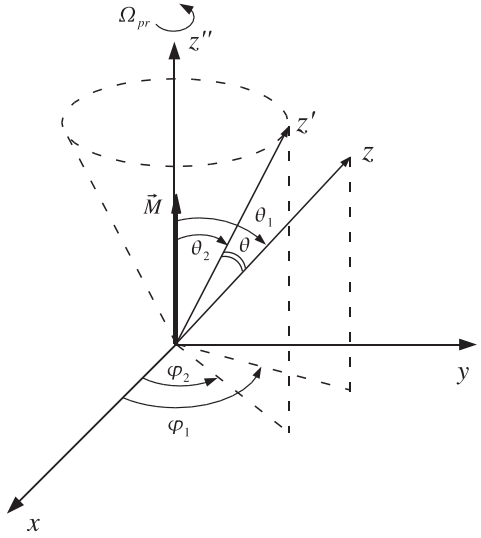


Fig. 6. Shows the relative orientation of the angular momentum of a particle $\vec{M}$, the symmetry axis of the particle $z'$ and the "fixed-frame" $z$-axis, directed along the vector $\vec{e}_\odot$. In the coordinate system with $M$ directed along $z''$-axis, the azimuthal and polar angles for the directions $z$ and $z'$ are, respectively, $\theta_1$, $\varphi_1$ and $\theta_2$, $\varphi_2$.

Correspondingly, the precession angular velocity may be written as (see e.g. Landau and Lifshitz, 1965)

$$\Omega_{\rm pr} = \frac{M}{I_\perp} = \sqrt{\Omega_1^2 + \Omega_2^2 + \beta^2\Omega_3^2}, \tag{A.8}$$

where $\beta \equiv I_\parallel / I_\perp$.

For (prolate) particles of a uniform density $\varrho_g$ the principal components of the inertia tensor read as

$$I_\parallel = \pi\varrho_g l^5(\alpha + \tfrac{8}{15}),$$
$$I_\perp = \tfrac{1}{2}\pi\varrho_g l^5[\alpha(1 + \tfrac{4}{3}\alpha^2) + \tfrac{8}{15}(\alpha + \tfrac{3}{8})^2]. \tag{A.9}$$

Hence, the coefficient $\beta$, which defines the precession frequency, depends on the aspect ratio $\alpha$ as

$$\beta = \frac{2\alpha + 16/15}{\alpha(1 + 4\alpha^2/3) + (8/15)(\alpha + 3/8)^2}. \tag{A.10}$$

Let the angle between $z$-axis of the fixed frame, which is directed along the vector $\vec{e}_\odot$ and the angular momentum $\vec{M}$ be $\theta_1$, while the angle between $\vec{M}$ and the symmetry axis $z'$ of the particle be $\theta_2$. Since the symmetry axis $z'$ makes a precession with a constant angular velocity $\Omega_{\rm pr}$ around $\vec{M}$, the angle $\varphi(t)$ between the projection of the $z$-axis on the plane perpendicular to the vector $\vec{M}$ and projection of the symmetry axis $z'$ on the same plane (see Fig. 6) evolves in time as

$$\varphi(t) = \varphi_1 - \varphi_2 = \varphi_0 + \Omega_{\rm pr} t, \tag{A.11}$$

where $\varphi_0$ is some initial angle (see Fig. 6). According to the elementary geometry, the angle $\theta$ between the $z$-axis and the symmetry axis $z'$ may be expressed in terms of the above angles as

$$\cos\theta(t) = \cos\theta_1\cos\theta_2 + \sin\theta_1\sin\theta_2\cos\varphi(t), \tag{A.12}$$

where the angles $\theta_1$ and $\theta_2$ do not change with time for a freely rotating particle. Correspondingly, we can write, $\sin\theta(t) = \sqrt{1 - \cos^2\theta(t)}$.

Due to the symmetry of the problem it is reasonable to assume that the direction of the vector $\vec{M}$ with respect to $z$-axis as well as the direction of the symmetry axis with respect to the $\vec{M}$ are spherically symmetric, that is we assume the following distribution functions:

$$P(\theta_1, \varphi_1) = P(\theta_2, \varphi_2) = \frac{1}{4\pi}. \tag{A.13}$$

Finally, we need the angular velocity distribution function, which characterizes the ensemble of rotating particles. It is natural to assume that the rotation energy of particles is distributed according to a Gaussian distribution, with a characteristic angular velocity $\Omega_0$ and that the equipartition between the rotational degrees of freedom holds: $\langle I_1\Omega_1^2/2\rangle = \langle I_2\Omega_2^2/2\rangle = \langle I_3\Omega_3^2/2\rangle = I_\perp\Omega_0^2/2$. Then the normalized distribution function reads as

$$f(\Omega_1, \Omega_2, \Omega_3) = \frac{\sqrt{\beta}}{\Omega_0^3\pi^{3/2}} \exp\left[-\frac{\Omega_1^2 + \Omega_2^2 + \beta\Omega_3^2}{\Omega_0^2}\right]. \tag{A.14}$$

As the result we obtain for the time-correlation function $\langle\sin\theta(t)\sin\theta(0)\rangle$:

$$\begin{aligned}\langle\sin\theta(t)\sin\theta(0)\rangle &= \left(\frac{1}{4\pi}\right)^2 \int_0^\pi \sin\theta_1\,{\rm d}\theta_1 \int_0^{2\pi} {\rm d}\varphi_1 \int_0^\pi \sin\theta_2\,{\rm d}\theta_2 \int_0^{2\pi} {\rm d}\varphi_2 \\ &\times \frac{\sqrt{\beta}}{\Omega_0^3\pi^{3/2}} \int_{-\infty}^\infty {\rm d}\Omega_1 \int_{-\infty}^\infty {\rm d}\Omega_2 \int_{-\infty}^\infty {\rm d}\Omega_3 \\ &\times \exp\left[-\frac{\Omega_1^2 + \Omega_2^2 + \beta\Omega_3^2}{\Omega_0^2}\right] \\ &\times \sqrt{1 - \cos^2[\theta(0)]}\sqrt{1 - \cos^2[\theta(t)]},\end{aligned} \tag{A.15}$$

where $\cos\theta(t)$ is given by Eq. (A.12) with $\varphi(t)$ expressed in terms of the precession angular velocity by Eq. (A.11).

Noticing that the integration over $\Omega_i$, $i = 1, 2, 3$ in the last equation may be performed in terms of dimensionless variables $\omega_i = \Omega_i/\Omega_0$, and that the precession angular velocity may be written as $\Omega_{\rm pr} = \Omega_0(\omega_1^2 + \omega_2^2 + \beta^2\omega_3^2)^{1/2}$. One concludes that the correlation function $\langle\sin\theta(t)\sin\theta(0)\rangle$ and hence the function $k(t)$, indeed, depends on time through the product $\Omega_0 t$ (see Eqs. (A.11), (A.12)). Similar conclusion about the orientational correlation function for an ensemble of freely rotating symmetric tops has been made by Pierre and Steele (1969) and by Guissani et al. (1977). In these papers somewhat different orientational correlation functions were studied. These also depended on the product $\Omega_T t$, where $\Omega_T$ is the characteristic angular velocity of molecular gas, which is also called thermal velocity. Unfortunately, it is not possible to obtain an analytical expression for these correlation functions, even for the simpler case addressed in the over-mentioned papers.

However, one can use the model correlation function $k(t)$, defined in Eq. (A.6). The calculation detail will be published elsewhere, here we present only the final result,

$$\begin{aligned}\varkappa &= -\frac{{\rm d}^2}{{\rm d}t^2}k(t)\bigg|_{t=0} = -(32/3 - \pi^2)^{-1}\frac{{\rm d}^2}{{\rm d}t^2}\langle\sin\theta(t)\sin\theta(0)\rangle\bigg|_{t=0} \\ &= 0.138(1 + \beta/2)\Omega_0^2,\end{aligned} \tag{A.16}$$

where the aspect-ratio-dependent parameter $\beta$ is given by Eq. (A.10). Finally, we obtain the time integral of the correlation function $k(t)$ which is needed to find $K_0$ (see Section 3.2):

$$\begin{aligned}A\Omega_0^{-1} &= \int_0^\infty k(t)\,{\rm d}t = \int_0^\infty {\rm e}^{-\varkappa t^2/2}\,{\rm d}t = \sqrt{\frac{\pi}{2\varkappa}} \\ &= \left(\frac{3.37}{\sqrt{1 + \beta/2}}\right)\Omega_0^{-1}.\end{aligned} \tag{A.17}$$

Calculations of this quantity for the case of oblate particles are more involved, therefore we use presently the approximation $A \approx 1$ for these particles.

## Appendix B. Integration of the stochastic orbit-averaged equations

### B.1. Orbit-averaged equations of motion

The orbit-averaged equations of motion of particles governed by J2 (oblateness) and RP (radiation pressure) read (Krivov et al., 1996)

$$\frac{\mathrm{d}h}{\mathrm{d}\lambda} = -k\omega\frac{5I^2-2I-1}{2E^4} - \frac{C}{E(1+I)}\{[p-Hh]q\cos\lambda + [E^2(1+I)-p(p-Hh)]\cos\varepsilon\sin\lambda + [E^2(1+I)p-IKk]\sin\varepsilon\sin\lambda\}, \tag{B.1}$$

$$\frac{\mathrm{d}k}{\mathrm{d}\lambda} = h\omega\frac{5I^2-2I-1}{2E^4} + \frac{C}{E(1+I)}\{[q-Hk]p\cos\varepsilon\sin\lambda + [E^2(1+I)-q(q-Hk)]\cos\lambda - [E^2(1+I)q-IKh]\sin\varepsilon\sin\lambda\}, \tag{B.2}$$

$$\frac{\mathrm{d}p}{\mathrm{d}\lambda} = q\omega\frac{I}{E^4} + \frac{C}{E(1+I)}[Hp-(1+I)h] \times[(p\cos\varepsilon - I\sin\varepsilon)\sin\lambda - q\cos\lambda], \tag{B.3}$$

$$\frac{\mathrm{d}q}{\mathrm{d}\lambda} = -p\omega\frac{I}{E^4} + \frac{C}{E(1+I)}[Hq-(1+I)k] \times[(p\cos\varepsilon - I\sin\varepsilon)\sin\lambda - q\cos\lambda], \tag{B.4}$$

with

$$E=\sqrt{1-e^2}=\sqrt{1-h^2-k^2},\quad I=\cos i=\sqrt{1-p^2-q^2},\quad H=hp+kq,\quad K=hq-kp, \tag{B.5}$$

where $\varepsilon$ denotes the obliquity of a planet (e.g. 25° for Mars) and $C$ and $\omega$ are dimensionless parameters that characterize the strength of radiation pressure and oblateness (see Krivov et al., 1996, for the exact definition). The other notation are the same as in Section 4.

### B.2. Integration of the stochastic equations

Formally integrating Eqs. (32) for the purely random case, $C = C_\xi(\lambda)$ we obtain

$$h_\xi(\lambda) = \int_0^\lambda [\cos x\sin(\omega x-\omega\lambda) - \cos\varepsilon\sin x\cos(\omega x-\omega\lambda)]C_\xi(x)\,\mathrm{d}x, \tag{B.6}$$

$$k_\xi(\lambda) = \int_0^\lambda [\cos x\cos(\omega x-\omega\lambda) + \cos\varepsilon\sin x\sin(\omega x-\omega\lambda)]C_\xi(x)\,\mathrm{d}x, \tag{B.7}$$

where the Stratonovich calculus is assumed.[2] The latter relations read in a short notation

$$X_\xi(\lambda) = \int_0^\lambda F_X(\lambda,x)C_\xi(x)\,\mathrm{d}x, \tag{B.8}$$

where $X=\{h,k\}$. The integrands in Eqs. (B.6) and (B.7) are normally distributed random variables, hence the integrals are normally distributed as well. Since $\langle C_\xi\rangle = 0$, the mean values are zero, $\langle h_\xi\rangle = \langle k_\xi\rangle = 0$, while the second moments read as

$$\langle X_\xi(\lambda)Y_\xi(\lambda)\rangle = \sigma^2\int_0^\lambda F_X(\lambda,x)F_Y(\lambda,x)\,\mathrm{d}x,\quad X,Y=\{h,k\}. \tag{B.9}$$

The straightforward evaluation of the integral in the last equation yields rather lengthy result, which for $\lambda\gg 2\pi$ takes a simple form

$$\langle h_\xi^2(\lambda)\rangle \approx \langle k_\xi^2(\lambda)\rangle \approx \Lambda\lambda + \mathrm{O}(\sigma^2),\quad \langle h_\xi(\lambda)k_\xi(\lambda)\rangle \approx \mathrm{O}(\sigma^2), \tag{B.10}$$

where $\Lambda$ is defined in Eq. (35) and the results have been obtained neglecting purely oscillatory terms.

The moments $h_\xi^2$ and $k_\xi^2$ are distributed according to the Gamma distribution with the parameter $\frac{1}{2}$ (also known as $\chi^2$ distribution), or in compact notation $h_\xi^2 \sim \Gamma_{1/2}[2\Lambda\lambda]$. Although $h_\xi$ and $k_\xi$ are generally not independent, we may ignore their covariance as soon as $\lambda\gg 1$. Then $e_\xi^2 = h_\xi^2 + k_\xi^2$ is sum of two independent $\Gamma$-variates, which also gives a $\Gamma$-random number with the same scale factor, $2\Lambda\lambda$, while its parameter is sum of two initial parameters, or in short notation $e_\xi^2 \sim \Gamma_1[2\Lambda\lambda]$. Finally, for the eccentricity $e_\xi$ we obtain that it is distributed in accordance with the Rayleigh distribution,

$$f(e_\xi) = \frac{e_\xi}{\Lambda\lambda}\exp\left[-\frac{e_\xi^2}{2\Lambda\lambda}\right],\quad \langle e_\xi(\lambda)\rangle = \sqrt{\pi\Lambda\lambda/2},\quad \langle e_\xi^2(\lambda)\rangle = 2\Lambda\lambda. \tag{B.11}$$

Due to the linearity of Eq. (32) the total solution reads $h_\mathrm{t} = h_\mathrm{d} + h_\xi$ and $k_\mathrm{t} = k_\mathrm{d} + k_\xi$, and Eqs. (33) and (34) are easy to verify. Similarly, the second moment of eccentricity is $\langle e_\mathrm{t}^2(\lambda)\rangle = e_\mathrm{d}^2(\lambda) + 2\Lambda\lambda$, but the calculation of the mean

$$\langle e_\mathrm{t}\rangle = \langle (h_\mathrm{t}^2+k_\mathrm{t}^2)^{1/2}\rangle = \langle [(h_\mathrm{d}+h_\xi)^2 + (k_\mathrm{d}+k_\xi)^2]^{1/2}\rangle \tag{B.12}$$

cannot be carried out explicitly since its components $h_\mathrm{t}$ and $k_\mathrm{t}$ have a non-zero mean. Instead, in the case of $\Lambda\lambda \gg e_\mathrm{d}^2$ using Taylor expansion we approximate the first moment by

$$\langle e_\mathrm{t}(\lambda)\rangle \approx (e_\mathrm{d}^2(\lambda) + \langle e_\xi\rangle^2)^{1/2} = (e_\mathrm{d}^2(\lambda) + \pi\Lambda\lambda/2)^{1/2}. \tag{B.13}$$

In the opposite case $\Lambda\lambda \ll e_\mathrm{d}^2$ a similar expression may be obtained with the numerical factor $\frac{1}{2}$ in place of $\pi/2$. Hence we arrive at Eq. (37).

[2] The choice of the Stratonovich calculus is appropriate here as the derivation of the perturbation equations uses the ordinary differentiation chain rule, as opposed to Ito calculus (see, for instance, Gardiner, 1983).

## References


Binder, K., Heermann, D.W., 1983. Monte Carlo Simulations in Statistical Physics. Springer, Berlin.

Brilliantov, N.V., Revokatov, O.P., 1996. Molecular Motion in Disordered Media. Moscow University Press, Moscow (in Russian).

Brilliantov, N.V., Sremčević, M., Makuch, M., Spahn, F., 2006. Rotation dynamics of dust particles. Preprint.

Burns, J.A., 1976. Elementary derivation of the perturbation equations of celestial mechanics. Amer. J. Phys. 44, 944–949.

Burns, J.A., Lamy, P.L., Soter, S., 1979. Radiation forces on small particles in the Solar System. Icarus 40, 1–48.

Burns, J.A., Showalter, M.R., Morfill, G.E., 1984. In: Greenberg, R., Brahic, A. (Eds.), Planetary Rings. University of Arizona Press, Tucson, pp. 200–272.

Dikarev, V.V., 1999. Dynamics of particles in Saturn's E ring: effects of charge variations and the plasma drag force. Astron. Astrophys. 346, 1011–1019.

Esposito, L.W., Brahic, A., Burns, J.A., Marouf, E.A., 1991. Particle properties and processes in Uranus' rings. Uranus, 410–465.

Everhart, E., 1985. An efficient integrator that uses Gauss–Radau spacing. In: Carusi, A., Valsecchi, G.B. (Eds.), Dynamics of Comets: Their Origin and Evolution. Dordrecht, Reidel, pp. 185–202.

Gardiner, C.W., 1983. Handbook of Stochastic Methods. Springer, Berlin, Heidelberg.

Guissani, Y., Leicknam, J.C., Bratos, S., 1977. Vectorial correlation functions for a classical system of free asymmetric rotors. Phys. Rev. A 16 (5), 2072–2079.

Hamilton, D.P., 1996. The asymmetric time-variable rings of Mars. Icarus 119, 153–172.

Horányi, M., Burns, J.A., Tatrallyay, M., Luhmann, J.G., 1990. Toward understanding the fate of dust lost from the Martian satellites. Geophys. Res. Lett. 17, 853–856.

Horányi, M., Tátrallyay, M., Juhász, A., Luhmann, J.G., 1991. The dynamics of submicron-sized dust particles lost from Phobos. J. Geophys. Res. 96, 11,283–11,290.

Ishimoto, H., 1996. Formation of Phobos/Deimos dust rings. Icarus 122, 153–165.

Juhász, A., Horányi, M., 1995. Dust torus around Mars. J. Geophys. Res. 100, 3277–3284.

Krauss, O., Wurm, G., 2005. Photophoresis and the pile-up of dust in young circumstellar disks. Astrophys. J. 630, 1088–1092.

Krivov, A.V., 1994. On the dust belts of Mars. Astron. Astrophys. 291, 657–663.

Krivov, A.V., Hamilton, D.P., 1997. Martian dust belts: waiting for discovery. Icarus 128, 335–353.

Krivov, A.V., Jurewicz, A., 1999. The ethereal dust envelopes of the Martian moons. Planet. Space Sci. 47, 45–56.

Krivov, A.V., Sokolov, L.L., Dikarev, V.V., 1996. Dynamics of Mars-orbiting dust: effects of light pressure and planetary oblateness. Celestial Mech. Dyn. Astron. 63, 313–339.

Krivov, A.V., Krüger, H., Grün, E., Thiessenhusen, K., Hamilton, D.P., 2002. A tenuous dust ring of Jupiter formed by escaping ejecta from the Galilean satellites. J. Geophys. Res. 107, 10.1029/2000JE001434.

Krivov, A.V., Feofilov, A.G., Dikarev, V.V., 2006. Search for the putative dust belts of Mars: the late 2007 opportunity. Planet. Space Sci., this issue.

Landau, L.D., Lifshitz, E.M., 1965. Mechanics. Oxford University Press, Oxford.

Makuch, M., Krivov, A.V., Spahn, F., 2005. Long-term dynamical evolution of dusty ejecta from Deimos. Planet. Space Sci. 53, 357–369.

Mannella, R., 2000. A gentle introduction to the integration of stochastic differential equations. In: Freund, J.A., Pöschel, T. (Eds.), Stochastic Processes in Physics, Chemistry, and Biology. Springer, Dordrecht, pp. 353–364.

Mannella, R., Palleschi, V., 1989. Fast and precise algorithm for computer simulation of stochastic differential equations. Phys. Rev. A 40, 3381–3386.

Milstein, G.N., Repin, Yu.M., Tretyakov, M.V., 2002. Symplectic integration of Hamiltonian systems with additive noise. SIAM J. Numer. Anal. 39, 2066–2088.

Pierre, A.G.S., Steele, W.A., 1969. Time correlations and conditional distribution functions for classical ensembles of free rotors. Phys. Rev. 184 (1), 172–186.

Purcell, E.M., 1979. Suprathermal rotation of interstellar grains. Astrophys. J. 231, 404–416.

Resibois, P., de Leener, M., 1977. Classical Kinetic Theory of Fluids. Wiley, New York.

Roatsch, T. (Ed.), 1988. Data of the Planetary System. Akademie-Verlag, Berlin.

Skoglov, E., 2002. The influence of the spin vectors of asteroids from the Yarkovsky effect. Astron. Astrophys. 393, 673–683.

Spahn, F., Krivov, A.V., Sremčević, M., Schwarz, U., Kurths, J., 2003. Stochastic forces in circumplanetary dust dynamics. J. Geophys. Res. 108, 5021, doi:10.1029/2002JE001925.

Spitale, J., Greenberg, R., 2001. Numerical evaluation of the general Yarkovsky effect: effects on semimajor axis. Icarus 149, 222–234.

Vokrouhlicky, D., Capek, D., 2002. Yorp-induced long-term evolution of the spin state of small asteroids and meteoroids: Rubincam's approximation. Icarus 159, 449–467.

# Appendix C

# E Ring Dust Sources: Implication from Cassini's Dust Measurements

SPAHN, F., ALBERS N., HÖRNING M., KEMPF S., KRIVOV, A. V., MAKUCH M., SCHMIDT J., SEISS M., SREMČEVIĆ, M. (2006).
E Ring Dust Sources: Implication from Cassini's Dust Measurements. **Planetary and Space Science**, 54:1024-1032.

Available online at www.sciencedirect.com
SCIENCE DIRECT
Planetary and Space Science 54 (2006) 1024–1032
Planetary and Space Science
www.elsevier.com/locate/pss

# E ring dust sources: Implications from Cassini's dust measurements

Frank Spahn[a,*], Nicole Albers[d], Marcel Hörning[a], Sascha Kempf[b], Alexander V. Krivov[c], Martin Makuch[a], Jürgen Schmidt[a], Martin Seiß[a], Miodrag Sremčević[d]

[a]*Universität Potsdam, Institut für Physik, Nichtlineare Dynamik, Am Neuen Palais 10, Potsdam, Germany*
[b]*Max-Planck-Institut für Kernphysik, Heidelberg, Germany*
[c]*Astrophysikalisches Institut und Universitäts-Sternwarte, Friedrich-Schiller-Universität Jena, Germany*
[d]*Laboratory of Atmospheric and Space Physics, University of Colorado, Boulder, USA*

Received 2 December 2005; accepted 4 April 2006
Available online 21 July 2006

**Abstract**

The Enceladus flybys of the Cassini spacecraft are changing our understanding of the origin and sustainment of Saturn's E ring. Surprisingly, beyond the widely accepted dust production caused by micrometeoroid impacts onto the atmosphereless satellites (the impactor-ejecta process), geophysical activities have been detected at the south pole of Enceladus, providing an additional, efficient dust source. The dust detector data obtained during the flyby E11 are used to identify the amount of dust produced in the impactor-ejecta process and to improve related modeling [Spahn, F., Schmidt, J., Albers, N., Hörning, M., Makuch, M., Seiß, M., Kempf, S., Srama, R., Dikarev, V.V., Helfert, S., Moragas-Klostermeyer, G., Krivov, A.V., Sremčević, M., Tuzzolino, A., Economou, T., Grün, E., 2006. Cassini dust measurements at Enceladus: implications for Saturn's E ring. Science, in press]. With this, we estimate the impact-generated dust contributions of the other E ring satellites and find significant differences in the dust ejection efficiency by two projectile families—the E ring particles (ERPs) and the interplanetary dust particles (IDPs). Together with the Enceladus south-pole source, the ERP impacts play a crucial role in the inner region, whereas the IDP impacts dominate the particle production in the outer E ring, possibly accounting for its large radial extent. Our results can be verified in future Cassini flybys of the E ring satellites. In this way poorly known parameters of the dust particle production in hypervelocity impacts can be constrained by comparison of the data and theory.


*PACS:* 94.10.Nh; 96.30.wr

*Keywords:* Saturn; Enceladus; E ring; Dust dynamics

## 1. Introduction

The E ring of Saturn extends from the orbit of the moon Mimas at 3 Saturnian radii ($R_\hbar = 60,268$ km) to Titan at $21R_\hbar$. It consists of icy dust grains of sizes $\approx 0.3,\ldots,3\,\mu$m in radius (Nicholson et al., 1996). The balance between the particle creation at Enceladus and to a lesser degree at the other satellites embedded in the E ring, and their annihilation in impacts on the same bodies and Saturn's A ring is responsible for the maintenance of this large dust complex. The particle creation process as well as their dynamics constrain the relatively narrow size range of particles that can stay in the ring (Showalter et al., 1991; Horányi et al., 1992).

Ejection of material by impacting projectiles (hereafter impactor-ejecta process) has been considered to be the most efficient process able to lift off particles into orbit around Saturn. The major impactor families are E ring particles (hereafter ERPs) and interplanetary dust particles (henceforth IDPs). However, it has not been clear which of both impactor types dominates the ring material supply. Hamilton and Burns (1994) discussed a self-sustainment of the E ring, but there are energetic arguments in favor of an additional support by IDP-projectile ejecta. Different IDP populations have been studied by Colwell (1993). His results have been used to predict the outcome of measurements of the cosmic dust analyzer (CDA) and to

*Corresponding author.
*E-mail address:* fspahn@agnld.uni-potsdam.de (F. Spahn).

0032-0633/$ - see front matter © 2006 Elsevier Ltd. All rights reserved.
doi:10.1016/j.pss.2006.05.022

discriminate between different impactor populations—the ERPs and IDPs (Spahn et al., 1999).

The view on the balance of the E ring matter has changed drastically when recently the high-rate detector (HRD) of the CDA uncovered an additional, efficient dust source near the south pole during the flyby E11 of the Cassini spacecraft with Enceladus on July 14th, 2005. A suite of Cassini experiments, infrared instruments (CIRS, VIMS), the neutral mass spectrometer (INMS), the magnetospheric imaging instrument (MIMI), the ultraviolet imaging spectrometer (UVIS), and the Cassini cameras (ISS), provided hints for geophysical activities at the south pole of Enceladus. The HRD has also registered at least five times more dust originating at the south pole than motes released in an impactor-ejecta process (Spahn et al., 2006). This region of the satellite is characterized by unusually high temperatures ($>90$ K compared to 70 K expected by solar irradiation) measured by CIRS and VIMS (Brown et al., 2006; Spencer et al., 2006), and clear signs of a geophysically active surface, the so-called "tiger-stripes", detected by the Cassini cameras—showing locally even higher temperatures $>100$ K. The data of ISS, UVIS, MIMI and INMS (Porco et al., 2006; Hansen et al., 2006; Jones et al., 2006; Waite Jr. et al., 2006) have found neutral gas escaping Enceladus' south pole.

In this paper, we investigate the dust production at all E ring satellites based on the results of the HRD/CDA measurements near Enceladus obtained during the E11 flyby (Spahn et al., 2006). The impactor-ejecta contribution of dust at Enceladus found with these measurements is used to calculate the impact-ejecta generated dust production at the satellites Mimas, Tethys, Dione and Rhea. For this purpose, it is reasonable to assume that the dust production at these moons is dominated by the impactor-ejecta process. With this assumption the efficiencies of the dust ejection by the different impactor families—ERPs or IDPs—are estimated. If there were significant differences in the related dust productions, future Cassini flybys of these satellites would allow us to distinguish between the dust contributions caused by IDPs and ERPs, so that their role in sustaining the E ring can be judged.

The paper is organized as follows. In Section 2 the physics of the impactor-ejecta process, driven by the different impactor families, is summarized. Dust contributions coming from different E ring satellites are derived and discussed in Section 3. Conclusions are drawn in Section 4.

## 2. Sources of E ring dust

The dust production processes at source satellites in the E ring provide the initial conditions for the dust particle dynamics governing the subsequent "life" of the dusty motes until they hit sinks—often their own sources, or the main rings. The balance between creation and removal of dust as well as the dynamical evolution of the grains between their "birth" and "death" determine largely the appearance of a dust ring. The major goal of this paper is to evaluate the dust production at the satellites embedded in the E ring based upon recent results of the Cassini mission at Saturn.

Observations (Showalter et al., 1991) and dynamical studies (Horányi et al., 1992) have convincingly pointed to Enceladus as the main source of the E ring of Saturn. The dust measurements performed during the flyby E11 of Cassini with Saturn on July 14, 2005, revealed that at least 85% of the grains are generated near Enceladus' south pole (Spahn et al., 2006), in geophysical processes (see Fig. 3). The remaining 15% of the dust rate detected by the HRD pose an upper limit on the dust creation rate in the impactor-ejecta process at Enceladus. It is plausible to assume that the impactor-ejecta process is also active at all other E ring satellites. In this paper we estimate the relative contributions of the dust production by the two projectile families at these satellites. To this aim in the following subsection we briefly summarize the physics of the impactor-ejecta mechanism.

### 2.1. The impactor-ejecta process

A common process of dust creation in the solar system is hypervelocity impacts of micrometeoroids onto surfaces of atmosphereless bodies—planets, asteroids, comets, satellites, ring particles, etc. Fig. 1 illustrates this mechanism schematically. A hypervelocity projectile may release considerably more material than its own mass. This cosmic erosion gave rise to speculations about the existence of dust rings around Mars (Soter, 1971), which still escape their discovery (see Showalter et al., 1991; Krivov et al., 2003; Makuch et al., 2006). Furthermore, such impacts play a major role in creating and sustaining circumplanetary dust rings (Hamilton and Burns, 1994; Showalter, 1998) and also dust clouds enveloping planetary satellites lacking a gas atmosphere (Krivov et al., 2003; Sremčević et al., 2003).

A quantitative description of the impactor-ejecta mechanism from first physical principles is complicated.

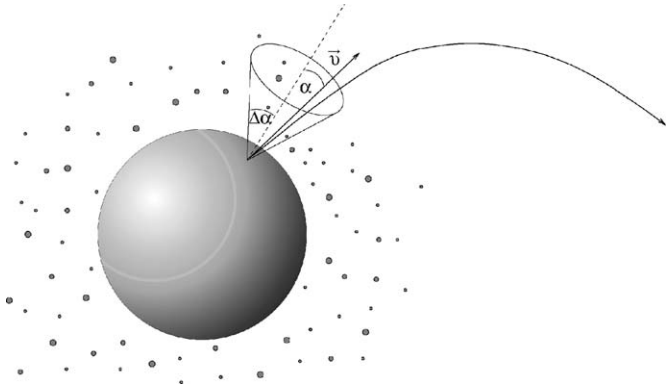


Fig. 1. Sketch of the impactor-ejecta model. An energetic projectile has hit the surface of a satellite, creating ejecta which leave the surface with the speed $\vec{v}$ in a cone of opening angle $\Delta\alpha$. The dashed line indicates the normal to the surface at the position of the impact.

Therefore, the following argumentation is mainly based on experimental data (Koschny and Grün, 2001) or dimensional analyses (Housen et al., 1983; Housen, 1991) reviewed in detail by Krivov et al. (2003). We recapitulate the most important relations characterizing the impactor-ejecta process, specified for Enceladus so that their validity can be judged with the Cassini HRD data. Then, we focus on the spatial dependencies of these relations in order to apply them to the other E ring moons.

Essential for the efficiency of cosmic erosion is the mass flux of the impacting projectiles defined as

$$F_{\mathrm{imp}} = \langle m_{\mathrm{imp}}\rangle n_{\mathrm{imp}}(r)\langle v_{\mathrm{imp}}\rangle(r), \tag{1}$$

with the mass of the impactors $m_{\mathrm{imp}}$, the related number density $n_{\mathrm{imp}}(r)$ and impact velocity $\langle v_{\mathrm{imp}}\rangle(r)$ at the target satellite $r$. The mass production rate caused by the impacting projectiles is then defined by

$$M^{+} = F_{\mathrm{imp}}\, YS, \tag{2}$$

with the cross section of the source satellite $S = \pi R^2$. The yield $Y$ is the fraction of the ejected mass to that of the projectile (IDP, ERP). Laboratory experiments (Koschny and Grün, 2001) suggest the relation (in SI units)

$$Y = 2.64 \times 10^{-5}\, \mathrm{m}_{\mathrm{imp}}^{0.23} v_{\mathrm{imp}}^{2.46}, \tag{3}$$

for icy surfaces. This choice of yield $Y$ assumes similar surface properties. We assume a power law for the cumulative size distribution in order to obtain the total number of ejected particles larger than a certain radius $s$

$$N^{+}(>s, r) = \frac{3-\gamma}{\gamma}\frac{F_{\mathrm{imp}}\, YS}{m_{\max}}\left(\frac{s_{\max}}{s}\right)^{\gamma} \tag{4}$$

as a function of the distance $r$ from Saturn. For the mass distribution index $\gamma$ we choose $\gamma = 12/5$ (Krivov et al., 2003), but different values have been applied as e.g. $\gamma = 2.1$ at Enceladus (Juhász and Horányi, 2002). The parameters $s_{\max}$ and thus $m_{\max}$ are radii and masses characteristic for the impactor's family. The velocities of the $N^{+}$ particles are distributed according to a power law (Krivov et al., 2003)

$$f_v = \frac{\beta-1}{v_0}\left(\frac{v}{v_0}\right)^{-\beta}\Theta[v - v_0], \tag{5}$$

with the normalization

$$\int_0^{\infty} f_v(v) = 1, \tag{6}$$

where $\Theta(x)$ denotes the Heaviside function. The slope of the velocity distribution lies in the range $\beta \in (2, 3)$, where $\beta \approx 2$ is suitable for regolith and the steeper slope ($\beta \approx 3$) applies to solid surfaces.

The parameter $v_0$ ensures the convergence of the integral and is, together with the yield $Y$, source of rather large uncertainties of $N^{+}$. Both values, $v_0$ and $Y$, depend on each other according to

$$\frac{K_{\mathrm{e}}}{K_{\mathrm{i}}} = Y\frac{\beta-1}{3-\beta}\left(\frac{v_0}{v_{\mathrm{imp}}}\right)^2\left\{\left(\frac{v_0}{v_{\max}}\right)^{\beta-3} - 1\right\} \quad \text{for } \beta \neq 3,$$

$$\frac{K_{\mathrm{e}}}{K_{\mathrm{i}}} = 2Y\left(\frac{v_0}{v_{\mathrm{imp}}}\right)^2 \ln\frac{v_{\max}}{v_0} \quad \text{for } \beta = 3. \tag{7}$$

The ratio $K_{\mathrm{e}}/K_{\mathrm{i}}$ between the kinetic energies of the ejecta $K_{\mathrm{e}}$ and the impactors $K_{\mathrm{i}}$, respectively, depends on the mean impact speeds and projectile masses. For instance, one obtains for the IDPs $K_{\mathrm{e}}/K_{\mathrm{i}} \approx 0.3$ and for the E ring impactors $K_{\mathrm{e}}/K_{\mathrm{i}} < 0.05$ (Krivov et al., 2003).

The three-body escape velocity of the source moon of radius $R$ and mass $M$ is

$$v_{\mathrm{esc}} = \sqrt{2GM\left(\frac{1}{R} - \frac{1}{h_{\mathrm{Hill}}}\right)}, \tag{8}$$

where $h_{\mathrm{Hill}} = r\sqrt[3]{M/3(M_{\hbar} + M)}$ denotes the radius of the moon's Hill sphere with Saturn's mass $M_{\hbar}$. Now we can calculate the fraction

$$N_{\mathrm{esc}}^{+}(>v_{\mathrm{esc}}, >s, r) = (v_0/v_{\mathrm{esc}})^{\beta-1} N^{+}(>s, r) \tag{9}$$

of ejecta having velocities larger than the three-body escape velocity, i.e. providing an estimate for the efficiency of the dust source located at the distance $r$ from Saturn. Similarly, the total mass rate of escaping particles is

$$M_{\mathrm{esc}}^{+}(>v_{\mathrm{esc}}, r) = (v_0/v_{\mathrm{esc}})^{\beta-1} M^{+}(r). \tag{10}$$

To account for anisotropies of ejection efficiency the distribution (9) can be folded with an angular distribution of positions on the satellite surface (Sremčević et al., 2003). In this way it is possible to simulate isolated dust sources, which has, for example, led to the identification of the south-pole source at Enceladus in the CDA data (Spahn et al., 2006).

In the following we will estimate the respective $N^{+}(r)$ for the IDPs and ERPs. While for the IDPs the dependence of $N^{+}$ on radial distance from Saturn is caused by the varying strength of gravitational focusing by the planet, the production rate of particles in impacts of ERPs varies strongly with the projectile density, and thus, a model of the whole ring is necessary in order to estimate $N^{+}$ for the ERPs. These differences in the dust production efficiencies should be detectable with the CDA in future flybys of Cassini at E ring moons.

### 2.2. Interplanetary dust projectiles—IDPs

The mass flux of IDPs at Saturn (Divine, 1993)

$$F_{\mathrm{imp}}^{(\infty)} = 1.8 \times 10^{-16}\,\mathrm{kg\,m^{-2}\,s^{-1}} \tag{11}$$

and its corresponding velocity relative to Saturn

$$v_{\mathrm{imp}}^{(\infty)} = 9.5\,\mathrm{km\,s^{-1}} \tag{12}$$

are modified by the gravity of Saturn in its vicinity. The index $\infty$ indicates quantities far from Saturn but at the same distance from the Sun. Using the two-body energy integral and the dust production rate at one of the moons, e.g. at Enceladus ($r = r_{\mathrm{E}}$), one can derive the $r$-dependence of the dust production rate (Krivov et al., 2003, and

references therein) at a certain E ring moon (index M)

$$N^+(>s,r_M)=N^+(>s,r_E)\frac{f_{imp}(r_M)}{f_{imp}(r_E)}\frac{Y_M}{Y_E}\frac{R_M^2}{R_E^2} \tag{13}$$

of grains larger in radius than $s$ ejected in impacts of IDPs, with the normalized particle flux accounting for the gravitational focusing[1]

$$f_{imp}(r)=\sqrt{1+\frac{2GM_\hbar}{r(v_{imp}^\infty)^2}}\times\left\{\frac{1}{2}\sqrt{1+\frac{2GM_\hbar}{r(v_{imp}^\infty)^2}}+\frac{1}{2}\sqrt{1+\frac{2GM_\hbar}{r(v_{imp}^\infty)^2}-\left(\frac{R_\hbar}{r}\right)^2\left(1+\frac{2GM_\hbar}{R_\hbar(v_{imp}^\infty)^2}\right)}\right\}. \tag{14}$$

Here, the equatorial radius of Saturn is labeled by $R_\hbar$. The cumulative rate near Enceladus is found to be

$$N^+_{IDP}(>s,r_E)=3.6\times10^{12}\left(\frac{s}{(1\,\mu m)}\right)^{-\gamma}(s^{-1}), \tag{15}$$

where $m_{imp}=10^{-8}$ kg (corresponding to approx. $s_{imp}=100\,\mu m$), $m_{max}\approx m_{imp}$, and the resulting yield according to Eq. (3) of $Y=1.5\times10^4$ has been applied. With this, relation (9), where $v_0(\beta=2)=2.7\,ms^{-1}$ and $v_0(\beta=3)=29.9\,ms^{-1}$, yields the cumulative number of grains with radii larger than $s$ and velocities $v>v_{esc}^{(E)}=206.5\,ms^{-1}$ which escape Enceladus and contribute to the ring:

$$N^+_{IDP}(>v_{esc}^{(E)},>s,r_E)\approx\begin{cases}4.9\times10^{10}\left(\frac{s}{(1\,\mu m)}\right)^{-\gamma}(s^{-1}) & \text{for } \beta=2,\\ 7.7\times10^{10}\left(\frac{s}{(1\,\mu m)}\right)^{-\gamma}(s^{-1}) & \text{for } \beta=3.\end{cases} \tag{16}$$

Numerical values of $N^+_{IDP}$ have probably an order of magnitude or more uncertainty (Krivov et al., 2003). A comparison of the model predictions and Galileo measurements at Galilean satellites indicated that corresponding $N^+_{IDP}$ for Callisto, Europa, and Ganymede were systematically overestimated by a factor of 2–3 (Sremčević et al., 2005).

If the numbers (15) or (16), respectively, and the corresponding yield $Y$, could be specified by Cassini observations, Eqs. (9)–(13) are suitable to estimate the dust production by IDP impacts at the other E ring satellites. With these relations the number of particles (with radii larger than $s$) which may escape the gravity of the moon is

$$\frac{N^+_{IDP}(>v_{esc}^{(M)},>s,r_M)}{N^+_{IDP}(>v_{esc}^{(E)},>s,r_E)}=\left(\frac{v_0^{(M)}}{v_0^{(E)}}\frac{v_{esc}^{(E)}}{v_{esc}^{(M)}}\right)^{\beta-1}\frac{f_{imp}(r_M)}{f_{imp}(r_E)}\frac{R_M^2}{R_E^2}\frac{Y_M}{Y_E}, \tag{17}$$

where the escape velocity of the satellite is denoted by $v_{esc}^{(M)}$.

### 2.3. E ring impactors—ERPs

In addition to the IDP projectiles we need to estimate the mass flux of E ring impactors $F_{imp}(r)=\langle m_{imp}\rangle n_{imp}(r)\langle v_{imp}\rangle(r)$ as a function of distance from Saturn $r$ in the equatorial plane. To this end, we need a model for the configuration of particles in the E ring. For simplicity, we employ results from the modeling of Voyager observations derived by Showalter et al. (1991) (see also Juhász and Horányi, 2002)

$$n_{imp}(r)=n_{imp}(r_E)\frac{\langle H\rangle(r_E)}{\langle H\rangle(r)}\begin{cases}\left(\frac{r}{r_E}\right)^{15} & \text{for } r<r_E,\\ \left(\frac{r}{r_E}\right)^{-7} & \text{for } r>r_E,\end{cases} \tag{18}$$

with the particle number density near Enceladus $n_{imp}(r_E)\approx1\,m^{-3}$ and the mean vertical width $\langle H\rangle(r_E)\approx8\times10^3$ km up to about $\langle H\rangle\approx2\times10^4$ km near Rhea. For the mean impact speed we assume that $s\sim0.65\,\mu m$ E ring motes coming from Enceladus quickly develop large eccentricities, until they are absorbed by the A ring or the E ring moons after only a few years. Then, following Hamilton and Burns (1994), the mean impact velocity with the E ring satellites can be estimated as

$$\langle v_{imp}\rangle\approx\langle e\rangle v_K(r_M)\quad\text{with } v_K(r_M)=\sqrt{\frac{GM_\hbar}{r_M}}, \tag{19}$$

with the mean eccentricity $\langle e\rangle\approx0.5$.

The applicability of Eq. (19) is discussed in this paragraph using data from a simulation (Fig. 2). The evolution of one particle launched at Enceladus is simulated for two Saturnian years, subject to gravitational, electromagnetic and radiation forces which are plausible for the E-ring region (Horányi et al., 1992). The equilibrium potential of the particle is assumed to follow a form suggested by recent Cassini data (Kempf et al., 2006; Wahlund et al., 2005), ranging from about $-2$ to $-3$ V between 3 to $4R_\hbar$ with a transition to positive values between 6 and $8R_\hbar$ to an approximately constant value of about $+5$ V outside $10R_\hbar$. In this case, particles of a radius near 0.65 μm most rapidly develop eccentricities as high as 0.6–0.7. The lower left panel in the figure shows the relative velocity $v_{rel}$ of the dust particle in the simulation with respect to the velocity of a circular Keplerian orbit (labeled in the plot by $v_K$) at the instantaneous radial position $r$ (stored equidistantly in time) of the particle. When plotted vs the instantaneous eccentricities of the particle the linear

[1]Colombo et al. (1966) have a misprint in their Eq. (11). Evaluating their Eq. (7) actually results in Eq. (14) above which we verified using different methods.

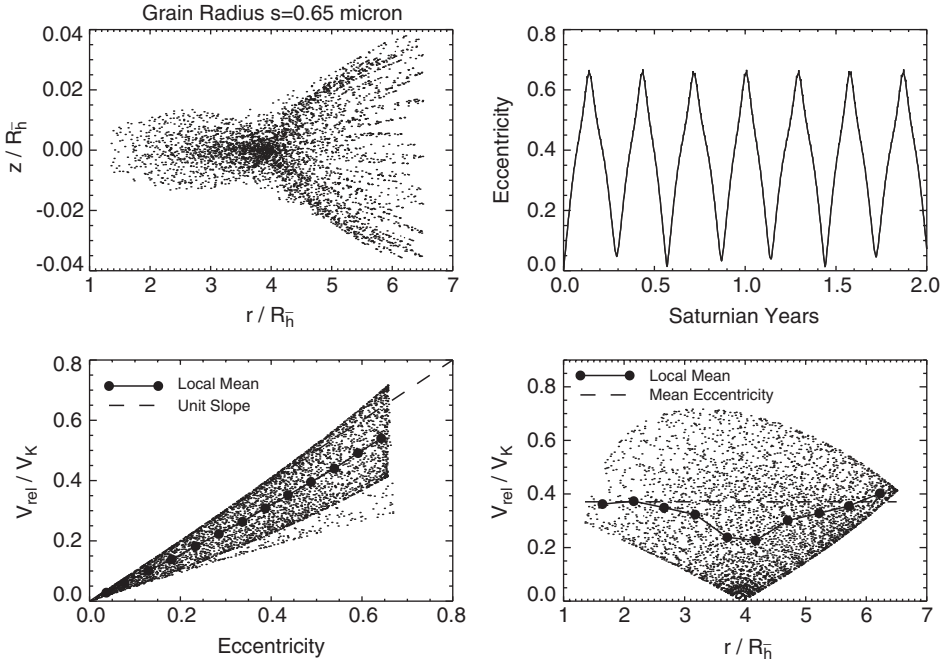


Fig. 2. Simulation of a dust particle launched on the orbit of Enceladus. *Upper left panel*: scatter plot of height $z$ of the particle above the equatorial plane vs radial distance from Saturn $r$. *Upper right*: evolution of the particle eccentricity. *Lower left*: ratio of the particle velocity relative to a circular Keplerian orbit at the instantaneous particle position vs the instantaneous eccentricity. *Lower right*: particle velocity relative to a circular Keplerian orbit normalized by the circular Keplerian orbit vs instantaneous radial position.

trend of Eq. (19) is clearly visible. The lower right panel of Fig. (2) shows that ratio $v_{\rm rel}/v_{\rm K}$ plotted vs the instantaneous radial particle position. For all radial positions reached by the particle the local mean of this velocity ratio is indeed on the order of the total mean eccentricity. A qualitatively similar behavior is observed in simulations with different grain sizes, for different forms of the electromagnetic equilibrium potential, or, if particle sinks, plasma drag, and the gravity of the moons are included in the simulation.

With Eqs. (18) and (19) the particle creation at Enceladus caused by 0.65 μm E ring projectiles ($\langle m_{\rm imp}\rangle = 2.3\times10^{-15}$ kg) with a yield $Y = 25.3$ according to Eq. (3) is found to be

$$N^{+}_{\rm ERP}(>s, r_{\rm E}) = 1.2\times10^{14}\left(\frac{s}{(1\,\mu{\rm m})}\right)^{-\gamma}({\rm s}^{-1}). \tag{20}$$

The fraction of ejected particles

$$N^{+}_{\rm ERP}(>v^{(\rm E)}_{\rm esc}, >s, r_{\rm E}) = \begin{cases} 1.5\times10^{13}\left(\frac{s}{(1\,\mu{\rm m})}\right)^{-\gamma}({\rm s}^{-1}) & \text{for } \beta = 2, \\ 3.3\times10^{13}\left(\frac{s}{(1\,\mu{\rm m})}\right)^{-\gamma}({\rm s}^{-1}) & \text{for } \beta = 3 \end{cases} \tag{21}$$

can escape Enceladus' vicinity (Eq. (9) for $v_0(\beta=2) = 26.5\,{\rm ms}^{-1}$ and $v_0(\beta=3) = 109.0\,{\rm ms}^{-1}$) and support the E ring. Varying the radius of the impacting E ring projectiles for $s\in[0.5; 1.0; 2.0]\,\mu$m and the mean eccentricity between $\langle e\rangle \in [0.25; 0.5]$ did result in changes of $N^{+}_{\rm ERP}$ of one order of magnitude or more. For instance, a power law distribution in the range $s\in[0.3\cdots3]\,\mu$m (Nicholson et al., 1996; Juhász and Horányi, 2002) gives larger rates, whereas a narrow distribution around $s\approx1\pm0.3\,\mu$m (Showalter et al., 1991) reduces it by an order of magnitude. Similar to Eq. (17) the dust production rate for the ERP at different E ring moons may be written as

$$\frac{N^{+}_{\rm ERP}(>v^{(\rm M)}_{\rm esc}, >s, r_{\rm M})}{N^{+}_{\rm ERP}(>v^{(\rm E)}_{\rm esc}, >s, r_{\rm E})} = \left(\frac{v^{(\rm M)}_0}{v^{(\rm E)}_0}\frac{v^{(\rm E)}_{\rm esc}}{v^{(\rm M)}_{\rm esc}}\right)^{\beta-1}\frac{n_{imp}(r_{\rm M})}{n_{imp}(r_{\rm E})}\frac{v_{\rm K}(r_{\rm M})}{v_{\rm K}(r_{\rm E})}\frac{R^2_{\rm M}}{R^2_{\rm E}}\frac{Y_{\rm M}}{Y_{\rm E}}. \tag{22}$$

## 3. Results and discussion

In the following we will use the CDA/HRD measurements performed during the Cassini–Enceladus flyby E11 on July 14, 2005 in order to estimate the different contributions of impactor-ejecta created dust at various satellites embedded in the E ring. In the subsequent subsections, we will

(1) briefly summarize the approach applied by Spahn et al. (2006) for the Enceladus flyby;
(2) compare the observational results with the impactor-ejecta rates;
(3) apply the impactor-ejecta model concerning ERPs and IDPs to all satellites embedded in the E ring and discuss the consequences.

### 3.1. Dust production rates at Enceladus from Cassini-HRD measurements

The left panel of Fig. 3 shows contours of particle density in Enceladus' vicinity simulated for isotropic ejection of grains from Enceladus' surface. The dynamics of freshly ejected grains has been tracked until they meet one of the E ring sinks. The phase-space variables have then been stored equidistantly in time mimicking a steady single particle distribution. In this way the E ring background has been modeled where in Fig. 3 only particles with radii $s > 2\,\mu m$ have been counted, in accordance with the HRD threshold. Superposing the freshly ejected fluxes with those of the E ring background we have calculated the dust impact rates expected at the HRD along the Cassini trajectory (E11) as a function of time. It turned out, that the dust launched by the impactor-ejecta process causes impact rates at the dust detector which are symmetric with respect to the time of the closest approach (C/A), independently of the type of the projectile family. Thus, the dust impact rate at the CDA/HRD is expected to peak at C/A. This result of the modeling has then been compared to the HRD data (diamonds). This flyby has provided a particularly good chance to identify the location of dust sources at the satellites' surface since the spacecraft pierced deeply through the Hill sphere of Enceladus.

Surprisingly, the dust impact-rate at the HRD has shown a maximum almost a minute before the C/A contradicting our expectations based upon impact-created dust cloud. An efficient dust source at the south pole of Enceladus offers a solution of this inconsistency (Brown et al., 2006; Hansen et al., 2006; Jones et al., 2006; Spahn et al., 2006). Our fit to the data has yielded the following absolute dust ejection rates:

$$N^{+}_{\mathrm{south}}(>v^{(\mathrm{E})}_{\mathrm{esc}}, >2\,\mu m, r_{\mathrm{E}}) \approx 5\times 10^{12}\ (\mathrm{s}^{-1}) \tag{23}$$

for the south-pole source and

$$N^{+}_{\mathrm{impact}}(>v^{(\mathrm{E})}_{\mathrm{esc}}, >2\,\mu m, r_{\mathrm{E}}) < 1\times 10^{12}\,(\mathrm{s}^{-1}) \tag{24}$$

for the impact-generated dust. The latter number is to be compared to the ejecta rates (16) and (21), applying a correction factor of $2^{-\gamma} \approx 0.2$ accounting for larger grains ($s \geqslant 2\,\mu m$) detectable with the HRD.

### 3.2. Comparison of the measured and predicted rates at Enceladus

Firstly, the number (24) accounts for both kinds of projectiles, IDPs and ERPs, creating dust by their impacts, i.e. it is a superposition of both contributions

$$N^{+}_{\mathrm{impact}} = N^{+}_{\mathrm{ERP}} + N^{+}_{\mathrm{IDP}}. \tag{25}$$

However, which of both contributions, $N^{+}_{\mathrm{ERP}}$ or $N^{+}_{\mathrm{IDP}}$, dominates the dust generated by impactors cannot be judged from the single flyby E11 of Cassini at Enceladus. Our estimates (16) and (21) indicate that the dust production caused by the IDPs is less efficient by a factor of $10^{-2}$ mainly due to the very large E ring flux compared to the IDPs. ERPs seem to dominate the creation of E ring grains near Enceladus, of course, in addition to the most efficient source at the south pole.

The questions remain: is there a possibility to discriminate between contributions ejected by the ERPs and the IDPs? And, can parameters characterizing the impactor-ejecta model be gauged using the HRD result obtained during the E11 flyby?

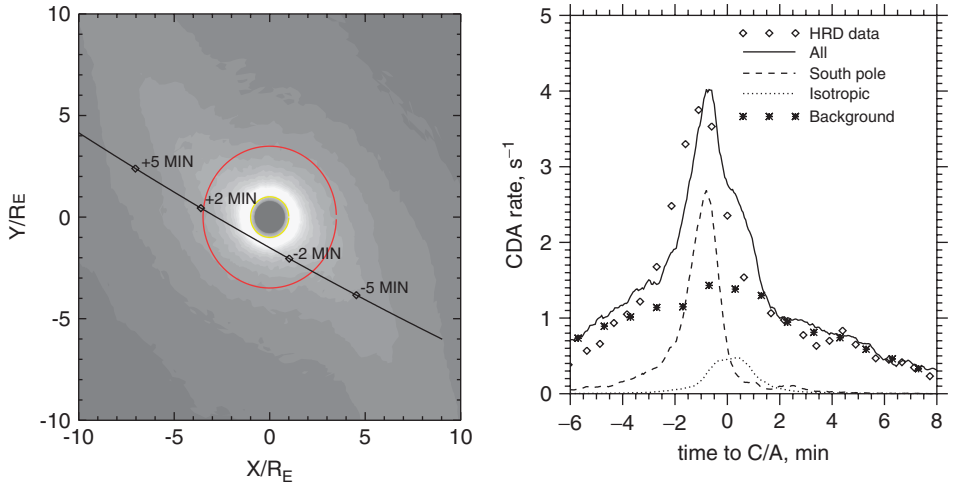


Fig. 3. *Left panel*: Contours of equal particle density in Enceladus' vicinity in the equatorial plane ($x$ points radially outward, $y$ in orbit direction). This dust configuration is produced by an isotropic distribution of dust sources on the satellite. A projection of the Cassini trajectory during the flyby E11 (14 July 2005) onto the plane is shown. The spacecraft crosses the plane from south. *Right*: HRD data (diamonds) and a fit from simulated dust configurations in the moon's vicinity. The model rate which is composed of south-pole dust (dashed line), grains launched by the impactor-ejecta process (dotted curve), and the E ring background (stars). For the simulation of the latter 1 μm particles have been chosen which are subject to the perturbations Saturn's oblateness, Lorentz force and radiation pressure force. The ratio between rate of the south-pole source and the impactor-ejecta generated one are chosen such that no secondary peak develops in the combined profile directly at C/A.

In order to compare the model and the measured HRD rates, we recall the dust production numbers (16) and (21) at Enceladus for grains larger than $s = 2\,\mu m$

$$N^{+}_{IDP}(>v^{(E)}_{esc}, >2\,\mu m) \approx \begin{cases} 9.2\times10^{9}\,(s^{-1}) & \text{for } \beta = 2, \\ 1.5\times10^{10}\,(s^{-1}) & \text{for } \beta = 3, \end{cases} \quad (26)$$

$$N^{+}_{ERP}(>v^{(E)}_{esc}, >2\,\mu m) \approx \begin{cases} 2.8\times10^{12}\,(s^{-1}) & \text{for } \beta = 2, \\ 6.2\times10^{12}\,(s^{-1}) & \text{for } \beta = 3. \end{cases} \quad (27)$$

Table 1
Physical properties of embedded satellites within Saturn's E ring

| Satellite | $r/R_h$ | $M$ ($10^{20}$ kg) | $R$ (km) | $v_{esc}$ (m s$^{-1}$) |
|---|---|---|---|---|
| Mimas | 3.3 | 0.4 | 198.8 | 127.2 |
| Enceladus | 4.1 | 1.1 | 252.3 | 204.8 |
| Tethys | 5.1 | 6.2 | 536.3 | 338.3 |
| Dione | 6.5 | 11.0 | 563.0 | 462.7 |
| Rhea | 9.1 | 23.1 | 765.5 | 591.8 |

$v_{esc}$ is the three-body escape velocity according to Eq. (8).

In view of these rough estimates the rates caused by E ring impactors at Enceladus meet the observations (Spahn et al., 2006) fairly well so that the relation defining the yield (3) specifies obviously essential aspects of dependence on the impactors mass $m_{imp}$ and impact speed $v_{imp}$. Further, the ERPs dominate the impactor generated creation of dust at Enceladus compared to that of the IDPs— by a factor of 100. Does this also apply to the other satellites embedded in the E ring?

### 3.3. Dust production rates at different moons

A comparison of the dust production rates $N^{+}_{IDP}$ and $N^{+}_{ERP}$ at the E ring moons from Mimas to Rhea (physical properties are given in Table 1) is presented in the Table 2. Values are based on Eq. (16) and (17) for the IDPs and Eqs. (21) and (22) for the ERPs. Values marked with (∗) are normalized to the corresponding value at Enceladus.

There is a clear difference in the dust production rates between the two projectile families—ERPs and IDPs. Whereas the ejecta created by the ERPs are only significant at Enceladus and perhaps at Tethys, the other satellites do

Table 2
Model parameters and calculated values for IDPs and ERPs

| Scenario | Parameter | Eq. | Mimas | Enceladus | Tethys | Dione | Rhea |
|---|---|---|---|---|---|---|---|
| | $f_{imp}(r_M)$ | (14) | 5.0 | 4.3 | 3.7 | 3.1 | 2.5 |
| | $F_{imp}$ ($10^{-15}$ kg m$^{-2}$ s$^{-1}$) | (1) | 0.89 | 0.77 | 0.67 | 0.56 | 0.46 |
| | $Y$ | (3) | 18,000 | 15,000 | 12,000 | 9,800 | 7,500 |
| | $N^{+}$ ($10^{12}$ s$^{-1}$) | (4) | 3.2 | 3.6 | 12.0 | 8.7 | 10.0 |
| | $v_0(\beta = 2)$ (m s$^{-1}$) | (7) | 2.6 | 2.7 | 2.8 | 3.0 | 3.1 |
| IDP | $N^{+}(>v_{esc};\beta = 2)$ ($10^{10}$ s$^{-1}$) | (9) | 6.6 | 4.9 | 9.7 | 5.6 | 5.3 |
| | $M^{+}(>v_{esc};\beta = 2)$ (kg s$^{-1}$) | (10) | 0.042 | 0.031 | 0.062 | 0.035 | 0.033 |
| | $v_0(\beta = 3)$ (m s$^{-1}$) | (7) | 29 | 30 | 30 | 31 | 32 |
| | $N^{+}(>v_{esc};\beta = 3)$ ($10^{10}$ s$^{-1}$) | (9) | 17.0 | 7.7 | 9.4 | 3.9 | 2.9 |
| | $M^{+}(>v_{esc};\beta = 3)$ (kg s$^{-1}$) | (10) | 0.11 | 0.049 | 0.060 | 0.025 | 0.019 |
| | $N^{+}(>v_{esc};\beta = 2)(*)$ | (17) | 1.4 | 1.0 | 2.0 | 1.1 | 1.1 |
| | $N^{+}(>v_{esc};\beta = 3)(*)$ | (17) | 2.2 | 1.0 | 1.2 | 0.5 | 0.4 |
| | $n_{imp}(r_M)$ (m$^{-3}$) | (18) | 0.03 | 1.0 | 0.2 | 0.02 | 0.002 |
| | $F_{imp}$ ($10^{-15}$ kg m$^{-2}$ s$^{-1}$) | (1) | 620 | 15,000 | 2,300 | 270 | 15 |
| | $Y$ | (3) | 33 | 25 | 19 | 14 | 10 |
| | $N^{+}$ ($10^{12}$ s$^{-1}$) | (4) | 3.9 | 120.0 | 63.0 | 6.0 | 0.41 |
| | $v_0(\beta = 2)$ (m s$^{-1}$) | (7) | 25 | 26 | 28 | 29 | 32 |
| ERP | $N^{+}(>v_{esc};\beta = 2)$ ($10^{10}$ s$^{-1}$) | (9) | 78 | 1,500 | 520 | 38 | 2.2 |
| | $M^{+}(>v_{esc};\beta = 2)$ (kg s$^{-1}$) | (10) | 0.50 | 9.5 | 3.3 | 0.24 | 0.014 |
| | $v_0(\beta = 3)$ (m s$^{-1}$) | (7) | 106 | 109 | 112 | 116 | 121 |
| | $N^{+}(>v_{esc};\beta = 3)$ ($10^{10}$ s$^{-1}$) | (9) | 270 | 3,300 | 690 | 37 | 1.7 |
| | $M^{+}(>v_{esc};\beta = 3)$ (kg s$^{-1}$) | (10) | 1.7 | 21.0 | 4.4 | 0.24 | 0.011 |
| | $N^{+}(>v_{esc};\beta = 2)(*)$ | (22) | 0.05 | 1.0 | 0.3 | 0.03 | 0.001 |
| | $N^{+}(>v_{esc};\beta = 3)(*)$ | (22) | 0.08 | 1.0 | 0.2 | 0.01 | 0.0005 |
| | $F^{ERP}_{imp}/F^{IDP}_{imp}$ ($10^{3}$) | | 0.69 | 19.0 | 3.4 | 0.47 | 0.033 |
| IDP | $Y_{ERP}/Y_{IDP}$ ($10^{-3}$) | | 1.8 | 1.7 | 1.6 | 1.5 | 1.3 |
| vs | $N^{+}_{ERP}/N^{+}_{IDP}$ | | 1.2 | 32.0 | 5.4 | 0.69 | 0.041 |
| ERP | $N^{+}_{ERP}/N^{+}_{IDP}(>v_{esc})$ $(\beta = 2)$ | | 12.0 | 310.0 | 53.0 | 6.8 | 0.42 |
| | $N^{+}_{ERP}/N^{+}_{IDP}(>v_{esc})$ $(\beta = 3)$ | | 16.0 | 420.0 | 73.0 | 9.5 | 0.59 |

(∗) denotes values normalized to respective Enceladus' values.

practically not contribute to the E ring dust. In the E ring outskirts the IDPs dust contribution is comparable and even exceeds the ERP production. However, one has to remember that the total share of dust creation beyond Dione is less than 1% and that the majority of the dust comes from Enceladus and Tethys. Nevertheless, even such a small dust supply in the outer E ring, driven to great extent by IDPs, might help to understand the large radial extent of the E ring.

These relatively large differences in the dust production efficiency caused by ERPs at the other moons in the E ring furnish an opportunity to discriminate between the two impactor classes. To this aim, further close Cassini flybys of the satellites embedded in the E ring, including Enceladus, are necessary. Especially, more flybys of Enceladus would be beneficial in order to study the nature of the south-pole source as well as the dust production caused by the "classical" impactor-ejecta mechanism.

In Table 2 we list the total mass production rate $M^+(>v_{esc})$ for IDPs and ERPs. The combined $M^+(>v_{esc})$ for IDPs is $\sim 0.1\,\mathrm{kg\,s^{-1}}$, while for ERPs it is $\sim 10\,\mathrm{kg\,s^{-1}}$. Based on the analysis of Voyager data, Juhász and Horányi (2002) give an estimate of $\sim \mathrm{kg\,s^{-1}}$ required to fit the observations for grain sizes of $s \in [0.1, 2.2]\,\mu\mathrm{m}$. Calculating $M^+(s \in [s_1, s_2]) = ((s_2/s_{\max})^{3-\gamma} - (s_1/s_{\max})^{3-\gamma})$ $M^+ \approx 0.1 M^+$ gives $\sim 2\,\mathrm{kg\,s^{-1}}$ for ERPs which is consistent with Voyager data.

It is interesting to emphasize that Tethys obviously serves as the second efficient dust source of the E ring (see Table 2) supporting the Earth-based observations with the W. M. Keck telescope by de Pater et al. (2004) during the ring plane crossing of the Earth in summer 1995.

## 4. Conclusions

In this paper we have investigated the role of the impactor-ejecta process for the dust production at satellites embedded in the E ring of Saturn. The study is based on the dust measurements during Cassini's Enceladus flyby E11 which have tightly constrained the rates of dust production by a source near the moon's south pole, as well as by hypervelocity impacts (Spahn et al., 2006). The latter rate has been compared to models describing the impactor-ejecta process driven by two impactor families: the E ring particles (ERPs) themselves and interplanetary dust projectiles (IDPs). In particular, the yield $Y$ and the flux $F_{\mathrm{imp}}^{\mathrm{IDP}}$ specified in Krivov et al. (2003) are found to be consistent with the E11 data.

Further, the impactor-ejecta model has been applied to both impactor families hitting other satellites embedded in the E ring. Significant differences have been obtained for the dust production efficiencies at these moons, as summarized in Tables 1 and 2. The inner region of the E ring (from Mimas to Tethys), where the highest densities are observed, is sustained by Enceladus' south-pole dust source and by ejecta due to ERP, in approximately 5:1 ratio. The dust production by IDPs is by a factor of 100 less efficient than that by the ERPs. Further out, the dust production efficiency by ERPs reduces, while the IDPs produce a comparable amount of dust at all E ring moons. For instance, at Dione the production rates caused by ERPs and IDPs become close. At Rhea the dust production caused by ERPs is reduced by three orders of magnitude compared to that at Enceladus. This means that at Rhea about 10 times more dust can be expected to be produced by IDPs than by ERPs.

Thus, it seems likely that both impactor classes play their role in sustaining the E ring. The IDP contribution dominates the particle production in the outer E ring, possibly explaining the large radial extent of the ring, whereas ERP impacts (and the Enceladus south-pole source, of course) play crucial role in the inner region.

The differences in the predicted dust production rates due to IDPs and ERPs at various moon locations can be verified in future flybys of the Cassini spacecraft with E ring satellites.

## Acknowledgments

The authors wish to thank Antal Juhász and an anonymous referee for the helpful comments in making the paper more convincing. The work has been supported by the *Deutsche Forschungsgemeinschaft (DFG)*: Grants Sp 384/17-2 and Sp 384/18-3, by the *Zentrum für Luft- und Raumfahrt (DLR)*: Grants 50 OH 0003 and 500 OH 91019, and by the *Cassini-UVIS*-project.

## References

Brown, R.H., Clark, R.N., Buratti, B.J., Cruikshank, D.P., Barnes, J.W., Mastrapa, R.M.E., Bauer, J., Newman, S., Momary, T., Baines, K.H., Bellucci, G., Capaccioni, F., Cerroni, P., Combes, M., Coradini, A., Drossart, P., Formisano, V., Jaumann, R., Langevin, Y., Matson, D.L., McCord, T.B., Nelson, R.M., Nicholson, P., Sicardy, B., Sotin, C., 2006. Composition and physical properties of Enceladus' surface from Cassini's visual and infrared mapping spectrometer. Science 311, 1425–1428.

Colombo, G., Lautman, D.A., Shapiro, I.I., 1966. The Earth's dust belt: fact or fiction? 2. Gravitational focusing and Jacobi capture. J. Geophys. Res. 71, 5705–5717.

Colwell, J.E., 1993. A general formulation for the distribution of impacts and ejecta from small planetary satellites. Icarus 106, 536–548.

de Pater, I., Martin, S., Showalter, M.R., 2004. Keck near-infrared observations of Saturn's E and G rings during Earth's ring plane crossing in August 1995. Icarus 172, 446–454.

Divine, N., 1993. Five populations of interplanetary meteoroids. J. Geophys. Res. 98, 17029–17048.

Hamilton, D.P., Burns, J.A., 1994. Origin of Saturn's E ring: self-sustained, naturally. Science 264, 550–553.

Hansen, C.J., Hendrix, A.R., West, R.A., Esposito, L.W., Stewart, A.I.F., Shemansky, D.E., Pryor, W., 2006. Cassini ultraviolet imaging spectrograph (UVIS) investigation of Enceladus' water vapor plume. Science 311, 1422–1425.

Horányi, M., Burns, J.A., Hamilton, D.P., 1992. The dynamics of Saturn's E ring particles. Icarus 97, 248–259.

Housen, K.R., 1991. Laboratory simulations of large-scale fragmentation events. Icarus 94, 180–190.

Housen, K.R., Schmidt, R.M., Holsapple, K.A., 1983. Crater ejecta scaling laws—fundamental forms based on dimensional analysis. J. Geophys. Res. 88, 2485–2499.

Jones, G.H., Roussos, E., Krupp, N., Paranicas2, C., Woch, J., Lagg, A., Mitchell, D.G., Krimigis, S.M., Dougherty, M.K., 2006. Enceladus's varying imprint on the Kronian magnetosphere. Science 311, 1412–1415.

Juhász, A., Horányi, M., 2002. Saturn's E ring: a dynamical approach. J. Geophys. Res. 107, doi:10.1029/2001JA000182.

Kempf, S., Beckmann, U., Srama, R., Horányi, M., Auer, S., Grün, E. 2006. The electro-static potential of E ring particles. Planet. Space Sci., submitted for publication.

Koschny, D., Grün, E., 2001. Impacts into ice-silicate mixtures: crater morphologies volumes depth-to-diameter ratios, and yield. Icarus 154, 391–401.

Krivov, A.V., Sremčević, M., Spahn, F., Dikarev, V.V., Kholshevnikov, K.V., 2003. Impact-generated dust clouds around planetary satellites: spherically symmetric case. Planet. Space Sci. 51, 251–269.

Krivov, A. V., Feofilov, A. G., Dikarev, V. V., 2006. Search for the putative dust belts of Mars: the late 2007 opportunity. Planet. Space Sci., this issue.

Makuch, M., Brilliantov, N. V., Sremcevic, M., Spahn, F., Krivov, A. V., 2006. Stochastic circumplanetary dynamics of rotating non-spherical dust particles. Planet. Space Sci., this issue.

Nicholson, P.D., Showalter, M.R., Dones, L., French, R.G., Larson, S.M., Lissauer, J.J., McGhee, C.A., Sicardy, B., Seitzer, P., Danielson, G.E., 1996. Observations of saturn's ring-plane crossing in August and November 1995. Science 272, 509–516.

Porco, C., Helfenstein, P., Thomas, P., Ingersoll, A.P., Wisdom, J., West, R., Neukum, G., Denk, T., Wagner, R., Roatsch, T., Kieffer, S., Turtle, E., McEwen, A., Johnson, T., Rathbun2, J., Veverka, J., Wilson, D., Perry, J., Spitale, J., Brahic, A., Burns, J., DelGenio, A., Dones, L., Murray, C., Squyres, S., 2006. Cassini images the active south pole of Enceladus. Science 311, 1393–1401.

Showalter, M.R., 1998. Detection of centimeter-sized meteoroid impact events in Saturn's F ring. Science 282, 1099–1102.

Showalter, M., Cuzzi, J., Larson, S., 1991. Structure and particle properties of Saturn's E ring. Icarus 94, 451–473.

Showalter, M. R., Hamilton, D. P., Nicholson, P. D., 2006. A deep search for Martian dust rings and inner moons using the Hubble space telescope. Planet. Space Sci., this issue.

Soter, S., 1971. The dust belts of Mars. Technical Report, Center for Radiophysics and Space Research.

Spahn, F., Thiessenhusen, K.-U., Colwell, J.E., Srama, R., Grün, E., 1999. Dynamics of dust ejected from Enceladus: application to the Cassini dust detector. J. Geophys. Res. 104, 24111–24120.

Spahn, F., Schmidt, J., Albers, N., Hörning, M., Makuch, M., Seiß, M., Kempf, S., Srama, R., Dikarev, V.V., Helfert, S., Moragas-Klostermeyer, G., Krivov, A.V., Sremčević, M., Tuzzolino, A., Economou, T., Grün, E., 2006. Cassini dust measurements at Enceladus: implications for Saturn's E ring. Science 311, 1416–1418.

Spencer, J. R., Pearl, J. C., Segura, M., Flasar, F. M., Mamoutkine, A., Romani, P., Buratti, B. J., Hendrix, A. R., Spilker, L. J., Lopes, R. M. C., 2006. Cassini encounters Enceladus: background and the discovery of a south polar hot spot. Science 311, 1401–1405.

Sremčević, M., Krivov, A.V., Spahn, F., 2003. Impact generated dust clouds around planetary satellites: asymmetry effects. Planet. Space Sci. 51, 455–471.

Sremčević, M., Krivov, A.V., Krüger, H., Spahn, F., 2005. Impact generated dust clouds around planetary satellites: model versus Galileo data. Planet. Space Sci. 53, 625–641.

Wahlund, J.-E., Boström, R., Gustafsson, G., Gurnett, D.A., Kurth, W.S., Averkamp, T., Hospodarsky, G.B., Persoon, A.M., Canu, P., Pedersen, A., Desch, M.D., Eriksson, A.I., Gill, R., Morooka, M.W., André, M., 2005. The inner magnetosphere of Saturn: Cassini RPWS cold plasma results from the first encounter. Geophys. Res. Lett. 32, doi:10.1029/2005GL022699.

Waite Jr., J. H., Combi, M.R., Ip, W.-H., Cravens, T. E., McNutt Jr., R. L., Kasprzak, W., Yelle, R., Luhmann, J., Niemann, H., Gell, D., Magee, B., Fletcher, G., Lunine, J., Tseng, W.-L., 2006. Cassini ion and neutral mass spectrometer: enceladus plume, composition and structure. Science 311, 1419–1422.

# Appendix D

# Cassini Dust Measurements at Enceladus and Implications for the Origin of the E Ring

SPAHN, F., SCHMIDT J., ALBERS N., HÖRNING M., MAKUCH M., SEISS M., KEMPF S., SRAMA R., DIKAREV V., HELFERT S., MORAGAS-KLOSTERMEYER G., KRIVOV, A. V., SREMČEVIĆ, M. TUZZOLINO A. J., ECONOMOU T., GRÜN, E. (2006).
Cassini Dust Measurements at Enceladus and Implications for the Origin of the E Ring. **Science**, Volume 311, Issue 5766, pp. 1416-1418.
doi: 10.1126/science.1121375

REPORT

# Cassini Dust Measurements at Enceladus and Implications for the Origin of the E Ring

Frank Spahn,[1] Jürgen Schmidt,[1]* Nicole Albers,[1] Marcel Hörning,[1] Martin Makuch,[1] Martin Seiß,[1] Sascha Kempf,[2] Ralf Srama,[2] Valeri Dikarev,[2,3] Stefan Helfert,[2] Georg Moragas-Klostermeyer,[2] Alexander V. Krivov,[3] Miodrag Sremčević,[5] Anthony J. Tuzzolino,[6] Thanasis Economou,[6] Eberhard Grün[2,4]

During Cassini's close flyby of Enceladus on 14 July 2005, the High Rate Detector of the Cosmic Dust Analyzer registered micron-sized dust particles enveloping this satellite. The dust impact rate peaked about 1 minute before the closest approach of the spacecraft to the moon. This asymmetric signature is consistent with a locally enhanced dust production in the south polar region of Enceladus. Other Cassini experiments revealed evidence for geophysical activities near Enceladus' south pole: a high surface temperature and a release of water gas. Production or release of dust particles related to these processes may provide the dominant source of Saturn's E ring.

The tenuous E ring is the outermost and largest ring in the saturnian system, consisting of particles with a peak size between 0.3 and 3 μm (*1*). The highest density of the E ring and its smallest vertical extent are both observed close to the orbit of Enceladus (*1*, *2*), which favors this moon as the main source of that faint ring. In situ dust measurements at Enceladus with the dust detector aboard the Cassini spacecraft offer the unique opportunity to learn about this satellite and about dust-production processes at its surface and, ultimately, to shed light on the origin of the E ring.

We report on measurements carried out with the High Rate Detector (HRD) of the Cosmic Dust Analyzer (CDA) during the flyby of Enceladus on 14 July 2005. The detector consists of two thin (28 μm and 6 μm) polyvenylidene fluoride sensors with cross sections of 50 $cm^2$ and 10 $cm^2$ (*3*). Here, we focus on the data collected by the 50-$cm^2$ sensor, which is sensitive for particles with a radius larger than 2 μm. An impacting hypervelocity grain changes the polarization in the sensor volume, resulting in a short, sharp pulse enabling the detector to register up to $10^4$ dust impacts $s^{-1}$ (*4*).

During the flyby, a significant increase in the count rate of dust particles was recorded about 10 min before to about 10 min after the closest approach of the spacecraft to the moon (Fig. 1). The peak count rate was 4 particles $s^{-1}$ at 1 min before the closest approach. Similarly, the Cassini Ion and Neutral Mass Spectrometer (INMS) (*5*) detected water gas, also at a peak rate before the closest approach, albeit with a somewhat smaller offset of 30 s. This gas plume was also seen by the Ultraviolet Imaging Spectrograph (UVIS) (*6*) and, indirectly at an earlier flyby, by the magnetometer (*7*). The time difference between the rate peaks points to a decoupling of gas and dust shortly after both components are released from the satellite surface (*8*). A gas and dust source near the south pole is compatible with these premature maxima of the rates, because the spacecraft approached the moon from the south and came closest to Enceladus at a latitude of ~25°S [figure 1 of (*5*, *9*)]. In contrast, a dust cloud generated by micrometeoroid impacts, as was observed by the Galileo mission around the jovian moons (*10*), would lead to a peak rate directly at the closest approach.

The observed particle count rate constrains the production rate of particles at Enceladus, while the time offset of its maximum from the closest approach can be used to locate those regions on the moon's surface from which the particles originate. Comparing the data to theoretical models of dust production, we can estimate the relative contributions of alternative mechanisms of particle creation, yielding implications for the dominant source of the E-ring particles. Besides geophysical processes (*11*, *12*), micrometeoroid bombardment has been proposed as a particle-creation process (*13*). Two families of micrometeoroids are relevant at Enceladus, namely E-ring particles and interplanetary dust particles. The typically large velocities of such projectiles relative to the moon, from a few to tens of kilometers per second, make the impacts energetic enough to abundantly produce ejecta at the moon's surface and create a dust cloud (*10*, *14*). However, the detection of an anomalously high temperature (*9*) in the south polar region of Enceladus near elongated cracked fractures (*15*) (dubbed "tiger stripes") lends new support to the idea of E-ring dust particles created by cryovolcanism (ice volcanoes).

We have modeled the distributions of dust in the vicinity of Enceladus for cases of isotropic ejection of grains from the entire surface and for a localized dust source at the south pole of the moon (Fig. 1). These two cases correspond to the particle production by the impactor-ejecta mechanism and by geological processes at the south pole, respectively. Because the spacecraft's trajectory near the closest approach (168.2 km above the surface) lies well inside the Hill sphere (*16*) of gravitational influence of the moon [$r_H \sim 948$ km, compared with a radius of 252.1 km (*15*)], an analytical model for the dust cloud developed in (*17*), based on the two-body approximation, should give an adequate estimate (*18*). However, to account for the full three-body dynamics near the Hill scale, we have numerically simulated the dust configuration around the satellite for both source models. In the simulations, particle paths are integrated subject to Saturn's and Enceladus' gravity (*18*, *19*). In both simulations, 1 million particles are launched from the satellite's surface, with starting conditions that are plausible for particles created in an impactor-ejecta process (*20*, *21*). To simulate the impactor-ejecta source, the starting positions are chosen uniformly over the entire surface of the moon. The localized source is simulated with starting positions distributed uniformly in a circular area of an angular diameter of 30° centered at the south pole, which is on the order of the size of the hot region (*9*). The motion of the particles governed by the gravity of the planet and the satellite does not depend on the particles' mass or radius; thus, grains with different radii need not be distinguished in the simulations. Therefore, the size distribution in the model dust cloud near the moon derives from the particle size distribution assumed for the particle-creation process.

In the simulations, the impactor-ejecta process is found to generate a highly symmetric dust configuration in the vicinity of the satellite, as expected, so that the HRD on a flyby through this cloud would observe a maximal count rate directly at the closest approach (Fig. 1A). In contrast, the simulated dust ejection from the south pole source reproduces well the observed maximal count rate 1 min before the closest approach.

[1]Institut für Physik, Universität Potsdam, Am Neuen Palais 10, Haus 19, D-14469 Potsdam, Germany. [2]Max Planck Institut für Kernphysik, Saupfercheckweg 1, 69117 Heidelberg, Germany. [3]Astrophysikalisches Institut, Friedrich Schiller Universität, 07745 Jena, Germany. [4]Hawaii Institute of Geophysics and Planetology, University of Hawaii, Honolulu, HI 96822, USA. [5]Laboratory for Atmospheric and Space Physics, University of Colorado, Boulder, CO 80303, USA. [6]Laboratory for Astrophysics and Space Research, University of Chicago, Chicago, IL 60637, USA.

*Corresponding author: jschmidt@agnld.uni-potsdam.de

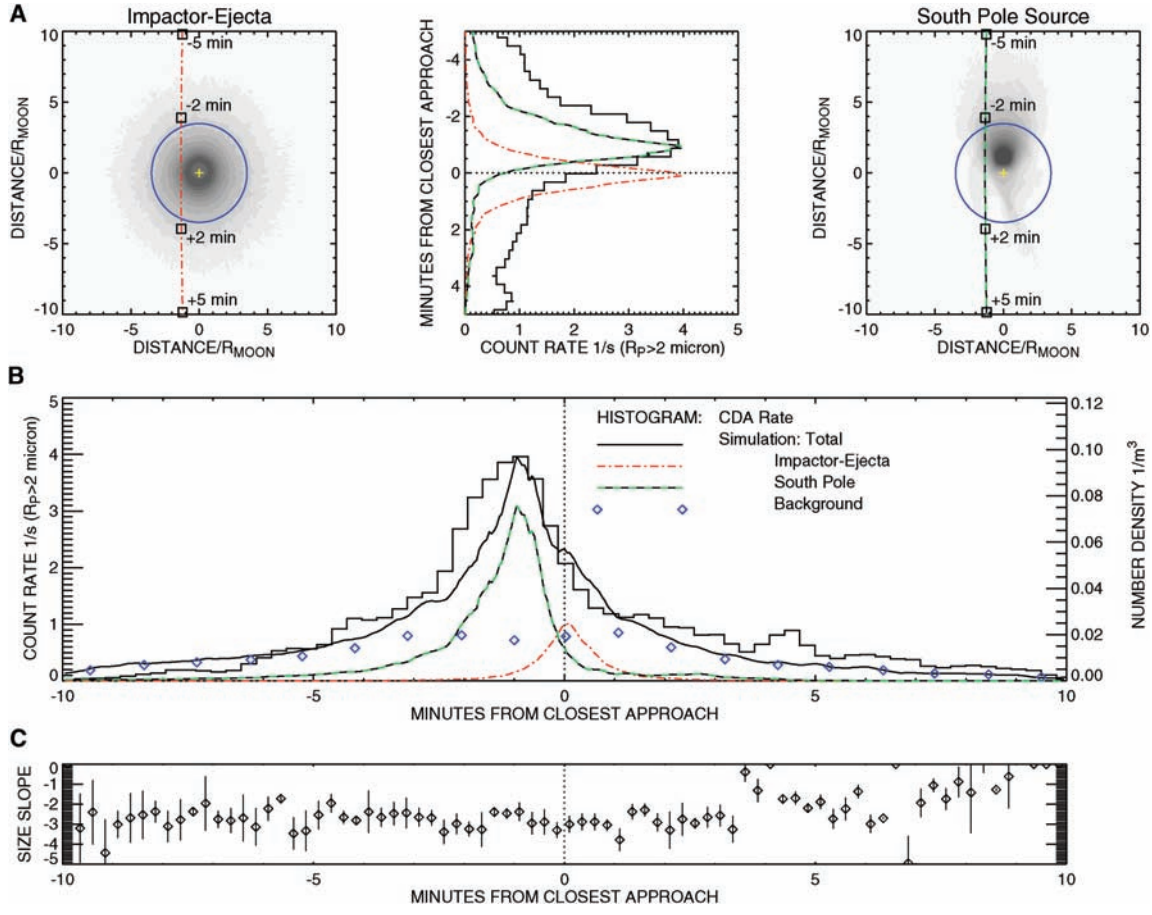


**Fig. 1.** Comparison of the CDA data to simulations. (**A**) Particle density in the plane of Cassini's trajectory estimated from simulations, darker shades referring to a higher density. The impactor-ejecta process (left) leads to a more symmetric dust cloud, whereas a localized source at the south pole of the moon (right) shows a strong asymmetry. Circles denote the intersection of the plane with the Hill sphere of gravitational influence, and the normal projection of the moon's center (not in that plane) is marked by a cross symbol. Cassini's trajectory is plotted as a dash-dotted or dashed line, respectively. The central plot shows the count rates predicted by the simulations computed along the actual spacecraft trajectory, both normalized to the peak rate of the data shown in histogram mode. (**B**) The sum of the rates derived from the two simulations and the simulated E-ring background, normalized to the observed peak rate. The maximal strength of the impactor-ejecta process relative to that of the south pole source is chosen in a way that no secondary peak develops in the combined rate near the closest approach. (**C**) The slopes of the differential size distribution $n\ (R_p) \propto R_p^{\alpha}$ versus time to the closest approach. The increase of $\alpha$ for $t > 4$ min is due to a maneuver of Cassini and the related change in the instrument's boresight.

Fitting combinations of both contributions with a consistent E-ring particle background to the data, and requiring that no second peak develops in the rate at the closest approach, we can estimate the maximal strength of the impactor-ejecta dust creation at Enceladus relative to that of the south pole source (Fig. 1B). From this fit (HRD data for $R_p > 2$ μm), we can infer the rate of particles larger than 2 μm emitted by the south pole source and escaping the moon's gravity to amount to $5 \times 10^{12}$ particles $s^{-1}$, whereas the impactor-ejecta mechanism would produce at most $10^{12}$ such particles $s^{-1}$. These numbers correspond to an escaping mass of at least 0.2 kg $s^{-1}$, assuming $R_p = 2$ μm for all grains. For an extended size distribution, this rate may extend to kilograms per second. The E-ring particle background, which is naturally contained in the HRD data, has been simulated, following the motion of particles subject to gravity and perturbation forces (*18*, *19*), until they are lost in collisions with Enceladus, other E-ring moons, or the main rings. A self-consistent combination of the simulated dust populations is in reasonable agreement with the observed HRD rate (Fig. 1B).

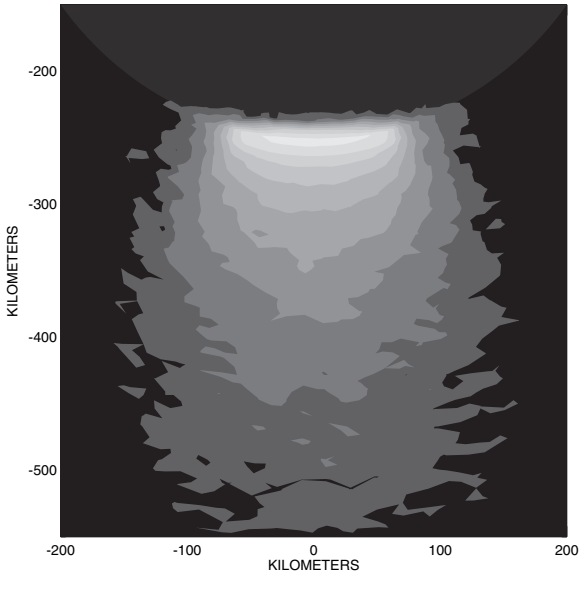


**Fig. 2.** Side view of a simulated dust plume at Enceladus' south pole. Contours of equal column particle density are shown in a Cartesian frame fixed at the center of the moon. The brightest contour denotes $10^7$ particles per $m^2$, the column density dropping by one-half from level to level.

A differential particle size distribution inferred from the data of both HRD sensors fits to a power law $n\ (R_p) \propto R_p^{\alpha}$ with a slope $\alpha \sim -3$ that remains almost constant during the flyby (Fig. 1C). This near constance of the exponent indicates that the dynamics of larger grains is

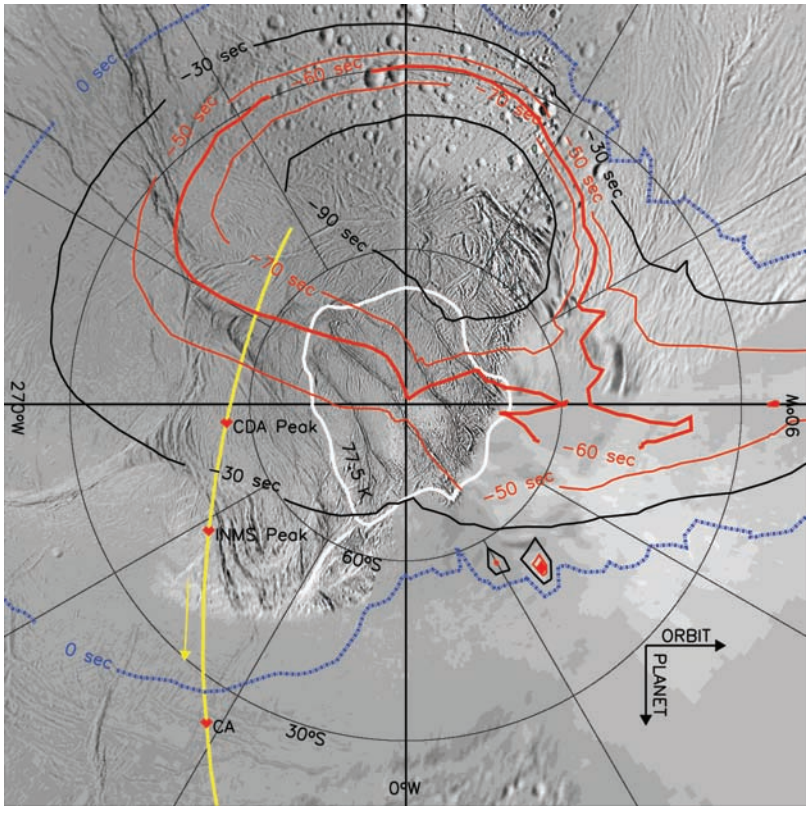


**Fig. 3.** Results of a series of simulations where the position of the source is varied systematically over the moon's surface. For each simulation, the particle count rate along the Cassini trajectory is computed. The contours of equal time offsets of the maximal count rate from the closest approach are plotted over a base map of Enceladus' south pole (*15*). The thick red line marks the contour of a –60-s offset of the maximal count rate, which was about the value observed by the CDA. Other contours correspond to offsets of –90, –70, –50, –30, and 0 s. The white line around the pole denotes the 77.5-K isotherm from the Composite Infrared Spectrometer (*9*). Cassini's ground track is shown in yellow, and the times of rate maxima of the CDA (–50 s) and INMS (–30 s) (*5*), as well as the closest approach (CA), are marked.

dominated by gravity. Such a power law is expected for an impactor-ejecta particle formation scenario (*20*). On the other hand, we showed that the south pole source should be the dominant source of particles. A possible explanation would be that the particles are formed in meteoroid impacts and lifted by south polar gas venting. However, an effective acceleration of grains in the gas plume seems implausible for the gas densities inferred from UVIS (*6*, *15*).

A side view of the dust configuration from the simulation of the south pole source is shown in Fig. 2, where the absolute numbers are fixed by HRD data at the closest approach. A similarly strong stratification of the dust density is evident in images of the dust plume (*15*). In the simulation, the stratification results basically from the power-law distribution of particle starting velocities (*21*).

To investigate the influence of the particle source location on the rate profile measured by HRD, we performed a series of about 2600 simulations, where the source position was systematically varied over the moon's surface. Here, we used 50,000 particles per simulation, employing for simplicity the initial conditions for the impactor-ejecta mechanism (*20*). For each source, we determined the time offset of the peak count rate to the closest approach for this flyby. In this way, we obtained a contour map of offset times over the moon's surface, which is plotted over an Image Science Subsystem base map (*15*) of the geologically active south pole region in Fig. 3. It was found that only a small part of the total surface of Enceladus can have sources that would match the actually observed offset of –1 min. Interestingly, the region of the tiger stripes (covering latitudes > 70°S) is indeed compatible with the data, yielding offsets from –50 to –70 s.

On the basis of simulations of the dust environment around Enceladus, we conclude that the Cassini CDA data of the Enceladus flyby on 14 July are compatible with a dust source in the south polar region of the moon. A particle ejection mechanism caused by hypervelocity micrometeoroid impacts alone cannot explain the data. New in situ measurements of Enceladus' dust cloud will be obtained during a flyby in 2008 at an altitude of only 100 km over 69°N.

### References and Notes


1. P. D. Nicholson *et al.*, *Science* **272**, 509 (1996).
2. M. R. Showalter, J. N. Cuzzi, S. M. Larson, *Icarus* **94**, 451 (1991).
3. R. Srama *et al.*, *Space Sci. Rev.* **114**, 465 (2004).
4. This property of the HRD becomes crucial in regions of high particle density (parts of the E ring and in the vicinity of its source satellites) where the impact ionization detector of the CDA is saturated.
5. J. H. Waite Jr. *et al.*, *Science* **311**, 1419 (2006).
6. C. J. Hansen *et al.*, *Science* **311**, 1422 (2006).
7. M. K. Dougherty *et al.*, *Science* **311**, 1406 (2006).
8. Early decoupling of gas and dust is in accordance with the reported low gas densities [Knudsen regime (*5*)] found in the gas plume (*6*), making molecule-dust collisions unlikely during the time (tens of minutes) from ejection to the impact of the grain at the HRD.
9. J. R. Spencer *et al.*, *Science* **311**, 1401 (2006).
10. H. Krüger, A. V. Krivov, D. P. Hamilton, E. Grün, *Nature* **399**, 558 (1999).
11. P. K. Haff, G. L. Siscoe, A. Eviatar, *Icarus* **56**, 426 (1983).
12. J. S. Kargel, S. Pozio, *Icarus* **119**, 385 (1996).
13. J. E. Colwell, *Icarus* **106**, 536 (1993).
14. M. Sremčević, A. V. Krivov, H. Krüger, F. Spahn, *Planet. Space Sci.* **53**, 625 (2005).
15. C. C. Porco *et al.*, *Science* **311**, 1393 (2006).
16. Within the Hill sphere, the satellite's gravity dominates Saturn's gravity. The Hill radius is defined in terms of the masses of Saturn $M_S$ and Enceladus $M_E$, and of the distance $a_E$ between them, as $r_h = a_E \sqrt[3]{M_E/3(M_S + M_E)}$.
17. M. Sremčević, A. V. Krivov, F. Spahn, *Planet. Space Sci.* **51**, 455 (2003).
18. Materials and methods are available as supporting material on *Science* Online.
19. Perturbation forces (Saturn's oblateness, Lorentz force, and radiative forces) are crucial for the long-term dynamics of the particle and the configuration of the E ring (*22*–*26*). They can be neglected for the simulation of dust in the vicinity of Enceladus.
20. A. V. Krivov, M. Sremčević, F. Spahn, V. V. Dikarev, K. V. Kholshevnikov, *Planet. Space Sci.* **51**, 251 (2003).
21. Initial velocities follow a cumulative power law $N\,(>v) \propto v^{-2}$, $0.15\ v_{esc} < v < 2\ v_{esc}$, where $v_{esc} \sim 239$ m s$^{-1}$ is Enceladus' escape velocity. Starting directions are uniformly distributed in a cone of semi-opening angle of 25° normal to the surface at the starting location.
22. M. Horányi, J. A. Burns, D. P. Hamilton, *Icarus* **97**, 248 (1992).
23. D. P. Hamilton, J. A. Burns, *Science* **264**, 550 (1994).
24. V. V. Dikarev, *Astron. Astrophys.* **346**, 1011 (1999).
25. F. Spahn, K.-U. Thiessenhusen, J. Colwell, R. Srama, E. Grün, *J. Geophys. Res.* **104**, 24111 (1999).
26. A. Juhász, M. Horányi, *Geophys. Res. Lett.* **31**, 19703 (2004).


27. We thank T. V. Johnson for comments on the manuscript. The Potsdam group was supported by Deutsche Forschungsgemeinschaft grants Sp 384/16, Sp 384/17, and Sp 384/18; Deutsches Zentrum für Luft und Raumfahrt (DLR) grant 50OH0003; and the Studienstiftung des deutschen Volkes. The group at the Max Planck Institut für Kernphysik was supported by the Max Planck Society and by DLR under grant 50OH9802. The work in Chicago was supported by Jet Propulsion Laboratory contract 96 11 70, and M. Sremčević is funded by the Cassini UVIS project.


**Supporting Online Material**

www.sciencemag.org/cgi/content/full/311/5766/1416/DC1
Materials and Methods
Figs. S1 to S7
References

14 October 2005; accepted 19 January 2006
10.1126/science.1121375

# Appendix E

# Supporting Online Material for Paper D

SPAHN, F., SCHMIDT J., ALBERS N., HÖRNING M., MAKUCH M., SEISS M., KEMPF S., SRAMA R., DIKAREV V., HELFERT S., MORAGAS-KLOSTERMEYER G., KRIVOV, A. V., SREMČEVIĆ, M. TUZZOLINO A. J., ECONOMOU T., GRÜN, E. (2006).
Supporting Online Material for Cassini Dust Measurements at Enceladus and Implications for the Origin of the E Ring. **Science**, Volume 311, Issue 5766, pp. 1416-1418
www.sciencemag.org/cgi/content/full/311/5766/1416/DC1

www.sciencemag.org/cgi/content/full/311/5766/1416/DC1

# Supporting Online Material for

## Cassini Dust Measurements at Enceladus and Implications for the Origin of the E Ring

Frank Spahn,* Jürgen Schmidt, Nicole Albers, Marcel Hörning, Martin Makuch, Martin Seiß, Sascha Kempf, Ralf Srama, Valeri Dikarev, Stefan Helfert, Georg Moragas-Klostermeyer, Alexander V. Krivov, Miodrag Sremčević, Anthony J. Tuzzolino, Thanasis Economou, Eberhard Grün

*To whom correspondence should be addressed. E-mail: fspahn@agnld.uni-potsdam.de

Published 10 March 2006, *Science* **311**, 1416 (2006)
DOI: 10.1126/science.1121375

**This PDF file includes:**

# Supporting Online Material for

## Cassini Dust Measurements at Enceladus: Implications for the Origin of the E Ring

Frank Spahn,* Jürgen Schmidt, Nicole Albers, Marcel Hörning,
Martin Makuch, Martin Seiß,
Sascha Kempf, Ralf Srama, Valeri Dikarev,
Stefan Helfert, Georg Moragas-Klostermeyer,
Alexander V. Krivov, Miodrag Sremčević,
Anthony Tuzzolino, Thanasis Economou, Eberhard Grün

*To whom correspondence should be addressed, E-mail:
fspahn@agnld.uni-potsdam.de

**File includes:**
Materials and Methods
Figs. S1 to S7
Notes and References

## Introduction

In this appendix we provide additional material, methods and information which had been necessary to perform the analyses presented in the main paper. This concerns mainly information about the impactor ejecta process, the spatial ejecta-distribution and the dust dynamics in order to obtain the dust configuration around the satellite Enceladus, which is material mentioned only marginally in the main paper.

## The Impactor-Ejecta Mechanism

Micrometeroid impacts in the solar system are energetic enough to abundantly lift debris and dust particles from the moon's surfaces. A model of an impact-generated steady-state dust cloud around an atmosphereless planetary satellite has been developed [1, 2]. In this model, dust grains are ejected within a cone of an opening angle $\Delta\alpha$. Their initial velocity is determined by the distribution $f_v$ of ejection speed $v$

$$f_v \;=\; \frac{1}{v_0}\left(\frac{v}{v_0}\right)^{-q}\Theta[v-v_0] \tag{1}$$

and ejection angle $\alpha$, filling the cone uniformly, as shown in Fig. S1. The Heaviside function is labeled by $\Theta[v-v_0]$ restricting the range of velocities to the interval $(v_0,\infty)$. The slope of the power law has been chosen as $q \in (2,3)$ depending on whether the surface is covered by regolith or consists of solid ice.

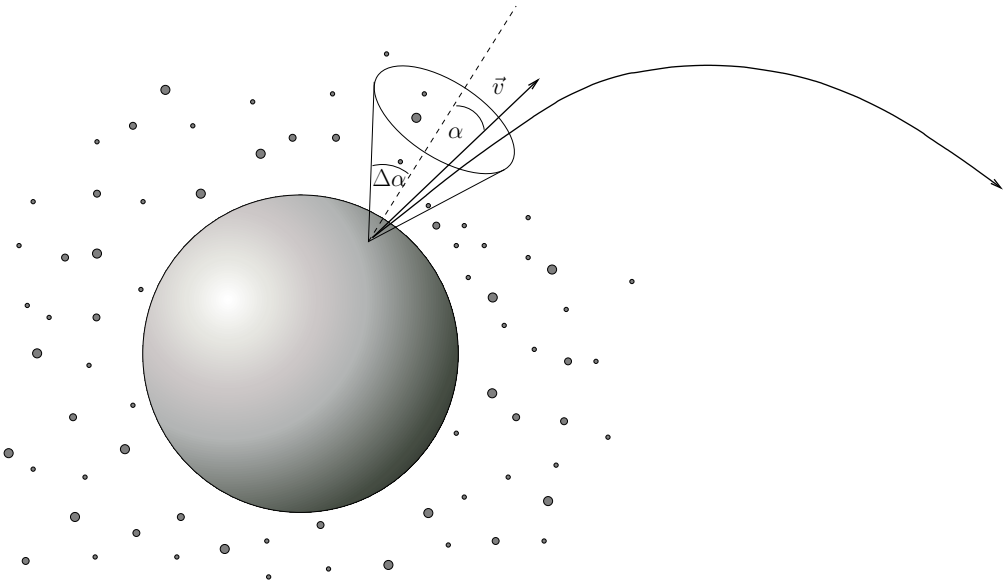


Figure S1: Geometry of the ejection process.

Within the Hill sphere of radius $r_h$, which denotes Enceladus' range of gravitational influence,

$$r_h = a_E \sqrt[3]{\frac{M_E}{3(M_E + M_S)}} \tag{2}$$

all perturbing forces besides the moon's gravity are negligibly small and were neglected [1, 2] to describe the dust clouds around atmosphereless celestial bodies. The masses of Saturn, Enceladus and the semi-major axis of the latter are denoted by $M_S$, $M_E$ and $a_E$, respectively. The comparison of the analytical model to data obtained with the Galileo dust detector [3, 4] proved the existence of these dust clouds for the Galilean moons.

Although the dynamics of a dust grain in the vicinity of Enceladus is almost independent of the mass $m$ (mass-dependent perturbations are negligibly small inside the Hill sphere), the size distribution remains an important characteristics of the dust production process. For the impactor ejecta mechanism a power law has been derived from field experiments and theoretical studies (for details see Krivov et al. [1])

$$N^+(> R_p) \;\propto\; R_p^{-12/5} \quad , \tag{3}$$

for the number of particles larger than a certain radius $R_p$.

The size distribution can be derived from HRD data yielding a power law $N^+ \approx R_p^{-b}$ $[b \in (2.5, 3.0)]$ representing a dependency often observed for geophysical processes.

## Equations of motion and perturbation forces

After the particles have been created and lifted off from the surface of their parent body they are governed by forces acting in Saturn's environment.

In the direct vicinity of a satellite the dynamics of a particle is affected mainly by the gravity of the satellite and to smaller extent by the planet described by the three-body problem

$$\ddot{\mathbf{r}} \;=\; G\,\nabla\left(\frac{M_S}{|\mathbf{r}-\mathbf{r_S}|} + \frac{M_E}{|\mathbf{r}-\mathbf{r_E}|}\right) \tag{4}$$

where $G$ is the gravitational constant. The positions of the dust particle, and Saturn's and Enceladus' center are labeled by $\mathbf{r}, \mathbf{r_S}$, and $\mathbf{r_E}$. Trajectories were integrated using Eqs. (4) until the particles leave Enceladus' vicinity (we define as the region inside 5 $r_h$) or until they fall back on the moon's surface. Analytical expressions for the flux of dust originating at Enceladus can be derived if Saturn's tides, the first term in Eqs. (4), were neglected. This is an useful description for the region inside Enceladus' Hill sphere discussed in figure S2. In order to obtain the dust impact rates expected at the Cassini-HRD in a

larger domain around the satellite Eqs. (4) must be solved numerically. These results are discussed below in the context with figure S3.

For the simulation of the E ring background, which is an important contribution to the HRD signal besides the dust coming directly from Enceladus, non-gravitational perturbations have to be taken into account in order to address the long-term dynamics of an E ring grain from its creation until its annihilation at the certain sinks. The complete equations of motion read [6, 8]

$$\begin{aligned}
\ddot{\mathbf{r}} &= G\nabla\left(\frac{M_S}{|\mathbf{r}-\mathbf{r_S}|}-\frac{M_S R_S^2}{|\mathbf{r}-\mathbf{r_S}|^3}\mathcal{J}_2\mathcal{P}_2(\cos\theta)+\frac{M_E}{|\mathbf{r}-\mathbf{r_E}|}\right)\\
&+\frac{Q}{m}\left(\mathbf{E}+\dot{\mathbf{r}}\times\mathbf{B}\right)\\
&-\frac{Q_{PR}}{m}\frac{\pi R_p^2}{c}q_\odot\left(\frac{R_\oplus}{R}\right)^2\mathbf{e}_\odot\\
&-\pi\, n_I\, m_I\, R_p^2\, u^2\,\mathbf{e_u}
\end{aligned}\tag{5}$$

where the acceleration terms signify in the order or their appearance the gravity of oblate Saturn and Enceladus, the Lorentz force, solar radiation pressure, and plasma drag. The angle $\theta$ denotes the angular distance of the particle's position $(\mathbf{r}-\mathbf{r_S})$ from the north pole $\mathbf{e}_z$. The second harmonic $J_2 \approx 1.67\cdot 10^{-2}$ measures the oblateness of Saturn responsible for the deviations of its potential from spherical symmetry. The opposing dynamical effects of Saturn's oblateness and the Lorentz force select the 1 micron particles to make up mainly the E ring, its shape and extent [7]. Here we are interested in larger particles ($R_p > 2\mu$m) registered by the HRD which stay closer to their sources.
The induced electric $\mathbf{E}$ and the magnetic field $\mathbf{B}$ are given by

$$\begin{aligned}
\mathbf{E} &= \{(\mathbf{r}-\mathbf{r_S})\times\mathbf{\Omega}_S\}\times\mathbf{B}\\
\mathbf{B} &= \frac{\mathbf{B_0}}{|\mathbf{r}-\mathbf{r_S}|^3}-\frac{3(\mathbf{r}-\mathbf{r_S})\left[\mathbf{B}\cdot(\mathbf{r}-\mathbf{r_S})\right]}{|\mathbf{r}-\mathbf{r_S}|^5}
\end{aligned}\tag{6}$$

where $\mathbf{\Omega}_S = 1.64\cdot 10^{-4}$ sec$^{-1}$ and $\mathbf{B_0} = B_0 R_S^3 \mathbf{e}_z$ with $B_0 = -2\cdot 10^{-5}$Vs m$^{-2}$ are Saturn's rotation period and dipole moment, respectively.

The speed of light, radiation pressure coefficient, and the solar constant are denoted by $c, Q_{PR}$, and $q_\odot = 1.37$ kW m$^{-2}$, respectively. The distances Sun-particle and Sun-Earth are given by $R = |\mathbf{r}-\mathbf{r}_\odot|$ and $R_\oplus$. The vector $\mathbf{e}_\odot$ points from the particle to the Sun, i.e. the direct radiation pressure force acts in anti-Sun direction.
The direct plasma drag is essentially determined by the density $n_I$ and mass $m_I$ of heavy ions and the relative velocity $\mathbf{u} = \dot{\mathbf{r}} - \mathbf{\Omega}_S\times(\mathbf{r}-\mathbf{r_S})$ between the dust-grain and the plasma. For the E ring of Saturn the indirect Coulomb drag component is negligibly small and the grain velocities are supersonic, $|\mathbf{u}|/v_{th} \gg 1$ ($v_{th}$ – thermal speed of heavy ions). Thus, we can apply the simple formulation of the plasma drag [8] in Eq. (5).

Equations (5) have been solved numerically for grains of certain sizes ($1, 2, 3, 4, ...10\mu$ m) just emitted from the moon's surface at rates corresponding to both creation processes. This gives $\approx 10^{13}\mathrm{s}^{-1}$ particles escaping the gravity of Enceladus. Their trajectories were followed until the particles hit Enceladus, other E ring moons or they reach the main rings. The phase space coordinates of each particle were stored in equidistant time-intervals. In this way a stationary phase-space density $n(\mathbf{r}, \dot{\mathbf{r}})$ of the population can be constructed from which the impact rate onto the Cassini HRD of larger particles ($R_p > 2\mu$m) in the vicinity of Enceladus' orbit can be calculated. Using this, contributions of freshly ejected particles at Enceladus originating from the impactor-ejecta process and the south-pole source have been combined with the E ring background to give the total model rate (see Fig. 1, main paper) expected at the Cassini HRD.

## Localized ejecta start positions

In the main paper the comparison between the expected dust impact rates with the Cassini HRD data is presented and the moment of maximum-rate is outed as a decisive quantity. In order to relate this moment in time with a certain dust source region at Enceladus' surface various simulations based upon the two-body as well as the three body equations of motion have been performed. Figs. S2 and S3 depict the time offset of the moment of the rate-maximum from the closest approach for various ejection points on Enceladus' surface by different colors. The actual Cassini flyby trajectory is projected onto the surface (blue line) and the point of closest approach is especially marked (red point). The two different presentations base upon the two-body problem (first term in Eq. (4) neglected, Figure S2) and the three-body problem (4) (Figure S3).

According to the results of the flyby E11 the regions from which the dust grains most likely originate from are shown in red, corresponding to the observed time offset of -1 minute of the maximum peak rate to that of the closest approach. In addition the brightness measures the intensity of the dust flux expected at the dust-detector where dark and bright signify small and large fluxes at the HRD corresponding to a low and a high efficiency of the source region, respectively.

From the Figures S2 and S3 one may deduce that both approaches, the two-body as well as the three-body description, lead to comparable results. This means that the analytical solution in terms of the two-body problem provides reasonably good results for flyby sections well inside the Hill-sphere of gravitational influence, which applies to Cassini's position when the maximum rate occurred (red areas in the plot).

## Influence of start positions and velocities

In order to study the source region we performed simulations where dust grains were ejected according to a 2D Gaussian distribution of start positions from the satellite's surface with the mean at the south pole. Then, the size of the source region is characterized by the standard deviation $\sigma$. Using a 2D Gaussian or a uniform distribution – as in the main paper – yields nearly the same impact rates along the flyby trajectory (Fig. S4). The influences of width $\sigma$, cone opening angle $\Delta\alpha$, and the maximum ejecta speed $v_{\max}$ on the impact rate and offset times are illustrated in Figs. S5, S6, and S7.

# References


[1] A. Krivov, M. Sremčević, F. Spahn, *Planet. Space Sci.*, **51**, 251 (2003).

[2] M. Sremčević, A. Krivov, F. Spahn, *Planet. Space Sci.*, **51**, 455 (2003).

[3] H. Krüger, A. Krivov, M. Sremčević, E. Grün, *Icarus*, **164**, 170 (2003).

[4] M. Sremčević, A. Krivov, H. Krüger, F. Spahn, *Planet. Space Sci.*, **53**, 625 (2005).

[5] D. Hamilton, J. Burns, *Science*, **264**, 550 (1994).

[6] F. Spahn, K.-U. Thiessenhusen, J. E. Colwell, R. Srama, E. Grün, *J. Geophys. Res.*, **104**, 24 111 (1999).

[7] M. Horányi, J. A. Burns, D. P. Hamilton, *Icarus* **97**, 248 (1992).

[8] V. V. Dikarev, *Astron. Astrophys.* **346**, 1011 (1999).

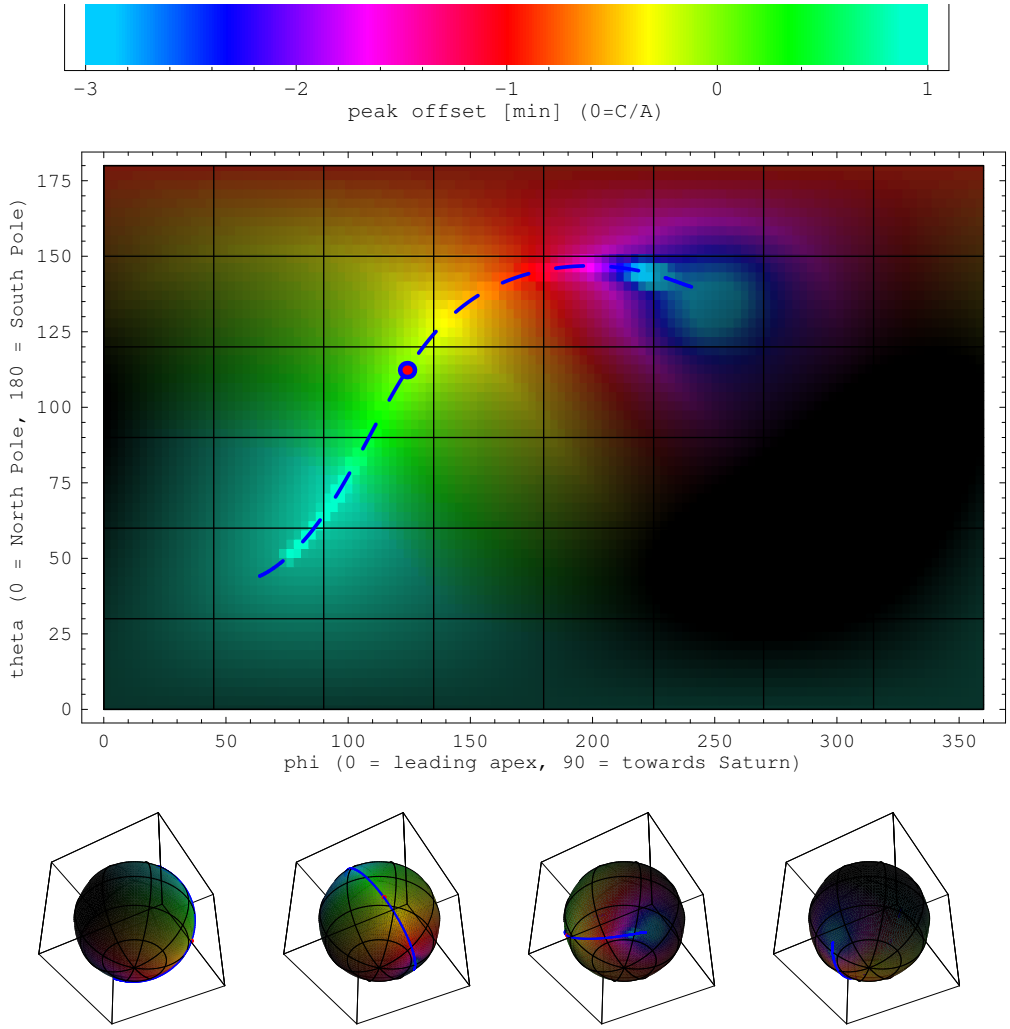


Figure S2: Analytical solution in terms of the two-body problem similar to models of [1, 2], but with dust particles produced from a surface point instead of an extended area. A point source on the surface of the moon in spherical coordinates at $(\theta, \phi)$ has been chosen with a non-zero cone opening angle in the interval $[0°, 45°]$ and a mean $\langle \Psi \rangle \approx 9°$ strongly favoring normal ejecta, and the velocities are assumed to obey a differential power law distribution with index $-3$. With these assumptions, the time offset with respect to the closest approach is represented by colors (color scale above). Brighter and darker regions refer to stronger and weaker impact signals and thus give information about the relative efficency of a source at given location. Clearly the bright regions are expected close to the ground-track of the Cassini trajectory, indicated by the blue dashed line where the red dot is the moment of closest approach. Dark regions are located diametrically opposite from the trajectory track. The closest approach is just where the offset time is zero (green area). The lower panels provide a 3D illustration of the color coded time offset with a view onto the south pole of Enceladus (from left to right: rotations of 90° from leading apex to the side opposite to Saturn).

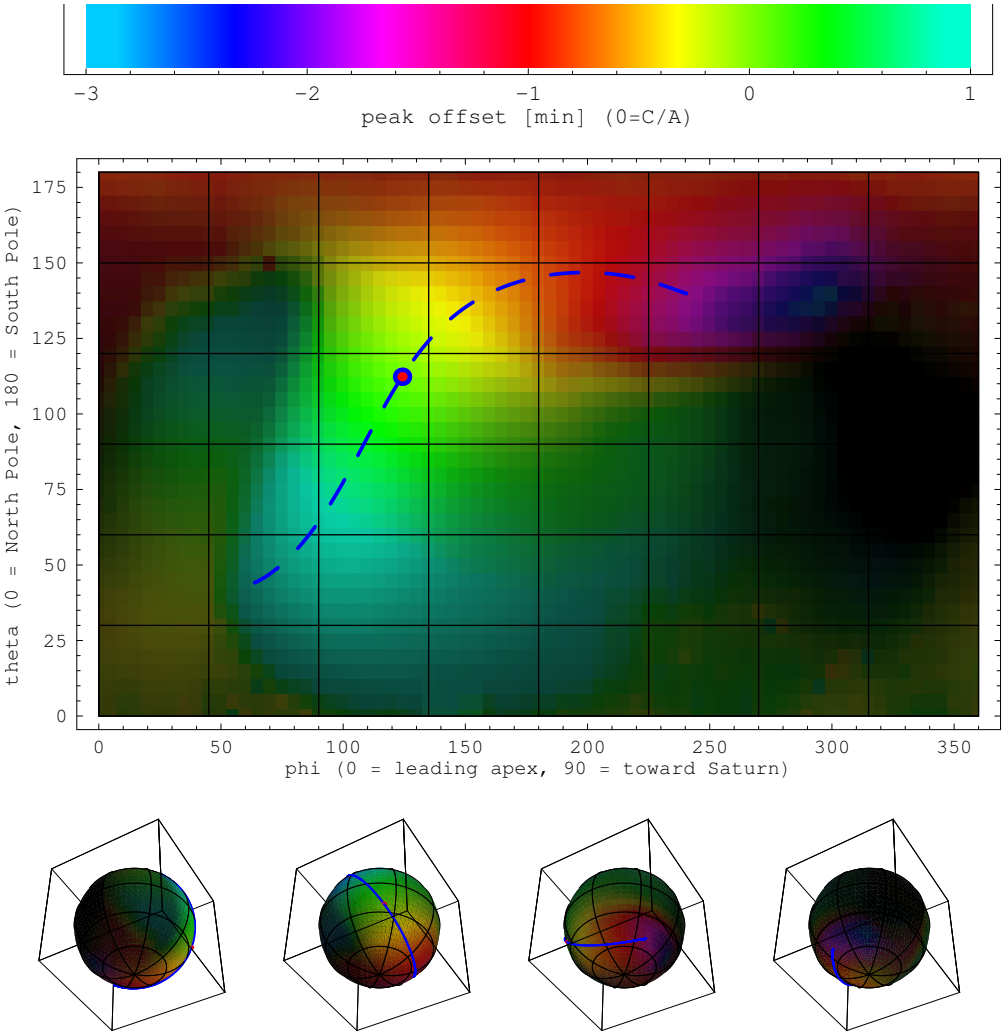


Figure S3: Numerical solution of the full three-body problem [Eqs. (4)] using the same notation and illustration as in Fig. S2. The ejected dust grains originate from a small surface area of a (semi-) angular width of $\xi = 15°$ with an ejecta cone opening angle of 25°. Within this area the start positions are distributed isotropically and a differential power law velocity distribution with index $-2$ was used. The overall picture is similar to the analytic solution (Fig. S2). The main differences arise since the analytic solution is considering the two-body problem and is thus applicable within the Hill sphere (corresponding to just $\pm 90$ seconds around closest approach).

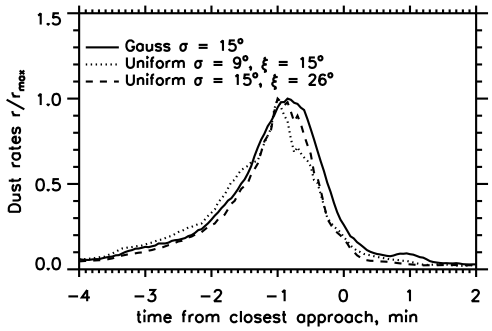


Figure S4: Comparison between a 2D Gaussian and a uniform distribution of the ejecta starting positions on the surface. In the latter case particles were ejected from a source region of (semi-) angular width of $\xi$. Using the same standard deviation ($\sigma = \sqrt{\langle \xi^2 \rangle - \langle \xi \rangle^2}$) yields similar impact rates along the flyby trajectory.

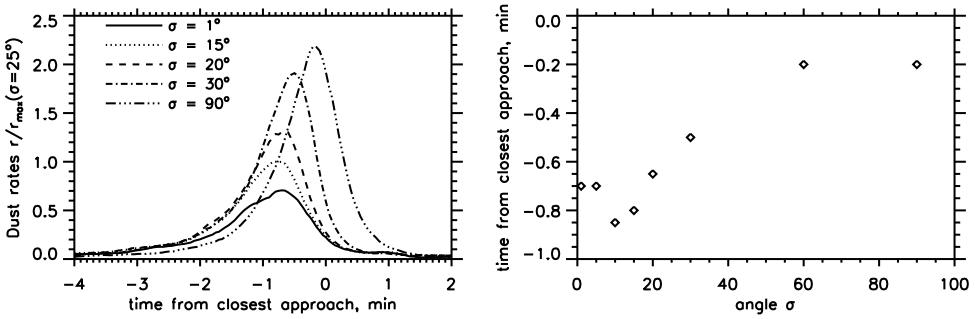


Figure S5: Dependence of impact rate and offset time on the standard deviation $\sigma$ of the 2D Gaussian distribution. It has been varied for angles of 1°, 5°, 10°, 15°, 20°, 30°, 60°, and 90°. The left panel shows the dust rate along the flyby trajectory for different width angles $\sigma$. The rates are normalized with respect to the maximum rate of the model presented in the main paper ($\sigma = 15°$, $\Delta\alpha_{max} = 25°$, differential power law for the velocity dependence in the range of 0.5 until 2.0 escape velocities with a power law index of -2). The rate maxima increase with growing $\sigma$. The right panel shows the offset time for different angles $\sigma$. The largest modulus of the offset time is obtained for a width of about 10°. For larger widths the offset time approaches zero. This can be understood by considering that large $\sigma$ correspond to the isotropic case.

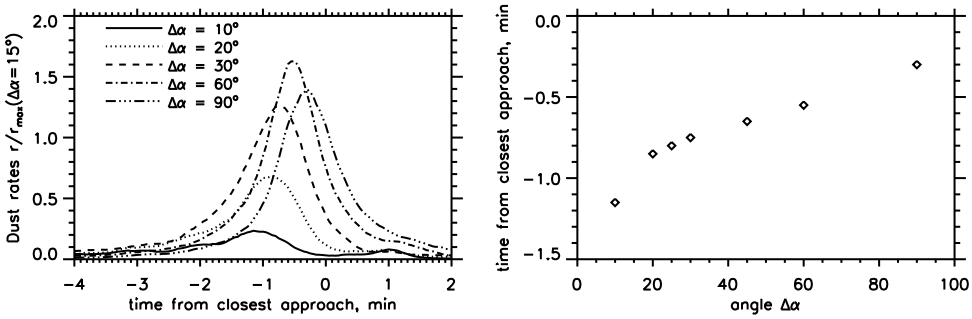


Figure S6: Dependence of impact rate and offset time on the maximum opening-angle of the ejecta cone. The ejecta cone angle $\Delta\alpha$ has been varied as 10°, 20°, 25°, 30°, 45°, 60° and 90°. The left panel shows the respective dust rate along the flyby trajectory. The rates are normalized as in Fig. S5. The maximum rate can be found for $\Delta\alpha \approx 60°$ being an optimum for this trajectory. A wider ejection cone results in an decreased offset time (right panel) and larger rate maxima. According to these tests the value $\Delta\alpha = 30°$ yields the best agreement with the observed HRD-rate.

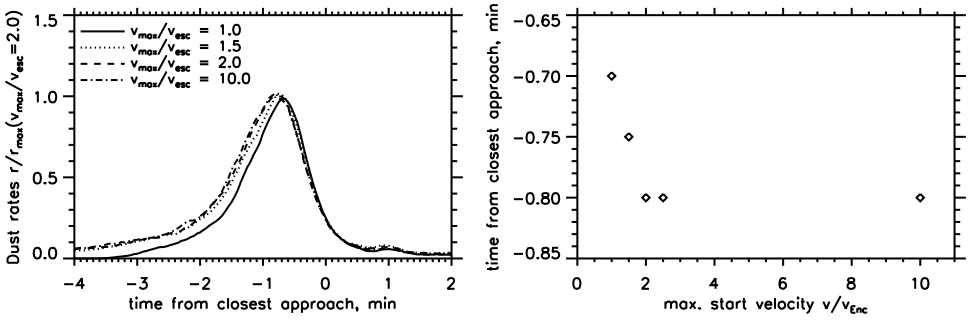


Figure S7: Dependence of impact rate and offset time on the maximum ejecta velocity. Values of 1.0, 1.5, 2.0, 2.5 and 10.0 escape velocities have been used for the maximum of the velocity distribution $v_{max}$. The left panel shows the dust rate along the flyby trajectory for different maximum velocities. The rates are normalized as in Fig. S5. The right panel shows the offset time which is decreasing for $v_{max} < 2.0$ but leveling off for $v_{max} > 2.0$.